PROGRESS IN RESEARCH

April 1, 2021 - March 31, 2022

CYCLOTRON INSTITUTE

Texas A&M University

College Station, Texas

PROGRESS IN RESEARCH

APRIL 1, 2021 - MARCH 31, 2022

Prepared By

The Cyclotron Institute Staff

Texas A&M University

College Station, TX 77843-3366

Phone: (979) 845-1411
Fax: (979) 845-1899

Web: http://cyclotron.tamu.edu

July 2022

TABLE OF CONTENTS

SECTION II: HEAVY ION REACTIONS

SECTION III: NUCLEAR THEORY

Introduction
April 1, 2021 – March 31, 2022

Progress in research and operations at the Texas A&M Cyclotron Institute is summarized in this report for the period April 1, 2021 through March 31, 2022. The period covered by this report was impacted as the COVID-19 pandemic continued to impact the world. The CI continued operations throughout this time with new procedures to ensure that we could run as safely as reasonably achievable. The CI has had a remarkably productive year despite the circumstances and I am indebted to the dedicated operations staff that kept the facility running during this challenging period.

The discovery science program continues to produce exciting results. Additionally new equipment has been brought on –line that expands the scientific capability of the institute. TexNuet and Dapper have both been fully commissioned and utilized in first experiments.

The Cyclotron Institute continued to explore the capability of producing radioisotopes for medicine, in particular the alpha particle emitter ^{211}At. Several runs were conducted, the highest quantity of ^{211}At produced in one run being approximately 100 mCi. We have been able to purify the At-211 on a column and ship an air-dried column to MD Anderson. An automated target retrieval system will be a future priority in this project.

During this period the K500 provided 6246.5 hours and the K150 provided 5416 hours of beam for both science and radiation-effects testing. The new ECR4 ion source was able to take over in supplying injected beam for the K500 while the damaged ECR1 ion source was being rebuilt. Development has continued with the K150, most notably with a program dedicated to detecting faint beams and their contaminants after acceleration. A minor upgrade to the ECR2 ion source injecting the K150 has increased its magnetic containment field with the goals of greater stability and larger intensities of high-charge states, and indeed several higher charge-state, accelerated beams have been detected after this upgrade.

As in previous reports, I include here a few scientific highlights.

- The long-standing problem of the importance of the neutron up-scattering process in nucleosynthesis of carbon in a stellar environment was resolved by directly measuring the cross section for this process using an active target detector (TexAT). It turned out that this process does not play an as significant role as previously assumed. (Nature Communications **13**, Article number: 2151 (2022)).
- Evidence against additional resonances below the Hoyle state in carbon-12, which were previously suggested and linked to the Efimov effect, was presented in the 12N beta-decay study with an active target detector (TexAT). (Phys. Rev. C **103**, L051303 (2021).
- Direct measurements of the ^{8}B+^{40}Ar fusion excitation function found no evidence for a previously suggested sub-Coulomb enhancement, which was linked to the special ground state proton-halo structure of ^{8}B.

- STAR Time-of-Flight analysis code improvements developed at TAMU and intended for use with pp and p+Au data were adopted by the collaboration for analysis of all the Beam Energy Scan II data that STAR recorded in 2019-21.
- Completed the construction, installation, and commissioning of the STAR Forward Upgrade, and utilized it to take data throughout RHIC Run 22.
- Two new Trojan horse measurements were suggested to pinpoint the low-energy S-factor for ^{12}C-^{12}C (Eur. Phys. J. A **58**, 29 (2022).
- Demonstrated via a transport model that the ratio NtNp/Nd2 of the triton yield Nt, deuteron yield Nd, and proton yield Np in relativistic heavy ion collisions is enhanced by the spinodal instability if the produced quark-gluon plasma undergoes a first-order transition to a hadronic matter.
- Showed via the RVUU transport model the need of reduced Delta production cross section from the nucleon-nucleon inelastic scattering for describing the yields and spectra of charged pions measured by the HADES Collaboration from Au+Au collisions at the nucleon-nucleon center-of-mass energy of 2.4 GeV.
- Performed a first demonstration of the use of self-assembled monolayers on gold-coated silicon detectors to measure chemical properties of nuclides produced in a gas-filled separator.
- Developed techniques to forensically analyze a sample of legacy radium pigment
- Calculated the effects of shell-structure and isotopic asymmetry on nuclear level density, within the semiclassical micro-macroscopic approach MMA and compared with experimental data.
- Carried out mean-field based random-phase-approximation calculations of centroid energies and branching ratios of direct one nucleon decay of isoscalar giant multipole resonances of 208Pb and compared with experimental data.
- Developed a new microscopic global optical potential with quantified uncertainties from chiral effective field theory (Phys. Rev. Lett. **127**, 182502 (2021)).
- Implemented a new machine learning algorithm for the efficient evaluation of high-dimensional integrals arising in many-body perturbation theory (Phys. Rev. Lett. 127, 062701 (2021)).
- Implemented transported charm-quark phase space distributions into the calculation of *J/ψ* regeneration in Pb-Pb collisions at the LHC, synergizing open and hidden heavy-flavor transport, which led to a decisive improvement in the description of the elliptic flow (v_2) data at the LHC, resolving the so-called "*J/ψ* v_2 puzzle". (Phys. Rev. Lett. **128**, 162301 (2022).
- Carried out detailed predictions for production of the excited y(2S) state in Pb-Pb collisions at the LHC, whose small binding energy provides high sensitivity to in-medium kinetics. The predictions for the centrality and pT dependence turned out to be in excellent agreement with new ALICE data, providing strong support for the TAMU transport approach.
- Used ^{25}Mg(*d,p*) reaction measurement to establish the existence of a new resonance in ^{25}Al proton capture, with potential relevance for ^{26}Al synthesis in novae.
- Commissioned phoswich focal plane detector for the MDM and used it a measurement of ^{21}Ne(*p,t*) in inverse kinematics.
- An automated apparatus for rapid astatine recovery has been developed (Chem. Eng. J. **442**, 136176 (2022)).

Institute scientists remain active in a number of collaborative research efforts around the world. Major programs include: measurements of beta decays with the TRINAT collaboration at TRIUMF; nuclear structure measurements with TexAT at TRIUMF; continued work with the STAR collaboration at RHIC; fusion studies at MSU; and participation in the SAMURAI collaboration at RIBF in Tokyo, Japan.

The format of this report follows that of previous years. Sections I through III contain reports from individual research projects. Operation and technical developments are given in Section IV. Section V lists the publications with Cyclotron Institute authors and outside users and the Appendix gives additional information including talks presented by members of the Institute during the past year. Once again, the full volume of this year's Progress in Research is available only on our web site (http://cyclotron.tamu.edu). *Since most of the contributions presented here are truly reports on progress in research, results and conclusions should not be quoted from the report without the consent of the authors*.

I am indebted to Dr. Y.-W. Lui for assembling this report.

S.J. Yennello
July 18, 2022

SECTION I

NUCLEAR STRUCTURE, FUNDAMENTAL INTERACTIONS AND ASTROPHYSICS

Progress in the search for an excited state in tritium via the ^{6}He(p,t)α reaction

C.E. Parker,[1] G.V. Rogachev,[1] J. Bishop,[1] E. Aboud,[1] M. Barbui,[1] E. Harris,[1] C. Hunt,[1] E. Koshchiy,[1]
Z. Luo,[1] M. Roosa,[1] A. Saastamoinen,[1] and D.P. Scriven[1]
[1]*Cyclotron Institute, Texas A&M University, College Station, Texas 77843*

Although the ^{3}H nucleus, or triton, is a well-studied system there remains uncertainty as to whether an excited state (t*) exists. To help address this open question, an experiment using the Texas Active Target Time Projection Chamber (TexAT TPC) to measure the ^{6}He(p,t)α reaction has been performed. Further details on the physics motivation, experimental setup, and analysis technique can be found in the previous year's Progress in Research report [1].

Events corresponding to the ^{6}He(p,t) ground state Q-value of 7.5 MeV have been identified and reconstructed, however the next challenge is to eliminate those easier-to-identify events and focus on potential t* events. For the beam energies of the current measurement, the t* signature will decay via d+n; the three-body decay to p+n+n is not possible. Following a similar process for the ground state analysis, the first step in reconstructing potential t* events is by identifying a Z=2 hit in a silicon detector for a minimum detected energy of about 2 MeV. This detector hit would also have a corresponding α-particle track in the Micromegas (MM) portion of the detector.

It is then assumed based on the dE/dx in the isobutane that the other particle is a deuteron, with track length >50 mm; shorter track lengths are likely from interactions with ^{12}C in the target gas, and therefore are not of interest. Fig. 1 shows the reconstructed vertex α-particle energy versus α-particle angle for a subset of the silicon detectors compared with the expected kinematics for the ^{6}He(p,t) ground state and potential excited state for two possible beam energy slices in the MM region. An anti-gate for the MM versus silicon energy has been implemented as an additional check to make sure the second track is either from a triton or deuteron (t*) event. As expected, there is separation between the ground state and the potential t* events.

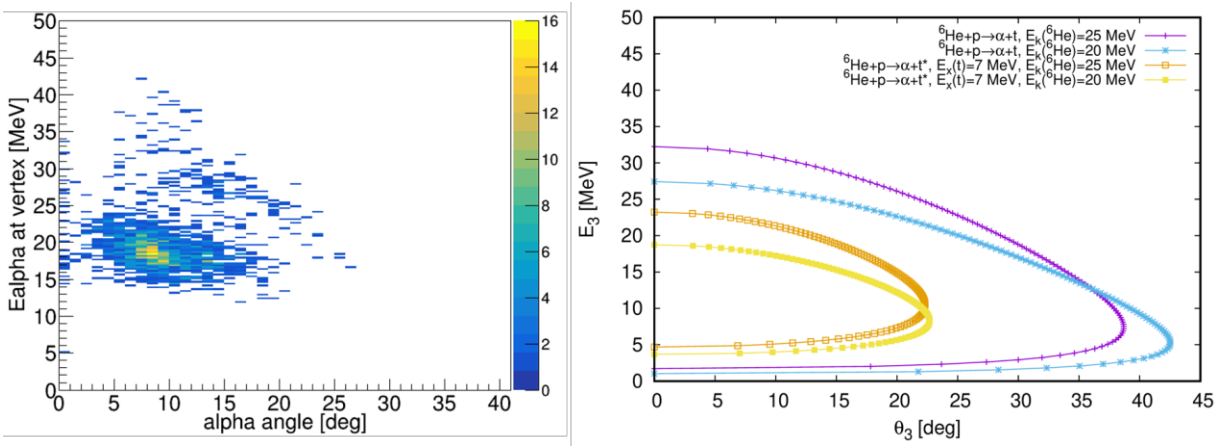

Fig. 1. Reconstructed α-particle energy versus angle (left) for small-angle detectors from fitted track data and (right) for expected kinematics for the ground state and a 7 MeV excitation in the triton.

The resulting Q-value reconstruction for these possible t* events is shown in Fig. 2. Included with the potential t* events, multiple background reaction channels are likely present. The bulk of the ^{6}He(^{12}C,X) events have likely been removed due to the length requirement of the particle tracks. However, α-particles can result from other reactions such as ^{6}He(p,d)^{5}He where the unbound ^{5}He breaks up into α+n. This process will not result in a single Q-value peak, therefore modifying the TexAT GEANT4 simulation tools is needed to help model the expected breakup lineshape. Another possible source of background would be ^{6}He(p,p')^{6}He(2^{+}) where it is important to differentiate the proton versus deuteron via energy loss in the TPC. The contribution of misidentifying proton tracks as deuterons tracks is another ongoing simulation task.

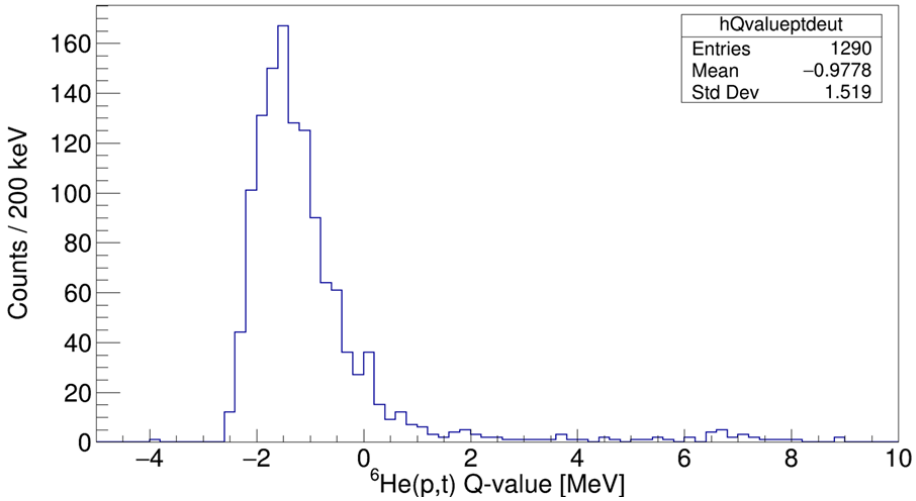

Fig. 2. Q-value reconstruction for possible ^{6}He(p,t*) events and background reaction channels; the events of interest at this energy will mainly be t*→ d+n rather than t*→p+n+n.

In addition to the simulation work, future data analysis will include grouping the silicon detector hits into smaller vertical zones of fixed laboratory angle to check the energy dependence of the reconstruction. Further refinements of the track reconstruction within the MM region can also be considered, as that will impact the calculated Q-values. An additional refinement could be to implement track reconstruction for interactions that occur prior to the MM region to help extend the range of beam energies covered in the Q-value reconstruction.

[1] C.E. Parker et al., *Progress in Research*, Cyclotron Institute, Texas A&M University (2020-2021), p. IV-8.

Precise half-life measurement for ^{29}P

V.E. Iacob, D.G. Melconian, N.Nica, D. McClain, M. Nasser, G. Chubarian, V. Kolhinen,
B. Roeder, and A. Saastamoinen

Precision measurements for *ft*-values for positron emitters are providing a precise value for the up-down quark mixing element V_{ud} in the Cabbibo-Kobayashi-Maskawa (CKM) matrix, a pillar of the standard model. This allows for a very demanding test: the unitarity in the upper row of the CKM matrix. While superallowed decays provide to date the most precise value for V_{ud}, five mixed Fermi and Gamow-Teller decays between T=1/2 mirror nuclei (^{19}Ne, ^{21}Na, ^{29}P and ^{37}K) have been identified to have a high potential to add to the experimental body of data [1]. However, as both vector and axial vector components contribute in these decays, the *ft*-value needs to be complemented by one of the angular correlation coefficiens.

We measured the half-life of ^{29}P in a seven-day experiment. The radioactive beam was produced by bombarding with ^{30}Si at 24 *A* MeV a hydrogen gas target kept at liquid nitrogen temperature and a pressure of 2 atm. The ejectiles were sorted with the Magnetic Achromat Recoil Spectrometer (MARS). The average beam intensity was 10,000 ions/s, and the beam purity (MARS focal plane) was 99%. We tested the beam composition once a day during this experiment.

With an energy of 22 A MeV, the radioactive beam passed through a 51 mm thick Kapton window, then through a 0.3 mm-thick BC404 plastic scintillator, a series of aluminum degraders, eventually being stopped in a 76 mm-thick Mylar tape. The degraders were adjusted to place the implanted ^{29}P ions close to the back side of the tape. We chose this position to get the best possible further purification of the beam: Less than 0.1% radioactive impurities were retained in the Mylar tape.

Keeping the beam on for up to 8 s (about two half-lives) we collected a radioactive sample and scaled the implanted ions with the plastic scintillator. Then we turned the beam off, moved the radioactivity within ~0.15 s in the center of a 4π proportional counter where it was multiscaled for 84 s (about twenty half-lives). We repeated such collect-move-detect cycles until we obtained the desired statistics.

The 4π proportional counter signals were sent to a fast preamplifier followed by fast timing amplifier; the amplifier's signals were clipped with a Schottky diode, to speed-up the base-line recovery. The amplifier's output was passed to a leading-edge discriminator, then split and sent to two non-retriggering gate generators, that inserted in the event-stream major non-extending dead-times. The two dead-time-distorted streams were eventually passed to two multichannel scalers

During this experiment we collected more than 100 million events. The total decay spectrum is presented in Fig.1. Note the low relative background rate: We could follow the decay for almost four decades. This is what enables us to claim a precision that significantly exceeds 0.1%.

To allow for stability-tests of the result, we split the experiment in sub-runs, with statistics ranging between 4 and 5 million events. We changed from a sub-run to another the acquisition parameters that could affect the result: discrimination threshold (150-, 200-, and 250-mV), major dead-times (4-, 6-, and 8-ms) and bias used to polarize the 4p detector (from 2350 to 2600 V, in steps of 50 V). To test for

the possible presence of a long-lived unidentified impurity, in one of the sub-runs, the beam-move-collect cycling was set to 30-0.15-300 s.

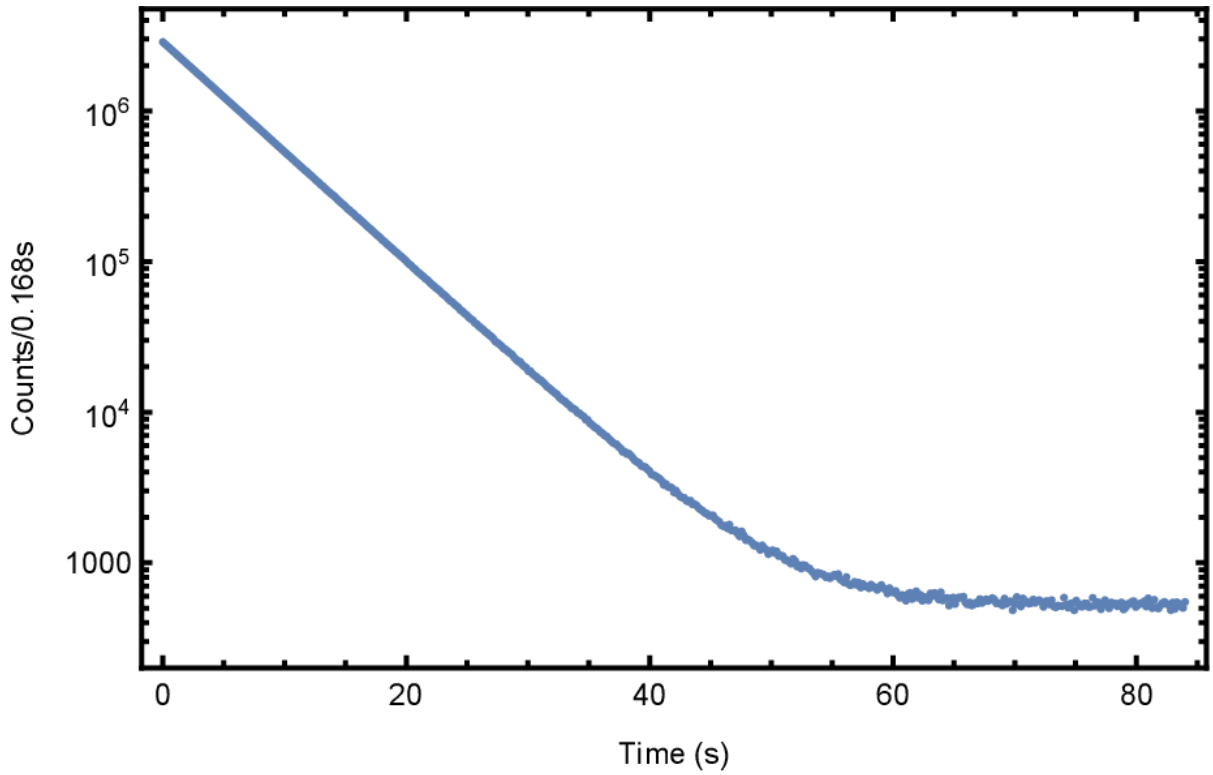

Fig. 1. Selected total decay spectrum observed in the decay of ^{29}P. The decay events are distributed in 500 channels, each 0.168 s wide.

We performed maximum likelihood fits on pre-sorted the dead-time corrected data: We carefully analyzed each cycle, and accepted it in the fit only if:

(1) the implantation beam provided more than 5000 ^{29}P nuclei,

(2) the ratio of detected betas to implanted nuclei was at least 90% of the expected value, and

(3) the cycle χ^2 was below an upper limit set such that the probability for higher values is less than 10^{-4}.

We couldn't identify any abnormality in the data: The sub-run fit results were fully consistent with one another. Our preliminary result is 4.1144(8) s. This value is more precise but above the recent result of J. Long *et. al.* [2], the only published measurement with a precision close to 0.1%. Their result is 4.1055(44) s; we assume it was probably contaminated by unknown impurities.

[1] O. Naviliat-Cuncic and N. Severijns, Phys. Rev. Lett. **102**, 142302 (2009).
[2] J. Long *et al.*, Phys. Rev. C **101**, 015501 (2020).

PENELOPE simulations as part of an independent analysis of β-delayed-proton measurements in ^{32}Ar

M. Nasser, G. Chubarian, V.E. Iacob, V.S. Kolhinen, D. McClain, and D. Melconian

TAMUTRAP aims to find physics beyond the Standard Model (BSM) via β-delayed-proton decays. The parameter of interest is the β-ν correlation parameter, $a_{\beta\nu}$, holding an empirical value of 1. Measuring with confidence a value less than this indicates scalar currents in beta decay and consequently new physics. As of now, this amounts to a measurement of <0.1%.

TAMUTRAP's goal is to perform the measurement of $a_{\beta\nu}$ using its novel Penning Trap, which is the world's largest [1]. The WISArD group is pursuing a similar program using ^{32}Ar implanted on a mylar catcher-foil [2]. Half of the betas will travel upwards towards a plastic scintillator for coincidence triggering. By measuring the protons on silicon detectors positioned on the scintillator-side of the foil, and an equal amount on the other side, $a_{\beta\nu}$ is inferred from the separation of the two spectra resulting from the Doppler shift caused by the kinematics of the beta decay. An image of the prototype-experiment's geometry in the Monte Carlo simulation package PENELOPE and an example of the two spectra/peaks can be seen in Figs. 1 and 2.

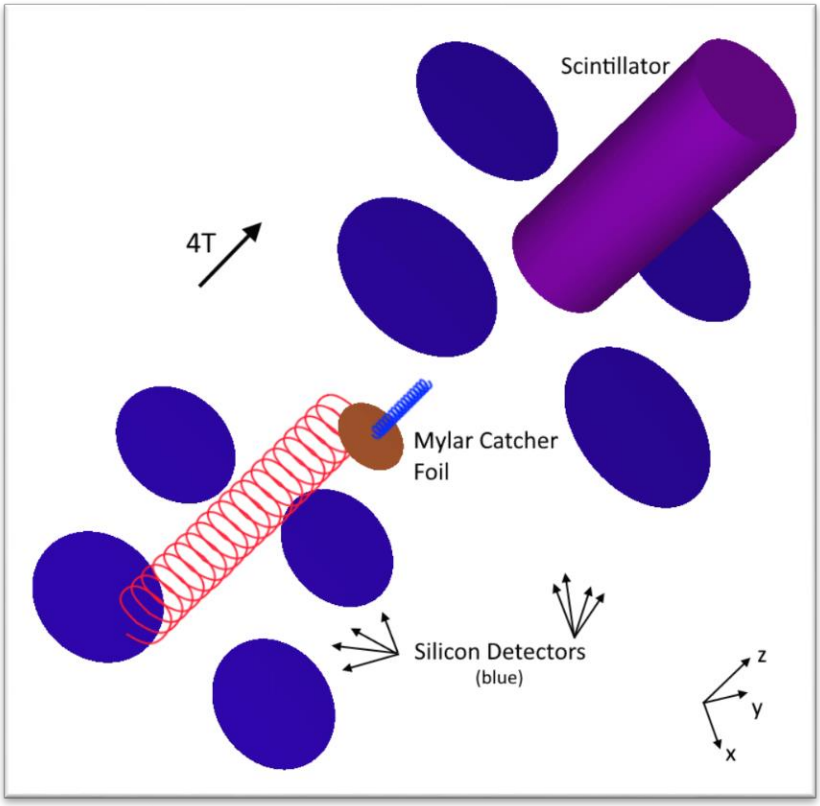

Fig. 1. WISArD's prototype-experiment geometry in PENELOPE. The positron (blue) and proton (red) tracks are simple sketches to help visualize the experiment and are not drawn to scale.

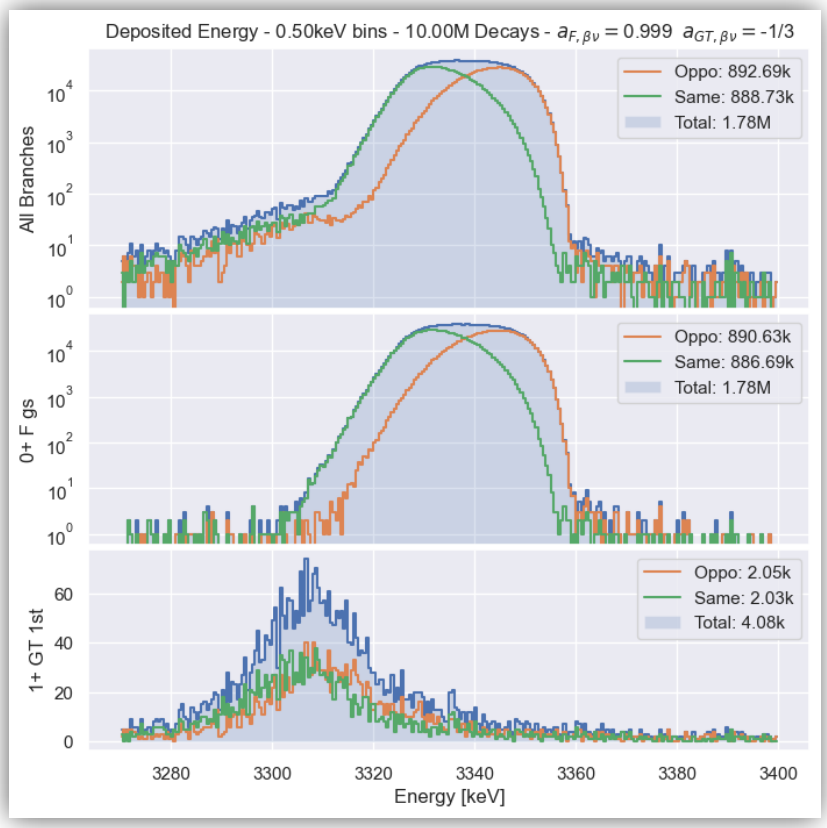

Fig. 2. Proton energy spectrum of main peak per a GEANT4 simulation with $a_{\beta\nu} = 0.999$. Same (green) refers to an angular separation between the beta and proton being less than $\pi/2$. This means the proton was shifted downward in energy due to the ^{32}Cl recoil. Opposite (orange) is the inverse of this. The lower two subplots show the decay path components making up the total spectrum.

PENELOPE [3] is a Monte Carlo simulation software for the Penetration and ENErgy Loss of Positrons and Electrons. As the name implies, it is specialized in the handling of betas (and photons). By developing simulations utilizing PENELOPE, we can simulate the transport and absorption of the positrons in ^{32}Ar's decay. The choice of PENELOPE over the more-popular GEANT4 [4] comes from many reasons. Being a high-precision measurement (<0.1%) means that the backscatter of positrons off the scintillator's surface and not triggering a coincidence can be a crippling occurrence [2]. GEANT4 uses a multiple scattering model that depends greatly on the step size. PENELOPE uses a scattering model that does not. PENELOPE is more ideal, or even "correct," as a simulation in addressing this concern. The second reason being that the WISArD group has GEANT4 simulations already that handle the full decay. Our PENELOPE simulations will serve to complement their GEANT4 simulations under independent simulation and analysis.

The collective simulation begins with the calculation of decay-product kinematics via a separate program. This program is altered/improved code inherited from A. Garcia, which using fitted data from experimentation performs the beta-delayed proton decays in sequence. Their decay-path, energy, and directions of emission are then written to disk for external simulations. Fig. 3 shows the main proton energy peak stemming from this program, dubbed RMat, due to it using the R-matrix determined from the fitted experiment.

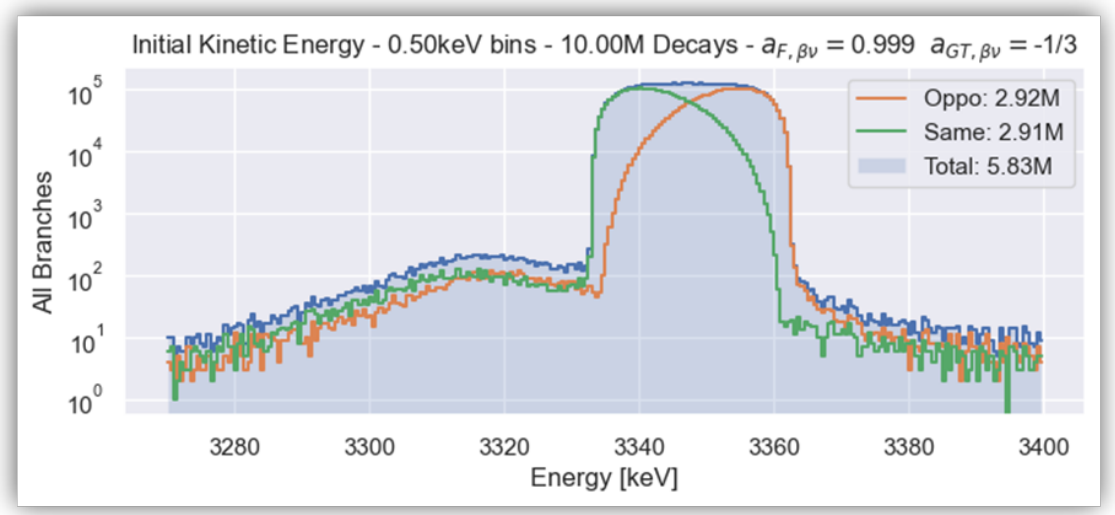

Fig. 3. Proton energy spectrum resulting from RMat calculations. Two main peak-shapes can be seen as interfering decay paths per Fig 2. The main peak lacks the shoulder however, due to there being no attenuating factors.

PENELOPE transports the betas from the RMat output through the mylar catcher foil's geometry up towards the scintillator (or down, in which they disappear). These are the only geometries implemented in the simulation as the experiment will occur in a 4T magnetic field. I.e. the positrons are ignorant of the silicon detectors and other materials due to a Larmor radius significantly smaller than the radius of the centered scintillator. Upon an event's termination, the particle's energy and geometry-of-death are output to disk. This serves as triggering mechanism in analysis for the protons, which are run in GEANT4.

WISArD recently had a pre-run at ISOLDE with pending results. The main experiment is planned to take place later this year. The bulk of the RMat and PENELOPE development has seen completion in that decay-products can be correctly generated and the positrons transported.

[1] V.S. Kolhinen *et al.*, *Progress in Research*, Cyclotron Institute, Texas A&M University (2018-2019) p. IV-45.

[2] V. Araujo-Escalona, D. Atanasov, X. Fléchard, P. Alfaurt, P. Ascher, B. Blank, *et al.*, Phys. Rev. C **101**, 055501 (2020). Simultaneous measurements of the β-neutrino angular correlation in 32Ar pure Fermi and pure Gamow-Teller transitions using β-proton coincidences. DOI: 10.1103.

[3] NEA (2019), PENELOPE 2018: A code system for Monte Carlo simulation of electron and photon transport: Workshop Proceedings, Barcelona, Spain, 28 January – 1 February 2019, OECD Publishing, Paris, https://doi.org/10.1787/32da5043-en.

[4] GEANT4: A Simulation toolkit - GEANT4 Collaboration (S. Agostinelli, *et al.*) Nucl. Instrum. Methods Phys. Res. **A506**, 250 (2003); SLAC-PUB-9350, FERMILAB-PUB-03-339.

Constraining globular cluster abundance anomalies

Q3D measurement:

D.S. Harrouz,[1] N. de Séréville,[1] P. Adsley,[2,3] F. Hammache,[1] R. Longland,[4,5] B. Bastin,[6] T. Faestermann,[7] R. Hertenberger,[8] M. La Cognata,[9] L. Lamia,[9,10] A. Meyer,[1] S. Palmerini,[11,12] R.G. Pizzone,[9] S. Romano,[9,10,13] A. Tumino,[9,14] and H.-F. Wirth[8]

[1]*Université Paris-Saclay, CNRS/IN2P3, IJCLab, 91405 Orsay, France*

[2]*School of Physics, University of the Witwatersrand, Johannesburg 2050, South Africa*

[3]*iThemba Laboratory for Accelerator Based Sciences, Somerset West 7129, South Africa*

[4]*North Carolina State University, Raleigh, North Carolina 27695, USA*

[5]*Triangle Universities Nuclear Laboratory, Durham, North Carolina 27708, USA*

[6]*Grand Accélérateur National d'Ions Lourds (GANIL), CEA/DRF-CNRS/IN2P3, Boulevard Henri Becquerel, 14076 Caen, France*

[7]*Physik Department E12, Technische Universität München, D-85748 Garching, Germany*

[8]*Fakultät für Physik, Ludwig-Maximilians-Universität München, D-85748 Garching, Germany*

[9]*Laboratori Nazionali del Sud–Istituto Nazionale di Fisica Nucleare, Via Santa Sofia 62, 95123 Catania, Italy*

[10]*Dipartimento di Fisica e Astronomia E. Majorana, Università di Catania, 95131 Catania, Italy*

[11]*Dipartimento di Fisica e Geologia, Università degli Studi di Perugia, 06123 Perugia, Italy*

[12]*Istituto Nazionale di Fisica Nucleare, Sezione di Perugia, 06123 Perugia, Italy*

[13]*Centro Siciliano di Fisica Nucleare e Struttura della Materia (CSFNSM), 95123 Catania, Italy*

[14]*Facoltà di Ingegneria e Architettura, Università degli Studi di Enna, 94100 Enna, Italy*

DRAGON measurements:

P. Adsley,[1, 2, 3, 4] Matthew Williams,[5, 6] Nicolas de S´er´eville,[7] Richard Longland,[8, 9] Barry Davids,[6] Uwe Greife,[10] Fairouz Hammache,[7] Sarah Harrouz,[7] David Hutcheon,[6] Annika Lennarz,[6] Alison M. Laird,[5] Fran¸cois d'Oliveira Santos,[11] and Christopher Ruiz6,[12]

[1]*Cyclotron Institute, Texas A&M University, College Station, Texas 77843, USA*

[2]*Department of Physics and Astronomy, Texas A&M University, College Station, Texas 77843, USA*

[3]*iThemba Laboratory for Accelerator Based Sciences, Somerset West 7129, South Africa*

[4]*School of Physics, University of the Witwatersrand, Johannesburg 2050, South Africa*

[5]*Department of Physics, University of York, Heslington, York, YO10 5DD, United Kingdom*

[6]*TRIUMF, Vancouver, BC V6T 2A3, Canada*

[7]*Institut de Physique Nucl´eaire d'Orsay, UMR8608, IN2P3-CNRS, Universit´e Paris Sud 11, 91406 Orsay, France*

[8]*North Carolina State University, Raleigh, North Carolina 27695, USA*

[9]*Triangle Universities Nuclear Laboratory, Durham, North Carolina 27708*,

[10]*Department of Physics, Colorado School of Mines, Golden, Colorado 80401*

[11]*GANIL, CEA/DRF-CNRS/IN2P3, Bvd Henri Becquerel, 14076 Caen, France*

[12]*Department of Physics and Astronomy, University of Victoria, Victoria, BC V8W 2Y2, Canada*

Globular clusters were once thought to be pristine relics of the first generation of stars in the Universe. This is incorrect: it is now obvious through stellar spectroscopy that the observed globular clusters consist of multiple generations of stars, the current generation of stars having been contaminated by some unknown previous generation. There are a number of abundance patterns observed in globular clusters. For example, there is a well known anticorrelation in the abundances of sodium and oxygen. A more recently identified pattern is the anticorrelation in magnesium and potassium abundances. Previous theoretical work by Dermigny and Iliadis [1] identified a number of important reactions which influence the elemental abundance pattern in globular clusters. The four more important reactions identified were ^{30}Si(p,gamma)^{31}P, ^{37}Ar(p,gamma)^{38}K, ^{38}Ar(p,gamma)^{39}K and ^{39}K(p,gamma)^{40}Ca. From this starting point, a campaign of four experiments was proposed at a variety of facilities around the world. Three of the experiments have now been performed and the third is planned for later in 2022.

One experiment performed was the ^{30}Si(^{3}He,d)^{31}P experiment with the Munich Q3D spectrometer at the Maier-Leibnitz Laboratory, Munich, Germany. In this experiment, the single-proton transfer reaction was used to determine the energy, spin and parity, and reduced proton width of resonance states in ^{31}P which could contribute to the ^{30}Si(p,gamma)^{31}P reaction. From this information a new reaction rate

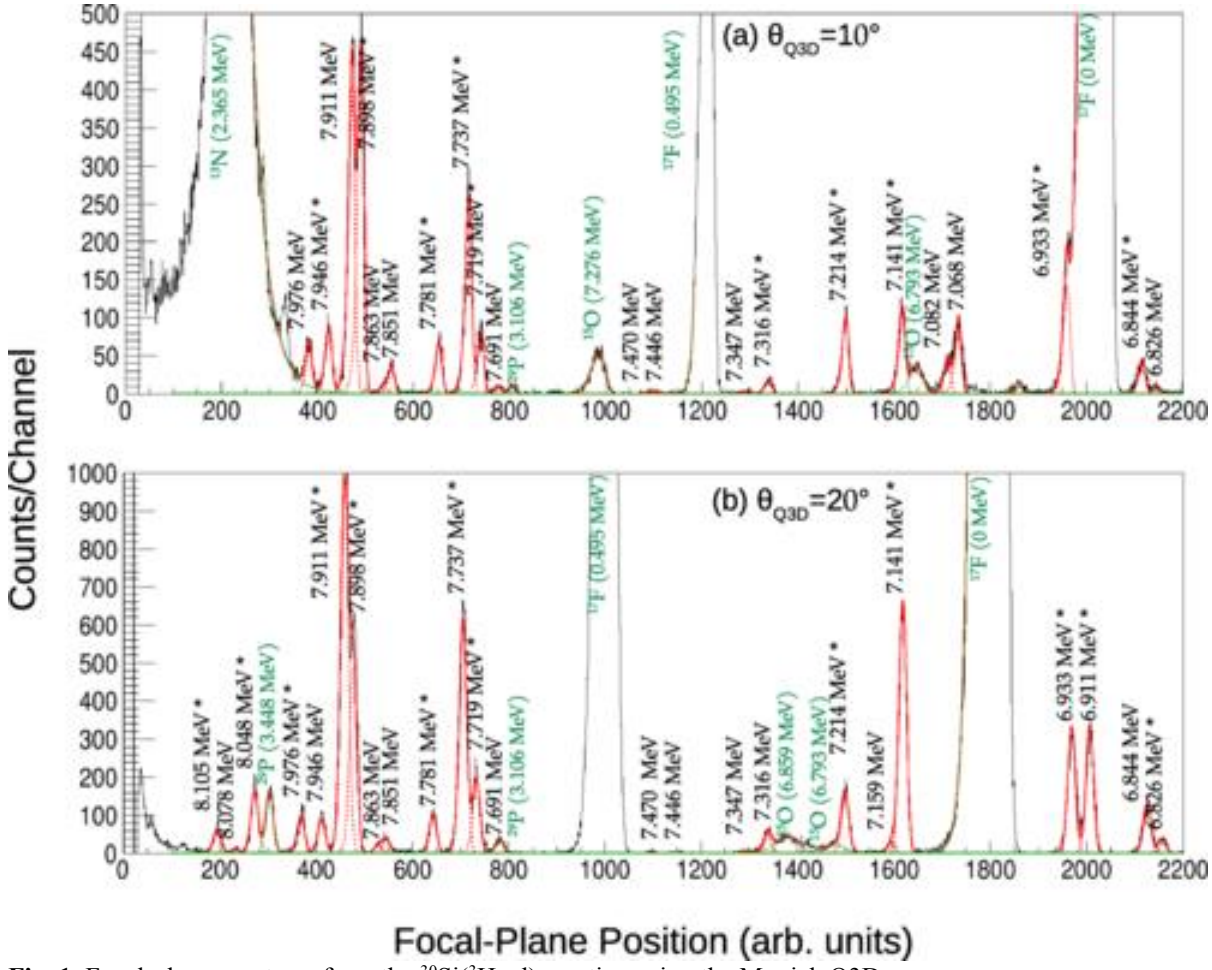

Fig. 1. Focal-plane spectrum from the ^{30}Si(^{3}He,d) reaction using the Munich Q3D.

was computed. This work was recently published as an Editors' Suggestion in Physical Review C [2].

Two further experiments have been performed of the ^{30}Si(p,gamma)^{31}P and ^{39}K(p,gamma)^{40}Ca reactions in inverse kinematics using the DRAGON recoil separator at TRIUMF, Vancouver, Canada. The analysis of these experiments is ongoing and the final data required for resonance strengths will be collected in September 2022. Publications are expected this year.

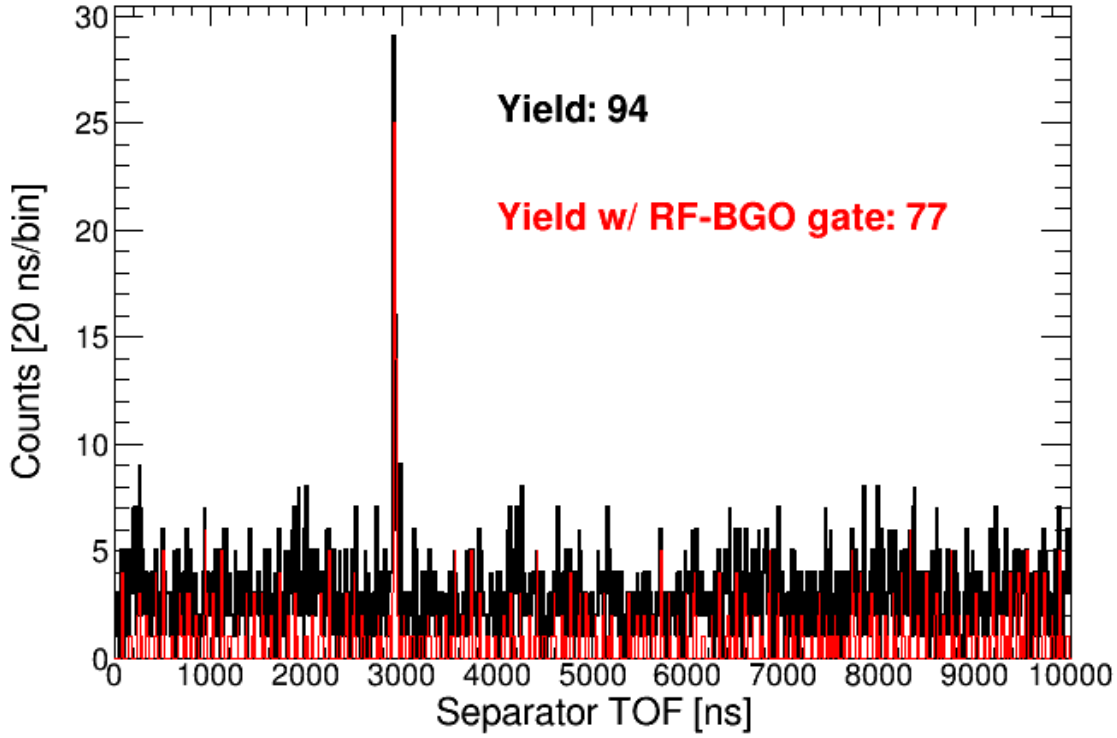

Fig. 2. Separator time-of-flight spectrum from the ^{39}K(p,gamma)^{40}Ca reaction for the 337-keV resonance. The black spectrum is without an additional gate on the time difference between the accelerator RF reference and the BGO hit which is imposed for the spectrum in red which reduces the time-random background from so-called "leaky beam".

[1] Dermigny and Iliadis, Astrophys. J. **848**, 14 (2017).

[2] D.S. Harrouz, N. de Sereville, P. Adsley *et al.*, Phys. Rev. C **105**, 015805 (2022).

Resolving discrepancies about the ^{38}K(p,gamma)^{39}Ca reaction in classical novae

S.D. Binda,[1, 2] P. Adsley,[1, 2, 3, 4] L.M. Donaldson,[2] and collabrators
[1]*School of Physics, University of the Witwatersrand, Johannesburg 2050, South Africa*
[2]*iThemba LABS, Somerset West 7129, South Africa*
[3]*Cyclotron Institute, Texas A&M University, College Station, Texas 77843, USA*
[4]*Department of Physics and Astronomy, Texas A&M University, College Station, Texas 77843*

Direct and indirect measurements of the ^{38}K(p,gamma)^{39}Ca reaction, which is important in understanding the potassium production in classical novae, are in disagreement over the energy of a critically important resonance at E_r = 515 keV. This resonance was measured by DRAGON to be at E_r = 515 keV but indirect measurements of the energy of a nearby state place it at E_r = 455 keV. Similar disagreements exist for other resonances. These discrepancies are rather worrying since the resonance energy enters into the reaction rate as an exponential factor; even small uncertainties in the resonance energy for a known resonance strength result in a significant uncertainty in the reaction rate.

To try to resolve some of these problems, a ^{40}Ca(p,d)^{39}Ca experiment was performed at iThemba LABS with the K600 magnetic spectrometer. This experiment is very similar in intent and operation to a previous nuclear-structure experiment performed at RCNP Osaka with two additional improvements. The first was that a thinner target was used for the experiment to optimise the energy resolution. The second was that the focal plane detection system consisted of two vertical drift chambers allowing the scattering angle to be reconstructed and used for the offline correction of kinematic aberrations in the rigidity

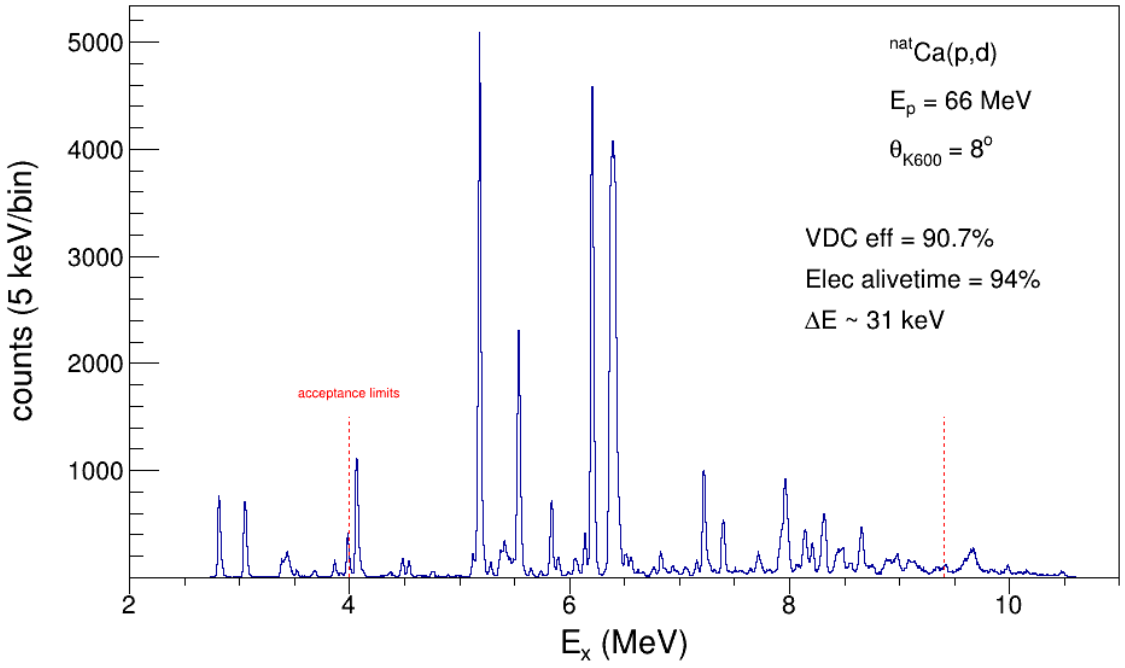

Fig. 1. Preliminary excitation-energy spectrum for the ^{nat}Ca(p,d) reaction with a proton beam of 66 MeV and the K600 magnetic spectrometer placed at 8 degrees.

spectrum. In addition, much higher statistics were taken in this experiment to observe weakly populated

states which were not observed in the previous $^{40}Ca(p,d)^{39}Ca$ measurement which was mainly focussed on understanding the shell structure and generally did not care about the population of weak states.

Resonance states of ^{23}Na and the ^{22}Ne(p,gamma)^{23}Na reaction

Diana P Carrasco-Rojas,[1] M Williams,[2] P Adsley[3,4]
[1]*University of Texas at El Paso, El Paso, TX 79968, USA*
[2]*TRIUMF, Vancouver, BC V6T 2A3, Canada*
[3]*Cyclotron Institute, Texas A&M University, College Station, Texas 77843, USA*
[4]*Department of Physics and Astronomy, Texas A&M University, College Station, Texas 77843*

The ^{22}Ne(p,gamma)^{23}Na reaction has a significant impact on the sodium-oxygen anticorrelation in globular clusters. Previous experimental studies with the DRAGON recoil separator and using a proton beam on a ^{22}Ne gas target at the Laboratory for Underground Nuclear Astrophysics (LUNA) at Gran Sasso, Italy, have located and measured a number of resonances of the ^{2}Ne(p,gamma)^{23}Na reaction. However, two resonances at E_r = 68 and 10 keV (E_x = 8862 and 8894 keV), which were assigned following a weak population in ^{22}Ne(^{3}He,d)^{23}Na single-proton transfer reactions, have eluded direct measurement. Unfortunately, their low energy means that these are the dominant resonances for much of the Hot-Bottom Burning region of intermediate-mass asymptotic giant branch stars.

Low-energy proton scattering is a powerful technique for populating excited states in nuclei without much sensitivity to the underlying structure of the state. In this experiment we used the Munich

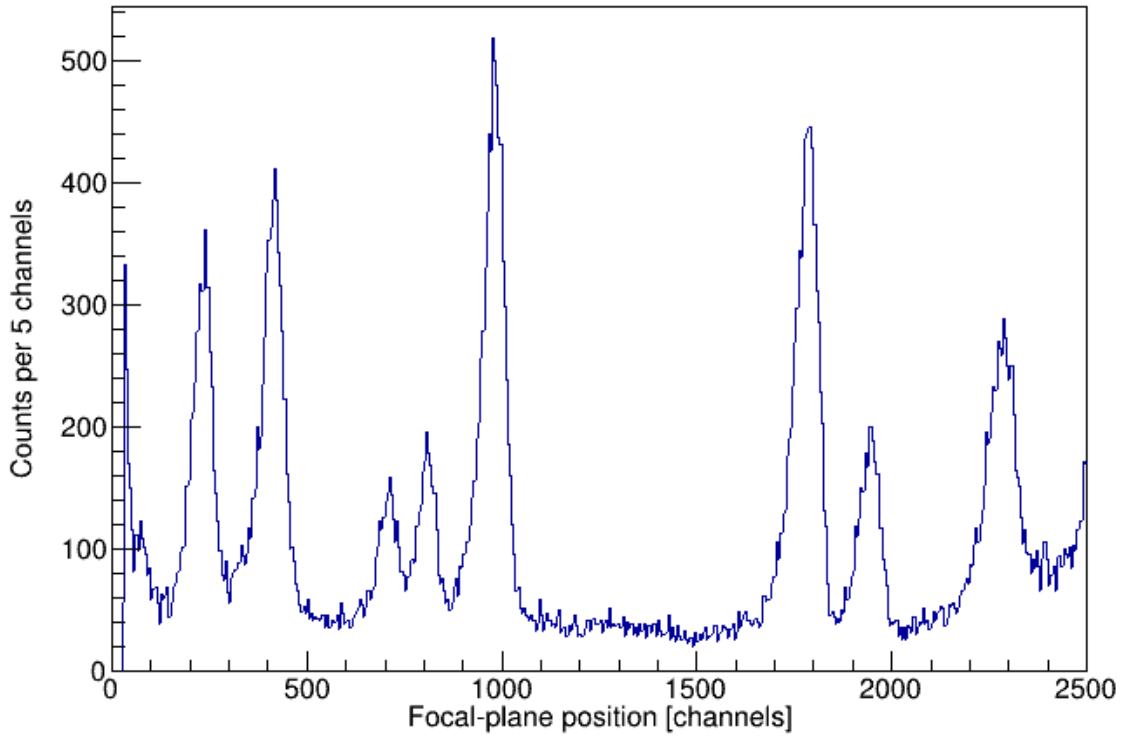

Fig. 1. Excitation-energy spectrum taken at 70 degrees scattering angle using a NaF target with states in ^{23}Na, ^{19}F, ^{16}O and ^{12}C populated on the focal plane. The region of interest is approximately between channels 1000 and 1500.

Q3D magnetic spectrometer and a 14-MeV beam of protons on a $^{23}Na^{19}F$ target to populate the excited resonance states in ^{23}Na which dominate the ^{22}Ne(p,gamma) reaction rate. A focal-plane spectrum for the reaction is shown in the figure below. In the region of interest there is no indication that the tentative resonance states exist, meaning that it is unlikely that they can contribute to the ^{22}Ne(p,gamma) reaction. This greatly reduces some of the remaining causes of uncertainty in the ^{22}Ne(p,gamma) reaction, and means that future direct measurements are likely not required.

Spectroscopy of ^{48}Cr and the expected yield of ^{44}Ti from core-collapse supernovae

S.D. Binda,[1, 2] A.M. Long,[3] P. Adsley,[1, 2, 4, 5] G. Berg,[3] J.W. Brümmer,[2, 6] M. Couder,[3] M. Kamil,[7] N.A. Khumalo,[2, 7] M.Köhne,[6] K.C.W. Li,[2, 6] D.J. Mar´ın-Lámbarri,[2, 7] S.H. Mthembu,[2, 7] Z. Meisel,[3, 8] R. Neveling,[2] P. Papka,[2, 6] L. Pellegri,[1, 2] V. Pesudo,[2, 7] E. Sideras-Haddad,[1] F.D. Smit,[2] M. Wiedeking,[1, 2] and M.C. Wiescher[3]

[1]*School of Physics, University of the Witwatersrand, Johannesburg 2050, South Africa*

[2]*iThemba LABS, Somerset West 7129, South Africa*

[3]*Department of Physics and the Joint Institute for Nuclear Astrophysics, University of Notre Dame, Notre Dame, Indiana 46556, USA*

[4]*Cyclotron Institute, Texas A&M University, College Station, Texas 77843, USA*

[5]*Department of Physics and Astronomy, Texas A&M University, College Station, Texas 77843, USA*

[6]*Department of Physics, Stellenbosch University, Private Bag X1, 7602 Matieland, Stellenbosch, South Africa*

[7]*Department of Physics, University of the Western Cape, P/B X17, Bellville 7535, South Africa*

[8]*Joint Institute for Nuclear Astrophysics, Michigan State University, East Lansing, Michigan 48824*

The interior dynamics of core-collapse supernovae (CCSNe) is a matter of considerable interest. Since observations inside these objects are not possible, other observables such as neutrino flux and the elements produced are used as proxies. One frequently used proxy is the abundance of ^{44}Ti ejected from the CCSN since this is dependent on the mass cut (the mass coordinate below which matter is not ejected). However, the ^{44}Ti ejected abundance depends strongly on a number of nuclear reactions including the ^{44}Ti(a,p)^{47}V which destroys ^{44}Ti, reducing its abundance. The self-conjugate nucleus ^{48}Cr is the compound nucleus for the reaction - this self-conjugate nucleus is expected to exhibit significant alpha-clustering. In addition, the ^{44}Ti+alpha reaction involves the fusion of two isoscalar, 0^+ nuclei vastly reducing the number of levels which may be populated in the ^{44}Ti(a,p) reaction. To test whether statistical model descriptions may be used for this reaction, the ^{50}Cr(p,t)^{48}Cr reaction was used to populate states in ^{48}Cr. A number of states have been observed within the astrophysical region of interest, a large number for the first time. A focal-plane excitation-energy spectrum from the experiment is shown in the Fig. 1 below. This work formed the basis of the MSc work of Mr Sifundo Binda of the University of the Witwatersrand, Johannesburg, and iThemba LABS, Cape Town. Mr Binda is continuing with his PhD work including the analysis of charged-particle decays from the ^{48}Cr states to gain more information on the ^{44}Ti(a,p)^{47}V reaction. A paper is in preparation.

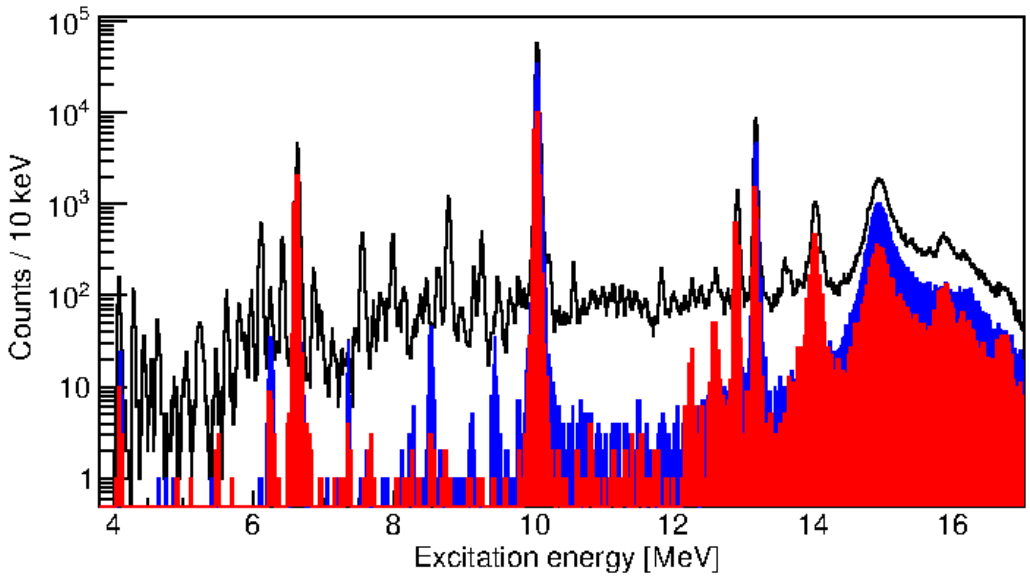

Fig. 1. Excitation-energy spectrum from the ^{50}Cr(p,t)^{48}Cr reaction. The red spectrum is the ^{16}O(p,t)^{14}O contamination and the blue is the ^{12}C(p,t)^{10}C contamination. There is clear population of ^{48}Cr states in the spectrum, many of these states being previously unknown.

The impact of ^{17}O+alpha uncertainties on the s-process

J. Frost-Schenk,[1] P. Adsley,[2,3,4,5] A.M. Laird,[1] R. Longland,[6,7] C. Angus,[1,8] C. Barton,[1] A. Choplin,[9] C.Aa. Diget,[1] R. Hirschi,[10,11] C. Marshall,[6,7] F. Portillo Chaves,[6,7] and K. Setoodehnia,[6,7]

[1]*Department of Physics, University of York, York, YO10 5DD, UK,*

[2]*School of Physics, University of the Witwatersrand, Johannesburg 2050, South Africa,*

[3]*iThemba LABS, National Research Foundation, PO Box 722, Somerset West 7129, South Africa*

[4]*Cyclotron Institute, Texas A&M University, College Station, Texas 77843, USA*

[5]*Department of Physics and Astronomy, Texas A&M University, College Station, Texas 77843, USA*

[6]*Department of Physics North Carolina State University, Raleigh, North Carolina 27695-8202, USA*

[7]*Triangle Universities Nuclear Laboratory, Durham, North Carolina, 27708-0308, USA*

[8]*TRIUMF, 4004 Wesbrook Mall, Vancouver, BC, Canada V6T 2A3*

[9]*Institut d'Astronomie et d'Astrophysique, Université Libre de Bruxelles, CP 226, B-1050 Brussels, Belgium*

[10]*Astrophysics Group, Lennard-Jones Laboratories, Keele University, Keele ST5 5BG, UK*

[11]*Kavli IPMU (WPI), The University of Tokyo, Kashiwa, Chiba 277-8583, Japan*

The s-process (the slow capture of neutrons on seed nuclei) is responsible for the production of half of the elements heavier than iron. The s-process occurs when alpha-particle capture reactions on the neutron sources ^{13}C and ^{22}Ne produce neutrons which capture on seed nuclei, typically iron-peak elements, building up the heavier elements. There are two main sites for the s-process, thermally pulsing AGB stars which cause the "main" s-process and the "weak" s-process occurring in massive stars. Rapidly rotating metal-poort massive stars can also play host to an s-process, the so-called "enhanced" s-process. This enhanced s-process is strongly dependent on not only the neutron source reactions but also the presence of ^{16}O which captures neutrons to produce ^{17}O. The competing ^{17}O(alpha,gamma) and ^{17}O(alpha,n) reactions can then either permanently absorb neutrons or release them, enabling s-process nuclei synthesis, respectively. The relative strengths of the ^{17}O+alpha reactions critically influences the neutron recycling and therefore the possible nucleosynthesis in the enhanced s-process.

An experiment using the ^{20}Ne(d,p)^{21}Ne reaction was performed using the TUNL Split-pole Enge spectrograph and the resulting differential cross sections were used to assign spins and parities, and extract neutron widths, of the ^{21}Ne states which control the ^{17}O+alpha reactions. As a result of this experiment, new ^{17}O+alpha reaction rates were computed with associated uncertainties for the first time. These new results show that the enhanced s-process is expected to produce heavy elements up to at least barium and, under extreme assumptions as to the reaction rates and the mixing of CNO material into the helium-burning region, up to around lead. This may help to explain some of the history of galactic chemical evolution since massive stars will enrich the Universe in s-process elements much sooner than AGB stars, and may provide an alternative site to the production of heavy elements before neutron-star mergers can contribute to chemical evolution.

This research was recently accepted for publication in the Monthly Notices of the Royal Astronomical Society https://doi.org/10.1093/mnras/stac1373

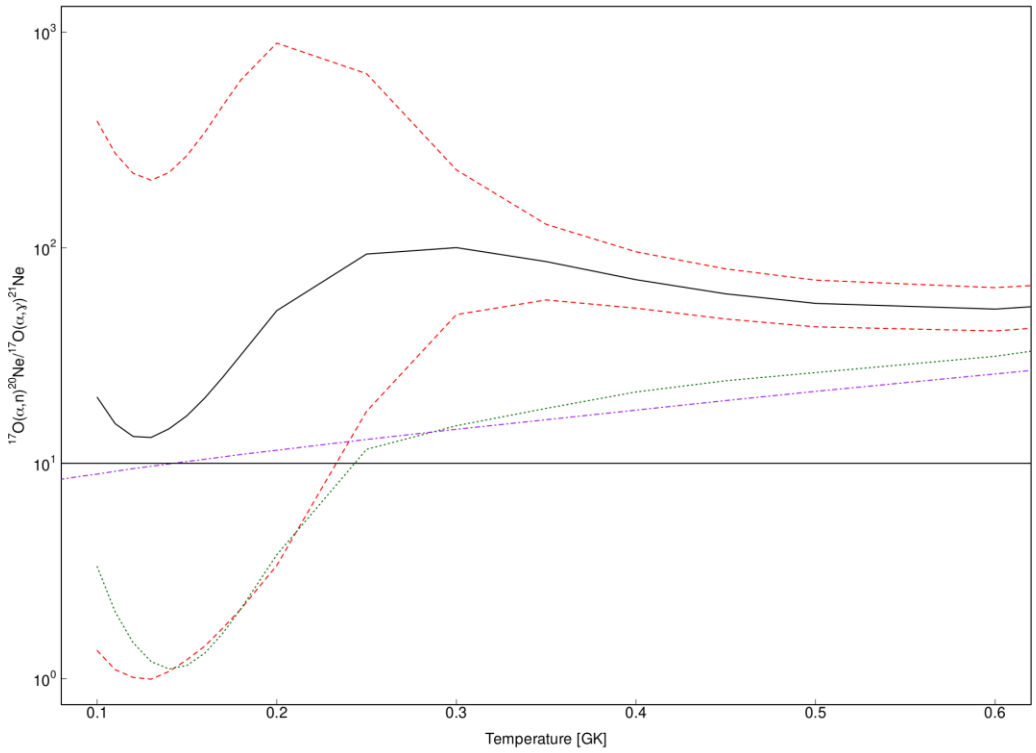

Fig. 1. The ratio of the ^{17}O(alpha,n)^{20}Ne/^{17}O(alpha,gamma)^{21}Ne reaction rates as a function of temperature. The green line is the previous ratio from Best (), the purple is the estimate from Caughlan and Fowler '88. The black is the ratio of the median rates from the current work. The red lines are the ratios of the 68% upper (lower) ^{17}O(alpha,n)^{20}Ne rate to the 68% lower (upper) ^{17}O(alpha,gamma)^{21}Ne rate.

Radiative decay branching ratio of Hoyle state in ^{12}C

Zifeng. Luo,[1,2] G. Rogachev,[1,2] M. Barbui,[2] J. Bishop,[2] G. Chubaryan,[2] V. Goldberg,[2] E. Harris,[1,2] H. Jayatissa,[3] E. Koshchiy,[2] M. Roosa,[1,2] A. Saastamoinen,[2] and D. Scriven,[1,2]

[1]*Department of Physics and Astronomy, Texas A&M University, College Station, Texas 77843*

[2]*Cyclotron Institute, Texas A&M University, College Station, Texas 77843*

[3]*Argonne National Laboratory, Lemont, Illinois, 60439*

The triple-alpha process is one of the most important reactions in nuclear astrophysics. It is a sequence of two reactions a) $\alpha+\alpha \rightarrow {}^{8}\mathrm{Be}$(g.s.) and b) ${}^{8}\mathrm{Be}+\alpha \Leftrightarrow \gamma+{}^{12}\mathrm{C}$ leading to the production of carbon. The second reaction proceeds through a special excited 0^+ state at 7.65 MeV excitation energy in ^{12}C, the so-called Hoyle state. Most of the time the Hoyle state decays back to ^{8}Be(g.s.) and an α-particle. But the $\alpha+{}^{8}\mathrm{Be} \rightleftharpoons {}^{12}\mathrm{C}^{*}$ equilibrium is broken by the small leakage (1 in 2,500 cases) to the ^{12}C ground state facilitated by the radiative branches; either a cascade of two γ-rays, $0_2^+ \rightarrow 2_1^+ \rightarrow 0_1^+$, or e^+e^- pair production, $0_2^+ \rightarrow 0_1^+$ (Fig. 1).

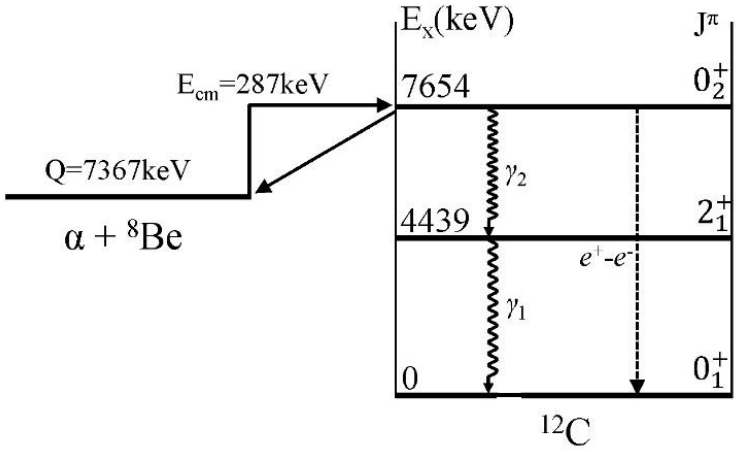

Fig. 1. Decay modes of Hoyle state.

The reaction rate of the triple-alpha process is proportional to $\langle\sigma v\rangle \propto \omega\gamma \exp\left(-\frac{E_R}{hT}\right)$, where $\omega\gamma = \frac{\Gamma_\alpha \Gamma_{\mathrm{rad}}}{\Gamma}$. Note that $\Gamma = \Gamma_\alpha + \Gamma_{\mathrm{rad}}$, $\Gamma_{\mathrm{rad}} = \Gamma_\gamma + \Gamma_\pi$, and $\Gamma_\alpha \gg \Gamma_{\mathrm{rad}}$, we have

$$\omega\gamma = \frac{\Gamma_\alpha \Gamma_{\mathrm{rad}}}{\Gamma} = \frac{\Gamma_{\mathrm{rad}}}{1 + \Gamma_{\mathrm{rad}}/\Gamma_\alpha} \approx \Gamma_{\mathrm{rad}}.$$

Therefore, the triple-alpha reaction rate is determined by the radiative width, Γ_{rad}. One way to establish the Γ_{rad} is to measure the branching ratio for electromagnetic decay and utilize the known partial width $\Gamma_\pi(\mathrm{E0})$ for the electron-positron pair production, as shown in the equation below:

$$\Gamma_{\mathrm{rad}} = \frac{\Gamma_{\mathrm{rad}}}{\Gamma} \times \frac{\Gamma}{\Gamma_\pi(\mathrm{E0})} \times \Gamma_\pi(\mathrm{E0}).$$

The adopted values and recent measurements are shown in Table I. It can be seen that the recently measured radiative branching ratio is 3σ greater than the adopted value; this needs to be verified.

Table 1. Summary of measurements of radiative branching ratio, pair-production branching ratio, and pair-production width of the Hoyle state.

Parameter	Adopted [1]	Recent
Γ_{rad}/Γ	$4.03(10) \times 10^{-4}$	$6.2(6) \times 10^{-4}$ [2]
$\Gamma_{\pi}(E0)/\Gamma$	$6.7(6) \times 10^{-6}$	$7.6(4) \times 10^{-6}$ [3]
$\Gamma_{\pi}(E0)$	$62.3(2)\mu eV$	-
Γ_{rad}	3.8×10^{-3} eV	$5.1(6) \times 10^{-3}$ eV [2]

The experiment was performed at the Cyclotron Institute using K150 cyclotron in September of 2021. The experimental setup is shown in Fig. 2 and the DAQ system is shown in Fig. 3. We applied the charged-particle coincidence method for this measurement. Hoyle state was populated through $^{12}C(\alpha, \alpha')^{12}C^{*}$. The inelastically scattered α′ was detected by a ΔE-E silicon telescope located at 81° with respect to the beam axis. The ^{12}C(g.s.) ion produced in the electromagnetic decay of the Hoyle state is detected by the MDM-TexPPAC system at 35.3°.

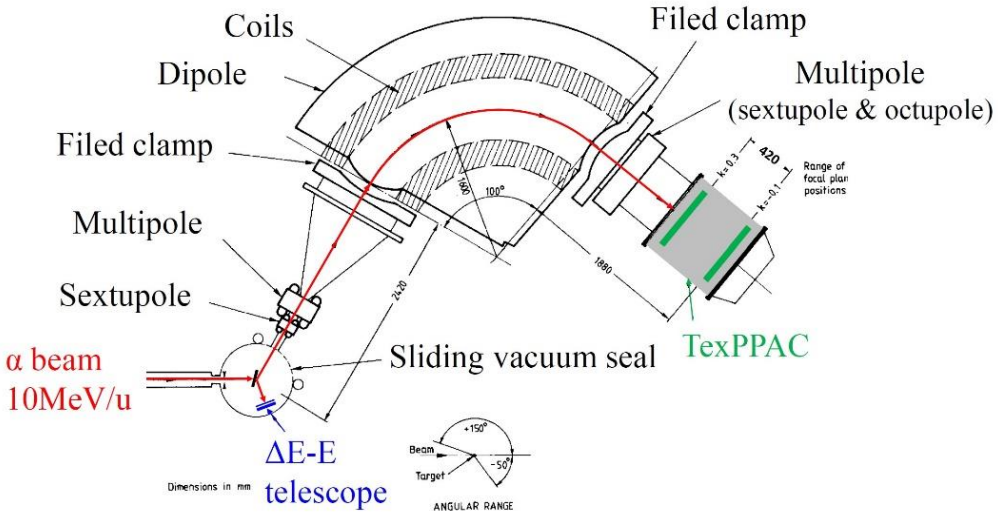

Fig. 2. Schematic of experimental setup.

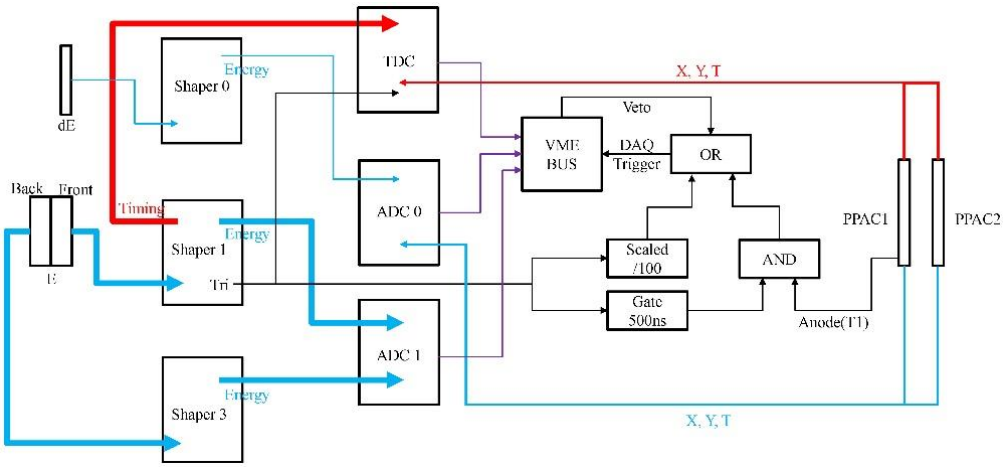

Fig. 3. Schematic of DAQ system. The blue, red, purple and black lines represent energy, timing, digital and trigger signals, respectively.

The magnetic rigidity of a particle is $B\rho = \frac{mv}{q} = \frac{m}{q}\sqrt{2\frac{E_k}{m}}$. Both $^{4}He^{2+}$ and $^{12}C^{6+}$ have the same *m/q* ratio. The spectrometer cannot separate them if they have the same kinetic energy per nucleon. Fig. 4 shows the Geant4 simulation for the energies of the ^{4}He and ^{12}C ions that enter the slit box (MDM

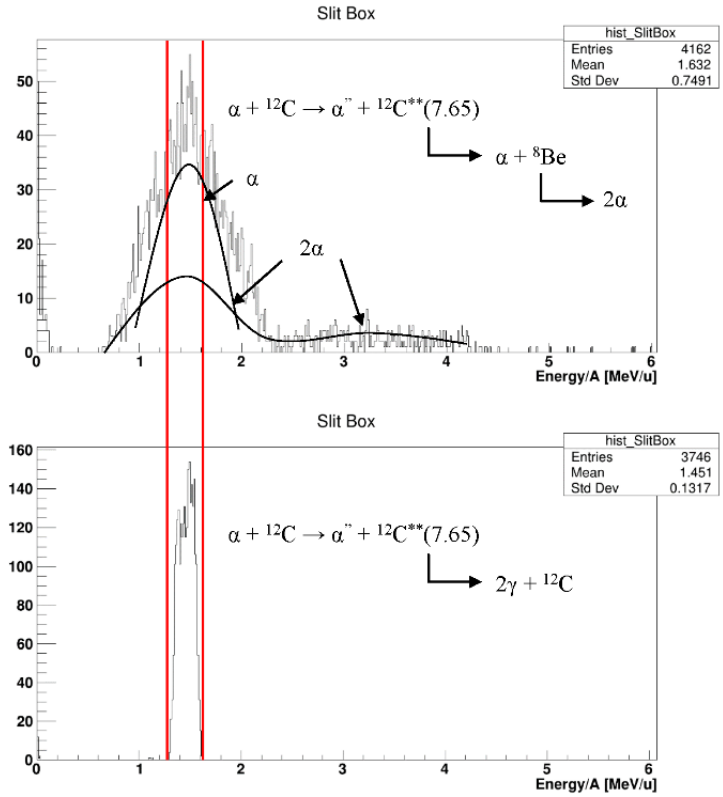

Fig. 4. Energy distribution of $^{12}C(\mathbf{0_2^+})$ decay products that enter MDM spectrometer.

spectrometer entrance). The spectrometer is set for $^{12}C^{5+}$ so that only small amount of $^{4}He^{2+}$ ions which fly 1.2 times faster than $^{12}C^{5+}$ ions can be transmitted. By measuring the time of flight (TOF), we can further separate the transmitted $^{4}He^{2+}$ ions and the $^{12}C^{5+}$ ions of our interests.

The ^{12}C ions coming out from the target are of charge states from 1+ to 6+. To determine the charge state distribution, the magnetic rigidity of MDM was tuned for ^{12}C in each charge state. The number of $^{12}C(0_2^+)$-related coincidence events was counted and normalized to the number of single events. The result is shown in Fig. 5. It can be seen that $^{12}C^{5+}$ has the highest fraction - F_{5+} = 0.495 ± 0.026. 2+ and 1+ charge states are of too small fractions, so they are neglected.

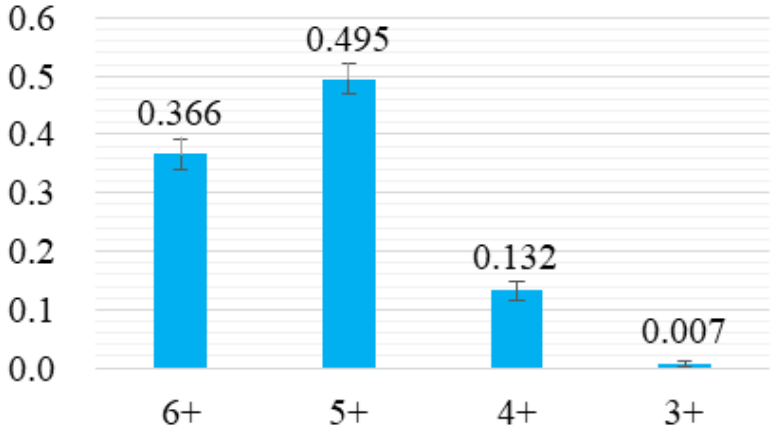

Fig. 5. Charge state distribution of 12C out of target.

Particles detected by TexPPACs traveled more than 7 m, while particles detected by silicon detectors traveled only 17 cm. TOF of the first type (T_1) is of the order of 300 ns while the second type (T_{Si}) is 10 ns. Hence, we can use T_1-T_{Si} to substitute the real TOF. Fig. 6 shows T_1-T_{Si} vs excitation

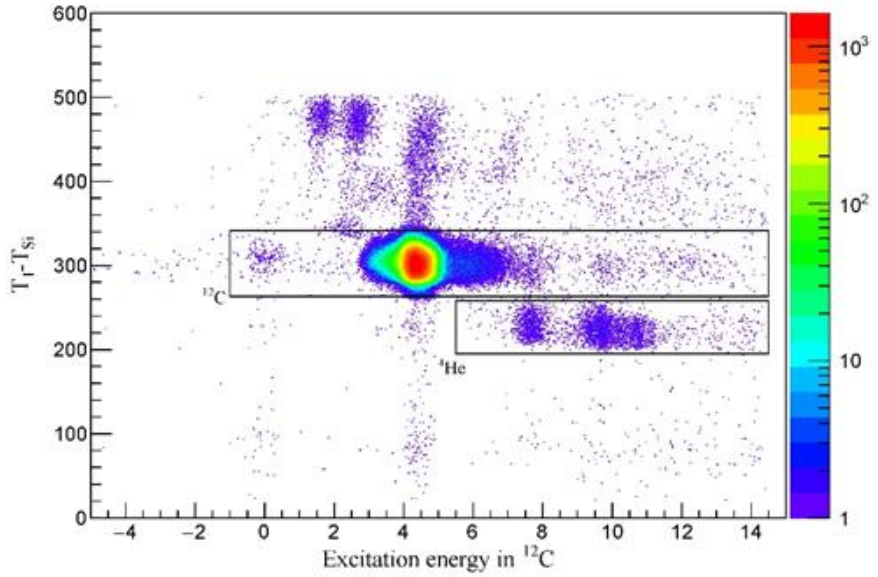

Fig. 6. TOF difference between TexPPAC1 and E detector. The boxes show the clusters of $^{12}C^{5+}$ ions and $^{4}He^{2+}$ respectively.

energy in ^{12}C. The blobs in the upper and lower boxes are associated with $^{12}C^{5+}$ and $^{4}He^{2+}$ events, respectively. As discussed, the TOF for α-particles are smaller than ^{12}C ions since they are 1.2 times faster; this allows a good particle discrimination.

The excitation energy spectrum of ^{12}C obtained are shown in Fig. 6. (a) shows the spectra for events when there were only pre-scale triggers. The excitation energy spectrum (c) for the radiative decay events was obtained from the coincidence events between α-particles in the E detector and $^{12}C^{5+}$ ions in TexPPAC1. (d) shows the coincidence events between α-particles in the E detector and $^{4}He^{2+}$ ions in TexPPAC1. Colored lines are fitted function for each peak and background. From fitted functions we extrapolate $N_{\mathrm{coinc}} = 369 \pm 19$ and $N_{\mathrm{Si}} = 15179 \pm 123$. Therefore, we have $\frac{\Gamma_{\mathrm{rad}}}{\Gamma}\epsilon^{-1} = 4.91(36) \times 10^{-4}$. The correction factor ϵ is still under analysis.

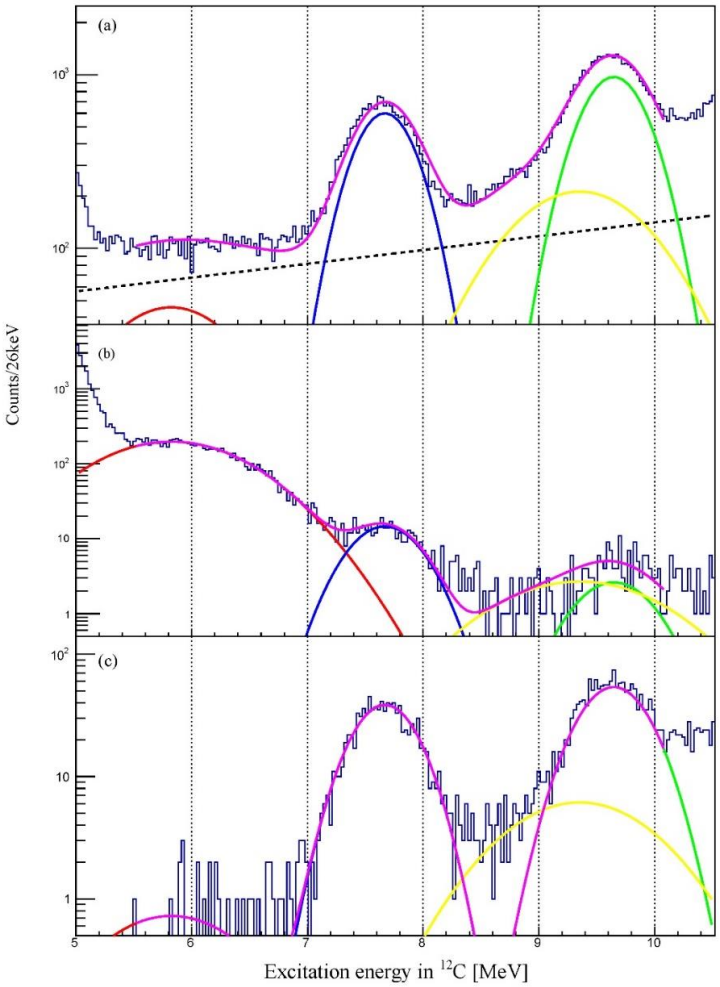

Fig. 7. Excitation energy spectra of ^{12}C around the $\mathbf{0_2^+}$ state for (a) the pre-trigger events, (b) the ^{12}C-α′ coincidence events, and (c) the ^{4}He-α′ coincidence events. The black dashed line shows the background estimated to be exponential. The blue and green lines show the fitted $\mathbf{0_2^+}$ and $\mathbf{3_1^-}$ states, respectively. The red line is expected to be an excitation state from ^{13}C contamination, and the yellow line is expected to be the background from α inelastic scattering on the aluminum target ladder. The purple lines present the sum of all the fit functions.

[1] T.K. Eriksen, T. Kibedi, M.W.Reed *et al*., Phys. Rev. C, **102**, 024320 (2020).
[2] M. Freer, and H. Fynbo, Prog. Part. Nucl. Phys. **78**, 1 (2014).
[3] T. Kibedi, B. Alshahrani, A.E. Stuchbery *et al*., Phys. Rev. Lett. **125**, 182701 (2020).

Determining ANCs relevant for the $^{12}C(\alpha,\gamma)^{16}O$ reaction

E.A. Harris,[1,2] G.V. Rogachev,[1,2] G. Chubaryan,[1] C. Hunt,[3] E. Koshchiy,[1] Z. Luo,[1,2]
C.E. Parker,[1] K. Rao,[4] M. Roosa,[1,2] A. Saastamoinen,[1] and D.P. Scriven[1,2]
[1]*Cyclotron Institute, Texas A&M University, College Station, Texas 77843*
[2]*Department of Physics & Astronomy, Texas A&M University, College Station, Texas 77843*
[3]*Facility for Rare Isotope Beams, Michigan State University, East Lansing, Michigan, 48824*
[4]*Department of Physics & Astronomy, Rice University, Houston, Texas, 77005*

The $^{12}C(\alpha,\gamma)^{16}O$ reaction is often considered one of the most important reactions in nuclear astrophysics. This reaction determines the absolute abundance of ^{12}C and ^{16}O in our universe and has a large influence on the later stages of stellar evolution. However, direct measurement of radiative α-capture on ^{12}C at the relevant astrophysical energy is not possible with current experimental methods. This is because the Gamow energy peak at 300 keV is far below the Coulomb barrier where the cross section is too small for direct measurements ($\sim 10^{-17}$ b) [1]. Therefore, we must rely on extrapolations from higher energy measurements down to lower energies of interest. But low energy extrapolations for this reaction are challenging because the cross section within the Gamow window is characterized by broad, interfering resonances in ^{16}O. Despite efforts to constrain the properties of these resonances, the reaction rate is not known to the desired uncertainty of 10%. One of the remaining sources of uncertainty for R-matrix extrapolation is the α-particle Asymptotic Normalization Coefficient (ANC) for the ground state of ^{16}O.

The ANC method uses peripheral direct transfer reactions to study direct capture at astrophysical energies. This technique relies on the fact that direct capture at stellar energies occurs at large distances from the nucleus. The cross section thus depends mostly on the asymptotic tail of the wave function whose amplitude is given by the ANC [2]. By ensuring that the chosen transfer reaction is peripheral, the ANC value can be determined for the corresponding direct capture reaction. Additionally, when the transfer is done at sub-Coulomb energies, the DWBA calculations depend mostly on the Coulomb potential rather than the nuclear potentials of the entrance and exit channels [3]. This allows the reaction to be nearly model-independent. The experimental cross section is related to the ANCs (C) of the initial and final states of the system by [2]:

$$\left(\frac{d\sigma}{d\Omega}\right)_{exp} = \frac{\left(C^{A}_{a,x}\right)^2}{b_A^2}\frac{\left(C^{B}_{b,x}\right)^2}{b_B^2}\left(\frac{d\sigma}{d\Omega}\right)_{DWBA} \quad (1)$$

This equation holds for a direct peripheral transfer reaction of A + b → B + a, where A = a + x and B = b + x, with x being the transferred particle.

Currently, α-ANCs of all bound excited states in ^{16}O have been measured [4, 5]. The ANCs of these sub-threshold states play a crucial role in the determination of the capture cross section. However, at higher energies, the direct capture to the ground state plays a more dominant role. Thus our goal is to measure the ANC of the ground state of ^{16}O to constrain the direct capture cross section. In order to

extract this α-ANC, we have used the α-transfer reaction of $^{12}C(^{20}Ne,^{16}O)^{16}O$ populating the ground state of both ^{16}O products. The energy of the beam was chosen such that both the entrance and exit channels of this reaction are sub-Coulomb, which minimizes model dependence and uncertainties.

Three experiments have been completed using the MDM spectrometer and newly built TexPPAC detector in preparation for the extraction of ANCs of interest. The first experiment measured the elastic scattering of $^{12}C(^{16}O,^{16}O)^{12}C$ to define the charge state fractions of ^{16}O at the energy of interest for the sub-Coulomb $^{12}C(^{20}Ne,^{16}O)^{16}O$ α-transfer reaction. An ^{16}O 3^+ beam at 1.25 MeV/u was delivered to the scattering chamber and impinged on a thin ^{12}C target. Separate charge states of the elastically scattered beam ions were then sent through the MDM and into the TexPPAC detector, allowing us to construct a full charge state distribution for ^{16}O (Fig. 1). We concluded that ^{16}O 6^+ has the largest charge state fraction and would be the most favorable for detecting the ^{16}O(g.s.) product from the α-transfer reaction.

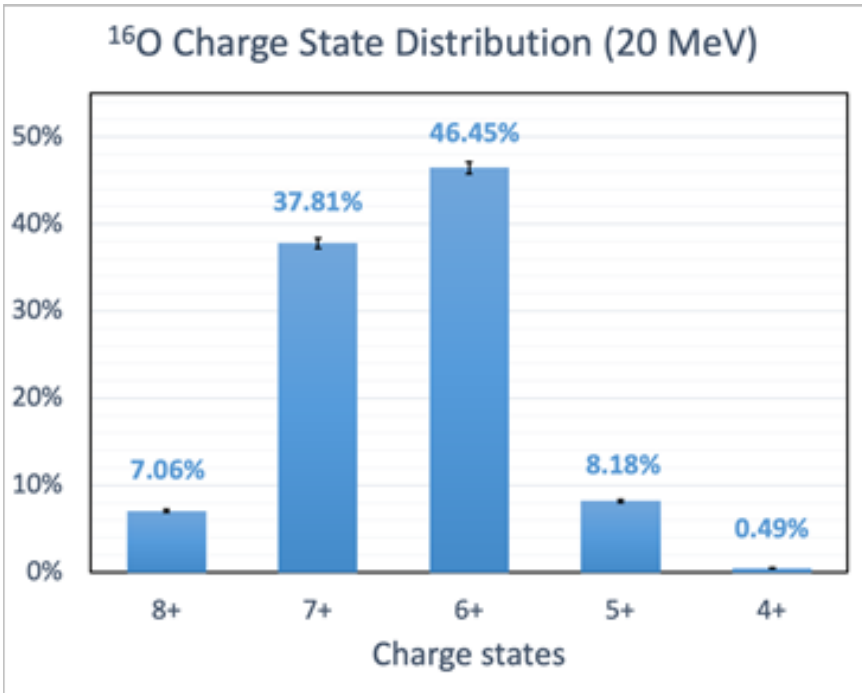

Fig. 1. Charge state fractions of ^{16}O at 20 MeV.

The main experiment to measure the α-ANC of ^{16}O using the $^{12}C(^{20}Ne,^{16}O)^{16}O$ reaction was performed in June 2021. To reduce the background from the beam, modifications were made to the TexPPAC detector. Optimal background reduction was found for a distance of 42 cm between PPAC detectors and a gas pressure of 4 Torr. At this setting, the ^{16}O from the α-transfer reaction has enough energy to reach the second PPAC detector, while the ^{20}Ne does not. A coincidence trigger between PPAC-1 and PPAC-2 was employed in order to filter out the beam background. A ^{20}Ne 3^+ beam at 1.0 MeV/u was delivered to the scattering chamber and impinged on a thin ^{12}C target. A silicon detector was placed inside the scattering chamber to collect signals from all charge states that were elastically scattered from the target. Meanwhile, TexPPAC collected signals from specific charge states sent through the MDM. Charge state measurements were taken for ^{20}Ne, as well as ^{12}C from elastic scattering to be used

for normalization. The position along the X-plane of the detector along with TOF between PPACs was used for particle identification of ^{16}O (Fig. 2). With a theoretical cross section of 10 μb/sr, an assumption of 10 pnA of ^{20}Ne, target thickness of 0.02 mg/cm^2, and a solid angle of 8 msr, we expected to see about 10 events per hour for the ground state population.

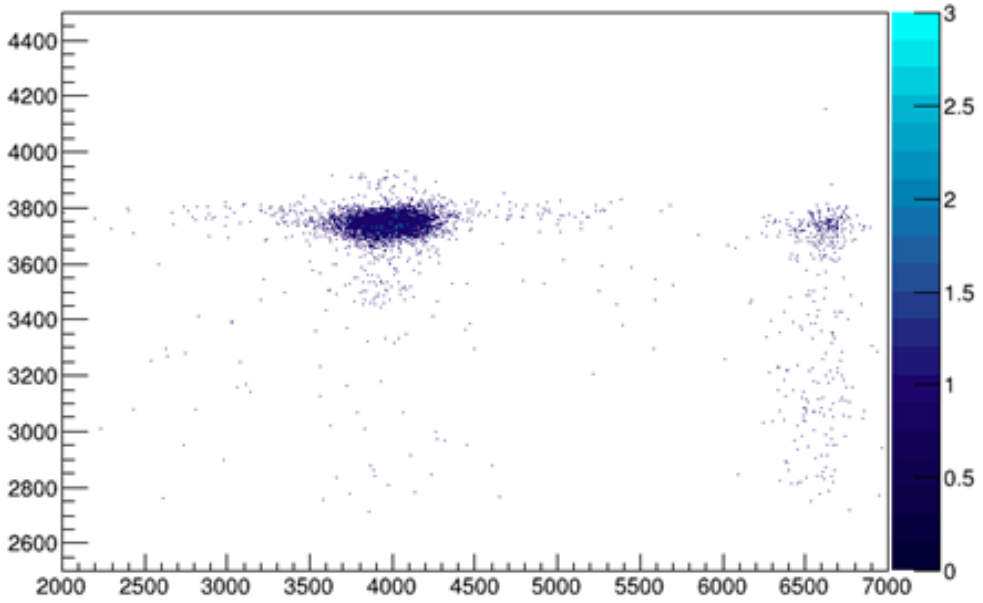

Fig. 2. Preliminary particle ID plot for the ^{12}C(^{20}Ne,^{16}O)^{16}O reaction. The X-axis is position on the focal plane in channels and the Y-axis is TOF in channels. The circle indicates ^{16}O events.

The final experiment was a supplemental measurement to find the ANC of the ground state of ^{20}Ne, which is currently unknown. The same α-transfer reaction was used, but with a higher ^{20}Ne beam energy of 1.525 MeV/u to populate the ^{16}O(6.05 MeV) excited state. Using the known ANC of ^{16}O(6.05 MeV) along with Eq. 1, the ANC of ^{20}Ne can be easily determined. The setup for this measurement was changed slightly from the previous experiment. TexPPAC was used to detect the ^{16}O(6.05 MeV) excited state while the Si was angled to detect the ^{16}O(g.s.) product from the same α-transfer reaction. We then used a coincidence trigger between TexPPAC and Si to reduce the background further. ^{12}C charge state fractions were experimentally determined at this energy and used for normalization of the beam. The analysis of data collected during these experiments is ongoing at this time.

[1] R.J. DeBoer *et al.*, Rev. Mod. Phys. **89**, 035007 (2017).
[2] A.M. Mukhamedzhanov *et al.*, J. Phys. Conf. Ser. **202** 012017 (2010).
[3] F. Hammache and N. de Séréville, Front. Phys. **8**, 602920 (2021).
[4] M.L. Avila *et al.*, Phys. Rev. Lett. **114**, 071101 (2015).
[5] C.R. Brune, W.H. Geist, R.W. Kavanagh, and K.D. Veal, Phys. Rev. Lett. **83**, 4025 (1999).

^{170,174,176}Yb+^{40}Ar fusion-induced fission reactions studies with ENCORE

E. Lopez-Saavedra,[1,*] S. Almaraz-Calderon,[1,†] B.W. Asher,[1] A.B. Morelock,[1] J.F. Perello,[1] A. Hood,[2] A. Saastamoinen,[2] and B.T. Roeder[2]

[1]*Department of Physics Florida State University Tallahassee Florida 32306*

[2]*Cyclotron Institute Texas A&M University College Station Texas 77843*

Evidence of rapid-neutron capture process (r process) nucleosynthesis in binary neutron star mergers via multi- wavelength observations of kilonova emission and gravitational waves has generated great excitement in the scientific community [1-2]. The reliable determination and theoretical prediction of nuclear properties like: fission barriers, fission fragment distributions, as well as the balance between the neutron separation energy and fission-barrier heights, are decisive for determining the nature of the termination of stellar nucleosynthesis in the r process. The path of the r process proceeds through very neutron-rich nuclei that cannot (yet) be studied experimentally. Therefore, experimental investigations are needed to validate the theoretical predictions and provide benchmark information in order to reliably extrapolate theoretical calculations.

A study of the fusion-induced fission excitation functions of the ^{170,174,176}Yb +^{40}Ar systems was carried out at the Cyclotron Institute at Texas A&M University. Fission in the compound nuclei ^{210,214,216}Ra, allowed to study fission excitation functions around the neutron shell closure N = 126. These measurements were performed using beams of ^{170,174,176}Yb at E = 7 MeV/u from MARS and the ENCORE active-target detector [3] filled with 40Ar gas at a pressure of 90 Torr.

ENCORE is an ionization chamber operated in an active target mode where the gas in the detector serves at the same time as target and counting gas. The segmentation in the anode strips allowed for a measurement of a large portion of the fusion-induced fission excitation function using a single beam energy. The schematics of ENCORE is shown in Fig.1.

Fission fragments from the ^{170,174,176}Yb +^{40}Ar → ^{210,214,216}Ra reactions were measured in the energy range E*lab* = 1000 - 650 MeV. The experimental data was compared with simulations and events were identified by their energy loss signals (traces) in ENCORE. A typical fusion-induced fission trace happening in strip 6 of the detector is shown in Fig. 2. The fission event (blue line) is characterized by a beam-like trace from strip 0 to strip 6, followed by a sudden jump in energy loss (strips 7 - 9), and a rapid fall in the energy loss of the trace reaching a minimum in strip 13. The fission event is confirmed by the two large fragments measured in each side of the detector (yellow and green lines) in strips 7 - 12.

* elopezsaavedra@fsu.edu

† salmarazcalderon@fsu.edu

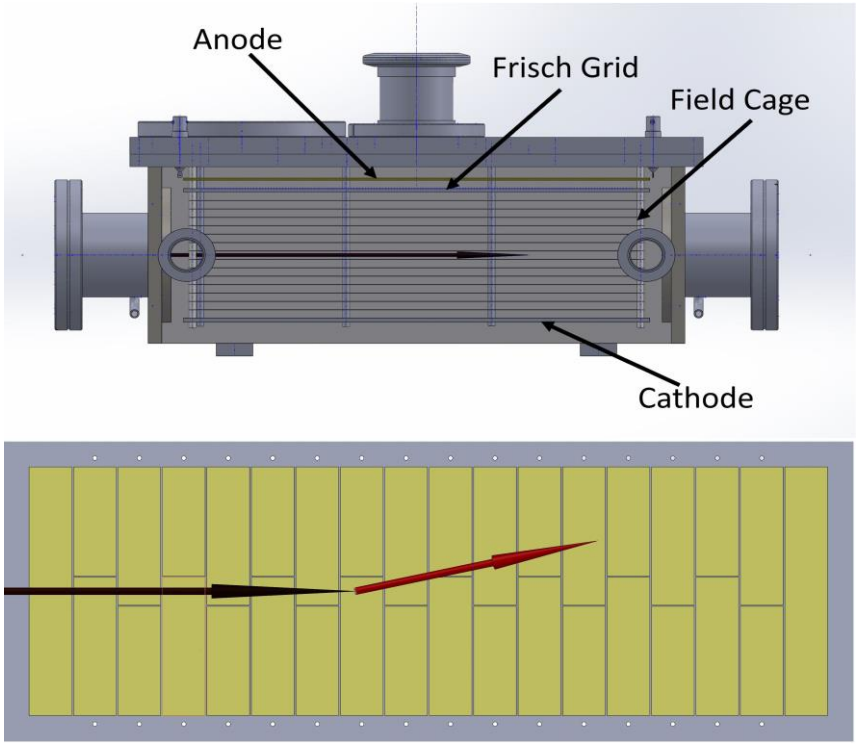

Fig. 1. Schematics of the ENCORE detector (upper figure) and the segmented anode (lower figure). The arrows indicate a reaction happening in strip 6.

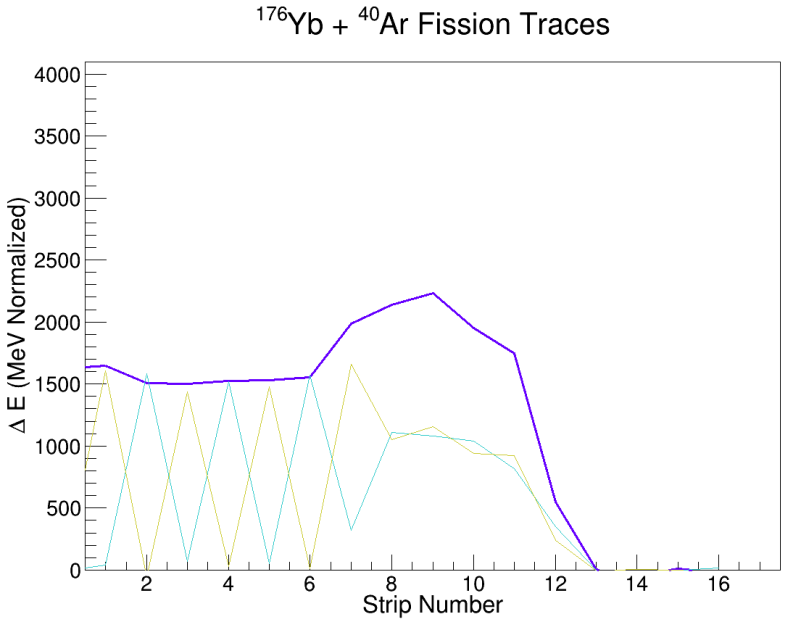

Fig. 2. Typical fusion-induced fission trace measured in strip 6 with ENCORE in the present experiment. The fission event is identified by its energy loss as it travels through the detector.

Preliminary results are shown in Fig.3, where the obtained excitation function for the ^{174}Yb +^{40}Ar ^{214}Ra system is compared with a previous measurement by H.-G. Clerc *et al.*[4], showing good agreement between data sets. The analysis is ongoing for the ^{170,176}Yb +^{40}Ar→^{210,216}Ra systems.

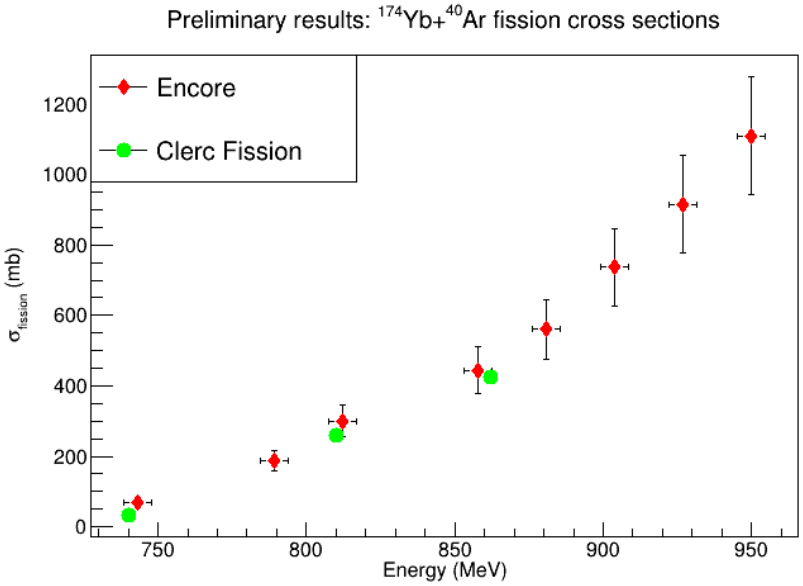

Fig. 3. Preliminary experimental cross section of fusion-induced fission measured with ENCORE for the ^{174}Yb+^{40}Ar→^{214}Ra system as a function of beam energy, in comparison with values from Ref. [4].

Results from this experiment will be used to study the evolution of fission-barrier heights, a key component in r-process network calculations. By studying the N = 126 shell closure reached with stable systems, we will benchmark our approach and validate theoretical predictions. Our technique will then be used with FRIB beams to study the evolution of fission-barrier heights around N = 126 and N =182 with exotic beams, where barrier heights are expected to rise, greatly influencing the path of the r-process [5].

[1] P. Möller, A.J. Sierk, T. Ichikawa, A. Iwamoto, and M. Mumpower, Phys. Rev. C **91**, 024310 (2015).

[2] N. Vassh, R. Vogt, R. Surman, J. Randrup, T. M. Sprouse, M. R. Mumpower, P. Jaffke, D. Shaw, E. M. Holmbeck, Y. Zhu, and G. C. McLaughlin, J. Phys. G **46**, 065202 (2019).

[3] B. Asher, S. Almaraz-Calderon, L. Baby, N. Gerken, E. Lopez-Saavedra, A. Morelock, and J. Perello, Nucl. Instrum Methods Phys. Res. **A1014**, 165724 (2021).

[4] H.-G. Clerc, J. Keller, C.-C. Sahm, K.-H. Schmidt, H. Schulte, and D. Vermeulen, Nucl. Phys. **A419**, 571 (1984).

[5] K.T. Lesko, W. Henning, K.E. Rehm, G. Rosner, J.P. Schiffer, G.S.F. Stephans, B. Zeidman, and W. S. Freeman, Phys. Rev. C **34**, 2155 (1986).

Constraining (n,γ) cross Sections via surrogate measurments with hyperion at Texas A&M University

J. Koros,[1] A. Simon,[1] P. Adsley,[2] B. Alan,[3] O. Gomez,[1] J. Harke,[3] R. Hughes,[3]B. Longfellow,[3]
M. Matney,[1] L. McIntosh,[2] C. Reingold,[3] and A. Saastamoinen[2]
[1]*Department of Physics and Astronomy, University of Notre Dame*
[2]*Cyclotron Institute & Department of Physics and Astronomy, Texas A&M University*
[3]*Lawrence Livermore National Laboratory*

The surrogate method uses an indirect reaction mechanism to populate a compound nucleus (CN) of interest so that its γ emissions may be measured in the laboratory. Fig. 1 depicts this: the desired reaction a + A → B∗ is replaced with the surrogate reaction d+D → b+B∗. The CN (B∗) then decays, and the γ-rays may be measured in coincidence with the outgoing particle b in order to select the correct CN.

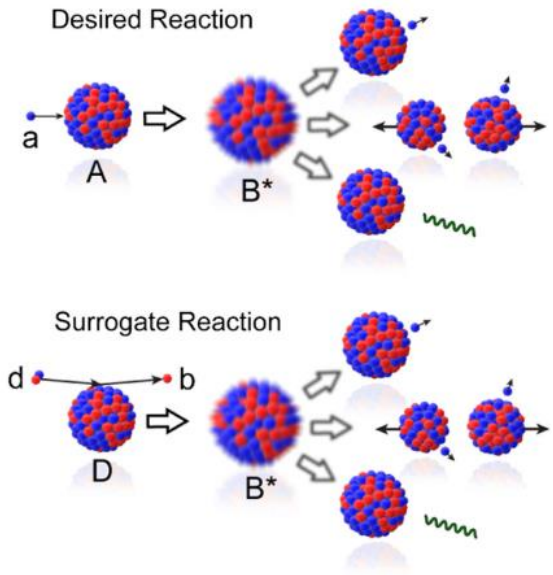

Fig. 1. The desired reaction a+A → B∗ (top) is replaced by the surrogate reaction d+D → b+B∗ (bottom), producing the same desired compound nucleus B∗ [1].

Important to the validity of this method is the assumption that the formation of the CN is independent of its decay. The spin-parity distribution of the CN must also be considered, as different reaction channels may give differing distributions which influence the decay of the CN [1].

With these considerations, the surrogate analysis then uses the experimental γ decay probabilities in statistical Hauser-Feshbach calculations. These calculations model the desired and surrogate reactions using nuclear level densities, optical model potentials, and γ- strength functions. γ-strength functions are typically the least well known othese necessary values. Therefore experimental γ decay probabilities may be used to constrain the γ-strength functiomodels and resulting cross sections.

This project involves the surrogate analysis of data taken with Hyperion, a particle-γ detector array, during an experimental campaign in October-November of 2021. The targets used were 64,70Zn. These isotopes have been chosen because their medium mass allows for use of both Hauser-Feshbach statistical model calculations in the continuum approach and shell-model calculations in the discrete states approach. This is also a region of moderate deformation, although without rapid shape change [2].

The (p,p'), (p,d), and (p,t) reactions were used as surrogates for (n,γ). A beam energy of 27 MeV was selected to access as many of these reaction channels as possible given the telescope design. A three layer Si telescope was used, with thicknesses of 150μm, 1500μm, and 1000μm. The experiment was performed at Texas A&M University's Cyclotron Institute with beam from the K150 cyclotron over 7 days. Detector calibration and efficiency measurements were taken following the run using appropriate γ and α sources. Carbon, lead, and mylar targets were periodically used to take calibration runs throughout as a benchmark for calibration.

Hyperion is a particle-γ detector array consisting of a Si telescope for particle detection and up to 14 high-purity germanium (HPGe) clovers for γ detection. Hyperion was preceded by STARLiTeR, which used a Si telescope paired with 6 HPGe clovers in the reaction plane. As of summer 2021 Hyperion has been moved to its current location behind the NIMROD apparatus in cave 4 at Texas A&M University's Cyclotron Institute; see Fig. 2.

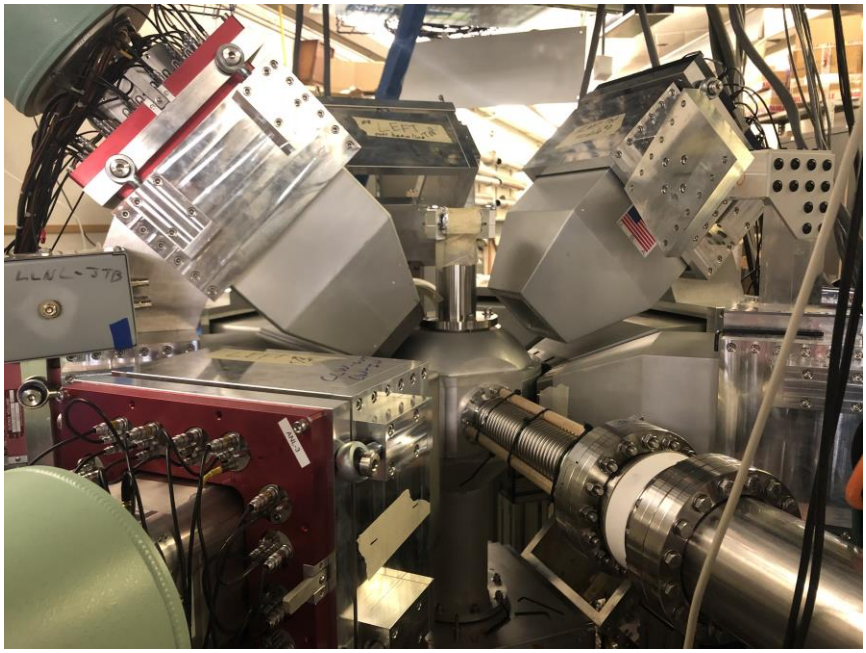

Fig. 2. The Hyperion particle-γ array. The target chamber is seen in the center, with the upstream beamline entering from the front. The clovers surround the target chamber in the operating configuration, but may be moved away for access to the target chamber.

The Si telescope design allows for particle identification, ray tracing, and measurement of particle energy. The telescope is located inside the target chamber directly downstream from the target position, as seen in Fig. 3. Each of the clovers contains 4 HPGe leaf crystals which are under vacuum and cooled with liquid nitrogen during operation. Each clover is surrounded by a BGO for Compton suppression,

shown in blue in Fig. 3. This allows for add-back of γ-rays scattered between crystals and rejection of events which scatter out of the clover volume. Data acquisition is triggered on a coincident ΔE-E signal, which indicates a particle has been detected in both layers of the telescope needed for particle identification.

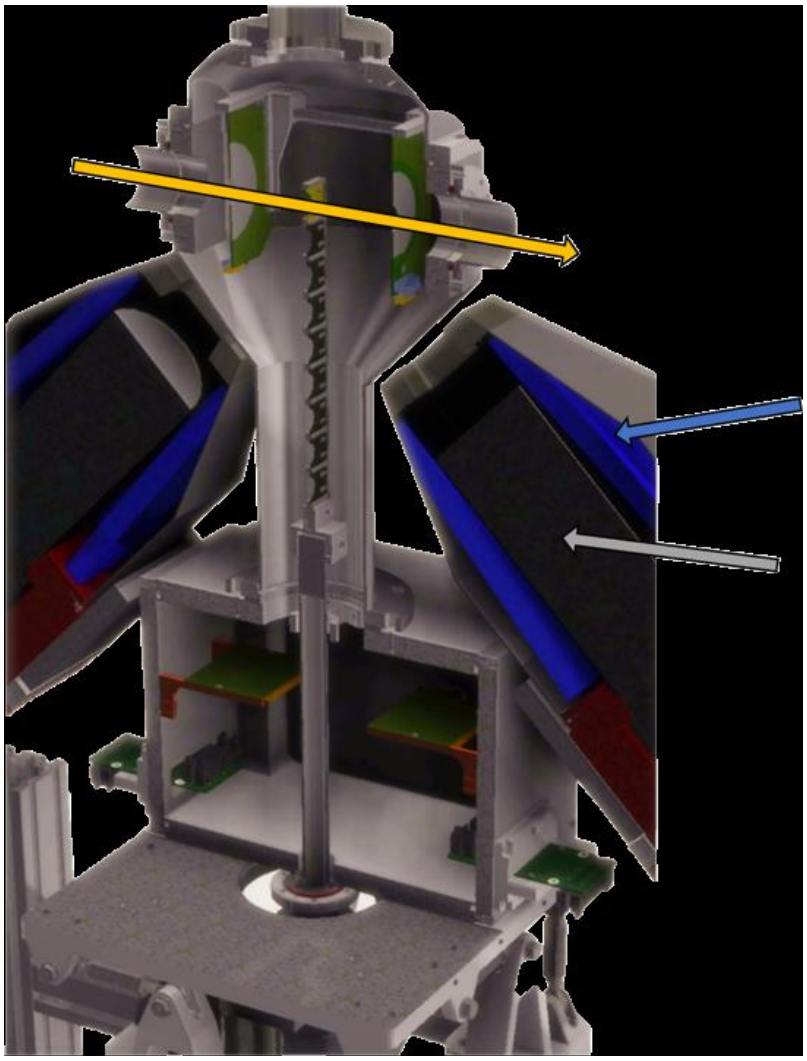

Fig. 3. Hyperion target chamber surrounded by the clover and BGO assembly [3]. The target ladder is located in the center of the chamber, and the segmented Si detectors comprising the telescope are located inside the target chamber downstream from the target position, where the yellow arrow represents the beam direction. Additional particle detectors may be placed upstream from the target for fission applications. The clovers are located directly outside the target chamber and are aligned with the target position. The internal cylinder represents the clover itself (grey arrow), surrounded by the BGO active volume in blue (blue arrow). The BGO and clover are surrounded by a shield from room background, and affixed with a Hevimet which shields the BGO from the target position.

The particle ID allows for selection of the desired CN, and therefore the appropriate surrogate reaction. The particle energy also gives the excitation energy of the CN, which for the surrogate analysis must be observed over

an appropriate range of a few MeV around the CN's neutron separation energy. Together with the γ coincidence information, a matrix may be constructed that gives the γ deexcitation energy as a function of the CN excitation energy. This matrix and particle singles info (all particles detected, regardless of γ coincidence) are then used to extract the γ decay probabilities of individual γ transitions. At this time the experimental campaign has been concluded and analysis of the data is currently ongoing.

[1] J.E. Escher, J T. Burke, F.S. Dietrich, N.D. Scielzo, I.J. Thompson, and W. Younes, Rev. Mod. Phys. **84**, 353 (2012).

[2] Nudat 3.0.

[3] R.O. Hughes, J.T. Burke, R.J. Casperson, S. Ota, S. Fisher, J. Parker, C.W. Beausang, M. Dag, P. Humby, J. Koglin, E. McCleskey, A. B. McIntosh, A. Saastamoinen, A.S. Tamashiro, E. Wilson, and T. C. Wu, Nucl. Instrum Methods Phys. Res. **A856**, 47 (2017).

Measurement of 3α+p states in ^{13}N via β-delayed charged-particle spectroscopy

J. Bishop,[1] G.V. Rogachev,[1,2,3] S. Ahn,[4] M. Barbui,[1] S. Cha,[4] E. Harris,[1, 2] C. Hunt,[1,2] C. Kim,[5] D. Kim,[4] S. Kim,[5] E. Koshchiy,[1] Z. Luo,[1,2] C. Park,[4] C.E. Parker,[1] B.T. Roeder,[1] M. Roosa,[1,2] A. Saastamoinen,[1] and D.P. Scriven[1,2]

[1]*Cyclotron Institute, Texas A&M University, College Station, TX 77843, USA*

[2]*Department of Physics & Astronomy, Texas A&M University, College Station, TX 77843, USA*

[3]*Nuclear Solutions Institute, Texas A&M University, College Station, TX 77843, USA*

[4]*Institute of Basic Science (IBS), Daejeon 34126, Republic of Korea*

[5]*Department of Physics, Sungkyunkwan University (SKKU), Republic of Korea*

Clustering phenomena are prevalent in light nuclei and are an excellent test ground for understanding few-body systems that are theoretically accessible. These clustering phenomena have been well-studied in α-conjugate nuclei and are less-well studied off the line of stability. Of particular interest is the nucleus, ^{13}N, where 3α cluster states in ^{12}C are perturbed by the extra proton. Additionally, the well-clustered ^{9}B may be perturbed by an extra α-particle. Resonant ^{9}B+α or α-transfer is not possible due to the extremely short half-life of the ^{9}B nucleus. Instead, one may use β-delayed charged-particle spectroscopy to populate states in ^{13}N via ^{13}O and observe the decays to a final state of 3α+p. The β-delayed proton channel has previously been studied for ^{13}O [1] where limited statistics showed only a very small sensitivity to populating the p+^{12}C(0_2^+) (Hoyle state) which results in a 3α+p final state. Utilizing the TexAT TPC [2] to perform one-at-a-time β-delayed charged-particle spectroscopy, the β-**.**

Using a ^{14}N(^{3}He,xn)^{13}O production mechanism, an ^{13}O beam of typical intensity of 5 pps was implanted into TexAT. Using a small area Micromegas, 'MM Jr', the beam impurities (mainly ^{7}Be) were identified by their smaller energy loss upon the entrance to the TexAT chamber. Using the established technique with TexAT to provide one-at-a-time implantation [2], a total of 1.9 x 10^5 ^{13}O ions were stopped inside the sensitive region of TexAT. The cleanliness of the technique was demonstrated by a

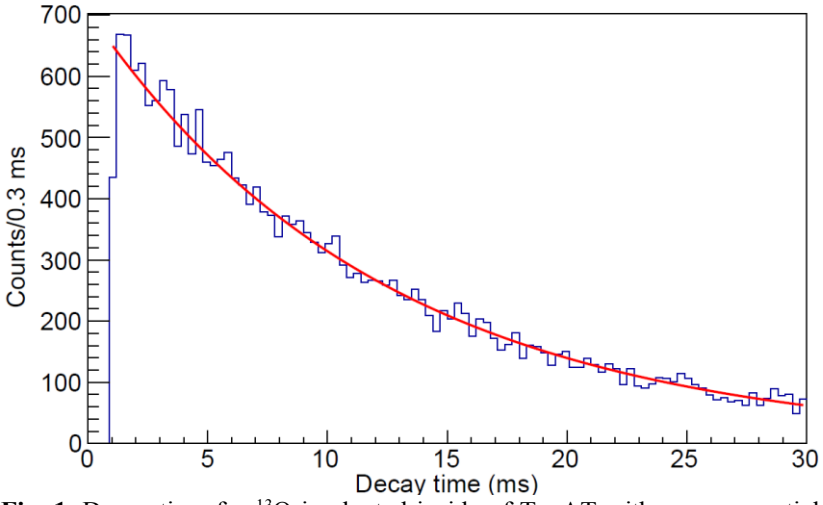

Fig. 1. Decay time for ^{13}O implanted inside of TexAT with an exponential decay curve in red. The value extracted from our data is 8.55±0.09 ms, in good agreement with the adopted value of 8.58±0.05 ms.

background-free half-life measurement of $t_{1/2}$=8.55±0.09 (stat.) ms, in good agreement with the adopted value of 8.58±0.05 ms. The decay curve is shown in Fig. 1.

In total, 1.86 x 10^4 β-delayed proton-decay events were identified (shown in Fig. 2) in addition to 150 β-delayed 3α+p events which were observed for the first time. The current analysis is working to identify the states these events originate from and identify the decay channel. The latest results suggest these events are dominated by ^{9}B+α decays with only around 10% arising from p+^{12}C(0_2^+).

Analysis is still ongoing and will be published in Summer 2022.

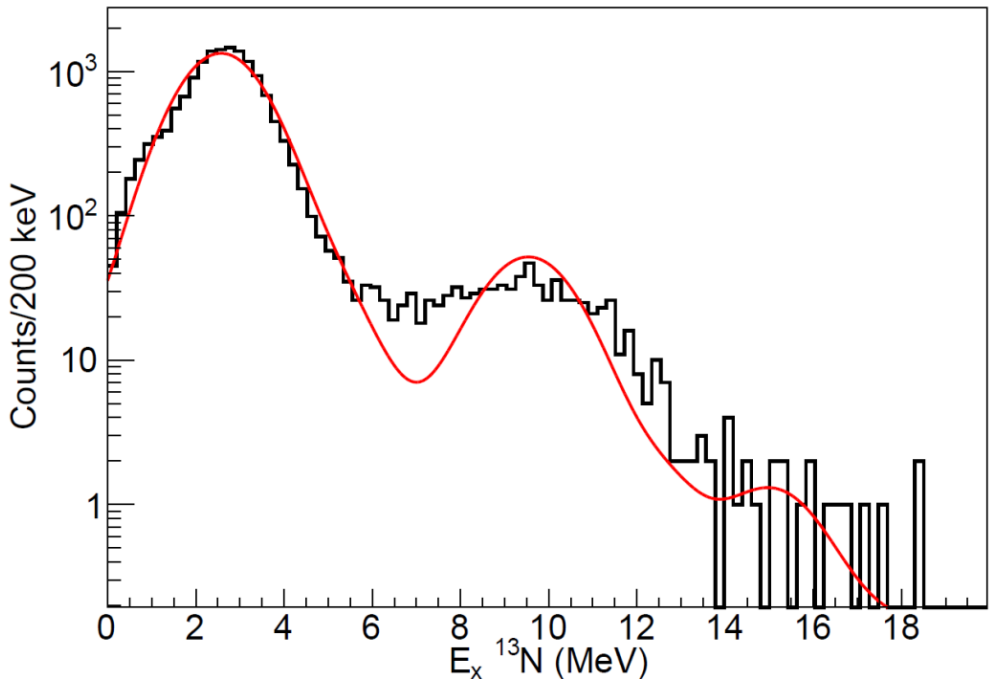

Fig. 2. Selection of (^{13}N, p) events. Proton energy spectrum from these data obtained from the ^{12}C recoil. The expected yield using previously-obtained branching ratios [1] is overlaid in red after being convoluted with a Gaussian profile to best replicate the data.

[1] H. H. Knudsen *et al.*, Phys. Rev. C **72**, 044312 (2005)

[2] E. Koshchiy *et al.*, Nucl. Instrum. Methods Phys. Res. **A957** 163398 (2020),

[3] J. Bishop *et al.*, Nucl. Instrum. Methods Phys. Res. **A964**, 163773 (2020)

Shell structure and evolution through spectroscopy of beryllium isotopes

M. Roosa, G. Christian, G. Rogachev, S. Ahn, E. Bennett, J. Bishop, S. Dede, C. Hunt, H. Jayatissa, E. Koshchiy, R. Malecek, S. Ota, C.E. Parker, D.P. Scriven, and S. Upadhyayula

This project aims to develop the capacity to use the TEXas Active Target (hereafter TexAT) Time Projection Chamber (TPC) for transfer reaction studies [1]. We plan to accomplish this with a two-step experimental program, extracting the spectroscopic factors from low-lying states in ^{11}Be and ^{12}Be with the ^{12}B(d,^{3}He)^{11}Be and ^{13}B(d,^{3}He)^{12}Be reactions respectively. The first experiment aims to compliment existing neutron-removal and neutron-addition spectroscopic data for ^{11}Be studying the overlap between the ^{12}B ground state and low-lying excited states in ^{11}Be, the variability of which indicates sensitivity to reaction model calculations [2]. Because the ^{11}Be system is well studied, this experiment will also help to establish the validity of using an Active Taget Time Projection Chamber (AT-TPC) for transfer reaction studies – with the eventual goal of coupling TexAT to the forthcoming TexNEUT p-Terphenyl neutron detector to study neutron-unbound states. Lessons learned from the ^{11}Be experiment will be applied to the less-studied ^{12}Be nucleus where we will again investigate the overlap between ^{12}Be$^{(gs)}$and low-lying states in ^{13}B.

Data for the ^{11}Be study was taken during May 2019 at the TAMU Cyclotron Institute using the K500 cyclotron and MARS [3]. Starting with a ^{14}C^{4+} beam at 30MeV/u, we used a 1 mm ^{9}Be target to produce 10^{5} pps of ^{12}B at 259.5 MeV/u ± 4%. This beam was delivered to the TexAT experimental set-up where it was impinged on a 200 torr deuterated methane target composing the TexAT active volume. TexAT includes a MicroMeGAS pad plane which provides full momentum reconstruction in the gas target, which, as shown illustrated in Fig. 1, is accompanied by a wall of Si-CsI telescopes positioned perpendicular to the beam axis with a plastic scintillator at the 0^{o} position relative to the beam axis. The solid-state detectors are used to identify particles that do not stop in the gas volume.

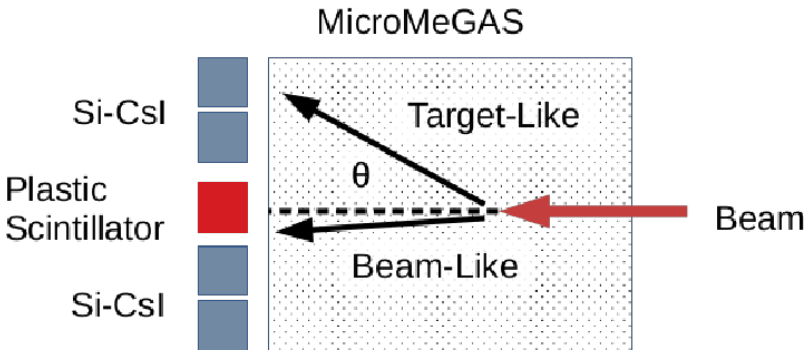

Fig. 1. Cartoon showing the arrangement of detectors inside the TexAT chamber with the target-like ejectile and beam-like ejectile of a beam induced event labeled.

Shown in Fig. 2, light-ion particle identification (PID) has been finalized for the ^{11}Be experiment. Energy deposited in the Si detector is plotted against the mean energy loss in the gas volume (the 3He ions of interest are not energetic enough to reach the CsI detectors). Two distinct loci are evident in the

plot, which are consistent with expected locations of Z=1 and Z=2 particles. Further analysis of this experiment has been hindered by challenges establishing clean track reconstruction largely associated with beam pile-up.

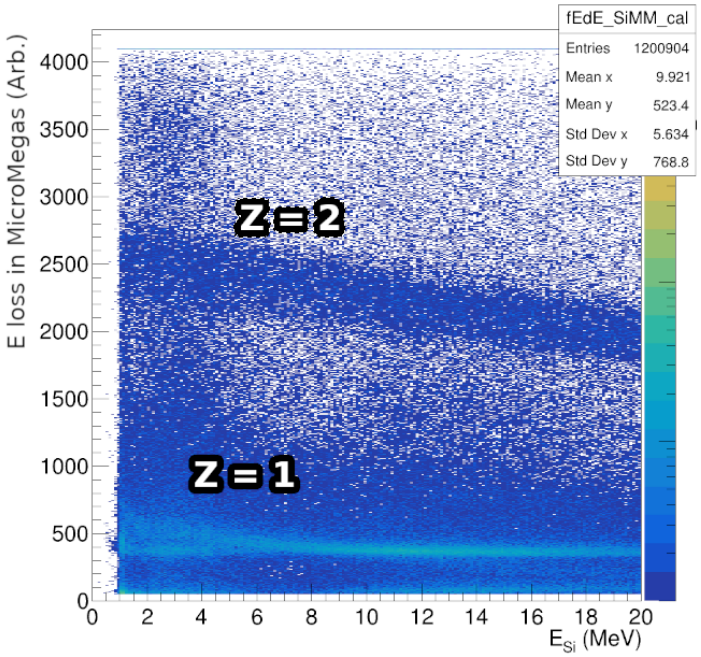

Fig. 2. We can construct a typical E-dE plot by comparing energy deposited in Silicon to the average energy loss in the MicroMeGAS. Z=1 and Z=2 bands are labeled.

As such, we have pivoted our focus to simulation of the experiment in Geant4; both to check the existing analysis software and to prepare for the ^{13}B(d,^{3}He)^{12}Be experiment. The beam for the ^{12}Be run has already been developed and we can expect 1.5x10^{4}pps of incident ^{13}B. This lower beam-rate, when coupled with a change in trigger scheme, from the MicroMeGAS to the Silicon detectors, will greatly simplify analysis.

We have also begun the development of a new YAP(Ce) and CsI(Ti) phoswich detector to be used in the 0^{o} position which will help us eliminate unreacted beam events from analysis. The proposed phoswich design was tested using a ^{14}N beam at 15MeV/u impinged on a 100µg/ cm^{2} Gold and 1mg/cm^{2} Carbon during a beam test in April 2022. Plots of the short integration against the total integration gate from that test are shown in Fig. 3. This gate pairing corresponds to energy loss in the YAP(Ce) vs Total energy and is analogous to a typical dE-E plot used for charged particle identification. When using the Gold target (Left), we can see a distinct grouping of events that correspond to elastically scattered ^{14}N. However, the data from the Carbon target (Right) does not show any distinct clustering; noise in the Gold run indicates that this could be due to poor beam optics as such we cannot conclusively determine the efficacy of the phoswich design at this point.

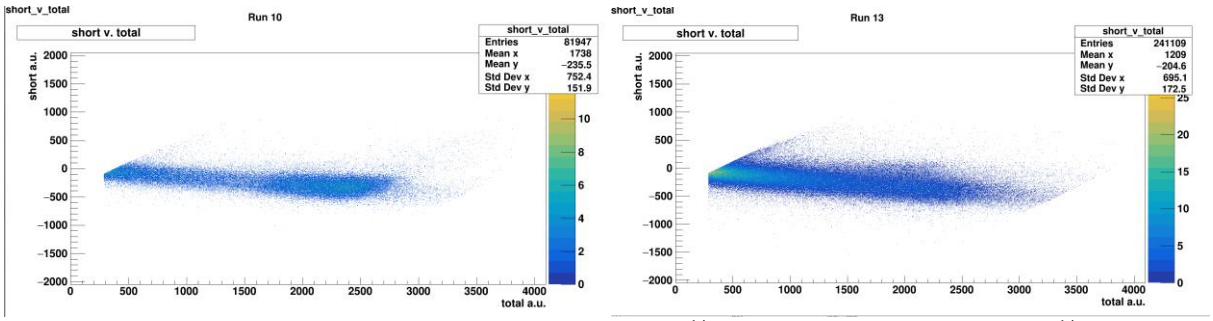

Fig. 3. Short Gate v. Total Integration is plotted for 15Mev/u ^{14}N on Gold (Left) and 15Mev/u ^{14}N on Carbon (Right). See text for discussion.

[1] E. Koshchiy *et al.*, Nucl. Instrum. Methods Phys. Res. A957,163398 (2020).

[2] K. T. Schmitt *et al.*, Phys. Rev. Lett. **108** 192701 (2012).

[3] R.E. Tribble *et al.*, Nucl. Instrum. Methods Phys. Res. **A285**, 441 (1989).

Cyclotron institute evaluation center report: US Nuclear Structure Data Program (USNDP)

N. Nica and J.C. Hardy

Nuclear data evaluation is the main activity designed to capitalize the results of nuclear science research. From its beginnings more than a century ago, it became evident that nuclear science evolves over the years in such a way that establishing the "best" parameters at any given time is an important and challenging task. Thus, very early in its development the scientific community became aware, as Marie Curie wrote [1], that "*the need has arisen for the publication of special Tables of the Radioactive Constants*", which she, together with a prestigious group of contemporary scientists, co-authored the first major international nuclear data evaluation paper, titled "*The Radioactive Constants as of 1930*". Moreover, as she continues, "*This responsibility has been assumed by the International Radium Standards Commission chosen in Brussels in 1910 (...)*", which means that, due to its practical importance, this type of activity got institutionalized from its beginnings. Therefore, the origins of what today is known as *nuclear data evaluation* dates to the dawn of nuclear science itself.

In more recent times, it was recognized that the diversity of published data, not to mention their occasional inconsistencies, demanded that all published results should be assembled and reconciled by a specialized group of experienced scientists. Even collecting the relevant information from all the world's publications, was a nontrivial task, but documented databases were gradually established. This culminated with today's *Nuclear Science Reference* (NSR) database, which is maintained at the National Nuclear Data Center (https://www.nndc.bnl.gov/nsr/). Gradually after several cycles of systematic data analyses the community arrived at "practical standards" of data, which are then revisited periodically to include the continuous updates of newly published data. In this way, nuclear data evaluation has become a new research domain with its own specificity.

A new turning point emerged after the Second World War when the United States got the leading position in the nuclear research field, and consequently the transatlantic nuclear data evaluation changed shores, with the US becoming its main contributor. The United States Nuclear Structure Data Program (USNDP) was started (with its two main subcomponents, one for nuclear reactions and one for nuclear structure), being designed to maintain the so-called Evaluated Nuclear Structure Data File (ENSDF) database, the most extensive nuclear structure data repository in the world. This effort was shared initially among several national institutes and was extended to gradually include a few universities, of which Texas A&M Cyclotron Institute has been one since 2005. It was first funded by a contract with Brookhaven National Laboratory, but in 2017 we started to receive direct funding through the DOE Grant DE-FG03-93ER40773, "Cyclotron-based Nuclear Science". At that time, we became the Texas A&M Cyclotron Institute independent ENSDF Data Evaluation Center, one of the important contributors to the USNDP, as well as to the Nuclear Structure and Decay Data international network hosted by the IAEA Vienna.

Between 2005 and 2020, we completed and published the following full mass-chain evaluations: the superheavy A=252 mass chain [2]; the very data-rich mid-mass chains, A=140 [3], A=141 [4], A=147 [5] and A=148 [6]; and the relatively lighter chains, A=97 [7] and A=84 [8], the latter in a large international collaboration. In collaboration with B. Singh and a group of authors from McMaster

University, Canada, we also published the A=77 [9], A=37 [10], A=36 [11], and A=34 [12] mass chains. At the beginning of 2016, we published another large mass chain, A=157, in Nuclear Data Sheets [13], followed by A=158 in 2017 [14], the renewed full evaluation of A=140 in 2018 [15], A=155 in 2019 [16], and A=153 at the end of 2020 [17]. In Aug 2020 we submitted the A=141 mass chain to NNDC which was reviewed and now awaits final publication.

As mentioned in our previous reports, our community has been passing through two crises: a critical shortage of evaluators, followed by a similar shortage of reviewers, due mainly to the retirement of several experienced evaluators. Moreover, the publication pipeline became more demanding, with a prereview process, followed by the main technical review with a couple of iterations, and finally by an editorial review, which together propagated substantial delays of 2-3 years to the currency of the ENSDF database.

In the interval of this report, Apr 1, 2021 – March 31, 2022, we have completed the work for A=162 full mass-chain evaluation, which we successfully submitted to the NNDC before the promised Oct 1, 2021, due date. (It is currently under review.) In parallel with the mainstream work, we also completed a technical review of a 477 pages manuscript on the A=31 mass chain, in a timely manner, after having worked consistently on it for about two months. We also completed the after-review and editorial work on the A=160 chain, which was published in Aug 2021 [18]. We also addressed the most substantial part of after-review and editorial work on the A=147 chain (our second full evaluation of A=147 after that in 2009).

After Oct 2021 we did a substantial part of the work on this fiscal year's commitment, the A=154 full mass-chain evaluation. This mass chain was studied in about 1200 experimental publications of which about 150 have been added since its last full evaluation in May 2008. This work is currently in progress and is to be submitted to NNDC by Sept 30, 2022.

[1] M. Curie, A. Debierne, A.S. Eve, H. Geiger, O. Hahn, S.C. Lind, S. Meyer, E. Rutherford, E. Schweidler, Rev. Mod. Phys. **3**, 427 (1931).
[2] N. Nica, Nucl. Data Sheets **106**, 813 (2005).
[3] N. Nica, Nucl. Data Sheets **108**, 1287 (2007).
[4] N. Nica, Nucl.Data Sheets **122**, 1 (2014).
[5] N. Nica, Nucl. Data Sheets **110**, 749 (2009).
[6] N. Nica, Nucl. Data Sheets 117, 1 (2014).
[7] N. Nica, Nucl. Data Sheets **111**, 525 (2010).
[8] D. Abriola *et al.*, Nucl. Data Sheets 110, 2815 (2009).
[9] B. Singh and N. Nica, Nucl. Data Sheets **113**, 1115 (2012).
[10] J. Cameron, J. Chen, B. Singh, and N. Nica, Nucl. Data Sheets **113**, 365 (2012).
[11] N. Nica, J. Cameron, and B. Singh, Nucl. Data Sheets **113**, 1 (2012).
[12] N. Nica and B. Singh, Nucl. Data Sheets **113**, 1563 (2012).
[13] N. Nica, Nucl.Data Sheets **132**, 1 (2016).
[14] N. Nica, Nucl.Data Sheets **142**, 1 (2017).
[15] N. Nica, Nucl.Data Sheets **154**, 1 (2018).

[16] N. Nica, Nucl.Data Sheets **160**, 1 (2019
[17] N. Nica, Nucl.Data Sheets **170**, 1 (2020).
[18] N. Nica, Nucl.Data Sheets **176**, 1 (2021).

Determining the ^{95}Zr(n, g) and ^{93}Zr(n, g) cross sections via ^{96}Zr(p, p') and ^{94}Zr(p, p') surrogate reactions

B. Wang,[1] C. Reingold,[1] J. Harke,[1] R. Hughes,[1] S. Burcher,[1] G.J. Kim,[2] J. Koros,[3] B. Longfellow,[1] W.-J. Ong,[1] A. Saastamoinen,[2] A. Tamashiro,[4] and B. Isselhardt[1]

[1]*Lawrence Livermore National Laboratory*

[2]*Cyclotron Institute, Texas A&M university, College Station, Texas 77843 Cyclotron Institute*

[3]*University of Notre Dame*

[4]*Oregon State University*

The surrogate-reaction method can improve our understanding of *s*-process nucleosynthesis. Branch-point nuclei are a crucial feature of the *s*-process that highly impact the elemental abundances. Knowing the (n, g) cross sections of these nuclei allows for powerful constraints to be placed on the stellar conditions of the parent stars in which the elements originated. However, many branch-point nuclei have half-lives on the order of months or less, making the use of direct-measurement techniques challenging, if not impossible. In Fall 2021, an experiment was performed at the Texas A&M University Cyclotron Institute in which the surrogate-reaction method was used to obtain the (n, g) cross section for ^{95}Zr (64-day half-life), whose branching has been observed in presolar stardust grains. Inelastic proton scattering from the stable isotope ^{96}Zr served as the surrogate. An enriched ^{96}Zr foil was bombarded with 21-MeV protons from the K150 Cyclotron. Scattered protons and coincident g rays were measured with the LLNL Hyperion array, which consists of three segmented annular silicon detectors in a dE-E1-E2 configuration surrounded by an array of BGO Compton-suppressed HPGe Clover detectors. A benchmark was also performed using ^{94}Zr(p, p') to determine the ^{93}Zr(n, g) cross section, which has been previously measured via direct methods.

Cold QCD physics with STAR at RHIC

B.E. Aboona, C.A. Gagliardi, R.E. Tribble, and the STAR Collaboration

Our group continues to play a major role in the STAR spin physics program. Over the past year, our analysis focus has been on measurements of the Collins effect in 200 GeV pp and p+Au collisions. In parallel, we played a substantial role in the completion, commissioning, and successful operation of the STAR Forward Upgrade during RHIC Run 22, which ran from November, 2021 to April, 2022.

The Collins effect involves the combination of the quark transversity in the proton and the Collins fragmentation function. It manifests itself as azimuthal modulations of identified hadrons about the axes of their parent jets. During the past year, we finalized the paper describing the STAR measurement of the Collins effect in 200 GeV *pp* data that were recorded during 2012 and 2015. The paper gives by far the most detailed look to date at the Collins asymmetry for pions in *pp* collisions, in addition to the first measurements ever of the Collins asymmetry for kaons and protons in *pp* collisions. Multi-dimensional binning provides the most precise determination to date of the kinematic dependence of the Collins fragmentation function. It also presents the most precise measurements to date of the Collins-like effect, which is sensitive to gluon linear polarization in transversely polarized protons, and the inclusive jet A_N, which at mid-rapidity is primarily sensitive to the gluon Sivers effect. The manuscript was approved by the STAR god parent committee in March. It was then submitted to *Physical Review D* in May [1] following the Collaboration review period. The principal authors are J.K. Adkins, J. Drachenberg, R. Fatemi, C.A. Gagliardi, and T. Lin.

Our graduate student B.E. Aboona is analyzing data that STAR recorded during 2015 to determine the size of the Collins effect in $\sqrt{s_{NN}}$ = 200 GeV *p*+Au collisions. This will provide unique insight into the possible factorization breaking that has been predicted for transverse-momentum-dependent phenomena in hadronic collisions, in addition to a spin-dependent probe of the hadronization mechanism in cold nuclear matter.

Last year's report discussed the substantial progress made by Mr. Aboona to improve the particle identification capabilities of STAR by improving the start-less TOF algorithm. One of the improvements involved a *dE/dx* time correction for the pions used for start-time calculations. Since our report from last year, further improvements have been made to the *dE/dx* time correction. The correction now depends on the pseudorapidity of the track and the *z* location of the primary vertex for a given event. This provides a more robust correction to the start time when compared to our earlier correction, which involved only a constant factor. Notably, this modification has a substantial effect on the *pp* and *p*+Au data that STAR recorded during 2015 when the STAR Heavy Flavor Tracker (HFT) was in place.

During the past year, STAR finalized the calibrations for several energies of the Beam Energy Scan II program, which took data during 2019-21. After that, the final production to convert the data from raw hits into physics objects in micro- and pico-DSTs began. The first few beam energies are now complete, and the rest will be completed late in 2022. Mr. Bassam's start-less TOF algorithms are being used for all of these final data production passes.

After finalizing the improvement to start-less TOF, Mr. Aboona turned his focus to the initial steps in the p+Au Collins analysis. Mr. Aboona produced ROOT jet trees for the 2015 p+Au period that

contain all the information needed for his Collins analysis. Prior to producing the jet trees, he made several edits to the standard jet tree routines. These edits included: making the appropriate changes to the codes to store the new start-less TOF information, adding user options that facilitate reducing the disk footprint of the jet trees by 30-40%, and fine tuning parameters for jets and particles in jets.

Mr. Aboona then performed a detailed Quality Assurance (QA) analysis of the 2015 p+Au dataset. STAR usually takes data in ~30-minute intervals; each interval is commonly referred to as a run. The QA process looked at means of various detector and physics quantities on a run-by-run basis to flag outlier runs with beam or detector issues that are difficult to simulate with the standard STAR GEANT routines. By looking at these time series plots and referring to shift log plots and notes during a given run, Mr. Aboona identified outlier runs to be excluded from the Collins analysis. As an example, Fig. 1 shows the z-coordinate of the collision vertex along the beam line as a function of run index. The plot shows three distinct jumps in the mean zvertex values. The jump at (a) corresponds to trigger configuration changes that had direct impact on zvertex. The jumps at (b) and (c) correspond to times when collider experts changed the z location of the collision point inside of STAR. Such information gained from the QA analysis will inform future steps in the Collins analysis, such as data simulations. Overall, the initial run list contained 973 runs, and the QA analysis rejected approximately 8% of the runs. Detailed notes have been made for the runs that have been rejected for future reference.

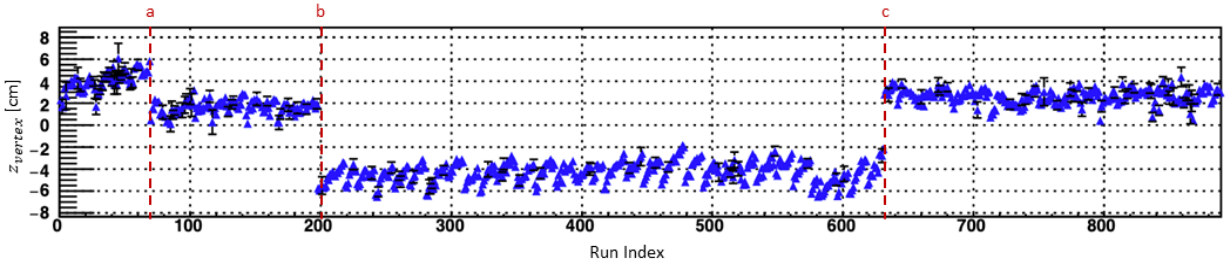

Fig. 1. Mean z_{vertex} of the events (in cm) vs. run index for those 2015 p+Au runs that passed the QA process.

During the past year, we played a major role in the successful completion, commissioning, and data taking with the STAR Forward Upgrade during RHIC Run 22, which ran from November, 2021 to April, 2022. Dr. Gagliardi was onsite at Brookhaven for November and December, where he served as STAR Shift Leader for six weeks. During this time, he led the final cosmic ray commissioning of the Forward Silicon Tracker (FST) and small Thin Gap Chambers (sTGC). He also led the final commissioning of the FST, sTGC, and Forward Calorimeter System (FCS) with beam. STAR then took the first physics data with the Forward Upgrade during his last week on shift. Finally, he continued to monitor the entire system remotely throughout the rest of Run 22, including oversight during a number of special low-luminosity periods to optimize the gains of the FCS, determine the alignment of the FST and sTGC, and to measure minimum bias cross sections at forward rapidities. The latter will be used to tune the production of underlying event activity close to beam rapidity in Monte Carlo event generators.

Our major responsibility during the construction of the Forward Upgrade was to develop the trigger algorithms for the FCS. We identified distinct patterns of electromagnetic and hadronic calorimeter energy depositions characteristic of high-pT photons or electrons, hadrons, and jets. We also

combined the calorimeter information with hits in the STAR Event Plane Detector (EPD) to distinguish electrons from photons. These various trigger primitives were then combined to produce 28 distinct triggers: 7 for jets with different pseudorapidities and pT thresholds, 2 for dijets, 3 for photons and $\pi 0$ with different pT thresholds, 3 for hadrons with different pT thresholds, 2 for Drell-Yan, 3 for J/ψ, and 8 for routine monitoring. During the run, four of the triggers were operated in "take-all" mode: the primary Drell-Yan trigger (which also provides most of the acceptance for J/ψ events in the Forward Upgrade), the highest-pT electromagnetic shower trigger, and two triggers designed to select ultra-peripheral J/ψ production where the one of the decay electrons falls within the acceptance of the Forward Upgrade and the other is detected by the STAR Endcap Electromagnetic Calorimeter. The remaining triggers were prescaled by various factors to fit into the available data acquisition bandwidth. Overall, STAR recorded slightly more than 10 billion Forward Upgrade events at an average rate of about 2 kHz, with a typical dead time of 8-10%. 1.9 billion of those events also included read-out of the STAR Time Projection Chamber.

Finally, we continue to carry various administrative responsibilities for STAR. Dr. Gagliardi served on the STAR Trigger Board for RHIC Run 22, where he had the primary responsibility for monitoring the data acquisition bandwidth allocations for all of the triggers, not just those associated with the Forward Upgrade. He also served as a member of the STAR TPC Review Panel during 2021, and is now serving as a member of the STAR TPC Data Acquisition Improvement Task Force. He served as chair of the god parent committee for a STAR spin paper [2], member of the god parent committee for a second spin paper [3], and as a member of the god parent committees for two heavy flavor papers [4,5]. Finally, he was appointed to a three-year term as a member of the RHIC Users' Executive Committee for 2021-24.

Mr. Aboona served as the Cold QCD delegate to the STAR QA Board for Run 22. During this period, STAR was collecting data from polarized pp collisions at ~510 GeV. As a QA board delegate, he developed QA analysis codes to validate the data taken by the mid-rapidity triggers during the run. He reported his weekly results to the QA Board on behalf the Cold QCD Physics Working Group. He also communicated and presented summaries to the Cold QCD group. The result of the mid-rapidity QA analysis is a compiled list of outlier runs that will serve as the first level QA for future analyses using Run 22 data.

[1] STAR Collaboration, arXiv:2205.11800.
[2] M.S. Abdallah *et al.* (STAR Collaboration), Phys. Rev. D **105**, 092001 (2022).
[3] J. Adam *et al.* (STAR Collaboration), Phys. Rev. D **103**, 092009 (2021).
[4] M.S. Abdallah *et al.* (STAR Collaboration), Phys. Rev. D **105**, 032007 (2022).
[5] M.S. Abdallah *et al.* (STAR Collaboration), arXiv:2111.14615.

SECTION II

HEAVY ION REACTIONS

Employing ternary fission of ^{242}Pu as a probe of very neutron rich (Yp=0.036) matter

J.B. Natowitz,[1] H. Pais,[2] and G. Roepke[3]
[1]*Cyclotron Institute, Texas A&M University, College Station, Texas 77843*
[2]*Department of Physics, University of Coimbra, 3004-516 Coimbra, Portugal*
[3]*University of Rostock, FB Physik, University of Rostock, 18059 Rostock, Germany*

Detailed assessments of the ability of two recent theoretical approaches to modeling existing experimental data for ternary fission [1,2] confirm earlier indications that the dominant mode of cluster formation in ternary fission is clusterization in *very neutron rich, very low density, essentially chemically equilibrated*, nucleonic matter [2-4]. An extended study and comparison of these approaches applied to ternary fission yields in the thermal neutron induced reaction ^{241}Pu(n,f)^{242}Pu [5] was recently undertaken to resolve some apparent differences of density, mass fractions and free neutron to free proton ratios obtained in the previous work. Resolution of these issues leads to a refined characterization of the source matter. Within the ideal resonance gas approximation in both approaches we find that a temperature of 1.29 MeV, density of 6.6 x 10^{-5} nucleons/ fm^3 and proton fraction Yp = 0.036 provide a good representation of yields of the ternary emitted light particles and clusters. See results for Z= 1 and 2 isotopes presented Figs. 1 and 2. The derived properties are comparable to that predicted for the

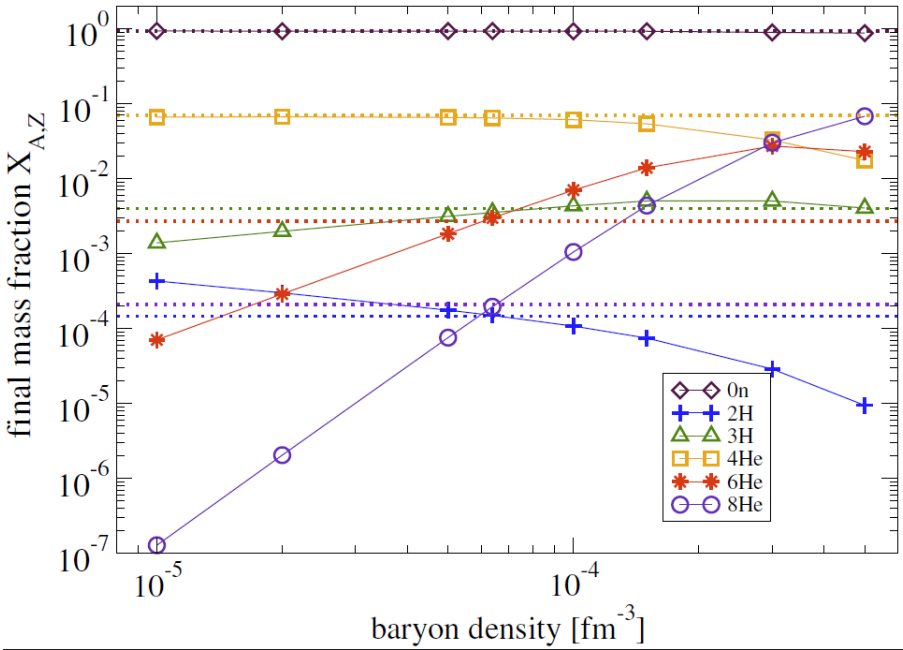

Fig. 1. Calculated light isotope yields (resonance-gas approximation) as a function of density (fixed temperature T= 1.288 MeV and proton fraction Yp = 0.0355) for Z=1,2 isotopes (represented by symbols) are compared with the observed experimental yields [5,6] represented by horizontal dotted lines. Optimum agreement based on a fit metric proposed by J. Lestone [7] is found

crystalline region in neutron star skins. This baseline calculation provides a foundation for the exploration of possible in-medium effects on the binding energies of larger clusters, even at such low densities. Those investigations are currently underway.

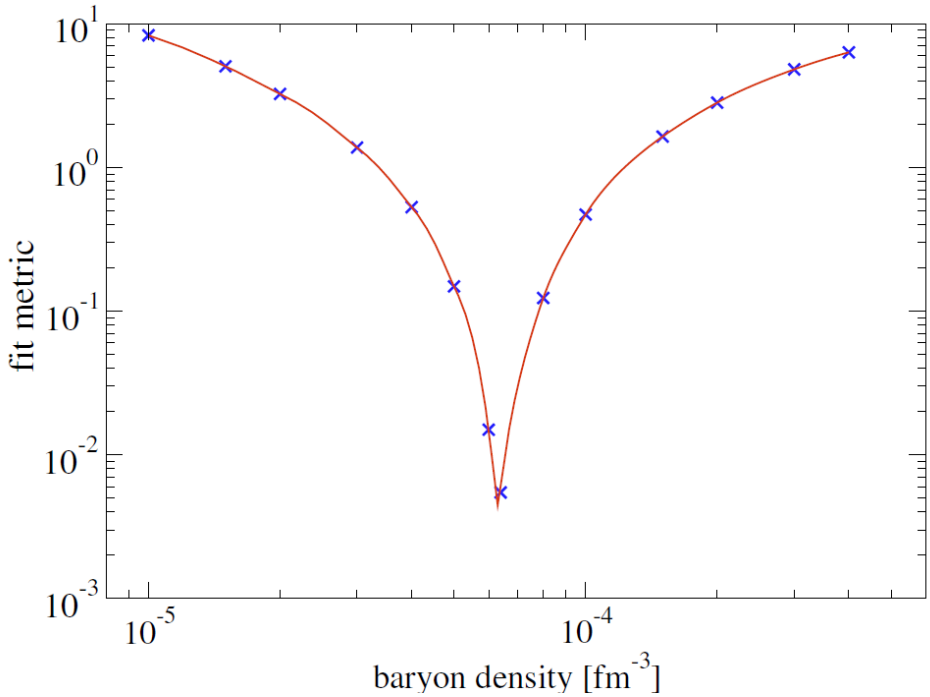

Fig. 2. Fit metric [7] vs. baryon density for T= 1.288 MeV and Yp = 0.0355.

[1] H. Pais, F. Gulminelli, C. Providência, and G. Röpke, Phys. Rev. C **97**, 045805 (2018).

[2] G. Röpke, J. B. Natowitz, and H. Pais, Eur. Phys. J. A **56**, 238 (2020).

[3] J.B. Natowitz, H. Pais, G. Röpke, J. Gauthier, K. Hagel, M. Barbui, and R. Wada, Phys. Rev. C **102**, 064621 (2020).

[4] G. Röpke, J.B. Natowitz, and H. Pais, Phys. Rev. C **103**, L061601 (2021).

[5] U. Koester et al., Nucl. Phys. **A652**, 371 (1999).

[6] A.S. Vorobyev *et al.*, J. Expt. Theor. Phys. **127**, 659 (2018).

[7] J.P. Lestone LA-UR-05-8860 (2006), Phys. Rev. C **72**, 014604 (2005).

Correcting for calculated excitation energy in DAPPER

A. Abbott, R. Rider, M. Sorensen, A.B. McIntosh, K. Hagel, and S.J. Yennello

The Detector Array for Photons, Protons, and Exotic Residues (DAPPER) was constructed to measure photon strength functions (PSFs). The commissioning run for DAPPER occurred in August 2021 and used a beam of 7.5 MeV/u ^{57}Fe and a collection of CD_2 targets of varying thicknesses to study the PSF of ^{58}Fe populated from the ^{57}Fe(d,pγ)^{58}Fe reaction. Over the course of the experiment, excited states calculated from the energy of the emitted proton exhibited less intense peaks in the spectrum when using a specific target. This was due to "burning" off the deuterium in the target. In addition, the thickness of the target at the beamspot position was changed over the course of its use. This changing of the target thickness results in improper excitation energy calculations. To correct for this, each of the CD_2 targets used in the experiment was characterized using a position sensitive Dual-Axis Duo-Lateral (DADL) silicon detector [1].

The test setup utilizes a DADL detector, a ^{228}Th source, and a CD_2 target used in the August experiment. The CD_2 target is placed ~1 cm away from the DADL and the ^{228}Th source is placed ~6 cm from the target. The alpha particles emitted from the source pass through the CD_2 target losing different amounts of energy based on the thickness of the material. Using SRIM calculations, the true thickness of the targets can be determined by this energy loss. We can use the average energy loss in the undamaged region of the target to determine the initial thickness and the energy loss in the damaged regions to determine the thickness of the target at the end of its use in the experiment. A thickness map of one of the CD_2 targets is shown below (Fig. 1) with a photo of the corresponding target (Fig. 2). The measured initial and final thicknesses of the target can be used alongside the calculated ratio of reactions on deuterium to total reactions (shown in Fig. 3) in order to make a run-by-run correction of the thickness of the CD_2 target allowing for the proper treatment of the proton energy loss.

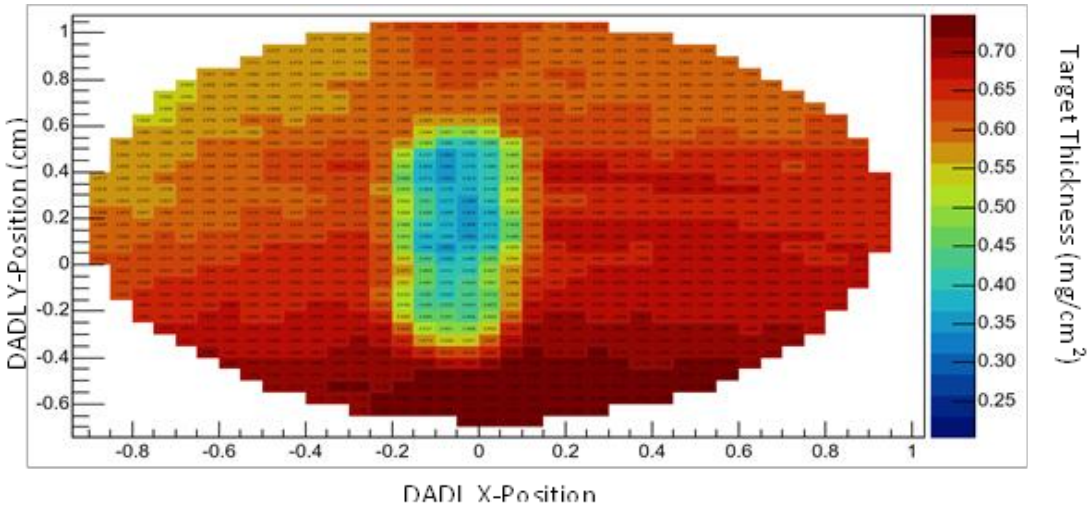

Fig. 1. DADL map of a CD2 target used in the August 2021 DAPPER experiment.

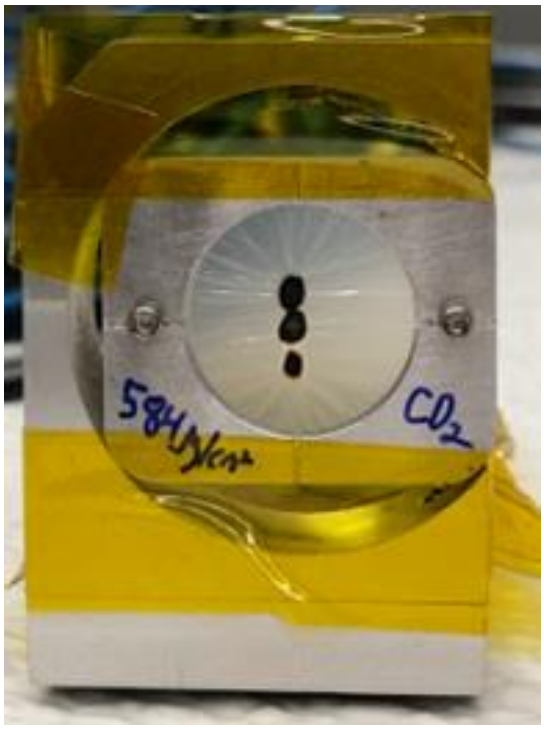

Fig.2. Target corresponding to the map in Figure.

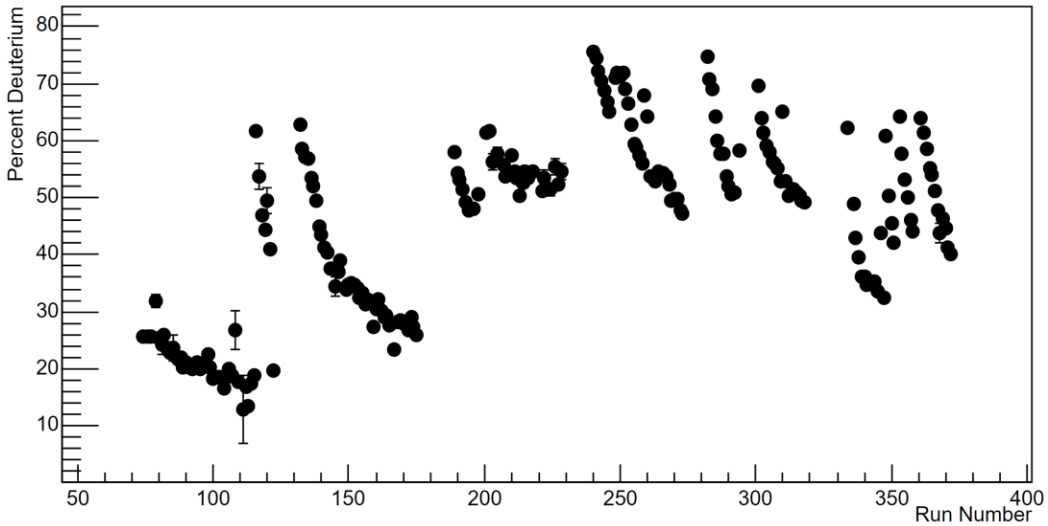

Fig. 3. Percent of reactions coming from deuterium compared to the total reactions from CD_2.

Part of the changing percentage of reactions from deuterium is also attributed to the movement of the beamspot between, and potentially during, runs on the ^{57}Fe beam. This will also broaden the peaks corresponding to excited states in ^{58}Fe. In order to correct for this shifting beamspot, a scan over the face of the target was performed while fitting the peak of a discrete state in ^{58}Fe (1.675 MeV state). The beamspot which provided the best resolution on that particular peak was assumed to be the position the

beam was in during that run. An example of the improvement in resolution is shown in Fig. 4 for a particular run. In order to improve the signal-to-noise ratio on the peak, a requirement that a single gamma-ray with an energy between 1.4 and 1.8 MeV was used.

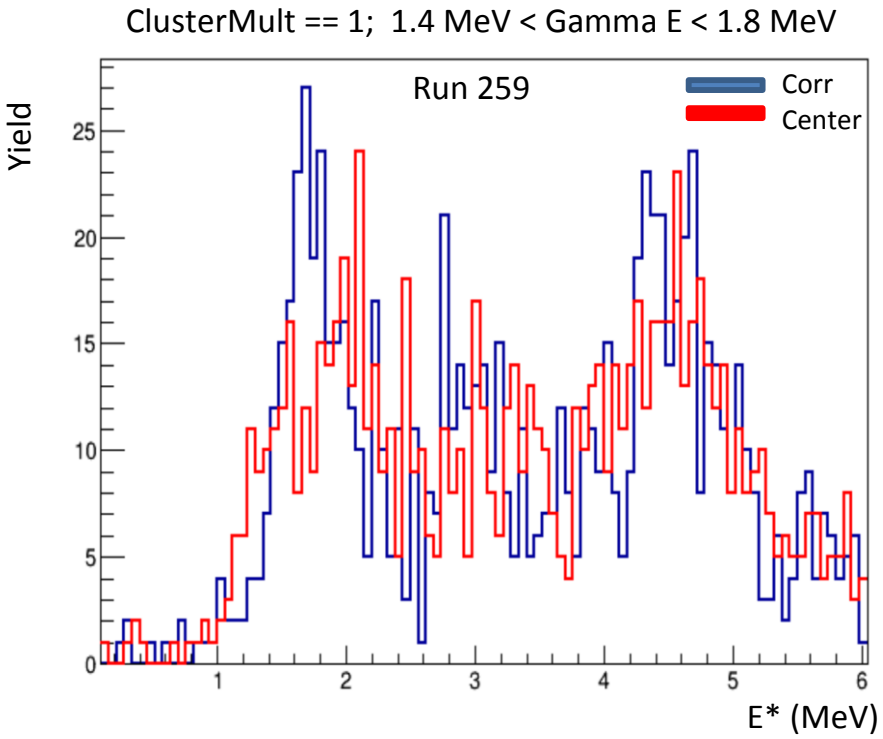

Fig. 4. Improved resolution on the 1.675 MeV second excited state peak in 58Fe when applying the corrected beamspot position for this run. Red spectrum assumes the center of the target while the blue uses the best case spot for this run (2 mm, 0.3 mm).

[1] S.N. Soisson *et al.*, Nucl. Instrum. Methods Phys. Res. **A613**, 240 (2010).

Investigation of ground state alpha cluster structure using the NIMROD detector array

Z. Tobin, K. Hagel, A. McIntosh, R. Wada, B. Harvey, and S.J. Yennello

Alpha clusterization is the phenomenon where a certain number of ^{4}He particles can make up the structure of nuclei. At certain excitation energies, these alpha cluster structures tend to dominate as a result of the large binding energy and high excitation energy of ^{4}He. At such excitation energies, the nucleus can be described as a low density, gas-like state consisting of a discrete number of alpha clusters. An example of such a state is the Hoyle state in ^{12}C, which can decay into three alpha particles. However, this type of cluster structure does not exclusively exist in excited states of nuclei. Models calculating the density distributions of alpha conjugate nuclei indicate that some degree of alpha cluster structure coexists with a dominate mean-field type structure at the ground state level and other low-lying states [1-3]. Such models also suggest that the energy levels of the alpha conjugate nuclei are sensitive to the degree of mixing between the mean-field structure and cluster structure at these states.

In order to measure the degree of clusterization at the ground state level, we examined quasifree knockout reactions with a 60 MeV/u ^{4}He beam on various light alpha-conjugate targets. This experiment was performed using the NIMROD 4π detector array (Fig. 1) so that the detection coverage of quasifree, energy conversing angle pairs is maximized. In other words, NIMROD provides good coverage for the detection of the knocked-out particle and scattered projectile at angles where the energies sum to the original projectile energy.

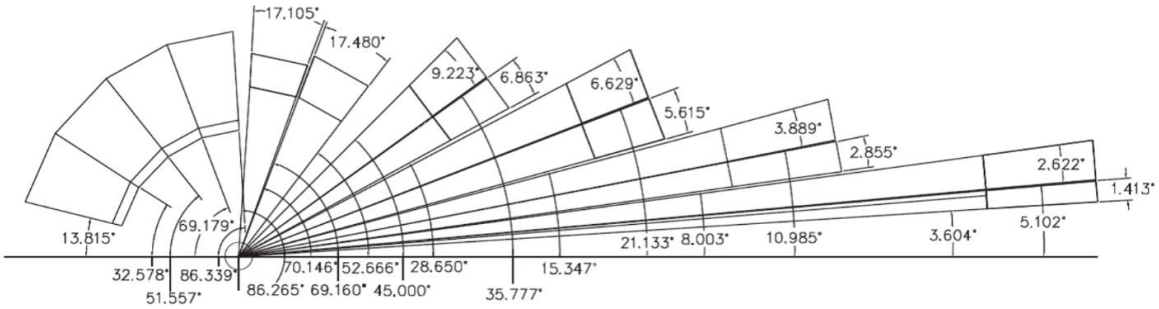

Fig. 1. Schematic of the detector module locations in the NIMROD detector array. NIMROD contains 156 detector modules consisting of Si-CsI and Si-Si-CsI telescopes.

This experiment was rerun in late March of 2022 for the purpose of enhancing the statistics of the knockout yield. This was done using the multi-event capabilities of the Struck Flash 3316 waveform digitizers. In the previous run of 2020, we were running with a live time of approximately 20-50%. This severely limited the amount of data we were capable of recording. With the multi-event mode, we were able to collect 20-40 times more data than the previous experiment.

Additionally, we were better able to quantify and correct for a detector anomaly observed in the data analysis of the 2020 run. The gain of approximately half of the CsI(Tl) detectors appears to be unstable with the rate of incident ions. As presented in Fig. 2, the measured energy increases with

increasing rate. This is inconsistent with conventional gain drifts observed with voltage sagging in PMTs at high rates. Oddly, the largest change in gain typically occurs at relatively low rates (~20-60 ev/s). There appears to be no detector location dependence to this effect. The severity of the gain drifts also varies across detector from approximately 2-9%. It also has been reproduced in several experiments after the 2020 run with proton and alpha beams. From those experiments, it was concluded that this effect is likely an issue with the detector, not with the electronics. More work needs to be done in order to better understand the issues with these detectors.

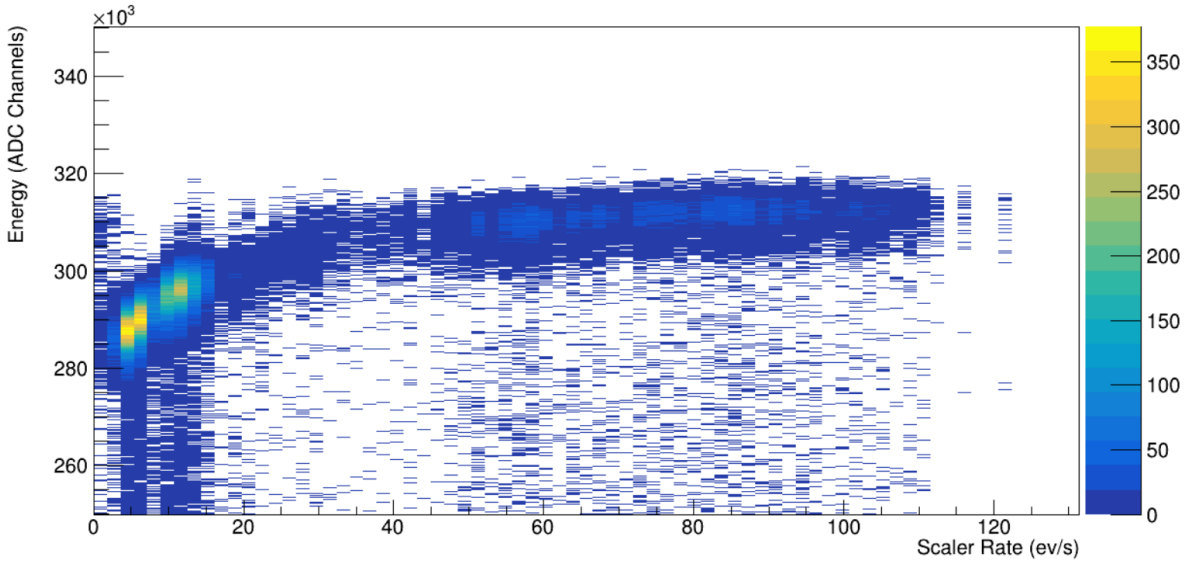

Fig. 2. Measured energy in a CsI(Tl) detector correlated with the rate of incident ions on the detector. Shown in this plot is the gain drift of 60 MeV/u alpha projectiles elastically scattered off of a Th target.

[1] H. Horiuchi, J. Phys. G **37**, 064021 (2010); DOI: 10.1088/0954-3899/37/6/064021

[2] Y. Kanada-En'yo and H. Horiuchi, Front. Phys. **13**, 132108 (2018); DOI: 10.1007/s11467-018-0830-y

[3] Y. Kanada-En'yo, Prog. Theo. Phys. **117**, 655 (2007); DOI: 10.1143/PTP.121.895

Proximity decay effect in ^{28}Si + ^{12}C at 35 MeV/u using FAUST

K.A. Hannaman, A.B. McIntosh, B. Harvey, K. Hagel, A. Abbott, J. Gauthier, T. Hankins, Y.-W. Lui, L. McCann, L.A. McIntosh, R. Rider, S. Schultz, M. Sorensen, Z. Tobin, R. Wada, and S.J. Yennello

In heavy-ion collisions near the fermi-energy, some collisions may result in an excited projectile-like fragment that may de-excite via light charged particle emission [1]. If the light charged particle is emitted in an excited state (LCP*), itself will further de-excite according to the decay pathways available. Given short enough lived LCP* states, the LCP* decay will on average occur in very close proximity to the source that emitted it. These decay products experience the coulomb field of the source remnant, affecting the distribution of relative energies between the LCP* decay products depending on the LCP* emission velocity (Ecm) distribution, lifetime, decay energy (ERel), and decay orientation (β). This effect for the 2+ excited state of ^{8}Be emitted from sources with $14 < Z < 47$ has been previously studied using LASSA [2]. The position sensitive FAUST (Forward Array Undertaking Search for Toroids) was recently used to measure reaction products from collisions of ^{28}Si at 35 MeV/u on ^{12}C. The excellent angular information afforded by FAUST has allowed for this effect to be studied in more detail.

The decay orientation angle, β, is defined as the angle between the center-of-mass energy vector (between the source remnant and the two LCP* decay products) and the relative energy vector between the two LCP* decay products as shown in Fig. 1. Events were selected that contain two ^{4}He(α)-particles and an isotope of Ne (Z = 10) to observe the proximity decay effect of ^{8}Be(2+) emission from an excited

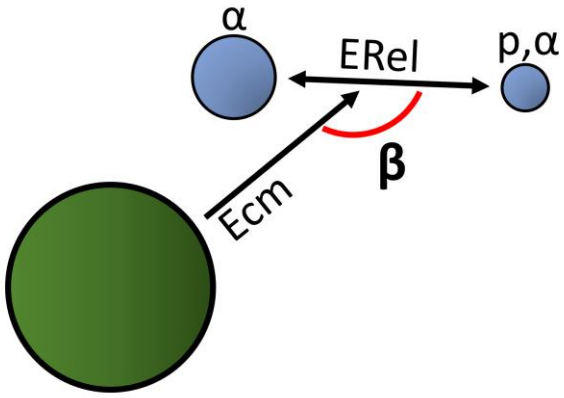

Fig. 1. (a) Diagram depicting the decay of an LCP* emitted from an excited projectile-like source. In this work, ^{8}Be(0+, 2+) → α + α and ^{5}Li(3/2-) → p + α LCP* decays are studied.

Si source. The α- α relative energy distributions in 5° ranges of β were produced from 0° to 90°, with the β = 20° - 25° range shown in blue in Fig. 2(a). The ^{8}Be(2+) state of interest can be seen as the broad peak centered at ~3 MeV, having an intrinsic width of 1.5 MeV. To extract the mean of this distribution, the uncorrelated background must be accounted for. One way to do this is by producing a mixed event distribution [3]. Here, two α-particles were chosen from different events and the relative energy between them was calculated. To obtain the mixed event β, the velocity vector of each α-particle relative to the

remnant measured in each respective event was first obtained. These remnant frame α-particle velocities were then joined to produce a mixed event decay where β could be calculated. The mixed event distribution with β = 20° - 25° is shown in red in Fig. 2(a). The mixed event distribution is then normalized to the real distribution in a range where there are no expected states (5 – 8 MeV relative energy in this case). By subtracting the mixed event distribution from the real event distribution, yield associated with excited state decays emerge as shown in Fig. 2(b). To obtain the mean relative energy of the ^{8}Be(2+) state, a gaussian fit is performed. This analysis procedure is repeated for all 5° ranges of β.

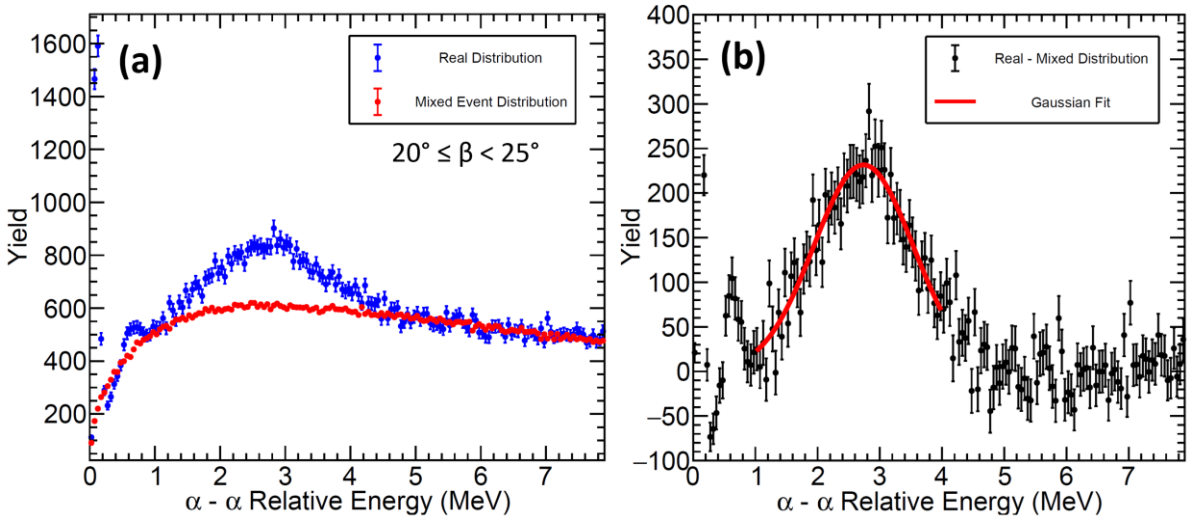

Fig. 2. Procedure for obtaining the ^{8}Be(2+) excited state relative energy mean for β = 20° - 25° in events with a measured Ne remnant. (a) Real (blue) and mixed (red) α – α relative energy distribution in MeV. (b) Real – mixed α – α relative energy distribution in MeV. Gaussian fit of the ^{8}Be(2+) peak is shown in red.

To examine the proximity decay effect for ^{8}Be(2+) emitted from a Si PLF*, the mean ^{8}Be(2+) relative energy is plotted as a function of the decay orientation in Fig. 3(a). For decays that occur in-line with the remnant Ne (β = 0°), the α-particle that is emitted back towards the Ne remnant experiences its coulomb field, kicking this α-particle away from the remnant towards the other α-particle. This reduces the measured α-α relative energy for this decay orientation by ~650 keV compared to the literature value of 3.12 MeV [4]. The results from this study show a similar trend to the LASSA result (blue open circles), however further modeling is necessary to make direct comparisons due to differences in detector acceptance, resolution, remnant mass, remnant charge, and event selection. One way to further test the validity of the proposed mechanism for this effect is to look for a lack of β-dependence on the mean energy for long-lived LCP* states. The same analysis is performed for the 0+ ground state of ^{8}Be (5.5 eV width), as emitted ^{8}Be(0+) decays will occur far from the remnant (~1 X 10^{6} fm for 8Be(0+) compared to ~5 fm for ^{8}Be(2+)). There is no observed β-dependence for the mean energy of this decay as shown by the black triangles in Fig. 1(a).

To further characterize and understand the interplay between the coulomb field, LCP* decay energy, LCP* lifetime, and decay orientation, it would be useful to observe this effect for asymmetric LCP* decays. The 1.23 MeV width (3/2-) ground state decay of ^{5}Li to p + α with a decay energy of 1.97 MeV is an excellent candidate. Events were selected that contained a proton, α, and heavy remnant with 7 < Z < 12, and the analysis procedure was repeated. Due to the decay producing two different isotopes, the decay orientation can be probed from β = 0° - 180°, showing the effect of having either the proton or α-particle emitted back towards the remnant as shown in Fig. 3(b). Decays where the proton is emitted backwards have a larger reduction in the mean relative energy than for decays where the α-particle is emitted backwards (~940 keV (β = 0°) compared to ~600 keV (β = 180°) less than the 1970 keV literature value) [5]. A coulomb trajectory model is currently being developed to better understand the contribution of all pertinent factors that may influence the degree of mean relative energy deviation as a function of β, as well as how the measured β relates to the initial β.

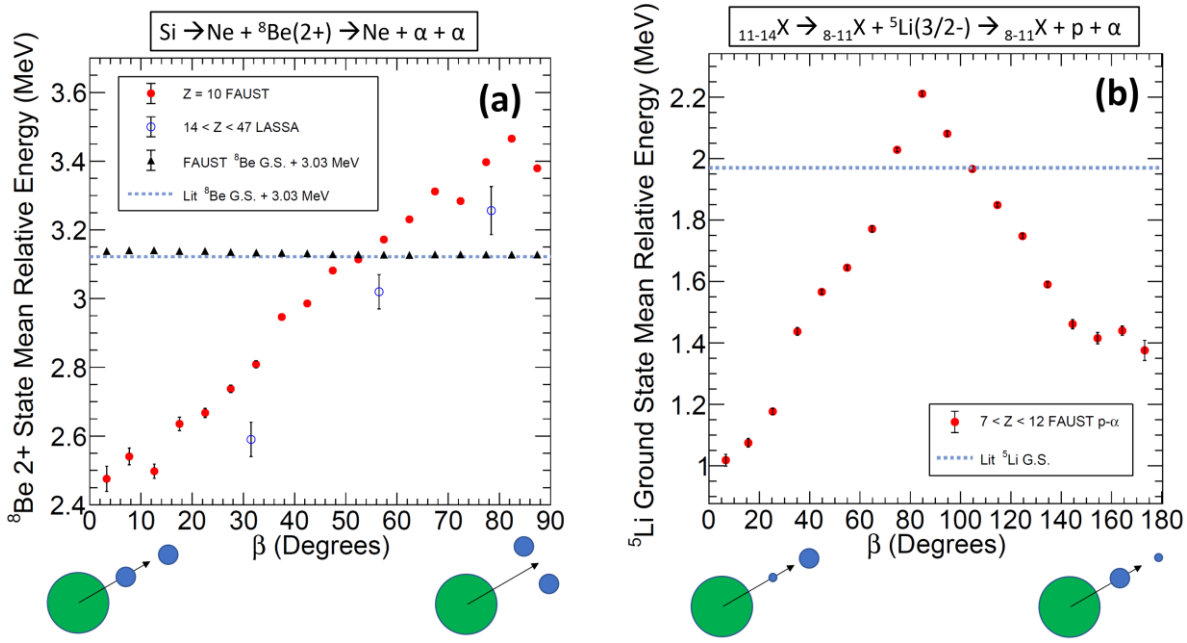

Fig. 3. Mean relative energy of LCP* decay in MeV as a function of decay orientation β in degrees. Diagrams depicting the physical orientation that each extreme of β corresponds to is shown below the x-axis. Event selection requirements are displayed in the legend. Errors on the means are obtained from the gaussian fits. (a) Mean α- α relative energy for the decay of ^{8}Be(2+) (red circles) and the decay of ^{8}Be(0+) (black triangles). Literature ^{8}Be(2+) mean relative energy is shown by the blue dashed line [4]. Results from the LASSA experiment is shown by the blue open circles [2]. (b) Mean p-α relative energy for the decay of ^{5}Li(3/2-) (red circles) with a measured remnant of 7 < Z < 12. Literature ^{5}Li(3/2-) mean relative energy is shown by the blue dashed line [5].

[1] R. Ghetti *et al.,* Nucl. Phys. **A765**, 307 (2006).

[2] A.B. McIntosh *et al.,* Phys. Rev. Lett. **99**, 132701 (2007).

[3] R.J. Charity *et al.,* Phys. Rev. C **52**, 3126 (1995).

[4] D.R. Tilley *et al.,* Nucl. Phys. **A745**, 144 (2004).

[5] D.R. Tilley *et al.,* Nucl. Phys. **A708**, 4 (2002).

Studying multinucleon transfer on the ^{197}Au +^{197}Au reaction

K. Zelga, A. Hood, K. Hagel, R. Wada, and S.J. Yennello

Studying multinucleon transfer (MNT) at the Cyclotron Institute at Texas A&M University began around 2002. Its main goal from the start was to look for new superheavy elements(SHE) with the use of the MNT as an alternative method for their production. Since that day detector setup evolved several times, from BigSol, Passive Catcher, Active Catcher based on BC-418 to the Active Catcher based on YAPs [1,2,3]. In one of the last experiments [3] from 2016 where the ^{197}Au +^{232} Th (7.5AMeV) were tested, several alpha-decay chains with high energies were found. It showed that superheavy elements can be created via MNT. Due to insufficient energy resolution of the used AC detectors and insufficient position information individual nuclides produced during experiments couldn't be identified.

In 2021 A. Hood projected an experiment with the use of the AC array and position-sensitive detector to study more carefully the process of the MNT and to confirm its usability in creating heavy nuclei [4]. The decision of using a position-sensitive detector was made to ensure greater granularity as well as better energy resolution.

Both types of modules, 30 single-anode PMT detectors and dynode + 4 anodes of the Position-Sensitive PMT (PSPMT), were connected to the SIS3316 digitizer. Each channel could trigger individually based on passing its threshold. Beam used during the experiment was 8.63 MeV/A ^{197}Au^{+31} in mode 100ms/100ms beam on/beam off. Data acquisition wasn't taken while the beam was in on mode and for the first 3 ms of the beam off-time - acquisition was turned off for 103 ms and on for 97 ms.

The tested reaction was ^{197}Au +^{197}Au. The experiment was optimized for the production and detection of isotopes like ^{220}Rn, ^{221}Ac, and ^{222}Th. Nuclides in alpha-chains which began with these isotopes are decaying via emission of the high energetic alpha particles (7-9 MeV) and have short lifetimes (on the level of ns-ms). Short lifetime is a desirable characteristic while SIS3316 ADCs allowed recording only 2 us of detected waveforms and while the experiment was focused on searching for (at least) two alpha particles that originated from the above-mentioned chains, presented in Fig. 1.

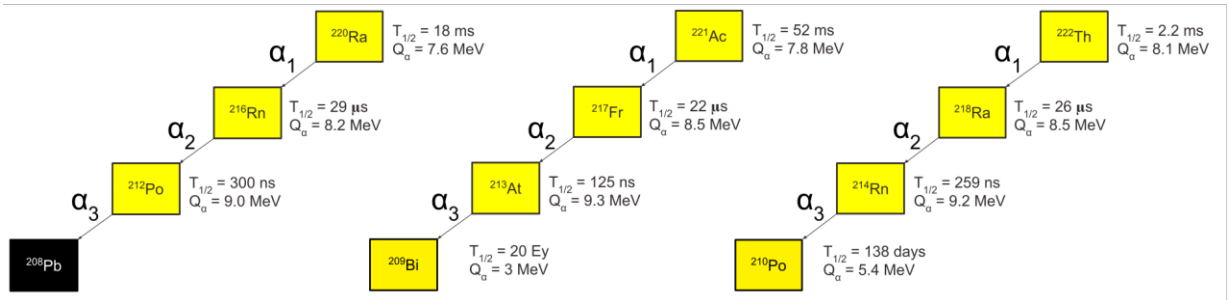

Fig. 1. Scheme of alpha decay chains for ^{220}Ra, ^{221}Ac, and ^{222}Th. Each of the chains ends with a stable (^{208}Pb) or long-lived (^{209}Bi, ^{210}Po) isotope.

Most promising results are collected by a position-sensitive detector borrowed from Robert Grzywacz from the University of Tennessee at Knoxville. This detector contains 64 segmented Hamamatsu H8500C position-sensitive photomultiplier tube, attached to the ISO100 flange, with a quartz light guide divided into 2 mm x 2 mm sections with 500micron YAP scintillator on it. This detector

ensures better position resolution (dictated by the size of the light guide) than used until this time single anode YAP detectors with 2 cm diameter.

In the currently conducted data analysis were found several cases correspond to the registration of two alpha particles (two pulses) in one time window. An example of such an event is presented in Fig. 2. This figure contains a set of five waveforms registered from four anodes (returning energy information) and a signal waveform from one dynode (responsible for returning time information).

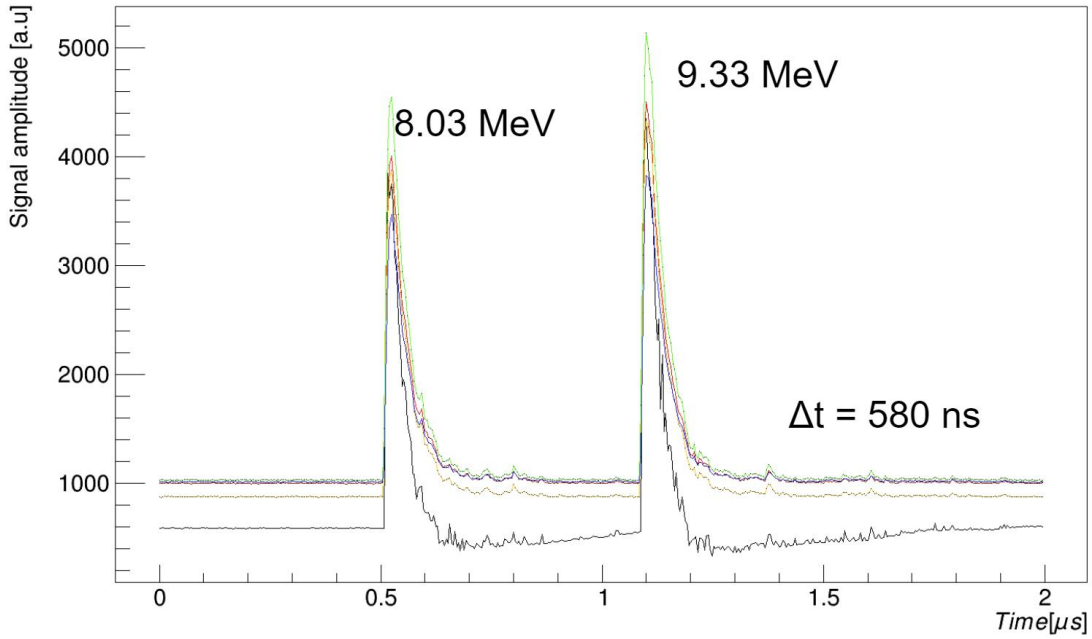

Fig. 2. The waveforms of the interesting event recorded during the experiment and detected in a position-sensitive detector. The waveforms recorded from the dynode are black, while the rest of the 4 colored signals are originating from 4 anodes of the PSPMT detector.

Energy calibration of such pulses and determination of their position is possible by using Anger logic. Knowing the energy value registered by four anodes (Q_{xa}, Q_{xb}, Q_{ya}, Q_{yb}) it is possible to calculate the position of the registered pulse in one of the pixels (1). The PSPMT detector is built out of 24 x 24 pixels, from which, due to poor statistics on the edges and corners, only 22 x 22 pixels can be considered in further data analysis.

$$X= Q_{xa}-Q_{xb} / Q_{xa} +Q_{xb} \quad , \quad Y= Q_{ya}-Q_{yb} / Q_{ya} +Q_{yb} \qquad (1)$$

Due to some imperfections of PSPMT, YAP, and light guide, it is necessary to conduct gain matching energy calibration for each pixel separately. For this purpose, the 2-dimensional distribution of the pixel's position was changed into 1-dimensional with the same algorithm (2) as Xiao et al. presented in their work [5].

$$N_{pixel} = \text{Row} \times 24 + \text{Column} \qquad (2)$$

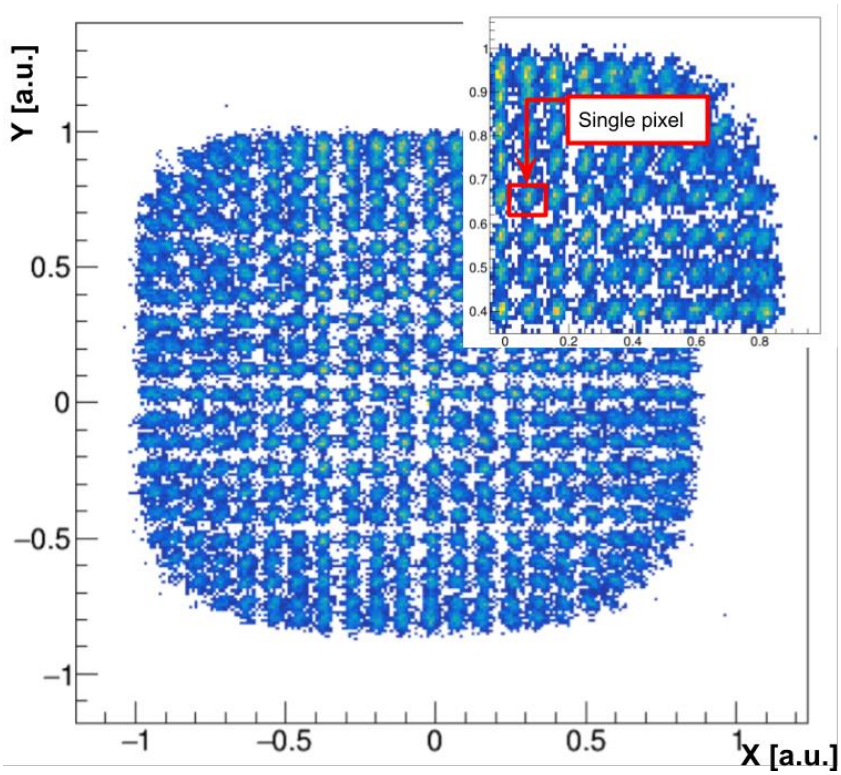

Fig. 3. Position distribution of signals reproduced by Anger logic plotted in arbitrary dimension unit. In the right-up corner, on the zoomed fragment of the distribution, by red rectangular is marked single pixel. Figure made for ^{228}Th source.

This step allowed not only control of the quality of the used calibration method but also made it possible to group pixels with similar amplitude amplification. This enabled the collection of better

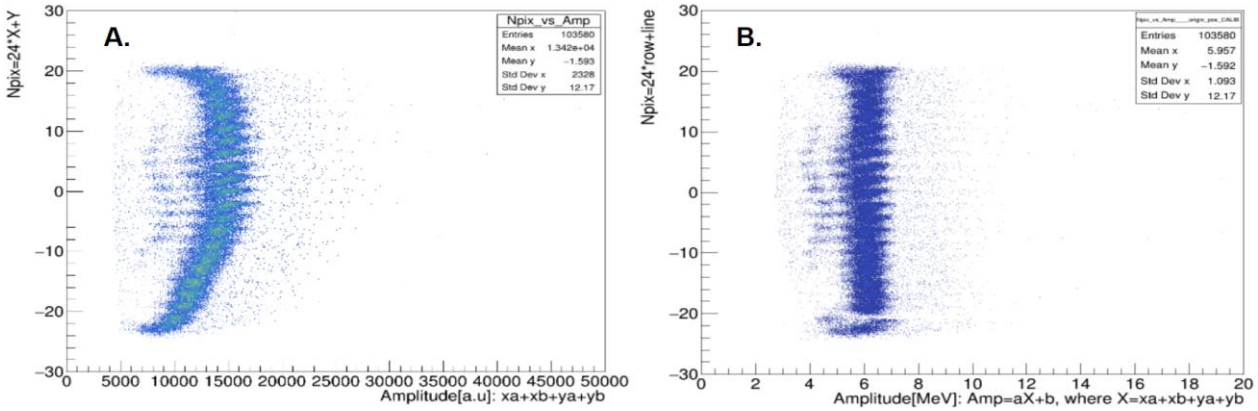

Fig. 4. 1-dimensional distribution of the pixel's position before (A) and after (B) energy calibration.

statistics for energy calibration and also made it easy to calibrate all pixels with the standard linear

regression method. For this purpose run with ^{228}Th source was used. The result of using this calibration method is presented in the 1-dimensional distribution of the pixels, in Fig 4.

Position and energy calibration allowed us to look for double alpha peaks in one time window with the condition that the second peak will be located in the same or adjacent pixels. In the situation where we are considered only the first layer of adjacent pixels, there were found 24 events with double pulses (Table I), where two of them (marked with orange color) are fulfilling conditions of the high energy alphas from one of the alpha decay chains presented in Fig. 1. Note, one of the registered events is also presented in Fig 2.

Table I. Energies of double pulses registered by the position-sensitive detector, with condition that both pulses were detected in the same or adjacent pixels.

Amplitude of registered particle [MeV]				
1st peak	**2ed peak**		**1st peak**	**2ed peak**
7.50686	4.10122		6.08946	8.41894
8.38808	**9.58383**		5.63571	6.23469
8.03168	**9.33001**		5.08403	5.8017
3.17162	4.81703		3.29297	3.09121
3.39697	8.99234		7.24412	3.79912
3.1063	8.83049		7.43248	6.01956
3.15005	12.4871		3.06675	2.99565
9.93843	3.87343		7.50019	3.3672
6.04716	3.15369		3.15085	3.56148
4.89464	12.4349		3.36784	8.9571
3.08115	3.23072		4.39458	3.24214
4.39458	3.24214		6.08946	8.41894

These results are encouraging to continue the analysis of collected data and to enlarge the distance of studying double peaks in another layer of pixels. It will be also worth comparing the results from PSPMT with those from single-anode YAPs. The main tools for analyzing those data, which are pulse shape discrimination methods based on slow & fast components of the recorded puls, and moments methods, like mean value, variance, skewness, and kurtosis, are already prepared and are currently in use. Results of such comparison will help decide if replacing active catcher's modules with PSPMTs will be useful for MNT-SHE experiments in the future.

[1] Z. Majka *et al.*, Acta Phys. Pol B **45**, 279 (2014).
[2] Z. Majka *et al.*, Acta Phys. Pol. B **49**, 1801 (2018).

[3] S. Wuenschel *et al.*, Phys. Rev. C **97**, 064602 (2018).
[4] A. Hood *et al.*, *Progress in Research*, Cyclotron Institute, Texas A&M University (2020-2021), p. II-1.
[5] Y. Xiao *et al.*, Phys. Rev. C 100, 034315 (2019).

The nuclear caloric curve: Temperatures of simulated quasi-projectiles

M. Sorensen, A.B. McIntosh , B. Harvey, Z. Kohley, and S.J. Yennello

The equation of state describes the bulk quantities of matter, and how they relate to each other. These quantities include the temperature, composition, density, pressure, volume and energy of the system. In the nuclear system there is still theoretical uncertainty in how strongly the asymmetry of the nucleus impacts the nucleus's thermodynamic quantities. One area requiring experimental constraints is the difference between "ays-stiff" and "ays-soft" equations of state, which have important astrophysical implications. In order to help constrain these theoretical models, various experiments were performed with NIMROD (Neutron Ion Multidetector for Reaction Oriented Dynamics) in (year of experiments) including the ^{70}Zn+^{70}Zn , ^{64}Ni+^{64}Ni, and ^{64}Zn+^{64}Zn systems at 35 MeV/u [1]. The charged particles produced in these reactions were detected, along with the neutron multiplicity. These runs would prove to be a rich data set, and were used to determine temperatures of reconstructed quasiprojectiles (QP) [2,3]. Analysis showed a dependence on the nuclear caloric curve based on the asymmetry of the reconstructed QP. The more neutron rich QPs had lower temperatures at the same excitation energy and this trend was seen in multiple kinetic and chemical probes. The purpose of this project is to use anti-symmetrized molecular dynamics (AMD) [4] and Gemini[5, 6] to attempt to reproduce and test the trends seen experimentally, and to see if there is a dependence between ays-stiff and ays-soft interactions on the nuclear caloric curves.

In the original data set roughly 10000 AMD-DS events were run by Z. Kohley to a time of 300fm/c for each system. Afterwards, Gemini was used to de-excite the nuclides, with each AMD event used as a starting point for Gemini 20 times. In addition to this data set, another 40000 AMD-DS events were generated for each system in 2019-2020. In 2021 an additional 227,400 AMD-DS data was run for the ^{70}Zn on ^{70}Zn system with the gogny stiff interaction, and 193,882 for the gogny soft system. If we allow ourselves to run each AMD event through Gemini 20X times we can greatly increase the apparent statistics, however this complicates the evaluation of the statistical error as now each event is not completely independent from others. These new events have been processed. These events were then subjected to the same event selection cuts used to shift through the data collected in the experiment. See paper for details on the event selection, as well as how these temperatures are calculated [2,3].

A weak dependence is seen between the gogny stiff and gogny soft interaction for the MQF temperatures calculated using protons as the probe. This is seen in Fig.1. A more noticeable dependence is seen using the (H/He) Albergo chemical probe (See Fig.2). Both seem to indicate that the stiff interaction is hotter than the soft interaction. While this is encouraging, there are challenges to comparing the AMD+Gemini results to the experimental data. Using the same AMD primary event 20 times to make different AMD+Gemini events may cause the statistical error bars to be too small, as each event is no longer completely independent of each other. This problem can be remedied by only using Gemini once for each AMD primary event and we can compensate for the loss of counts by running more AMD primary events. To reassure ourselves that the trend is robust to this effect, the H/He Albergo

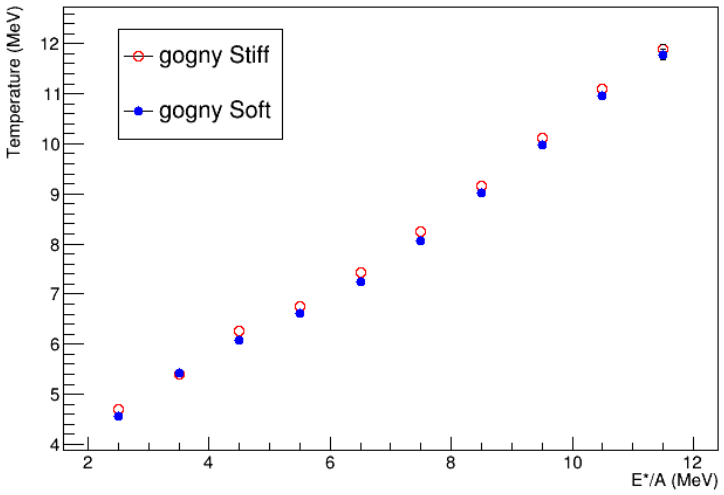

Fig. 1. Temperature of QP calculated using the MQF of protons as a function of excitation energy per nucleon. A weak difference is seen between the gogny stiff and gogny soft interaction, with the stiff having slightly higher temperatures.

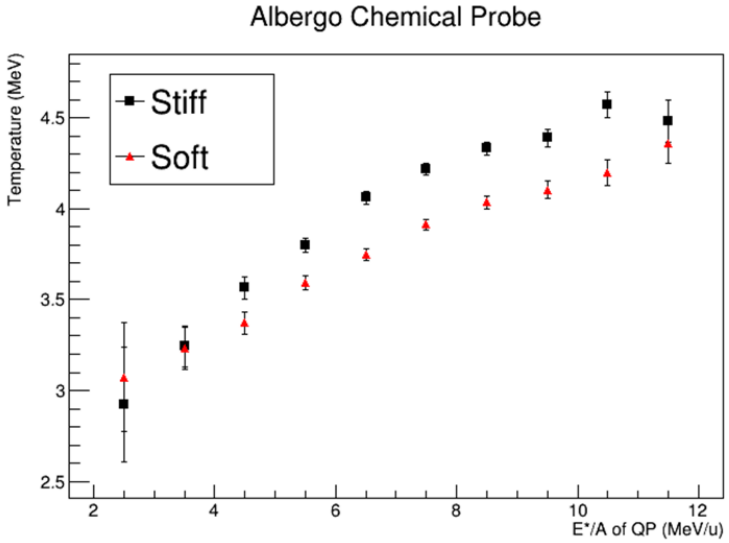

Fig. 2. Temperature of the QP calculated using H/HE Albergo temperature probe as a function of excitation energy per nucleon. A significant difference is seen between the two interactions.

temperatures were re-evaluated when only de-exciting the AMD primary event once in Gemini (see Fig. 3). From this test it looks like there is indeed a statistically significant difference between stiff and soft interaction on the H/He Albergo chemical probe. Even with a better understanding of the statistical error bars, there would still be the concern of systematic difference between AMD+Gemini and the real experimental reaction. For instance, while the calculated Albergo temperatures from AMD+Gemini

appear to line up well with the experimental ones, the MQF temperatures appear lower than seen in the experiment. In addition, for the MQF case there are differences in the ordering of which particle probe is hotter than what is seen in the experiment. These systematic differences complicate a direct comparison with experimental results.

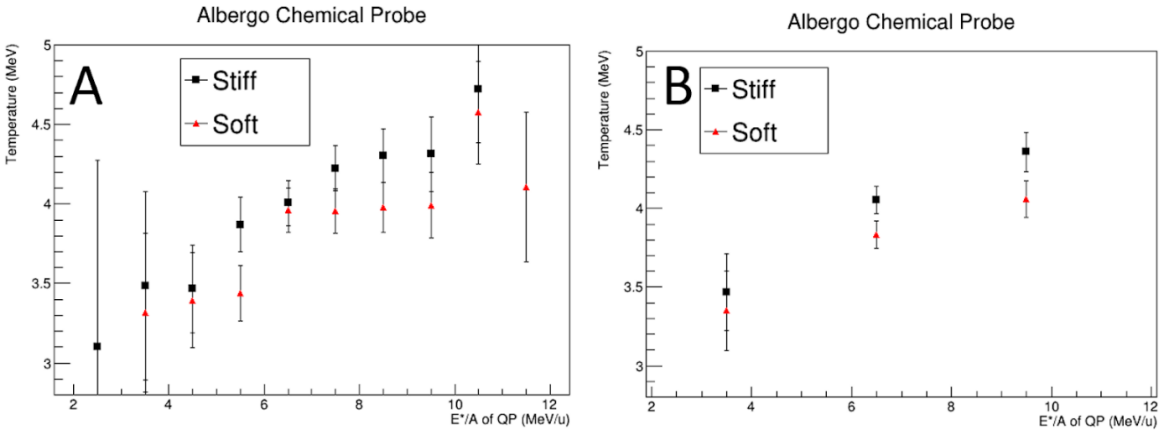

Fig. 3. A) Same as Figure 2, but with the data set only deexciting each AMD primary event once through Gemini. Error bars are quite large. B) Same as A) but re-binned, two points show a statistically significant difference between Stiff and Soft, with Stiff appearing to be hotter.

[1] Z.Kohley, Ph.D. Thesis, Texas A&M University 2010.

[2] A.B.McIntosh *et al.*, Eur. Phys. J. A **50**, 35 (2014)

[3] A.B. McIntosh *et al.*, Phys. Lett. B **719**, 337 (2013).

[4] A. Ono and H. Horiuchi, Prog. Part. Nucl. Phys. **53**, 501 (2004)

[5] R.J. Charity, Phys. Rev. C **82**, 014610 (2010).

[6] D. Mancusi, R.J. Charity, and J. Cugnon, Phys. Rev. C **82**, 044610 (2010).

The search for toroidal high-spin isomers in ^{28}Si + ^{12}C at 35 MeV/u using FAUST

A. Hannaman, K. Hagel, A.B. McIntosh, B. Harvey, A. Abbott, J. Gauthier, T. Hankins, Y.-W. Lui, L. McCann, L.A. McIntosh, R. Rider, S. Schultz, M. Sorensen, Z. Tobin, R. Wada, and S.J. Yennello

While ground state stable nuclei typically exhibit spherical geometries, given excitation energy and/or angular momentum, they may form ^{4}He(α)-particle clusters within their bulk and undergo deformation [1,2]. It is predicted that such clustering may promote the production of angular momentum stabilized toroidal nuclei due to local energy minima in the single particle potential [3,4]. An experiment performed on the NIMROD detector array observed evidence of very high excitation states in the same range as predicted toroidal high-spin isomer states in the 7-α disassembly of ^{28}Si in collisions of ^{28}Si +^{12}C at 35 MeV/u [5]. This evidence prompted the recent repeat measurement with improved angular resolution and statistics using the FAUST array. The present experiment measured 93,742 events containing 7 α-particles, a more than order of magnitude improvement over the 6,467 measured in the NIMROD experiment.

Understanding the process of 7-α disassembly, whether by sequential decay through intermediates, or by simultaneous democratic breakup, is of considerable interest. One way to probe the time-evolution of nuclear collisions is to observe states of parent nuclei in the relative energy distributions of the decay products [6]. The ground state and many of the excited states of ^{8}Be decay into 2 α-particles. The decay energy is dictated by the state energy and Q-value for the decay, while the width in the decay energy is dictated by the lifetime. The relative energy between every 2 α-particle pairing in 7-α events is shown in Fig. 1(a(I)). The peak in the relative energy associated with ^{8}Be ground state decay centered at 0.09 MeV has very little background due to uncorrelated α-particles, allowing for an event-by-event determination of the presence of this intermediate. A similar treatment can be performed for every 3-α combination to observe α-decaying ^{12}C excited state intermediates as shown in blue in Fig 1(a(II)). While the 0+ Hoyle state centered at 0.38 MeV has very little background, allowing for event-by-event determination, the 3- excited state centered at 2.35 MeV has roughly 75% uncorrelated background. The 0+ and 3- excited states predominantly decay via α + ^{8}Be ground state. By only calculating the 3-α relative energy containing 2-α pairings that have a relative energy consistent with ^{8}Be ground state (red shaded region in Fig.1(a(I))), the background for the 3- state is reduced by roughly 40%. Relative energy gates around the 0+ (blue shaded region) and 3- (green shaded region) states were made to further characterize the intermediates present. The yields and excitation energy distributions for the intermediate decay pathways consisting of these three states for 7-α events are shown in Fig. 1(b). Roughly 32% of 7-α events contain at least one of these intermediates. For this analysis, the requirement of little background limits the ability to gate on the many higher-lying excited states, however yields associated with them could be obtained through mixed-event subtraction.

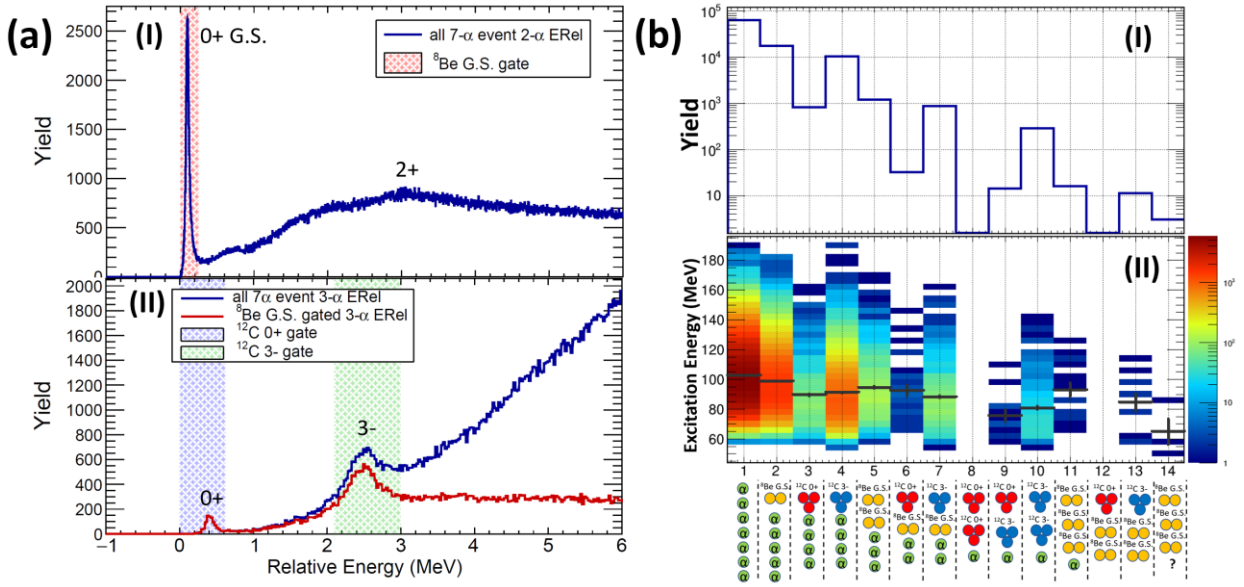

Fig. 1. 2,3-α particle relative energy distributions in 7-α events and the categorization of 7-α events based on intermediate decay pathways. (a(I)) Yield as a function of 2-α relative energy in MeV. The ^{8}Be ground state gate is shown by the red shaded region. (a(II)) Yield as a function of 3-α relative energy in MeV. Distribution for all 3-α pairings (blue line), and when gating on ^{8}Be ground state (red line). 0+ Hoyle state gate is shown by the blue shaded region, and 3- excited state gate is shown by the green shaded region. (b(I)) Yield as a function of intermediate decay pathway. (b(I)) Excitation energy in MeV as a function of intermediate decay pathway.

Evidence of toroidal high-spin isomer states in the NIMROD experiment emerged when studying the excitation energy distribution after mixed-event subtraction for 7-α events. Event mixing is performed

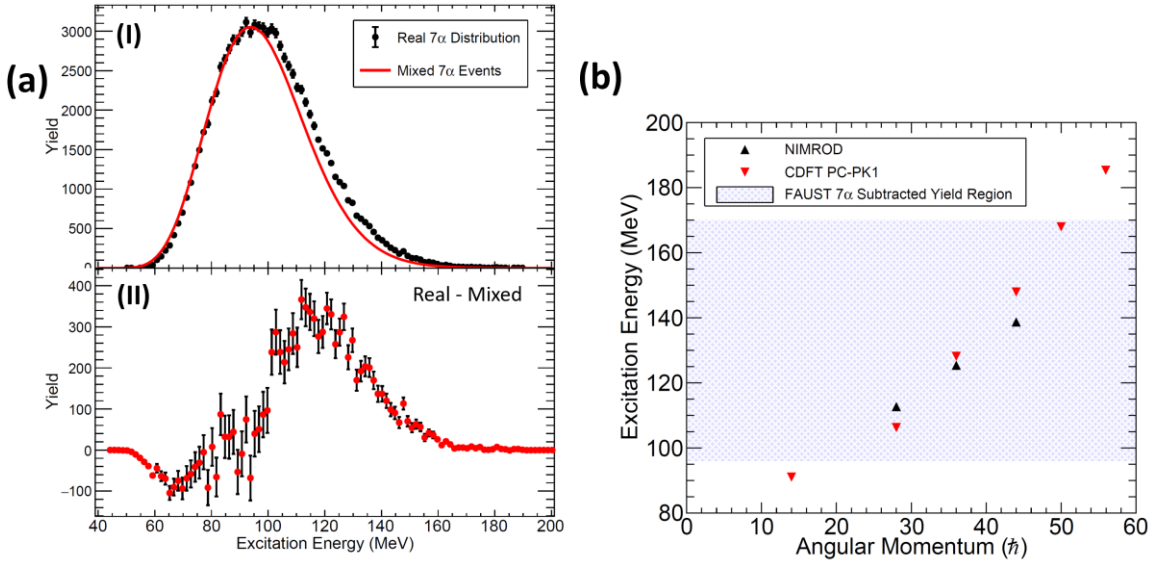

Fig. 2. 7-α excitation energy distribution and subtraction to observe correlated yield with comparison to NIMROD and CDFT results. (a(I)) Real experimental 7-α excitation energy (MeV) distribution is shown in black. Mixed event distribution normalized to real between 75 – 95 MeV is shown in red. (a(II)) Real – mixed excitation energy distribution. (b) Mean excitation energy (MeV) as a function of angular momentum (ħ) as predicted by CDFT calculations (red triangles) and claimed experimentally by the NIMROD experiment (black triangles) [4,5]. The region of correlated yield in the present study is shown by the blue shaded region.

by repeatedly taking 7 α-particles from different events and calculating the excitation energy to account for background associated with 7-α phase space. The real (black) and mixed event (red) distribution for the current study are shown in Fig. 2(a(I)). Mixed events ignore coulomb interactions, causing excess yield at low excitation energy. Due to this, the mixed events are normalized to the real distribution above 75 MeV and below 95 MeV (as predicted states begin at roughly 100 MeV). The subtracted distribution shows yield in a region consistent with the NIMROD results as shown in Fig. 2(a(II)). The region of correlated yield in the current study is compared to the excitation energy and predicted angular momentum for states observed in the NIMROD experiment and calculated using CDFT in Fig. 2(b) [4,5]. Work is ongoing to ensure that the extraction of possible state properties from this distribution is robust.

[1] M. Thoennessen *et al.,* Phys. Rev. C **37**, 1762 (1998).
[2] C. Beck, J. Phys. Conf. Ser. **436** (2013).
[3] A. Staszczak and C.Y. Wong, Phys. Lett. B **738**, 401 (2014).
[4] Z.X. Ren *et al.,* Nucl. Phys. **A996**, 121696 (2020).
[5] X.G. Cao *et al.,* Phys. Rev. C **99**, 014606 (2019).
[6] J. Pochodzalla *et al.,* Phys. Rev. C **35**, 1695 (1987).

Searching for long-lived superheavy elements produced during multinucleon transfer

K. Zelga, K. Hagel, R. Wada, and S.J. Yennello

Searching for superheavy elements (SHE) with the use of the multinucleon transfer (MNT) has been a subject of study at the Cyclotron Institute at Texas A&M University since 2002. It was a collaborative work of two institutes, TAMU and Jagiellonian University in Poland. Since the beginning, the detection setup has changed several times [1,2]. In the final form, it was using an active catcher (AC) detector. The first version of AC was built out of 63 modules based on the plastic scintillator BC-418 attached via LUCITE light guide to the photomultiplier Hamamatsu R9880U-110 [3,4]. The second version was built out of 40 modules based on YAP detectors connected to the photomultipliers Hamamatsu R1355 with the LUCITE light guide [5].

The last experiment dedicated to searching for superheavy elements conducted with AC based on YAP was studying MNT on ^{197}Au + ^{232}Th (7.5AMeV) reaction. Its results showed that it is possible to produce SHEs with this method [5]. The experiment was focusing on searching short-lived SHEs, with a lifetime on the level of several ns to 1 us. The obtained results, however, open possibilities to study if in irradiated by MNT reaction products YAP material were implanted any long-lived SHEs (with a lifetime on the level of several years).

The main motivation for studying the area of long-lived SHEs (LLSHE) is a desire of reaching an island of stability (Fig. 1) predicted and determined by scientists as N=184 or N = 196 and Z =114 [6,7,8]. Conducting this type of experiment is justified for two reasons. The first reason is the property of MNT which was used for irradiating YAP detectors during previous SHE-related tests (from 2018 to 2021). Lighter nuclei (Z<103) produced during MNT are neutron-rich nuclei, which is a property of stable/long-

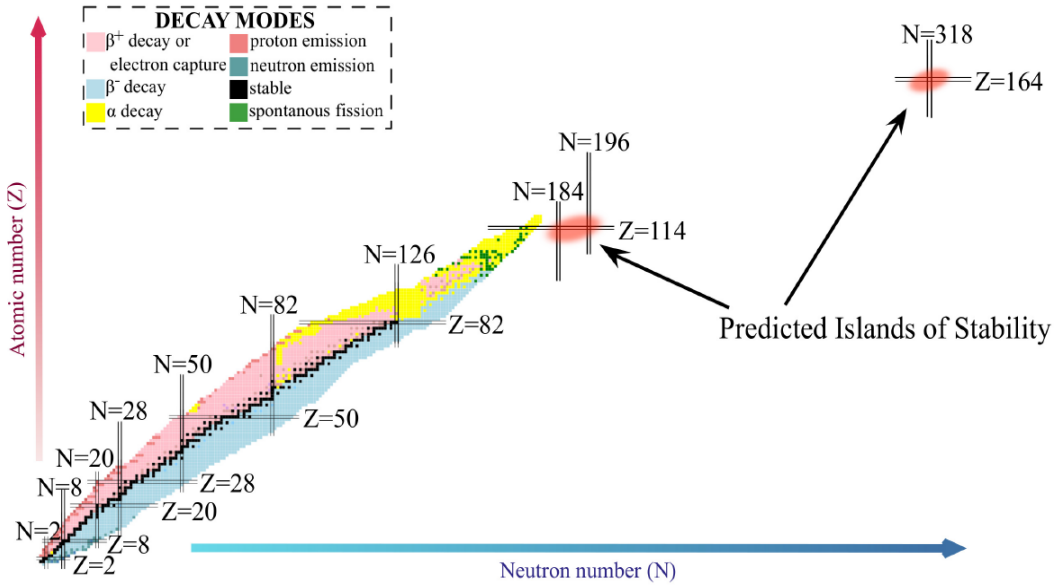

Fig. 1. Nuclide chart for already known elements with marked predicted islands of stability [9].

lived elements. Presently all of the already discovered nuclei are neutron-poor elements, which caused short lifetimes terminated with alpha decay or spontaneous fission. Results obtained by S. Heinz show the advantages of using MNT for producing long-lived SHE elements [10].

The second argument in favor of examining irradiated YAPs in terms of observing the decay of long-lived SHEs is the result of research carried out on scintillators used in AC before its upgrade [11,12]. These results showed that during experiments in 2016 in the BC-418 scintillator were implanted several long-lived nuclei with the energy of alpha decay above 10 MeV, which corresponds to the energy expected for the alpha decay of SHEs. During that experiment full identification of the implemented nuclei wasn't possible because of the poor energy resolution of the used scintillators. YAPs better energy resolution will return better information about implanted elements.

To test if LLSHE can be found in the irradiated YAPs, a new ΔE-E detector setup was prepared, Fig. 2. The prepared detector setup is built out of 8 pairs of Si detectors faced with YAP detectors. Seven out of eight YAP were irradiated during previous experiments (with reactions like ^{197}Au + ^{232}Th, ^{238}U +^{232}Th, ^{197}Au + ^{197}Au) while one remains clean, never used in the experiment before. The goal of that one detector pair is to be a control group to see how background radiation (including high energetic cosmic radiation) affects a counting rate in the energy area considered the interesting one in this experiment. The whole setup is placed in the vacuum chamber and connected with SIS 3316 ADC. Triggering of the acquisition is made by each of the detectors separately. The acquisition time window allows recording 2 us of the signal's waveform per event.

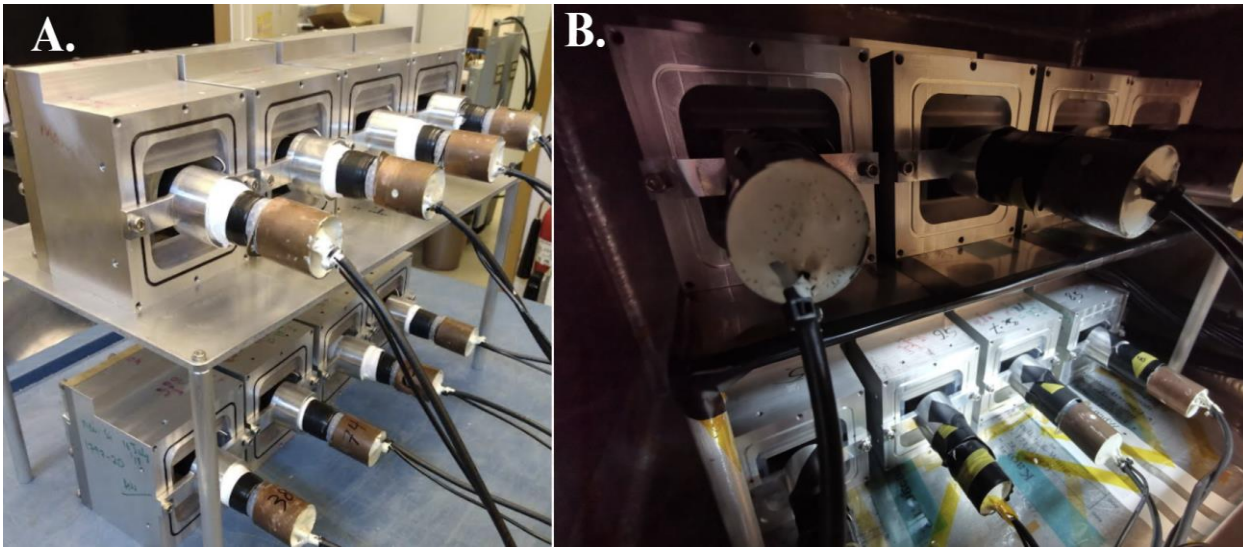

Fig. 2. Photo of the 8 pairs of detectors outside (A) and inside (B) the vacuum chamber.

There are two types of events that will be considered interesting during this experiment. First, case when implanted SHE decay with alpha particle emission outside the YAP detector in direction of the Si detector. Because implantation of the SHE should be rather shallow (several micrometers) the energy deposited (ΔE) in the YAP detector should be lower than 2 MeV, while the remaining energy (E) deposited in Si should be high. Recording such a coincidental event with total energy above 9 MeV/10 MeV will be considered a candidate for SHE decay. The second possibility is to record the alpha decay

chain only in the YAP detector. At this point, interesting events will be those with at least two pulses registered in the one time window. Oslo in that case the energy of at least one signal should be higher than 9 MeV/10 MeV. Such energy of the sought alpha decay was selected as a lower limit due to the dependence between the energy of the emitted alpha particle and the atomic number of the decaying element. Namely, with the increasing atomic number Z of the decaying element, the energy of the emitted alpha particle also increases, as shown in Fig. 3.

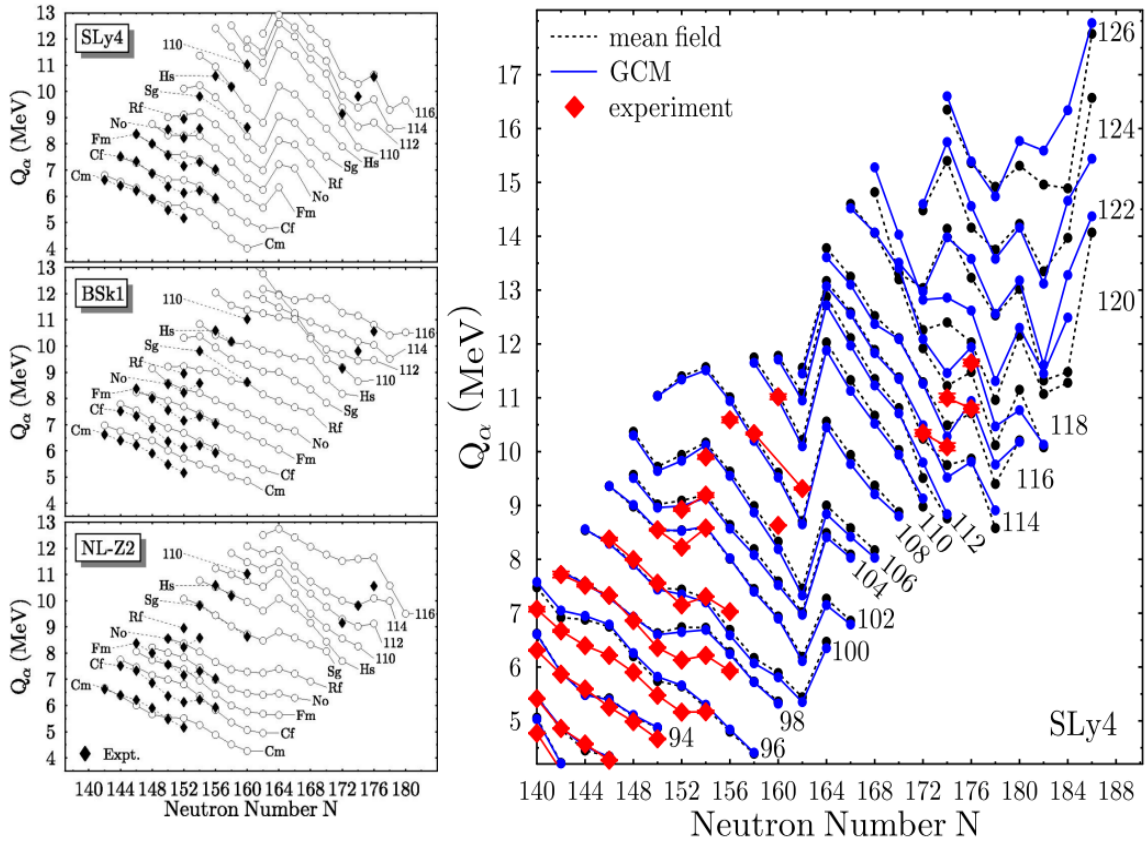

Fig. 3. Qα values for α particles emitted from even-even nuclei as a function of neutron number for increasing atomic number of heavy and superheavy nuclei [13][14].

To conduct this experiment special detector holders were prepared to allow mounting YAP detectors on the Si modules (how it is shown in Fig. 2). The process of calibration of all 16 modules was also made (8 Si and 8 YAPs detectors). For calibration purposes, a set of measurements with ^{241}Am, ^{252}Cf, and ^{228}Th sources were conducted. Due to the configuration of the ΔE - E detection setup and the size of the used vacuum chamber, it was necessary to make those measurements in two steps. Separately for the wall of Si detectors and the wall of YAP detectors. Its configuration is presented in Fig. 4 and Fig. 5.

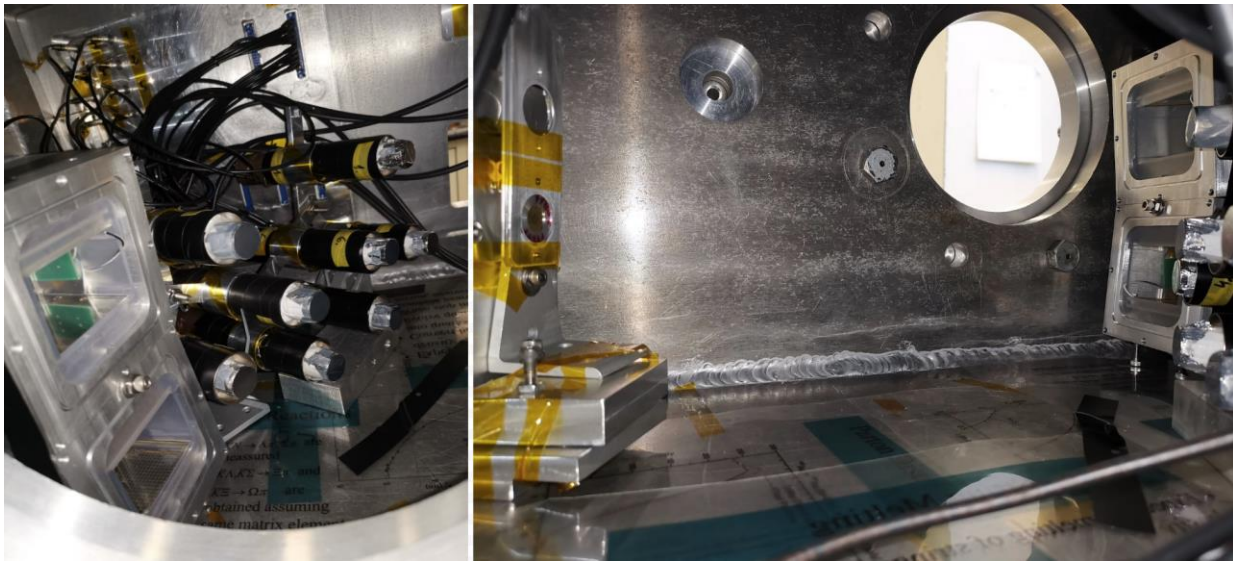

Fig. 4. Example setup of detection modules in the vacuum chamber during the calibration runs. The photo on the left figure presents the position of YAP modules and one pair of Si detectors. The photo on the right side presents the location of the source in front of the detector wall.

Fig. 5. Setup of detection modules in the vacuum chamber during the calibration runs. The photo on the left figure presents the position of Si modules in the vacuum chamber. The photo on the right side presents the location of the source in front of the detector wall.

Amplitude spectrums obtained from those runs are presented in Figs. 6 and 7. Used Si detectors have very good energy resolution which will provide reliable information about the deposited energy of the alpha particle emitted from the YAP detector. YAPs energy resolution is not satisfactory enough, but the results of its calibration will be supported by pulse shape analysis used before in the MNT experiments with AC for SHE identification. That should be enough to show if we can produce superheavy elements with long-lived times using MNT.

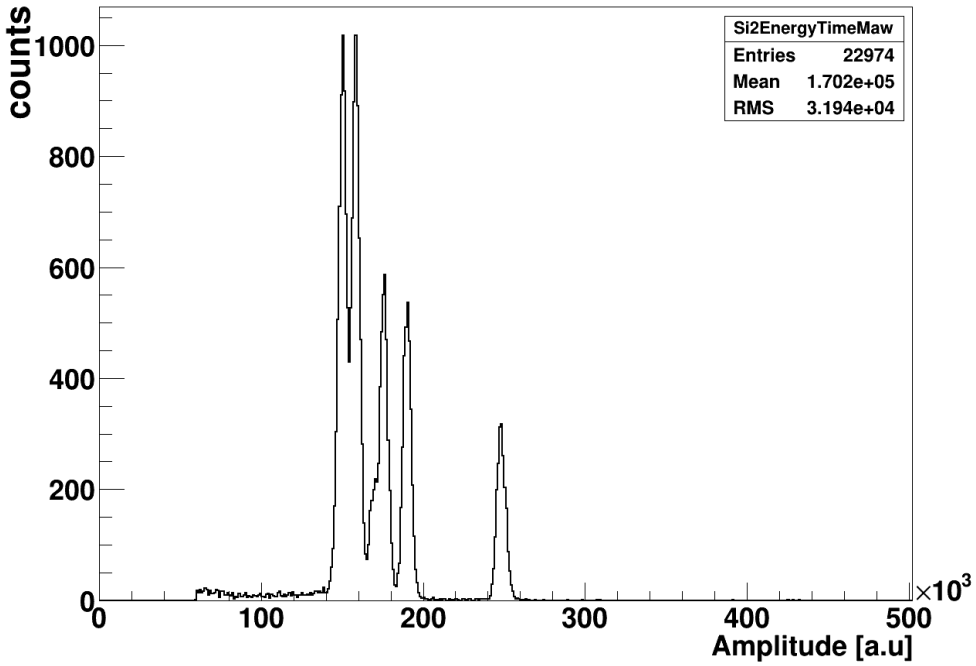

Fig. 6. Typical amplitude spectrum for Si detector, for run with ^{228}Th source.

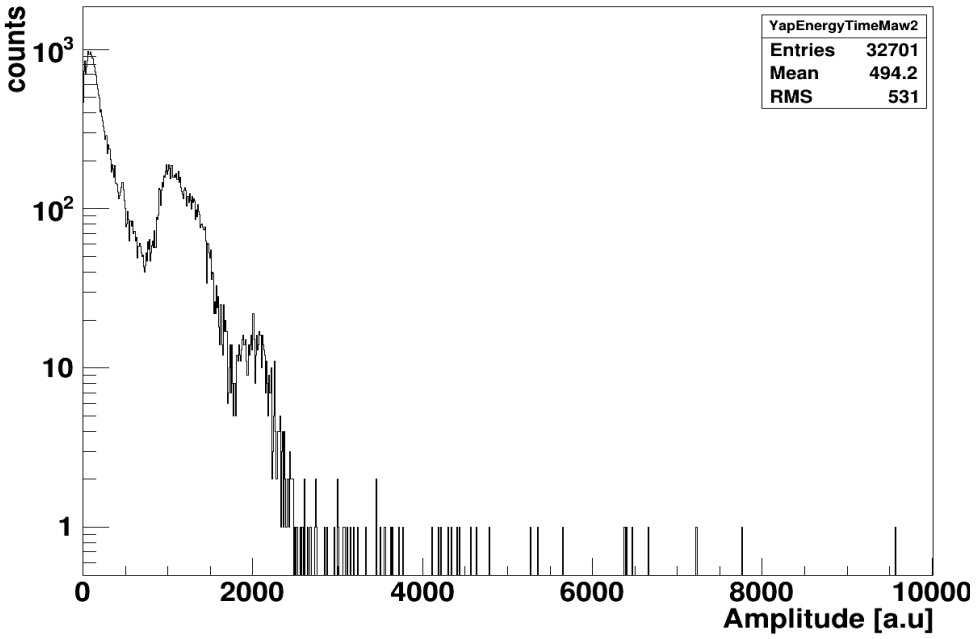

Fig. 7. Typical amplitude spectrum for YAP detector, for run with ^{228}Th source.

At the moment main measurements are started. They will last 2-3 months of offline counting. After this time and after careful analysis of already collected data, the decision of continuing measurements with the same or a new set of irradiated YAPs should be taken. If after this experiment in collected data any superheavy element will be found, then the next step may be preparing a dedicated detection setup which right after irradiation by MNT reaction products will be placed inside the vacuum chamber. Such a detector would be monitored constantly for several months or longer to enlarge the range of observable times of life.

[1] Z. Majka *et al.*, Acta Phys. Pol. B **45**, 279 (2014).
[2] M. Barbui *et al.*, Int. J. Mod. Phys. E **18**, 1036 (2009).
[3] A. Wieloch *et al.*, Eur. Phys. J. Web of Conferences **117** (2016).
[4] Z. Majka *et. al.*, Acta Phys. Pol. B **49**, 1801 (2018).
[5] S. Wuenschel *et. al.*, Phys. Rev. C **97**, 064602 ().
[6] G. Schar-Goldhaber. Nucleonics. Nucl. Phys. **15**, 122 (1957).
[7] W.D. Myers *et.al.*, Nucl. Phys. **81**, 1 (1966).
[8] A. Sobiczewski *et al.*, Phys. Lett. **22**, 500(1966).
[9] http://people.physics.anu.edu.au/ecs103/chart/.
[10] S. Heinz. J. Phys. Conf. Ser. **1014**, 012005 (2018).
[11] K. Zelga Ph.D. Thesis, Jagiellonian University, 2020.
[12] K. Zelga *et al.*, Acta Phys. Pol. B **50**, 579 (2019).
[13] M.Bender *et al.*, Rev. Mod. Phys. **75**, 121 (2003).
[14] M. Bender, J. Phys. Conf. Ser. **420** (2013).

Metal adsorption on functionalized silicon detectors for the future study of meitnerium chemistry

V. Zakusilova,[1,2] E.E. Tereshatov,[2] M. Boltoeva,[1] and C.M. Folden III[2,3]
[1]*Université de Strasbourg, CNRS, IPHC, UMR 7178, F-67000 Strasbourg, France*
[2]*Cyclotron Institute, Texas A&M University, College Station, Texas 77843*
[3]*Department of Chemistry, Texas A&M University, College Station, Texas 77843*

One of the first attempts to coat silicon detectors with gold was reported during the chemical characterization of element 112, Cn. Better chemical sorption of this element was observed on gold-modified surfaces rather than on non-modified ones [1]. However, element 113, Nh, showed an enhanced reactivity towards gold, which prevented the proper chemical characterization of this element [2, 3]. Therefore, a need for new chemically modified silicon detectors has emerged. Such detectors will selectively bind the atoms of interest but with weaker interactions. Element 109, meitnerium, which is expected to be a member of Group 9 of the periodic table, has never been chemically characterized before. Therefore, this project aimed to study the adsorption of meitnerium's two closest homologs, namely iridium (Ir) and rhodium (Rh), on functionalized surfaces. Preliminary results are reported here.

We successfully characterized 1-(11-mercaptoundecyl)imidazole (Im-C_{11}-SH) self-assembled monolayers (SAMs) on gold-coated substrates using several surface science techniques last year [4]. In our studies, we used silicon chips (10 mm x 10 mm x 0.5 mm) coated with 100 nm of gold and glass chips (10 mm x 10 mm x 0.7 mm) coated with 50 nm of gold. Both substrates are primed with a titanium adhesion layer with a thickness of 5 nm and 2.5 nm, respectively.

Over the past year, nanoprojectile secondary ion mass spectrometry (NP-SIMS) was employed to determine whether Ir(IV) and Rh(III) bind to Im-C_{11}-SH SAMs on gold-coated glass chips. The SAMs deposition was performed by submerging two chips into 5 mM ethanolic Im-C_{11}-SH solutions for 21 hours. The coverage of gold with Im-C_{11}-SH SAMs was measured to be (90±5)% and (80±5)%, respectively. After the SAMs formation, the functionalized chips were submerged into 5.2×10^{-6} M Ir(IV), or 9.7×10^{-6} M Rh(III) solutions in 0.55 M hydrochloric acid for approximately 21 hours. During the NP-SIMS analysis, a primary beam of 520 keV Au_{400}^{4+} clusters hits the surface of the functionalized chips, and the energy transfer from the beam to the surface causes the emission of cluster ions [5, 6]. In the NP-SIMS spectra of the functionalized chips, $Ir_2Cl_6^-$ and $RhCl_3^-$ cluster ions were observed with high intensities which leads to the conclusion that both Ir(IV) and Rh(III) bind to Im-C_{11}-SH SAMs. The coverage was measured to be (66.0±3.4)% and (81.3±3.8)%, respectively.

Subsequently, the SAMs deposition procedure was applied to the functionalization of gold-coated silicon detectors used during online cyclotron-based experiments. Three silicon detectors were coated with 50 nm of gold after being primed with 5 nm of titanium by Platypus Technologies, LLC (Madison, Wisconsin, USA). After this, Im-C_{11}-SH, or mercaptododecanoic acid (MDDA) SAMs were deposited on the gold-coated silicon detectors from 5 mM ethanolic solutions of the corresponding thiols. The SAMs deposition was performed on each detector twice to obtain the highest surface coverage. To remove the SAMs before the second deposition, the detectors were exposed to UV light.

Two experiments utilizing the following nuclear reactions were performed: ^{141}Pr(^{40}Ar, 5n)^{176}Ir, ^{118}Sn(^{40}Ar, 5n)^{153}Er, and ^{165}Ho(^{40}Ar, 5n)^{200}At on the AGGIE (Al Ghiorso's Gas-filled Ion Equipment) separator at the Cyclotron Institute, Texas A&M University. A simple Recoil Transfer Chamber (sRTC), composed of a funnel and a detector chamber, has been designed and used for the first time. Fig. 1 illustrates the AGGIE separator and the sRTC used in this study.

a)  b) 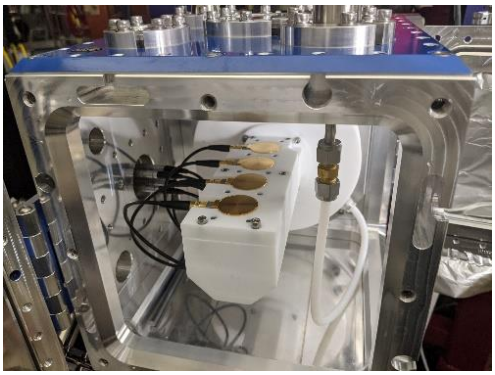

Fig. 1. The sRTC (blue box at far left) installed on the AGGIE separator (a). The (circular, gold colored) detectors installed inside the sRTC (b).

The goal of the sRTC is to stop the ions of interest in the funnel by their collision with atoms of helium gas (350 Torr) which goes through the sRTC with the flow of 500-1600 standard cubic centimeters per minute. In turn, this enables more efficient sorption and detection of the named nuclides on the non-modified and modified silicon detectors located in the detector chamber. In addition, a rotating degrader made of Mylar was installed upstream of the sRTC. Changing the angle of the rotating degrader results in the increase or decrease of the effective thickness of the material the ions are going through. As a result, we can select the rotating degrader angle at which the ions will be stopped mostly in the funnel due to their energy loss while traveling through the rotating degrader material of the corresponding thickness, and an aluminized Mylar window located in the entrance of the sRTC. Consequently, this increases the count rate of a produced nuclide.

The effect of the detector position in the detector chamber, and the detector material on the $^{173\text{-}176}$Ir, ^{152,153}Er, and $^{199\text{-}201}$At rates was investigated. The corresponding plots with rate as a function of detector position and material are shown in Fig. 2a-c. The materials tested were bare silicon (Bare Si), gold-coated silicon (Si+Au), gold-coated silicon functionalized with Im-C_{11}-SH SAMs (C11-Im), and gold-coated silicon functionalized with MDDA SAMs (MDAA). Four configurations were tested by cycling detectors through each position inside the detector chamber.

Results demonstrated that changing the detector position and material changes the nuclide adsorption. For ^{152,153}Er, the highest rate was observed on the gold-coated silicon and the bare silicon detectors at a 55° rotating degrader angle. For $^{199\text{-}201}$At, the highest rate was observed on the gold-coated silicon detector at a 45° rotating degrader angle. Other materials were equally effective. For $^{173\text{-}176}$Ir, all materials were equally effective at all rotating degrader angles summed up, which was done to enable fitting of the data with low statistics. In the case of MDDA, the count rate could not be determined. Regardless of the material, the highest rate was observed at position 1.

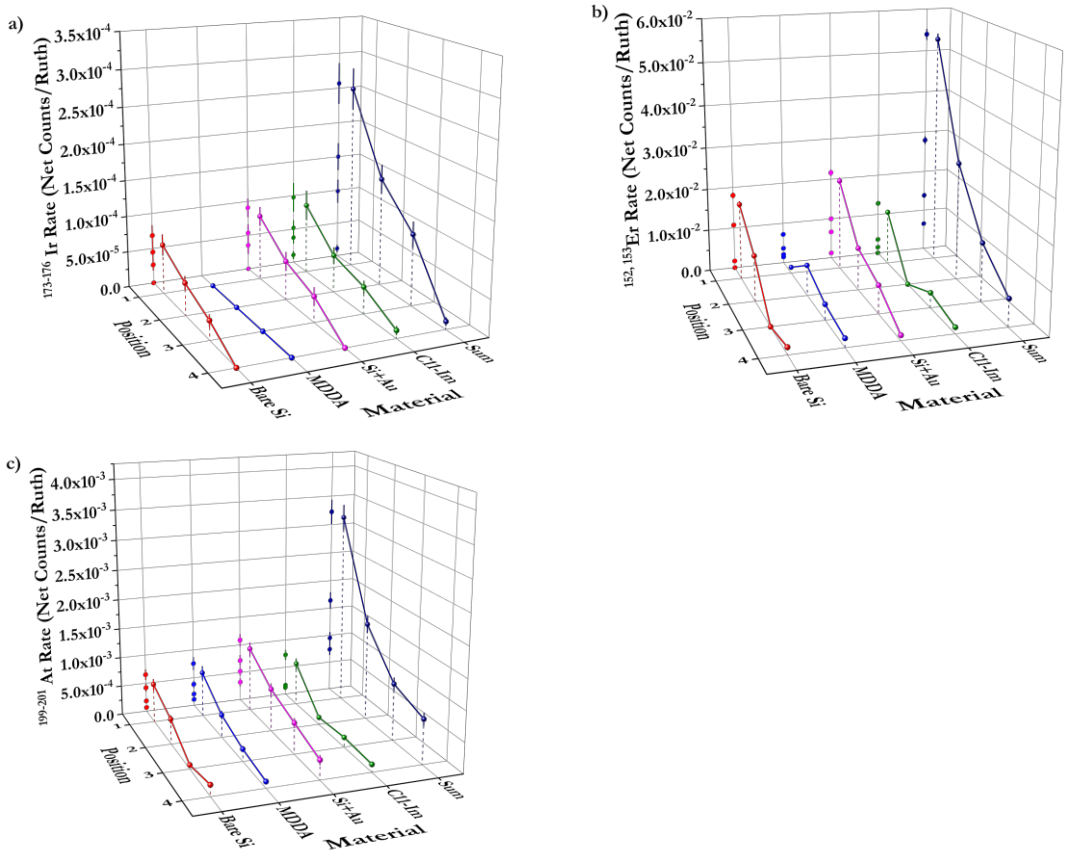

Fig. 2. (a) 3D plots of the $^{173\text{-}176}$Ir, (b) ^{152,153}Er, and (c)$^{199\text{-}201}$At. Rates as functions of the detector position and material. All data are preliminary.

In addition, the chemical behavior study of online-produced nuclides was performed. R_0 is the slope of curves obtained after fitting the sum of the event rates as a function of position as illustrated in Fig. 3a using an exponential function. R_0 is characteristic of the chemical behavior of elements in the sRTC; the comparison of the R_0 values confirmed that Er and Ir are non-volatile elements, whereas At is a volatile element. The R_0 values for $^{173\text{-}176}$Ir, ^{152,153}Er and $^{199\text{-}201}$At are 0.84±0.22, 0.72±0.05, 0.55±0.07, respectively.

The results suggest there are two possible processes: ions of interest can be adsorbed on the surface of the detector, or they can decay in flight. At the moment, we are still working to interpret the relative influence of these two effects. Fig. 3b shows that the total activity was constant regardless of the configuration. Therefore, if one detector has a higher rate than another detector within one configuration, it indicates that the variations are due to the interactions with the detector surface.

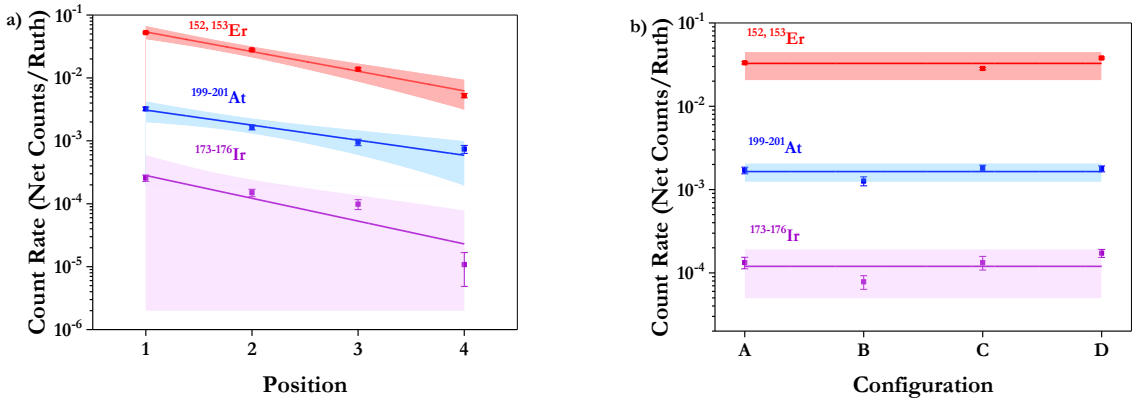

Fig. 3. (a) The count rate of $^{173\text{-}176}$Ir, ^{152,153}Er, and $^{199\text{-}201}$At as a function of the detector position, and (b) detector configuration.

A paper based on the offline experiments of this project is in the late stages of preparation. The results of the online experiments will be discussed in an additional paper and a dissertation is currently being written.

[1] R. Eichler *et al.*, Nature **447**, 72 (2007). DOI:10.1038/nature05761

[2] A. Yakushev *et al.*, Front. Chem. **9**, 1 (2021). DOI:10.3389/fchem.2021.753738

[3] S.N. Dmitriev *et al.*, Mendeleev Commun. **24**, 253 (2014). DOI:10.1016/j.mencom.2014.09.001

[4] V. Zakusilova, E.E. Tereshatov, and C.M. Folden III, *Progress in Research*, Cyclotron Institute, Texas A&M University (2020-2021), p. IV-3-5. https://cyclotron.tamu.edu/progress-reports/2020-2021/4%20Radiochemistry/IV_3_5__Iridium%20and%20rhodium%20adsorption%20on%20functionalized%20silicon%20chips%20for%20the%20future.pdf.

[5] C.-K. Liang, Ph.D. Thesis, Texas A&M University (2014), https://hdl.handle.net/1969.1/153571.

[6] M.J. Eller, S.V. Verkhoturov, and E.A. Schweikert, Anal. Chem. **88**, 7639 (2016). DOI:10.1021/acs.analchem.6b01466

High energy neutron production and three nucleon collisions in intermediate heavy ion collisions

R. Wada, Q. Hu and G. Tian

In our previous works in Ref.[1,2], the role of the Fermi-momentum fluctuation in collision process (FM Boost) and three nucleon collision (3NC) process are studied for the high energy proton production at the incident energy around 44-137 MeV/nucleon, incorporating the FM Boost and 3NC terms in the anti-symmetrized molecular dynamics (AMD) of Ono *et al.* [3]. We now extend these works for the high energy neutron production at higher incident energies.

The experimental data are taken from Refs. [4] and [5]. In both experiments, performed by two groups in the HIMAC facility of NIRS in Japan in 10 years apart, neutron energy spectra were measured by the time of flight technique using a plastic scintillator as a start and liquid scintillators as the stop timing detectors. In their experimental setups and reaction systems studied were slightly different, but some were overlapped. Here we used their results of $^{12}C+^{12}C$, $^{12}C+^{16}O$ at 290 MeV/nucleon.

AMD simulations are performed using the same code as that in Ref. [2] (AMD-FM(3N)) with 3NC or without 3NC. The simulated results are shown in Fig.1 for $^{12}C+^{12}C$ and in Fig.2 for $^{12}C+^{16}O$ both at 290 MeV/nucleon. Without 3NC, the results are denoted as AMD/DC-FM (blue histograms) and those with 3NC are as AMD/DC-3NC (red histograms) and compared with the experimental results in Refs. [4] and [5]. The experimental results are well reproduced with those of simulated ones with 3NC except for a small number of angles, these are 5° and 10° in Fig.1 and 75° in Fig.2. Since the FM Boost is ineffective

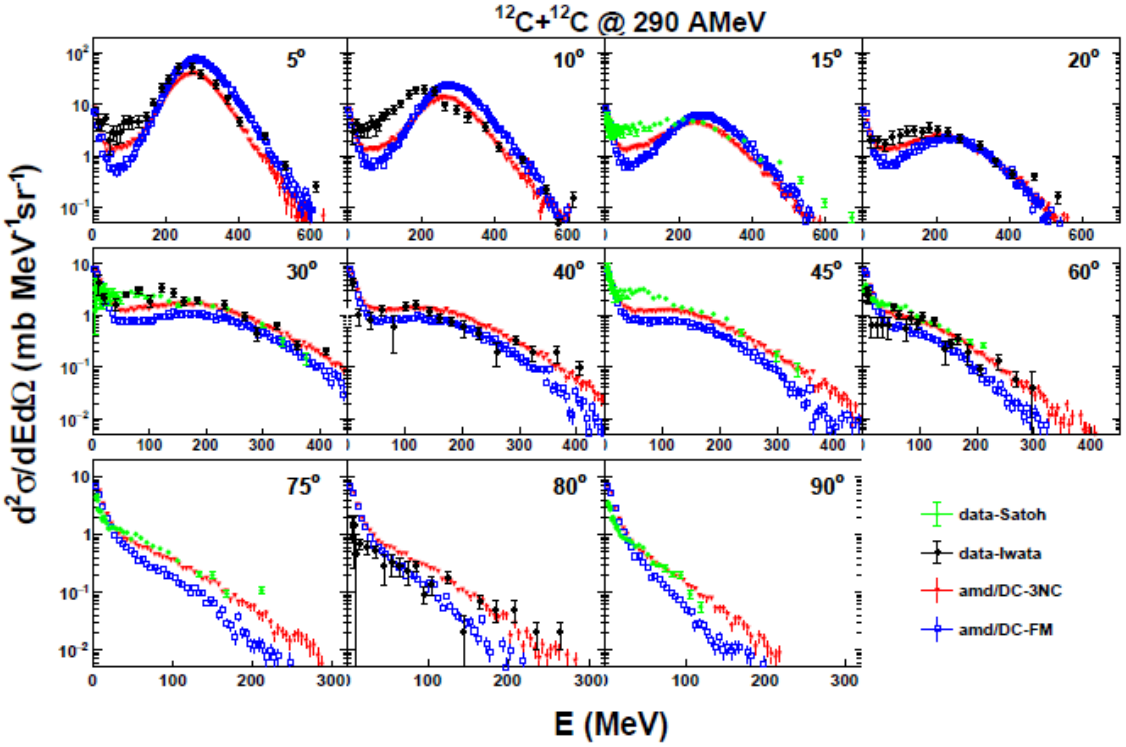

Fig. 1. Blue histograms represents the results of AMD/DC-FM and red histograms those of AMD/DC-3NC. The experimental data taken from ref.[4] are shown by black symbols and those from Ref.[5] by green symbols.

for the high energy neutron production above 50 MeV/nucleon as discussed in Ref. [2], these results strongly support the fact that these high energy neutrons are mainly produced by the 3NC process.

The 3NC terms are also sensitive to the nuclear stopping and now an investigation of the 3NC effect on the nuclear stopping is underway.

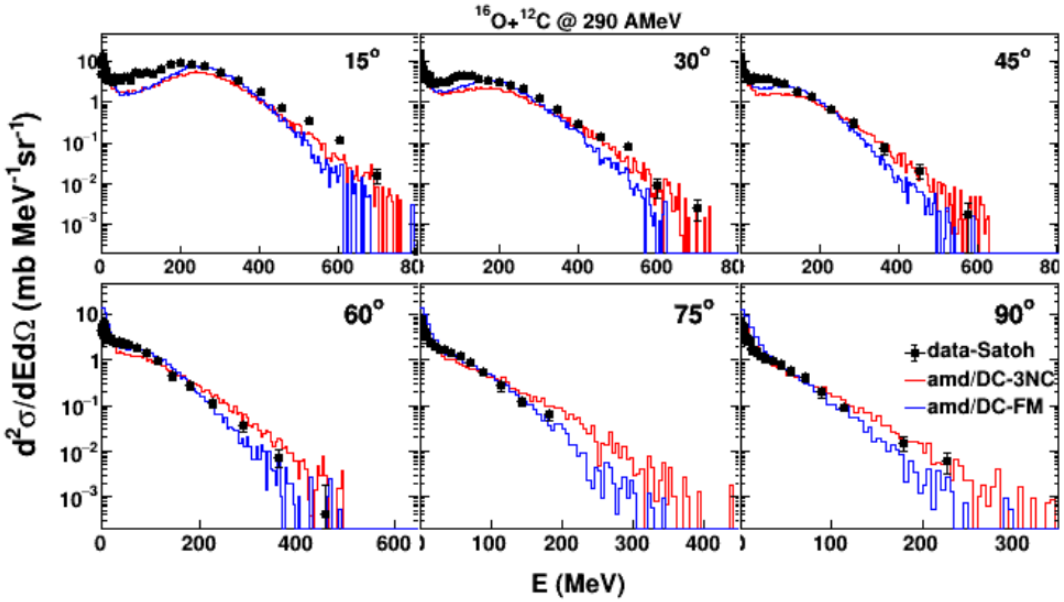

Fig. 2. Similar plots as Fig.1, but for 12C+16) at 290 MeV/nucleon. The same symbols and colors are used in Fug.1 for the experimental and simulated results.

[1] W. Lin, X. Liu, R. Wada, M. Huang, and P. Ren *et al.*, Phys. Rev. C **94**, 064609 (2016).

[2] R. Wada, Phy. Rev. C **96**, 031601(R) (2017).

[3] A. Ono, Phys. Rev. C **53**, 2958 (1996), Phys. Rev. C **59**, 853 (1999).

[4] Y. Iwata *et al.*, Phys. Rev. C **64**, 054609 (2001)

[5] D. Satoh **et al.**, Nucl. Instrum. Methods Phys. Res. **A644** 59, (2011).

Toward understanding relativistic heavy-ion collisions with the STAR detector at RHIC

D.M. Anderson, Y. Liu, S. Mioduszewski, J. Pan, J. Tyler, and the STAR Collaboration

This project is a study of high-energy heavy-ion collisions at the Relativistic Heavy Ion Collider (RHIC). The focus of the study is on two probes of the dense, partonic matter created in these collisions: 1) direct-photon-triggered jets and 2) heavy-quarkonium production in cold nuclear matter.

Investigating Energy Loss through Photon-Triggered Jet Measurements

The hard production of a direct photon back-to-back with a jet (γ-jet) is a probe of the parton energy loss in heavy-ion collisions [1]. In the "γ-jet" coincidence measurement, the measured energy of the trigger particle (the photon) serves as a calibrated baseline for the total energy of the jet particles on the recoil side (i.e. opposite in azimuth) of the trigger. The mean-free path of the γ in the medium is large enough so that its momentum is preserved, regardless of the position of the initial scattering vertex. Thus it does not suffer from the geometric biases, i.e. the non-uniform spatial sampling of hadron triggers due to energy loss in the medium, of *e.g.* π^0 triggers. Because of the difference in path length traversed, on average, between a direct- γ and a π^0 trigger, comparisons of γ-jet to hadron (π^0)-jet measurements can provide insight into the path-length dependence of the energy loss.

As the dominant background to direct photons are π^0 (decaying to two photons), the Barrel Shower Maximum Detector (BSMD) has provided the capability of distinguishing direct photons from neutral pions via the transverse shower shape. Our group has used this method in the measurement of direct photon+hadron correlations [2]. The γ-hadron correlation studies can be extended to studies of γ-triggered jet reconstruction measurements (as has been done at the LHC [3, 4]). The away-side jet will then be reconstructed in coincidence with triggers selected as direct photon candidates or (for $p_T<20$ GeV using the shower shape with the BSMD) identified π^0 triggers. The advantage of this should be the ability to reach lower energy fragments in the jet to study jet-shape modification and possible redistribution of energy.

Photon- and Pion-Triggered Recoil-Jet Measurements in p+p Collisions

The Run-9 data set in p+p collisions has been fully analyzed for charged jets recoiling from a high-energy neutral trigger particle. We have chosen to concentrate initially on charged-particle jets, for simplicity, recoiling from the trigger particle. Charged-jet reconstruction is performed using the anti-k_T algorithm from the Fastjet package [5]. In this analysis, charged particles with transverse momentum between $0.2 < p_T < 30$ GeV/c are included as constituents. A fiducial cut is made on the pseudorapidity of the jet axis, $|\eta_{jet}| < 1-R_{jet}$, where R_{jet} is the jet resolution parameter associated with the radial size of the jet.

STAR is able to selectively record events for a γ-jet analysis by triggering on a high-energy signal in the Barrel Electromagnetic Calorimeter (BEMC). Events are triggered on high-energy BEMC towers (requiring approximately 6 GeV in a single tower), Level-0 "High-Tower" triggers. In addition, our

group had previously implemented a Level-2 clustering algorithm in STAR to select events with approximately 8 GeV in a calorimeter cluster (1 or 2 towers) and produce a separate data stream ("L2Gamma") of these events. In the offline analysis, single photons are separated from closely positioned pairs of photons (in the BEMC), originating from high-p_T π^0 decays, based on their shower shape measured in the BSMD. The discrimination is done using cuts on the transverse-shower profile as measured by the BSMD. The shower shape is quantified by the Transverse Shower Profile (TSP), which was determined by optimizing the discrimination using a GEANT simulation. The cuts on the TSP are made to select a nearly pure sample of π^0 triggers and a sample of triggers denoted as γ_{rich}, with an enhanced fraction of direct photons. The purity of direct- γ triggers in the γ_{rich}, population is determined by the same procedure as in our group's previous publications of γ+hadrons [2], which is based on our definition of photon triggers not having a correlated near-side signal of charged hadrons within $\Delta\varphi<1.2$. The fraction of background triggers is determined statistically for each trigger E_T bin, using charged hadrons with $p_T > 0.9$ GeV/c in p+p collisions and 1.2 GeV/c in central Au+Au collisions.

To reconstruct jets, the "anti-kT" algorithm in the FastJet [5] package is used to cluster tracks into jets. The p_T threshold for clustering is kept low ($p_T>0.2$ GeV/c) in order to be able to access much of the lowest energy fragments in the jet (where the lost energy is expected to go). Reconstructed jets with resolution parameter R_{jet} varying between 0.2 and 0.5 are compared. The background energy (from the underlying event) is subtracted on an event-by-event basis using a background energy density also calculated by FastJet. The charged-jet p_T spectra are corrected for tracking efficiency and resolution by unfolding the measured-jet p_T spectra back to the true distributions (based on a GEANT simulation of the detector effects on PYTHIA-produced jets). PYTHIA is a Monte-Carlo event generator for p+p collisions [6].

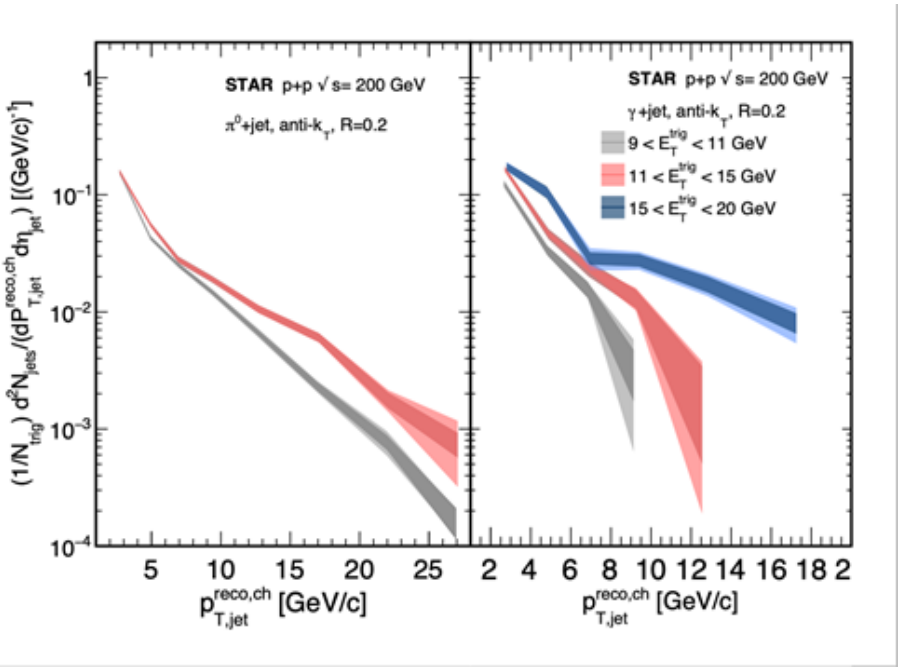

Fig. 1. Semi-inclusive jet yields per trigger for π^0 triggers (left) and direct-γ triggers (right) for different ranges in measured E_T of the trigger, in p+p collisions.

Fig. 1 shows the charged recoil-jet spectra for γ and π^0 triggers measured with transverse energy E_T=9-11 GeV, 11-15 GeV, and 15-20 GeV. These results have been shown by Derek Anderson at the Quark Matter 2022 conference and were the main results of his Ph.D. thesis (submitted to TAMU in the Spring semester of 2022).

Nuclear Modification (I_{AA}) of Per-Trigger Charged-Jet Yields

The analysis details in the Run-14 Au+Au data set largely mirror those employed in the p+p data, as discussed in the previous section. A mixed-event technique was developed to subtract the combinatoric background, which was also used in the published STAR results of semi-inclusive charged-jet reconstruction (using charged-hadron triggers) [7].

Fig. 2 shows the STAR results for the ratio of per-trigger jet yields in central (0-15%) Au+Au collisions to those in p+p collisions, IAA.

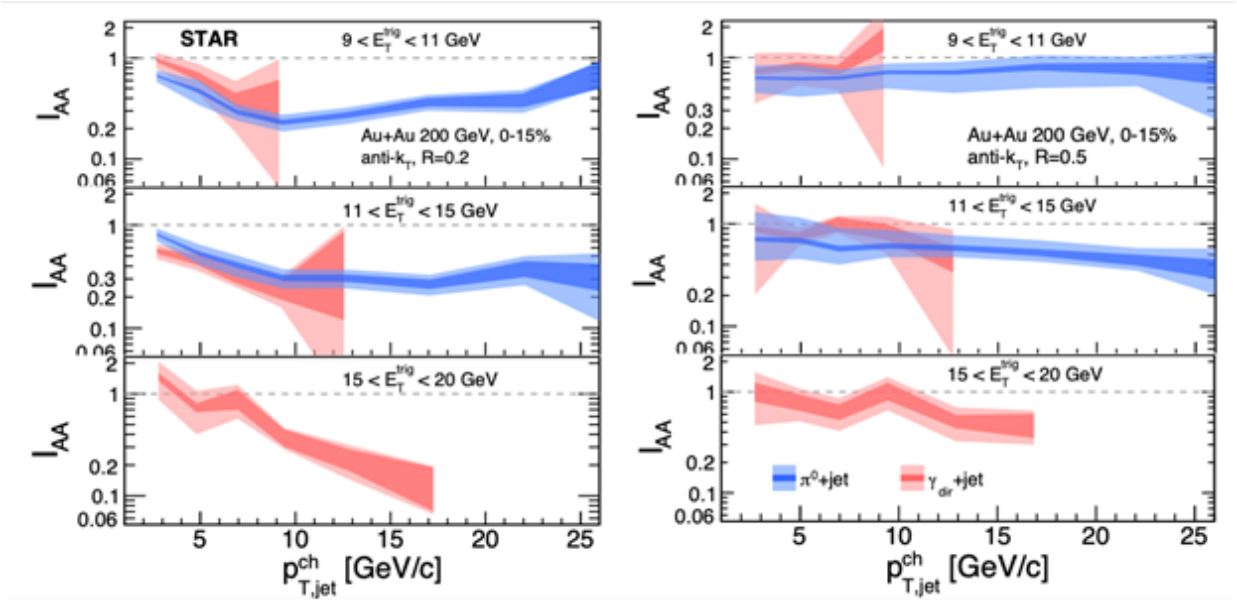

Fig. 2. I_{AA} of jets recoiling from neutral pions (blue) and direct photons (red), for trigger E_T measured within 9-11 GeV (top), 11-15 GeV (middle), and 15-20 GeV (bottom), for jet resolution parameter R=0.2 (left) and R=0.5 (right).

These results show the suppression of jet yields in central Au+Au collisions relative to the p+p baseline for both γ and π^0 triggers for jet resolution parameter R=0.2 (left panel). On the other hand, the larger jet radius of R=0.5 (right panel), shows significantly less suppression. In fact, the I_{AA} ratio is consistent with 1, which would indicate a full restoration of the lost energy within the larger jet cone.

Another direction that we have been pursuing with this analysis is the angular dependence of the jet yields relative to the trigger particle. Large angle scatterings due to parton interactions in the medium can be investigated by comparing the azimuthal direction of the trigger particle Φ_{trig} to the direction of the recoil jet axis Φ_{jet}.

Machine Learning to Discriminate and "isolated" triggers

When averaging over a sample of events, a clear near-side signal of associated hadrons can be seen in π^0 triggers, as opposed to γ triggers, since high-p_T pions are created as part of a jet. Our current method of discrimination requires very tight cuts on the π^0 selection based on the shower shape in the BSMD, greatly reducing the available statistics. For γ-triggered jet yields, the (non-direct) background contribution to the triggers must be subtracted on a statistical basis.

The question is whether machine learning can improve the γ/π^0 discrimination by "learning" the patterns of the near-side event activity. Jinjin Pan has worked on this question in Au+Au data. He provides thousands of images to different machine-learning algorithms that he has tested and further developed. For learning the near-side activity of π^0 triggers, he takes the nearly pure sample of π^0 that our shower-shape criteria selects. For the direct-γ triggers, he uses minimum-bias events and selects a random direction to be the photon. This gives the event activity of the underlying Au+Au background, which is what we expect for a direct-photon trigger. This project is still evolving, but we are anticipating results soon.

Unraveling Cold Nuclear Matter Effects in J/Y Suppression

The J/ψ has long been considered one of the most promising direct probes of deconfinement. According to theoretical predictions in 1986 [8], the produced $c\bar{c}$ pair will not be able to form a J/ψ bound state in the QGP, if a sufficiently high temperature is reached where the screening radius is smaller than the binding radius of the J/ψ resonant state. The "Debye" screening radius is the distance at which the color charges of two quarks are screened from one another, so that the confinement force is not able to hold the quarks together. A suppression in the yield of J/ψ was first observed in Pb+Pb collisions by the NA50 experiment at the CERN SPS (see, for example, [9]).

At RHIC, the predicted suppression of J/ψ due to screening in the QGP is much larger than the suppression observed at SPS due to the higher initial density of the produced medium [10]. The RHIC measurements, however, show a level of suppression similar to NA50 at mid-rapidity [11], which is significantly smaller than expectations due to color screening effects alone. This can be understood in a scenario where charmonium is regenerated due to the large initial production of charm + anti-charm quarks at $\sqrt{s_{NN}}$ = 200, in conjunction with their possible thermalization in the created medium [12]. If charm quarks (partially) thermalize in RHIC collisions, then the coalescence of $c\bar{c}$ could lead to a smaller than expected suppression [13].

With counteracting effects, it is a challenge to disentangle the suppression from the regeneration. In addition, there are cold nuclear matter effects [14], including modification of the parton distribution functions ("shadowing") and partonic multiple scattering, that also lead to suppression of heavy quarkonium and need to be disentangled from QGP suppression. In order to quantify effects of deconfinement, cold nuclear matter effects (via p+A collisions) must be measured and disentangled.

Our goal is to measure charmonium production in p+Au collisions as a function of "centrality". Ideally, centrality would be determined using the event activity in the forward region, away from the mid-rapidity region where the *J/ψ* is reconstructed. However, due to the performance of the STAR Beam-

Beam Counters (BBC) in the p+Au running period, we have concluded that we cannot use the BBC for this purpose. Alternatively, we have settled on using the number of primary tracks matched to a TOF hit in underlying event region (NMPTUE) as a measure of the event activity. The NMPTUE was chosen based on the following criteria. The number of tracks matched to TOF was found to be more robust for rejecting pile-up than other track-quality cuts. In order to remove the auto-correlation of centrality with the physics being measured as a function of the centrality, tracks are counted only in the underlying-event region, a region transverse to the direction of the reconstructed particle.

Charmonium Production in Run-15 p+Au data

Yanfang Liu's thesis project entails charmonium production in p+Au collisions as a function of "centrality" or "event activity". Yanfang has spent quite some time working on a centrality determination for this data set. However, there is a correlation between the J/ψ production and the number of charged particles produced in the event. In order to avoid this auto-correlation of the event classification to the physics observable, we studied different ways of classifying the event activity. Our first intention was to measure the multiplicities measured in the forward detectors, such as the Beam-Beam Counters (BBC's). However, the large beam backgrounds (and gain settings optimized for p+p collisions) rendered the distributions measured in the Au-going BBC unfavorable for extracting Glauber model quantities such as

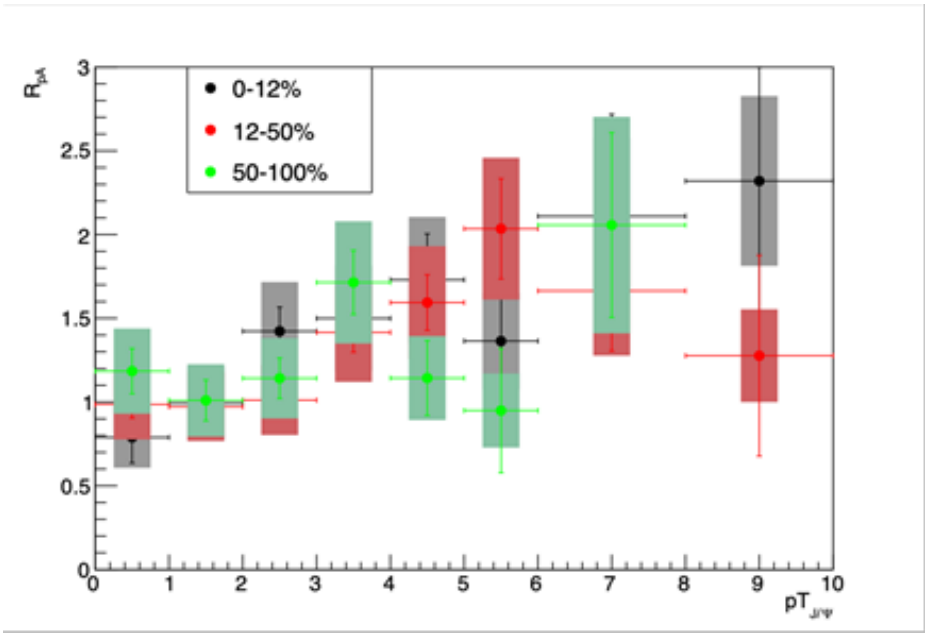

Fig. 3. Nuclear modification factor R_{pA} of J/ψ for different "centrality" p+Au events (with baseline being the yields measured in p+p collisions) as a function os p_T.

the number of binary nucleon-nucleon collisions (N_{binary}). We ultimately settled on a count of the number of charged tracks measured in a region separated from the reconstructed J/ψ candidate in the event ($1 < |\Delta\phi| < (\pi - 1)$). This region is within the so-called "underlying-event" region, since it is 1 radian away from the axis of the physics observable produced in a hard collision (in this case, the J/ψ). She now

has all of the ingredients to finalize the results. Fig. 3 shows a preliminary version of the results in the form of a nuclear modification factor,

$$R_{pA} = \frac{Yield^{p+Au}(p_T)}{N_{binary}^{p+Au} \times Yield^{p+p}}$$

In addition to the *J/ψ* analysis, we have looked into the feasibility of reconstructing the χ_c in p+A collisions. Since 30-40% of *J/ψ* are feed-down from χ_c and ψ‘ decays, it is important to measure cold nuclear matter effects on these separately.

[1] X.N. Wang, Z. Huang and I. Sarcevic, Phys. Rev. Lett. **77**, 231 (1996).

[2] L. Adamczyk *et al.* (STAR Collaboration), Phys. Lett. B **760**, 689 (2016); B.I. Abelev *et al.* (STAR Collaboration), Phys. Rev. C **82** (2010) 34909.

[3] S. Chatrchyan *et al.* (CMS Collaboration), Phys. Lett. B **718**, 773 (2013).

[4] (ATLAS Collaboration), ATLAS-CONF-2012-121.

[5] M. Cacciari and G. Salam, Phys. Lett. B **641**, 57 (2006); M. Cacciari, G. Salam and G. Soyez, JHEP **0804** 005 (2008), http://fastjet.fr.

[6] T. Sjöstrand, S. Mrenna, and P. Skands, Comput. Phys. Commun. **178**, 852 (2008).

[7] L Adamczyk *et al.* (STAR Collaboration), Phys. Rev. C **96** (2017) 24905.

[8] T. Matsui and H. Satz, Phys. Lett. B **178**, 416 (1986).

[9] M.C. Abreu *et al.* (NA50 Collaboration), Eur. Phys. J. C **39**, 335 (2005).

[10] L. Grandchamp, R. Rapp, and G.E. Brown, Phys. Rev. Lett. **92**, 212301 (2004); A. Capella and E.G. Ferreiro, Eur. Phys. J. C **42**, 419 (2005).

[11] A. Adare *et al.* (PHENIX Collaboration), Phys. Rev. Lett. **98**, 232301 (2007).

[12] P. Braun-Munzinger and J. Stachel, Phys. Lett. B **490**, 196 (2000).

[13] L. Grandchamp and R. Rapp, Phys. Lett. B **523**, 60 (2001).

[14] R. Vogt, Phys. Rev. C **71**, 054902 (2005).

SECTION III

NUCLEAR THEORY

Nuclear Theory – Nuclear astrophysics

J.W. Holt

Introduction:

The structure, phases, and dynamics of nuclear matter are crucial to understand stellar explosions, the origin of the elements, patterns in observed gravitational waves, and the composition of the densest observable matter in the universe. The appropriate tool to study strongly interacting matter at the typical scales relevant in nuclear astrophysics (well below the scale of chiral symmetry breaking $\Lambda_\chi \approx 1$ GeV) is chiral effective field theory [1-3]. In recent years, chiral effective field theory has become a cornerstone of the modern approach to nuclear many-body dynamics that provides a systematic framework for describing realistic microphysics, such as multi-pion exchange processes and three-body forces, within a well-defined organizational hierarchy. The long and intermediate-range parts of the nuclear potential result from one- and two-pion exchange processes, while short-distance dynamics, not resolved at the wavelengths corresponding to typical nuclear Fermi momenta, are introduced as contact interactions between nucleons. Chiral effective field theory is unique in its multichannel methods for quantifying uncertainties and especially in its ability to estimate the importance of missing physics.

Microscopic global optical potential with quantified uncertainties

Large-scale numerical simulations are essential for identifying the astrophysical site of the r-process, the primary candidates being the wind-driven ejecta from accretion disks surrounding binary neutron-star mergers or collapsars as well as the neutrino-driven winds of core-collapse supernovae. Neutron-capture rates on exotic neutron-rich isotopes are particularly important during the non-equilibrium freeze-out phase of r-process nucleosynthesis, but direct experimental studies at rare-isotope facilities remain unfeasible. The large uncertainties in these capture rates, due in part to difficulties in extrapolating phenomenological optical model potentials far from the valley of stability, limit the precision of predicted heavy-element abundances. Previously we have computed proton-nucleus and neutron-nucleus optical potentials [4,5] by combining the improved local density approximation [6] with chiral effective field theory calculations of the nucleon self-energy in homogeneous nuclear matter. Proton and neutron differential elastic scattering cross sections on calcium isotopes were found to be in good agreement with experimental data for projectile energies up to 150 MeV.

Recently, we have constructed [7] from chiral effective field theory two- and three-body forces a microscopic global nucleon-nucleus optical potential with quantified uncertainties. We started from the nuclear matter approach [8], in which the nucleon self-energy in infinite homogeneous matter at varying density and isospin asymmetry is used to construct nucleon-nucleus optical potentials by matching to the isoscalar and isovector densities of the target isotopes by way of the improved local density approximation. This was performed for proton and neutron projectiles on 1800 target nuclei in the mass range $12 < A < 242$ and for energies between $0\ \text{MeV} < E < 200\ \text{MeV}$. We then constructed a global optical potential parametrization that depends smoothly on the projectile energy as well as the target nucleus mass number and isospin asymmetry. This was then repeated for five different chiral interactions from which a covariance analysis of the parameters entering in the global optical potential could be used

to create a continuous distribution of optical potentials. This enabled the propagation of statistical uncertainties within the model. In Fig. 1 we show the predicted neutron elastic differential scattering cross section distributions for a range of isotopes and energies from the microscopic global optical potential of Ref. [7] compared to experimental data.

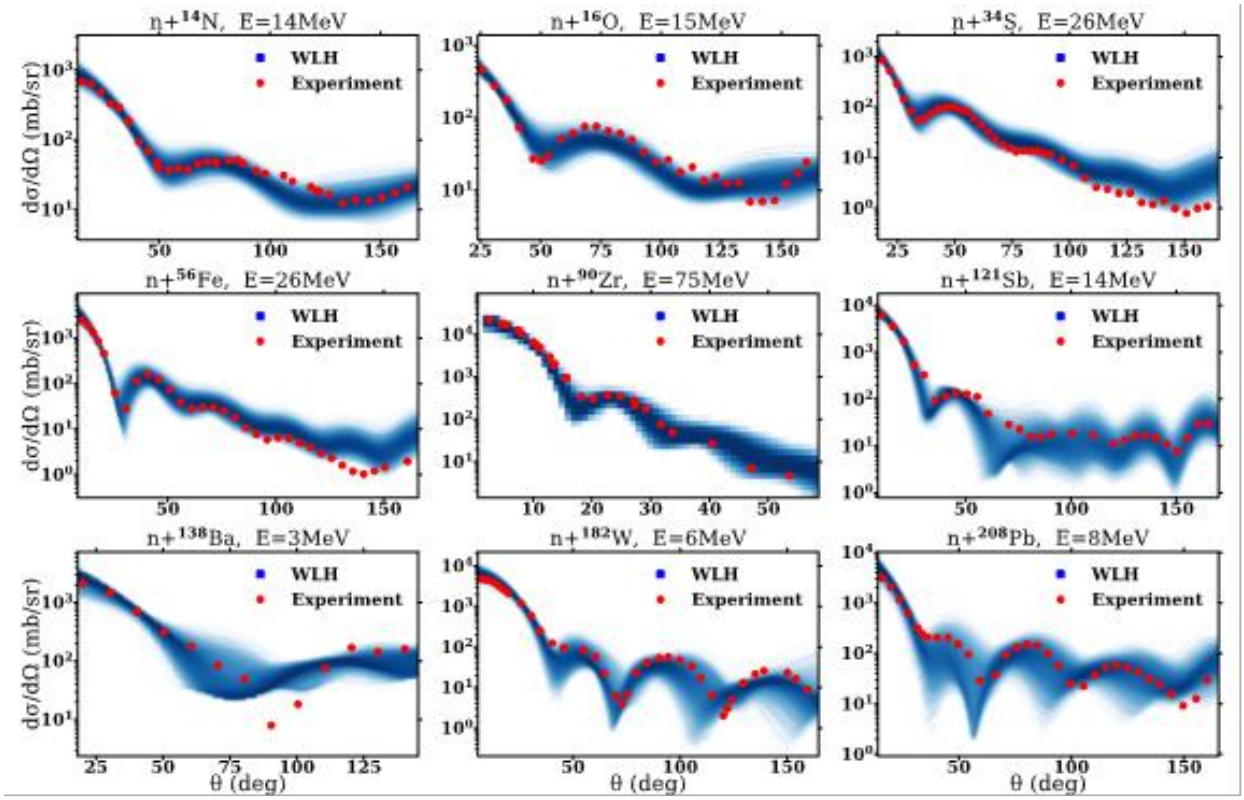

Fig. 1. Neutron elastic differential scattering cross sections from the microscopic global optical potential with quantified uncertainties of Ref. [WHI21] (blue) compared to experimental data (red dots).

Normalizing flows for efficient Monte Carlo importance sampling of many-body perturbation theory diagrams

Normalizing flows are a class of machine learning models used to construct a complex probability distribution through a bijective mapping of a simple base distribution. In recent work [9], we have demonstrated that normalizing flows are particularly well suited as a Monte Carlo integration framework for quantum many-body calculations that require the repeated evaluation of high-dimensional integrals across smoothly varying integrands and integration regions. As an example, the calculation of the finite-temperature nuclear equation of state could be precisely evaluated using normalizing flows, which resulted in a speedup factor of 100 compared to current state-of-the-art Monte Carlo importance sampling algorithms, such as VEGAS [10]. We also showed that a normalizing flow model trained on one target integrand can be used to efficiently calculate related integrals when the temperature, density, or even the nuclear force is varied. In Fig. 2 we show a comparison between the relative uncertainty $\sigma/\Omega^{(2)}$ in the evaluation of the second-order perturbation theory contribution to the grand canonical partition

function $\Omega^{(2)}$ of symmetric nuclear matter using normalizing flow importance sampling (nflow) and VEGAS importance sampling. The left panel demonstrates that normalizing flows can achieve a better sampling efficiency (for the accumulated total uncertainty σ_t over many iterations or the batch uncertainty σ_b with 5000 drawn samples per batch) over VEGAS. The right panel demonstrates that normalizing flow models can achieve the same improvement over VEGAS without further training when the temperature, density, and choice of nuclear force (either a one-boson-exchange "OBE" interaction or the next-to-leading-order chiral pion-exchange interaction "χNLO,π") is varied.

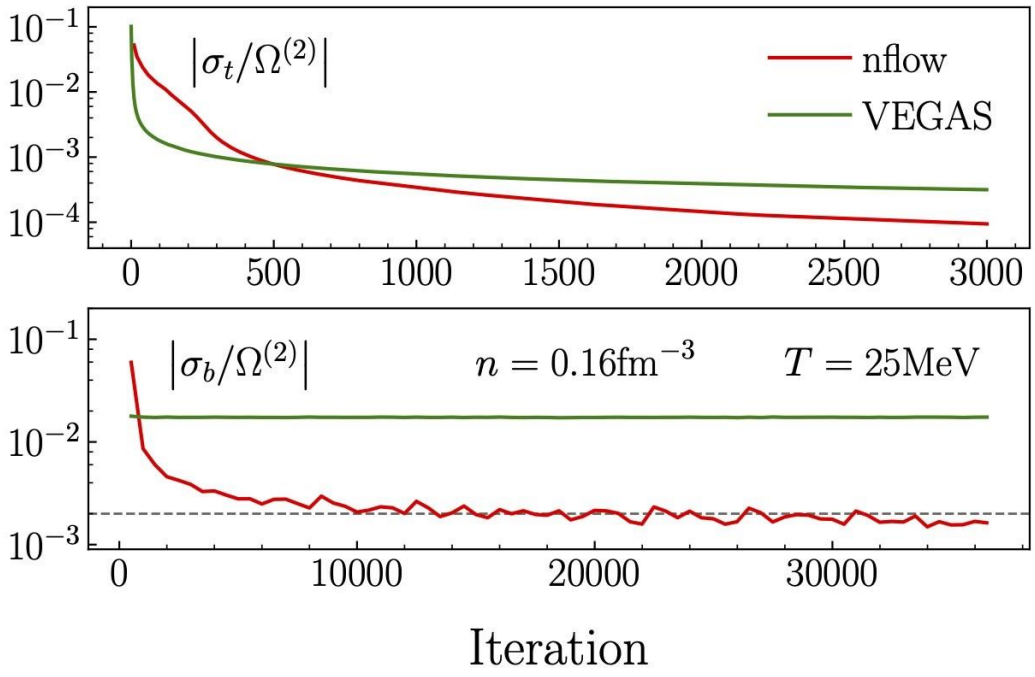

Fig. 2. Top: Comparison of the total relative uncertainty $\boldsymbol{\sigma_t/\Omega^{(2)}}$ in the calculation of the second-order grand canonical partition function of nuclear matter as a function of accumulated samples (5000 samples/iteration) for normalizing flow importance sampling and VEGAS importance sampling. Bottom: Same as top except for the batch relative uncertainty $\boldsymbol{\sigma_b/\Omega^{(2)}}$ with 5000 samples/batch.

[1] S. Weinberg, Physica A **96**, 327 (1979).

[2] E. Epelbaum, H.-W. Hammer and U.-G. Meissner, Rev. Mod. Phys. **81**, 1773 (2009).

[3] R. Machleidt and D. R. Entem, Phys. Rept. **503**, 1 (2011).

[4] T. R. Whitehead, Y. Lim, and J. W. Holt, Phys. Rev. C **100**, 014601 (2019).

[5] T. R. Whitehead, Y. Lim, and J. W. Holt, Phys. Rev. C **101**, 064613 (2020).

[6] J. P. Jeukenne, A. and Lejeune and C. Mahaux, Phys. Rev. C 16, 80 (1977).

[7] T. R. Whitehead, Y. Lim, and J. W. Holt, Phys. Rev. Lett. **127**, 182502 (2021).

[8] J. P. Jeukenne, A. Lejeune, and C. Mahaux, Phys. Rep. **25**, 83 (1976).

[9] J. Brady, P. Wen, and J.W. Holt, Phys. Rev. Lett. **127**, 062701 (2021).

[10] G.P. Lepage, J. Comp. Phys. **27**, 192 (1978).

Asymptotic normalization coefficients in nuclear reactions and nuclear astrophysics: A review

A.M. Mukhamedzhanov and L.D. Blokhintsev

The asymptotic normalization coefficient (ANC) is a fundamental nuclear characteristic of bound states and resonances. The ANC plays an important role in low-energy elastic scattering, transfer and radiative capture reactions, and provides a powerful indirect method in nuclear astrophysics. In this comprehensive review the main properties of the ANC and the role of the ANC in nuclear reactions and nuclear astrophysics are discussed. Also, different experimental and theoretical methods of determining the ANCs are addressed.

The paper has been published in Eur. Phys. J. A **58**, 29 (2022).

Indirect determination of the astrophysical S factor for the ^{6}Li(p, γ)^{7}Be reaction using the asymptotic normalization coefficient method

G.G. Kiss, M. La Cognata, R.E. Tribble, and A.M. Mukhamedzhanov

The astrophysical S factor) of the ^{6}Li(p, γ)^{7}Be reaction is known with large experimental uncertainties and the various extrapolated S factors differ significantly (by about 30%), making it very hard to draw astrophysical conclusions. For this reason, in the present work, the astrophysical S(E) factor of the ^{6}Li(p, γ)^{7}Be reaction was experimentally determined directly at solar energies based on the ANC indirect method. The aim of this method is to deduce the direct capture contribution to the radiative capture cross section and consequently the astrophysical factor by using the ANCs which, in turn, are obtained by studying peripheral transfer reactions. The direct capture cross section of the ^{6}Li(p, γ)^{7}Be reaction is proportional to the square of the ANC, which can be determined experimentally via transfer reactions. In particular, the study of the near barrier proton transfer ^{6}Li(^{3}He, d)^{7}Be reaction allows us to determine the ANCs in ^{6}Li+p→ ^{7}Be for both the ground and first-excited (0.429 MeV) states of the ^{7}Be nucleus. This independent experimental approach using the ANC indirect method, up-to-now never used to study the ^{6}Li(p, γ)^{7}Be reaction, not only improves our understanding on the low energy behavior of this reaction but also helps to identify the hidden systematic uncertainties of the measurements performed so far. Furthermore, to increase the accuracy of the astrophysical S factor derived here, the ANCs for the ^{6}Li+p→ ^{7}Be(g.s.) and ^{6}Li+p→ ^{7}Be(0.429 MeV) channels, were derived from the experimental total astrophysical S factor and the branching ratios m within the modified two-body potential method.

The paper was published in Phys. Rev. C **104**, 015807 (2021).

Status of deep subbarrier $^{12}C + ^{12}C$ fusion and advancing the Trojan horse method

A.M. Mukhamedzanov

I present an update the current status of the carbon–carbon fusion research taking into account that after the latest analysis (Beck et al. in Eur Phys J A 56:97, 2020) new important experimental and theoretical results had been published and will discuss how to advance new THM measurements to extract the low-energy astrophysical S-factors.

The paper has been published in Eur. Phys. J. A **58**, 71 (2022).

The ^{3}He+^{5}He→α+α reaction below the Coulomb barrier via the Trojan Horse Method

A.M. Mukhamedzhanov and collabrators

For the first time in an application to nuclear astrophysics, a process induced by the unstable ^{5}He = (^{4}He n) nucleus, the ^{3}He+^{5}He→2α reaction, has been studied through the Trojan Horse Method (THM). For that purpose, the quasi-free (QF) contribution of the ^{9}Be(^{3}He,α α)^{4}He reaction was selected at E(^{3}He) = 4 MeV incident energy. The reaction was studied in a kinematically complete experiment following a recent publication (Spitaleri *et al.* in Eur Phys J A **56** 18 (2020)), where for the quasi-free contributiothe momentum distribution between α and ^{5}He particle cluste in the ^{9}Be nucleus in the ground state have been extracted. The angular distribution of the QF ^{3}He+^{5}He→2α reaction was measured at $\theta_{c.m.}$ = 78–115 deg. The energy dependence of the differential cross section of the ^{3}He+^{5}He→2α virtual reaction was extracted in the energy range $E_{c.m.}$ = 0–650 keV. The total cross section obtained from the Trojan-horse method was normalized to absolute cross sections from a theoretical calculation in the energy range $E_{c.m.}$ =300–620 keV.

The paper was published in Eur. Phys. J. A **57**, 20 (2021).

A Semi-microscopic description of isoscalar giant multipole resonances in medium-mass closed shell nuclei

M.L. Gorelik,[1] S. Shlomo, B.A. Tulupov,[2] and M.H. Urin[3]
[1]*Moscow Economic School, Moscow 123022, Russia*
[2]*Institute for Nuclear Research, RAS, Moscow 117312, Russia*
[3]*National Research Nuclear University "MEPhI", Moscow 115409, Russia*

Being a microscopically based extension of the standard [1] and nonstandard [2] versions of the continuum-random-phase approximation (cRPA), by taking the spreading effect into account, the semi-microscopic particle-hole (p-h) dispersive optical model (PHDOM) has been proposed [3] and successfully implemented for describing properties of various giant resonances (GRs) in medium-heavy mass closed-shell nuclei (See Ref. [4] and references therein). Within the model, the main relaxation modes of (p-h)-type states, associated with GRs, are together taken into account. These modes are: (i) Landau damping; (ii) coupling mentioned states to the single-particle continuum, and; (iii) coupling to many-quasiparticle configurations (the spreading effect). Landau damping and coupling to the continuum are described microscopically (in terms of a phenomenological mean field and Landau-Migdal p-h interaction), while the spreading effect is treated phenomenologically (in terms of the energy-averaged p-h self-energy term). That allows one to describe within PHDOM the main GR characteristics for a wide excitation-energy interval: (i) double transition density; (ii) strength distribution, and one-body "projected" transition density both related to an appropriate probing operator, and (iii) probabilities of direct one-nucleon decay.

The PHDOM version proposed in Ref. [3] in a rather general form has been adopted in Ref. [4] for describing main characteristics of isoscalar Multipole GRs in medium-heavy mass closed-shell nuclei. The L = 0 - 3 multipole resonances together with L = 0, and 2 multipole overtones have been considered. A rather reasonable description of available experimental data has been obtained for the ^{208}Pb nucleus [4], taken as an appropriate example. Some of the results obtained within cRPA (i.e., in neglecting the spreading effect) were found to be in agreement with the results obtained within the microscopic RPA-based approach of self-consistent Hartree-Fock, using Skyrme-type forces [5].

The present work is a direct continuation of the above-described study of Ref. [4]. The study is extended to medium-mass closed-shell nuclei ^{40,48}Ca, ^{90}Zr, and ^{132}Sn. Calculation results are compared with available experimental data [6]. Some of cRPA results are compared with the results of Hartree-Fock (HF)-based RPA of Ref. [5].

[1] S. Shlomo and G. Bertsch, Nucl. Phys. **A243**, 507 (1975).
[2] M.H. Urin, Nucl. Phys. **A811**, 107 (2008).
[3] M.H. Urin, Phys. Rev. C **87**, 044330 (2013).
[4] M.L. Gorelik, S. Shlomo, B.A. Tulupov, and M.H. Urin, Phys. Rev. C **103**, 034302 (2021).
[5] G. Bonasera, M.R. Anders, and S. Shlomo, Phys. Rev. C **98**, 054316 (2018).
[6] M.L. Gorelik, S. Shlomo, B.A. Tulupov, and M.H. Urin, to be submitted.

Direct one-neutron decay of the isoscalar giant dipole resonance in medium-heavy spherical nuclei: A semi-microscopic approach description

M.L. Gorelik,[1] S. Shlomo,[2] B.A. Tulupov,[2] and M.H. Urin[3]
[1]*Moscow Economic School, Moscow, Russia;*
[2]*Institute for Nuclear Research, RAS, Moscow 117312, Russia*
[3]*National Research Nuclear University "MEPhI", Moscow, Russia*

Direct one-nucleon decay of giant resonances (GRs) is the subject of permanent (but not-too-intensive) experimental and theoretical studies. They allow one to get information on GR structure and decay mechanisms. Decay probabilities are usually deduced from a common analysis of cross sections of direct inclusive and "decay" reactions. In Ref. [1], direct one-neutron decay of Isoscalar Giant Dipole Resonance (ISGDR) in ^{90}Zr, ^{116}Sn, and ^{208}Pb have been studied via the (α, α')- and $(\alpha, \alpha' n)$-reactions. To some extent, this study has been stimulated by predictions made in Ref. [2] for partial branching ratios b_μ of direct one-neutron ISGDR decay accompanied by population of neutron-hole states μ^{-1} in product nuclei. A simple extension of standard and nonstandard continuum-RPA versions to taking phenomenologically the spreading effect into account has been exploited in Ref. [2].

In the present work, we have employed the semi-microscopic Particle-Hole Dispersive Optical Model (PHDOM)-based approach (see, e.g., Ref. [3] and references therein) to estimate the branching ratios for direct one-nucleon decay of an arbitrary GR. Unique abilities of the PHDOM where conditioned by a joint description of the main relaxation processes of high-energy p-h configurations associated with a given giant resonance. Two processes, Landau damping and coupling the mentioned configurations to the single-particle continuum, were described microscopically in terms of Landau-Migdal p-h interaction and a phenomenological mean field, partially consistent with this interaction. Another mode, the coupling to many quasiparticle states (the spreading effect) was described phenomenologically in terms of the imaginary part of the properly parameterized energy-averaged p-h self-energy term. The imaginary part determines the real one via a microscopically-based dispersive relationship. We, have first, specified the approach of Ref. [2], employing for evaluation of b_μ values the semi-microscopic PHDOM, see Ref. [3], and, secondly, use the alternative definition for b_μ employed in Ref. [1]. These points allowed us to reduce markedly the difference between theoretical and experimental b values related to direct one-neutron decay of ISGDR in the above-mentioned nuclei. The experimental values $b = \sum_\mu b_\mu$ (the sum is taken over a few valence neutron-hole states) of Ref. [1] were found to be essentially less than the respective values obtained in the calculations.

[1] M. Hunyadi, A.M. Van den Berg, B. Davids, M.N. Harakeh *et al.*, Phys. Rev. C **75,** 014606 (2007).
[2] M.L. Gorelik, I.V. Safonov, and M.H. Urin, Phys. Rev. C **69**, 054322 (2004).
[3] M.L. Gorelik, S. Shlomo, B.A. Tulupov, and M.H. Urin, Phys. Rev. C **103**, 034302 (2021).

Semiclassical shell-structure micro-macroscopic approach for nuclear level density

A.G. Magner,[1] A.I. Sanzhur,[1] S.N. Fedotkin,[1] A.I. Levon,[1] and S. Shlomo
[1]*Institute for Nuclear Research, 03028 Kyiv, Ukraine*

Many properties of heavy nuclei can be described in terms of the statistical level density. Usually, the level density $\rho(E,A)$, where E and A are the energy and nucleon number, respectively, is given by the inverse Laplace transformation of the partition function $Z(\beta,\alpha)$. Within the grand canonical ensemble, the standard saddle-point method (SPM) is used for integration over all variables, including β, which is related to the total energy E. This method assumes large excitation energy U, so that the temperature T is related to a well-determined saddle point in the integration variable β for a finite Fermi system of large particle numbers. However, data for the level density from many experiments also exist for regions of low excitation energy U, where such a saddle point does not exist. Therefore, to simplify the calculations of the level density, $\rho(E,A)$, we have carried out the integration over the Lagrange multiplier β in the inverse Laplace transformation of the partition function $Z(\beta,\alpha)$ more accurately beyond the SPM. However, for another variable related to the total particle number A, one can apply the SPM in a nuclear system with large A.

We have derived [1] the statistical level density $\rho(S)$ as function of the entropy S within the micro-macroscopic approximation (MMA) using the mixed micro- and grand-canonical ensembles beyond the standard saddle point method of the Fermi gas model. This function can be applied for small and, relatively, large entropies S or excitation energies U of a nucleus. For a large entropy (excitation energy), one obtains the exponential asymptotic of the standard SPM Fermi-gas model, however, with the significant powers of $1/S$ corrections. For small S one finds the usual finite combinatorics expansion in powers of S^2. Functionally, the MMA at linear approximation in $S^2 \propto U$ expansion, at small excitation energies U, coincides with the empiric constant "temperature" model (CTM), but was obtained without using free fitting parameters. Thus, MMA unifies the commonly accepted Fermi-gas approximation with the empiric CTM for large and small entropies S, respectively. The MMA clearly manifests an advantage over the standard full SPM approaches at low excitation energies, because of no divergences of the MMA in the limit of small excitation energies, in contrast to all of full SPM approaches, e.g., Bethe asymptotic and Fermi gas (FG) asymptotic. Another advantage takes place for nuclei which have much more states in the very low-energy states range. The values the inverse of the level density parameter a, $K=A/a$, were compared with those of experimental data for low energy states (LES) below neutron resonances (NRs) in spectra of several nuclei. The MMA results with only one physical parameter in the least mean-square fit, the inverse level density parameter K, is usually the better the larger number of the extremely low energy states, certainly much better than for the FG model in this case. The MMA values of the inverse level density parameter K for LESs can be significantly different from those of the neutron resonances within the FG model. We have also found [1] significant shell effects in the MMA level density for the nuclear LES range within the semiclassical periodic orbit theory (POT), which is based on the semiclassical time-dependent propagator, enables determining the total level-density, energy, free-energy, and grand canonical ensemble potential, in terms of the smooth extended Thomas-Fermi (ETF) term and periodic-

orbit-shell corrections. In particular, we generalized the known SPM results for the level density in terms of the full SPM generalized Fermi gas (GFG) approximation accounting for the shell effects using the POT. Exponential disappearance of shell effects with increasing temperature was analytically studied within the POT for the level density. A shift of the entropy *S*, and the inverse level density parameter K due to shell effects were also obtained at large temperature, but much smaller than the chemical potential.

[1] A.G. Magner, A.I. Sanzhur, S.N. Fedotkin, A.I. Levon, and S. Shlomo, Phys. Rev. C **104**, 044319 (2021).

Shell and asymmetry effects in nuclear statistical level densities

A.G. Magner,[1] A.I. Sanzhur,[1] S.N. Fedotkin,[1] A.I. Levon,[1] and S. Shlomo
[1]*Institute for Nuclear Research of the NAN Ukraine, Kyiv, Ukraine*

Many nuclear properties can be described in terms of the statistical level density, $\rho = \rho(E,N,Z)$ as function of the total energy E, and number of neutrons N and protons Z in a nucleus. Within the semiclassical periodic orbit theory (POT), using the mean field approach, the level density was derived [1] within the micro-macroscopic approximation (MMA) beyond the Fermi gas (FG) model. We obtain $\rho \propto I_\nu(S)/S^\nu$, with $I_\nu(S)$ being the modified Bessel function of the entropy $S = 2(aU)^{1/2}$, where U is the excitation energy, and a is the level density parameter (LDP). With subscripts (n,p), the LDP is given in term of the single particle (s.p.) level density g(ε), where ε is the s.p. energy, by $a = \pi^2 g(\lambda)/6 = a_n + a_p$. The s.p. level density, $g(\varepsilon) = g_n + g_p \cong \tilde{g}(\varepsilon) + \delta g(\varepsilon)$, taken at the chemical potential, $\varepsilon = \lambda$ ($\lambda_n \approx \lambda_p \approx \lambda$), depends on shell structure through the periodic-orbit shell correction $\delta g(\varepsilon)$. When the contribution of $\delta g(\varepsilon)$ is small (named as case MMA1), one obtains the Bessel function order $\nu = (n+1)/2$, where n is the number of integrals of motion. Strong oscillating components $\delta g(\varepsilon)$ (case MMA2) lead to the value $\nu = (n+3)/2$. For large entropy S the MMA level density reaches the FG limit, $\rho \cong \exp(S)[1+O(1/S)]/(2\pi S^{2\nu+1})^{1/2}$, while for the case of small S (the case of small excitation energy U) the level density reaches the finite combinatorics limit $\rho(S) \cong \rho(0)\left[1 + S^2/4(1+\nu) + O(S^4)\right]$.

In Fig. 1, we present some results of our calculations. The Figure shows a comparison of MMA approaches with our shell-structure FG (SFG) asymptotic for relatively large excitation energies U, and with the experimental data. These data are obtained by the sample method from the low energy states (LES) range below neutron resonances in ^{195}Pt (large number, L>>1, of very LES's below about 1 MeV) and in ^{196}Pt (for small number of LES's, L~1). The results for the MMA2b level density in ^{195}Pt (L>>1) and those for the close MMA2a and MMA1 (and SFG) approaches for ^{196}Pt (L~1) agree well with the experimental data. The values of inverse level density parameter (LDP) K, given by $K=A/a$, where A is the number of nucleons, are found to be significantly different from that of neutron resonances, due to major shell effects. We also investigated correlations of the shell corrections in $K(A)$ with those in $\delta E(A)$ as functions of particle numbers A within a large chain of the Pt isotopes.

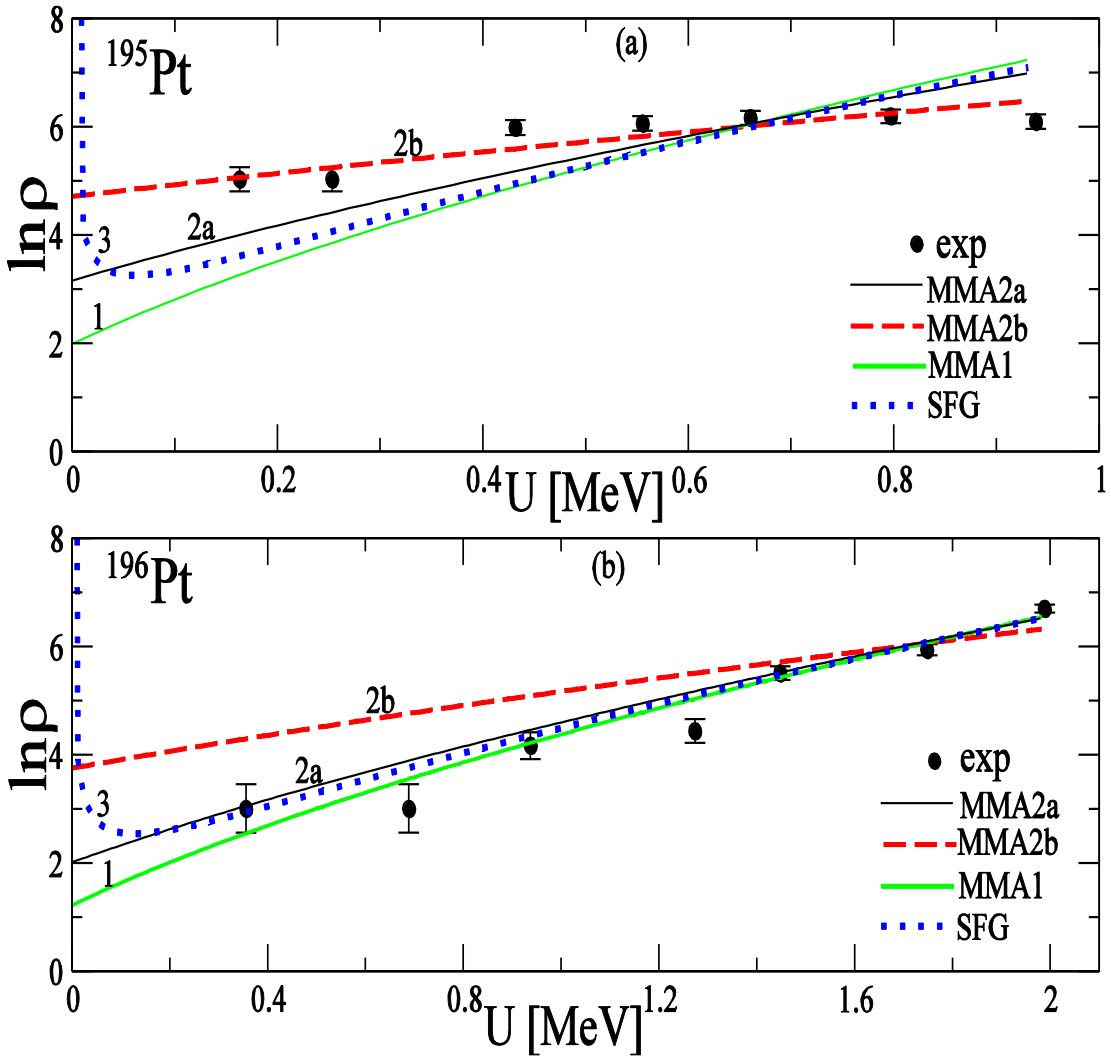

Fig. 1. Level densities, $\ln\rho$, for different MMA approaches. The MMA2a is the MMA2, taken at the fitted inverse level-density parameter, $K = \mathrm{A}/a$, for energy shell corrections δE from Moeller *et al.* [2]. The MMA2b is that in the limit of small shell corrections δE but with large contributions of their derivatives. SFG is the shell-structure Fermi-gas asymtotic for large excitation energies U. Dots are the experimental data obtained by the sample method on the plateau conditions over inverse level density parameter K.

[1] A.G. Magner, A.I. Sanzhur, S.N. Fedotkin, A.I. Levon, and S. Shlomo, Int. J. Mod. Phys. E **30**, 2150092 (2021).

[2] P. Moeller, A.J. Sierk, T, Ichikawa, and H. Sagawa, Atom. Data Nucl. Data Tables **109-110**, 1 (2016).

Number-of-constituent-quark scaling of elliptic flow: a quantitative study

M. Wang,[1] J.Q. Tao,[1] H. Zheng,[1] W.C. Zhang,[1] L.L. Zhu,[2] and A. Bonasera
[1]*School of Physics and Information Technology, Shaanxi Normal University, Xi'an 710119, China*
[2]*Department of Physics, Sichuan University, Chengdu 610064, China*

The number-of-constituent-quark (NCQ) scaling behavior of the elliptic flow of identified particles produced in A+A collisions is studied quantitatively using an empirical function that fits the experimental v_2 data available from the RHIC and LHC [1]. The most common approach for NCQ scaling involves (1) doing a scaling of the experimental v_2 data of an identified particle with its NCQ, (2) doing the same to its transverse momentum or energy, then (3) combining all the scaled data and identifying the NCQ behavior by intuitively looking (since the measured experimental data are discrete). We define two variables d_1, d_2 to describe NCQ scaling quantitatively and simultaneously, and identify the approximate region where the NCQ scaling holds. This approach could be applied to study NCQ or other scaling phenomena in future experiments.

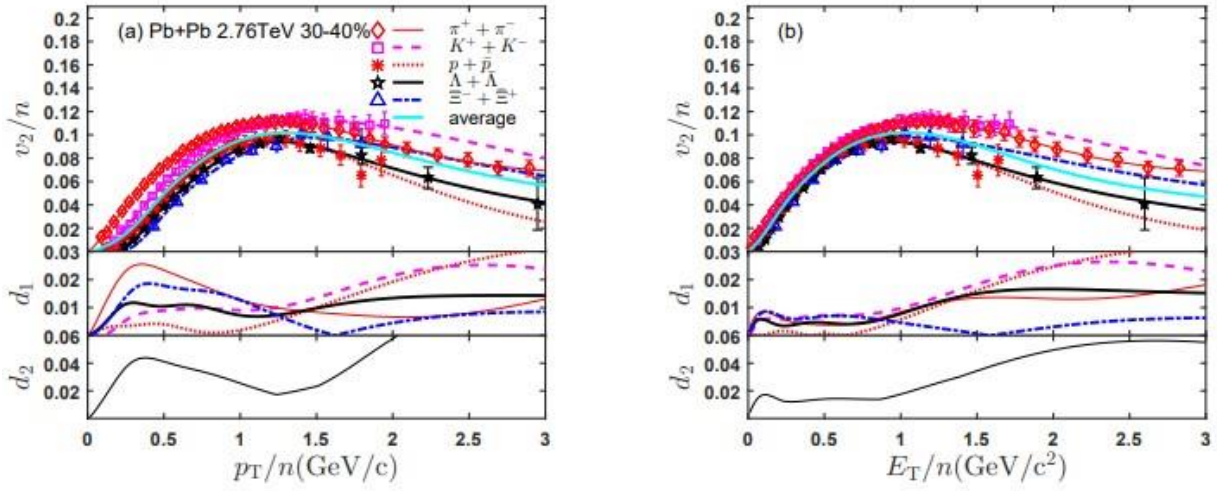

Fig. 1. (Color online) Scaled elliptic flow versus scaled transverse momentum (left panel) and energy (right panel) for the five identified particles (indicated in the legend) produced in Pb+Pb collisions at $\sqrt{s_{NN}} = \mathbf{2.76}$ TeV with centrality 30-40%. The curves for the fit results obtained using the empirical formula [1] and their averages are plotted. The two variables (d_1, d_2) are also plotted as functions of the scaled transverse momentum and energy, with appropriate scales for showing the details where NCQ scaling holds.

[1] M. Wang, J.Q. Tao, H. Zheng, W.C. Zhang, L.L. Zhu, and A. Bonasera, Nucl. Sci. Tech. **33**, 37 (2022).

The novel scaling of Tsallis parameters from the transverse momentum spectra of charged particles in heavy-ion collisions

J.Q. Tao,[1] W.H. Wu,[1] M. Wang,[1] H. Zheng,[1] W.C. Zhang,[1] L.L. Zhu,[2] and A. Bonasera
[1]*School of Physics and Information Technology, Shaanxi Normal University, Xi'an 710119, China*
[2]*Department of Physics, Sichuan University, Chengdu 610064, China*

The transverse momentum (p_T) spectra of charged particles measured in Au + Au collisions from the beam energy scan (BES) program, Cu + Cu collisions at $\sqrt{s_{NN}}$=62.4, 200 GeV at the RHIC and Pb + Pb, Xe + Xe collisions at the LHC are investigated in the framework of Tsallis thermodynamics [1]. The theory can describe the experimental data well for all the collision systems, energies and centralities investigated. The collision energy and centrality dependence of the Tsallis distribution parameters, i.e., the temperature T and the nonextensive parameter q, for the A + A collisions are also studied and discussed. A novel scaling between the temperature divided by the natural logarithm of collision energy ($T/\ln\sqrt{s}$) and the nonextensive parameter q is presented.

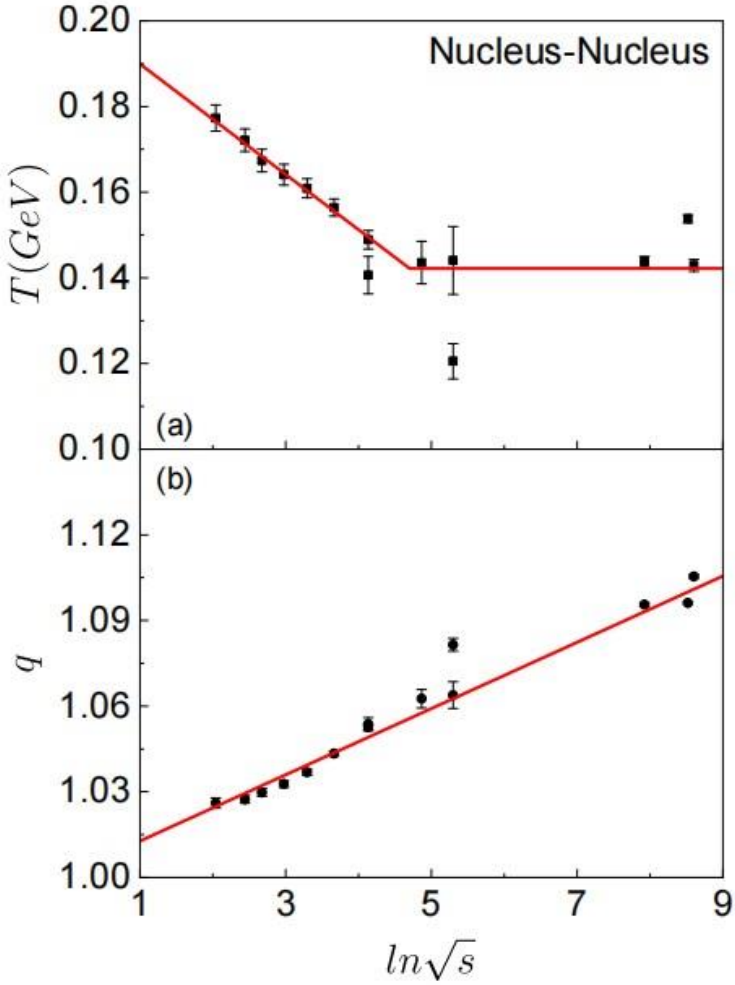

Fig. 1. (Color online) The collision energy dependence of the temperature T and nonextensive parameter q for the collision systems investigated at the most central collisions. See text for the lines.

In Fig. 1, the results of T and q versus collision energy from the RHIC to LHC for the most central collisions are shown. We use $\sqrt{s}$ to denote $\sqrt{s_{NN}}$ in units of GeV, i.e. $\sqrt{s}=\sqrt{s_{NN}}/1$ GeV. Thus, it is a dimensionless variable that is suitable used in an expression like $\ln\sqrt{s}$. For the temperature T, it is observed that a linear decrease from $\sqrt{s_{NN}}$=7.7 GeV to a certain collision energy and then it is approximately constant for the higher collision energies, which is the asymptotic value connected to the Hagedorn temperature, i.e., the pion mass. The lines are drawn to guide the eyes. Unlike the temperature T, the parameter q shows a linear monotonic increasing dependence on the collision energy in the whole energy region investigated. A linear fit gives $q=0.0116\ln\sqrt{s}+1.00116$ shown in the Fig. 1(b). This indicates that the higher the collision energy is, the less the collision system reaches thermal equilibrium during the evolution and the temperature fluctuation is larger. The parameters from the other centralities showing similar behaviors have been observed.

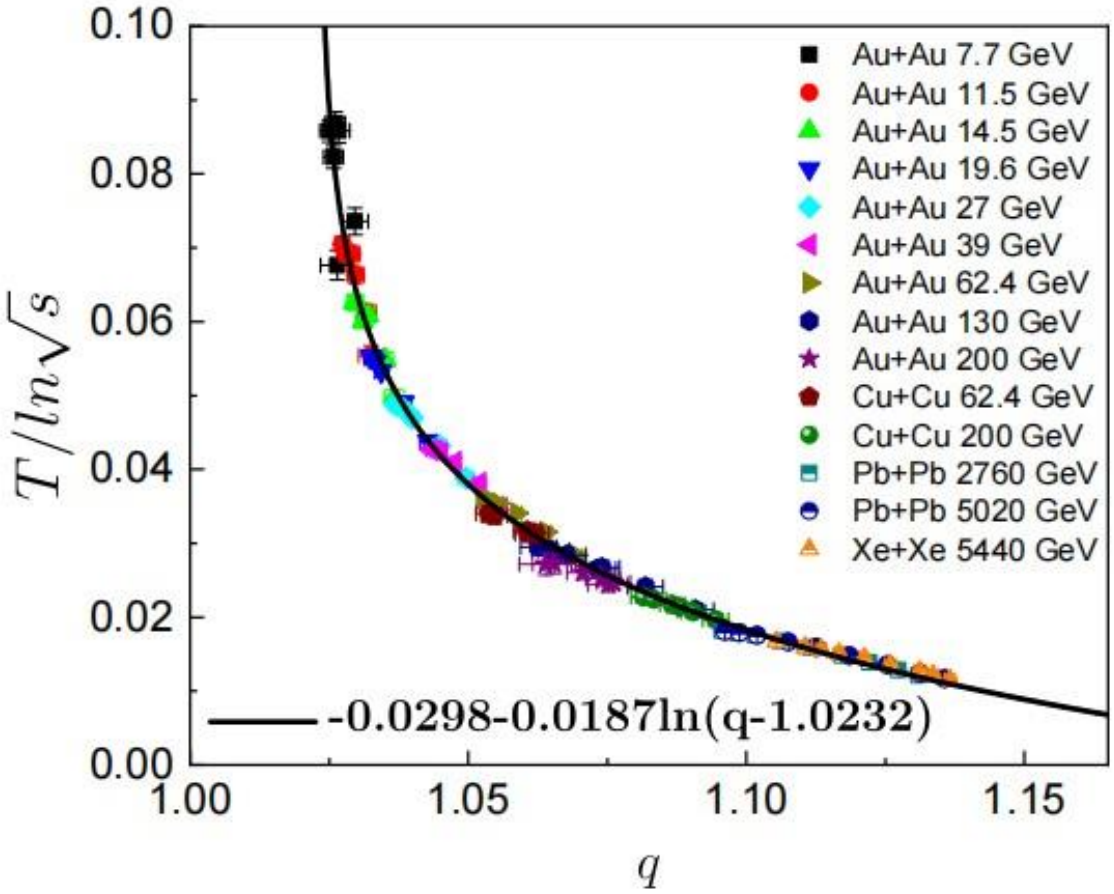

Fig. 2. (Color online) Nonextensive parameter q dependence of the temperature divided by the natural logarithm of collision energy $\mathbf{T/ln\sqrt{s}}$ in A + A collisions with different centrality. The curve is the fit results and the fit function is indicated in the legend.

In Fig. 2, the results of the novel scaling discovered between the temperature divided by the natural logarithm of collision energy $T/\ln\sqrt{s}$ and nonextensive parameter q for all the A + A collision systems and centralities investigated is shown. It is clear that all the data points are scaled into one curve.

We are able to fit it with the function indicated in the legend of Figure2. This observed strong scaling indicates that the parameters of Tsallis distribution obtained from the charged particle transverse momentum spectra are not independent of each other but are anticorrelated. It also suggests that further fundamental characteristics of the nonextensive statistics are yet to be studied. The emergence of this scaling maybe attributed to hydrodynamical scaling but further investigations are needed.

[1] J.Q. Tao, W.H. Wu, M. Wang, H. Zheng, W.C. Zhang, L.L. Zhu, and A. Bonasera, Particles **1**, (2022).

Charged pion production from Au + Au collisions at $\sqrt{s_{NN}}$ = 2.4 GeV in the relativistic Vlasov-Uehling-Uhlenbeck model

Kyle Dogbey, Zhen Zhang,[1] Jeremy Holt, and Che Ming Ko
[1]*Sino-French Institute of Nuclear Engineering and Technology, Sun Yat-sen University, Zhuhai 519082, China*

Using the isospin-dependent relativistic Vlasov-Uehling-Uhlenbeck (RVUU) model [1,2], extended from Refs. [3,4], we have studied charged pion ($\pi^{\pm}$) production in Au+Au collisions at $\sqrt{s_{NN}}$ = 2.4 GeV [5]. By fitting the density dependence of the Δ resonance production cross section in nuclear medium to reproduce the experimental $\pi^{\pm}$ multiplicities measured by the HADES Collaboration [6], we have obtained a good description of the rapidity distributions (Fig. 1) and transverse momentum spectra (Fig. 2) of $\pi^{\pm}$ in collisions at various centralities. Some shortcomings in the description of $\pi^{\pm}$ production

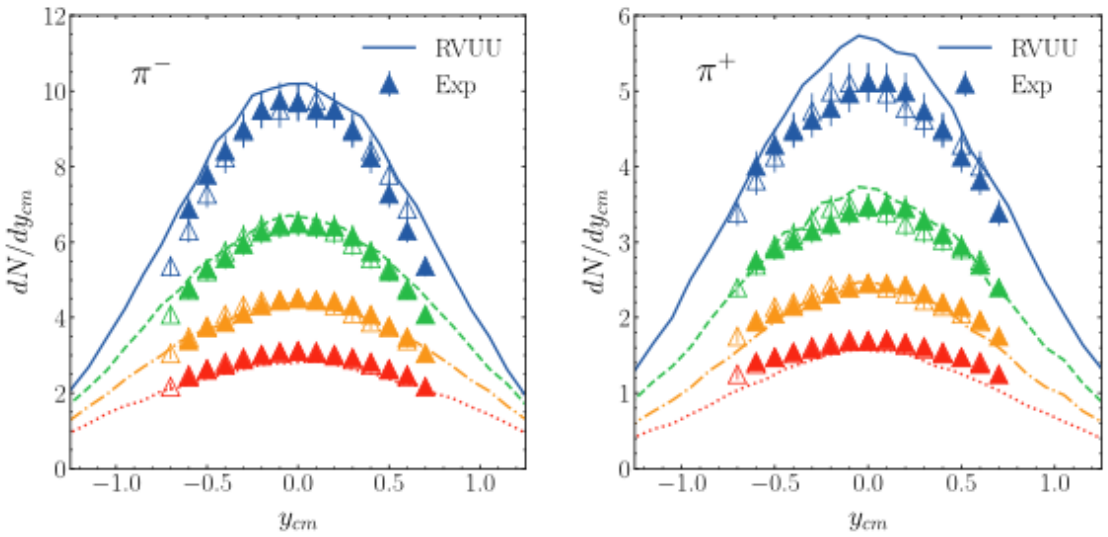

Fig. 1. Rapidity distributions of π^- (left window) and π^+ (right window) from RVUU (lines) and experimental data (triangles) from Ref. [6]. Results are shown across 4 centrality bins: 0% − 10% (blue, solid line), 10% − 20% (green, dashed line), 20% − 30% (orange, dot-dashed line), 30% − 40% (red, dotted line).

may indicate the need for including the strong potential on $\pi^{\pm}$ in RVUU, which is at present absent. We have also calculated the proton rapidity distribution in the most central collisions and found it a factor of 1.23 larger than the coalescence invariant proton rapidity distribution extracted from preliminary HADES data on protons, deuterons tritons, and helium-3 [7], which requires further theoretical and experimental studies.

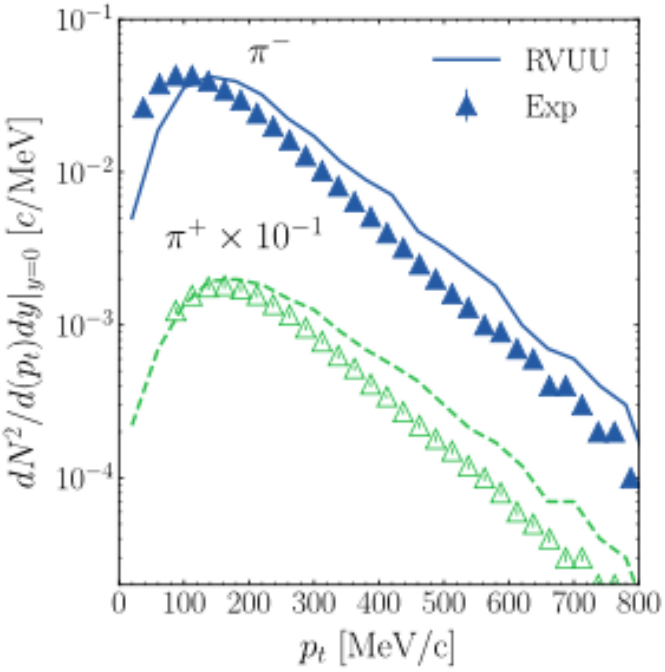

Fig. 2. Charged pion transverse momentum spectrum from RVUU (lines) and experimental data (triangles) from Ref. [35]. Negative pions are represented by filled blue symbols and solid blue line, while positive pions are scaled down by 10^{-1} and are drawn with hollow green symbols and green dashed line. Results are shown for mid-rapidity events for the most central (0% − 10%) class of collisions.

[1] T. Song and C.M. Ko, Phys. Rev. C **91**, 014901 (2015).

[2] Z. Zhang and C.M. Ko, Phys. Rev. C **95**, 064604 (2017).

[3] C.M. Ko, Q. Li, and R. Wang, Phys. Rev. Lett. **59**, 1084 (1987).

[4] C.M. Ko and Q. Li, Phys. Rev. C **37**, 2270 (1988),

[5] K. Dogbey, Z. Zhang, J.W. Holt, and C.M. Ko, Phys. Lett. B **829**, 137134 (2022).

[6] J. Adamczewski-Musch, O. Arnold, C. Behnke, A. Belounnas, A. Belyaev, J.C. Berger-Chen, A. Blanco, C. Blume, M. Böhmer, P. Bordalo, *et al.*, Eur. Phys. J. A **56**, 259 (2020).

[7] M. Szala (HADES), Light nuclei formation in heavy ion collisions measured with HADES, in: Proceedings of the ECT* Workshop: Light Clusters in Nuclei and Nuclear Matter: Nuclear Structure and Decay, Heavy Ion Collisions, and Astrophysics, 2019 (unpublished).

Comparison of heavy-ion transport simulations: Mean-field dynamics in a box

Maria Colonna,[1] Ying-Xun Zhang,[2,3] Yong-Jia Wang,[4] Dan Cozma,[5] Pawel Danielewicz,[6] Che Ming Ko and TEMP Collaboration

[1]*INFN-LNS, Laboratori Nazionali del Sud, 95123 Catania, Italy*

[2]*China Institute of Atomic Energy, Beijing 102413, China*

[3]*Guangxi Key Laboratory Breeding Base of Nuclear Physics and Technology, Guilin 541004, China*

[4]*School of Science, Huzhou University, Huzhou 313000, China*

[5]*IFIN-HH, 077125 Magurele-Bucharest, Romania*

[6]*National Superconducting Cyclotron Laboratory and Department of Physics and Astronomy, Michigan State University, East Lansing, Michigan 48824*

We have participated in the transport evaluation project (TMEP) of simulations for heavy-ion collisions to study zero-sound propagation due to the nuclear mean-filed potential in a neutron-proton symmetric matter that is enclosed in a periodic box at zero temperature and around normal density [1]. The results of several transport codes belonging to two families (BUU-like and QMD-like) have been compared among each other and to exact calculations. For BUU-like codes that employ the test particle method [2], which include our relativistic Vlasov-Uhling-Ulenbeck (RVUU) model [3,4], the results are found to depend on the combination of the number of test particles and the spread of the profile functions that weight integration over space. It is found that these parameters can be properly adapted to give a good reproduction of the analytical zero-sound features. For QMD-like codes, which are based on the molecular dynamics method firstly developed in Ref. [5], large damping effects are found, and they are attributable to the fluctuations inherent in their phase-space representation. Also, for a given nuclear

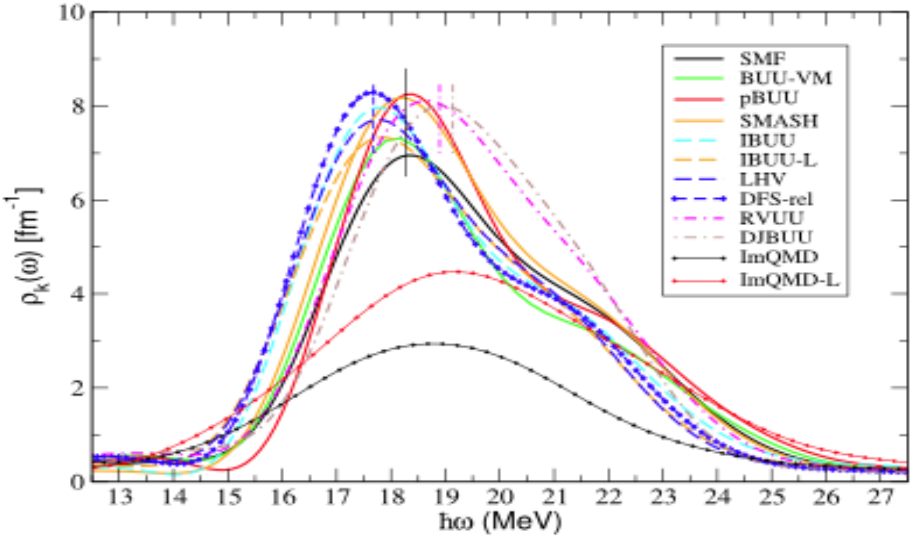

Fig. 1. Response function $\boldsymbol{\rho_k(\omega)}$, i.e., Fourier transform with respect to space and time, of the averaged density distribution from BUU-like and two QMD-like calculations. Results are shown also for DFS calculations with relativistic kinematics. The vertical lines indicate the analytical zero-sound energies for the different code types, downshifted by 2%.

effective interaction, QMD-like codes generally lead to slower density oscillations, as compared to BUU-like codes. The latter problem is mitigated in the more recent lattice formulation of some of the QMD codes as shown in Fig. 1 for the response function $\rho_k(\omega)$, i.e., Fourier transform with respect to space and time, of the averaged density distribution. We have further discussed the significance of these results for the description of real heavy-ion collisions.

[1] M. Colonna, Y.X. Zhang, Y.J. Wang, D, Cozma, P. Danielewicz, C.M. Ko *et al.* (TEMP Collaboration), Phys. Rev. C **104**, 024603 (2021).
[2] G.F. Bertsch and S.D. Gupta, Phys. Rep. **160**, 189 (1988).
[3] C.M. Ko, Q. Li, and R. Wang, Phys. Rev. Lett. **59**, 1084 (1987).
[4] C.M. Ko and Q. Li, Phys. Rev. C **37**, 2270 (1988),
[5] J. Aichelin, Phys. Rept. **202**, 233 (1991).

Elliptic flow splittings in the Polyakov–Nambu–Jona-Lasinio transport model

Wen-Hao Zhou,[1,2] He Liu,[3] Feng Li,[4] Yi-Feng Sun,[5] Jun Xu,[6,1] and Che Ming Ko

[1]*Shanghai Institute of Applied Physics, Chinese Academy of Sciences, Shanghai 201800, China*

[2]*University of Chinese Academy of Sciences, Beijing 100049, China*

[3]*Science School, Qingdao University of Technology, Qingdao 266000, China*

[4]*School of Physical Science and Technology, Lanzhou University, Lanzhou, Gansu, 073000, China*

[5]*Laboratori Nazionali del Sud, INFN-LNS, Via S. Sofia 62, I-95123 Catania, Italy*

[6]*Shanghai Advanced Research Institute, Chinese Academy of Sciences, Shanghai 201210, China*

To incorporate the effect of gluons on the evolution dynamics of the quark matter produced in relativistic heavy-ion collisions, we have extended the three-flavor Nambu–Jona-Lasinio (NJL) transport model to include the contribution from the Polyakov loops [1]. Imbedding the resulting pNJL partonic transport model in an extended multiphase transport (extended AMPT) model [2], we then studied the elliptic flow splittings between particles and their antiparticles in relativistic heavy-ion collisions at beam energy scan energies. We have found that a weak quark vector interaction in the partonic phase is able to describe the elliptic flow splitting between protons and antiprotons measured in heavy-ion collisions at 7.7 to 39GeV [3], as shown in Fig.1. Knowledge of the quark vector interaction is useful for understanding the equation of state of quark matter at large baryon chemical potentials and thus the location of the critical point in the QCD phase diagram.

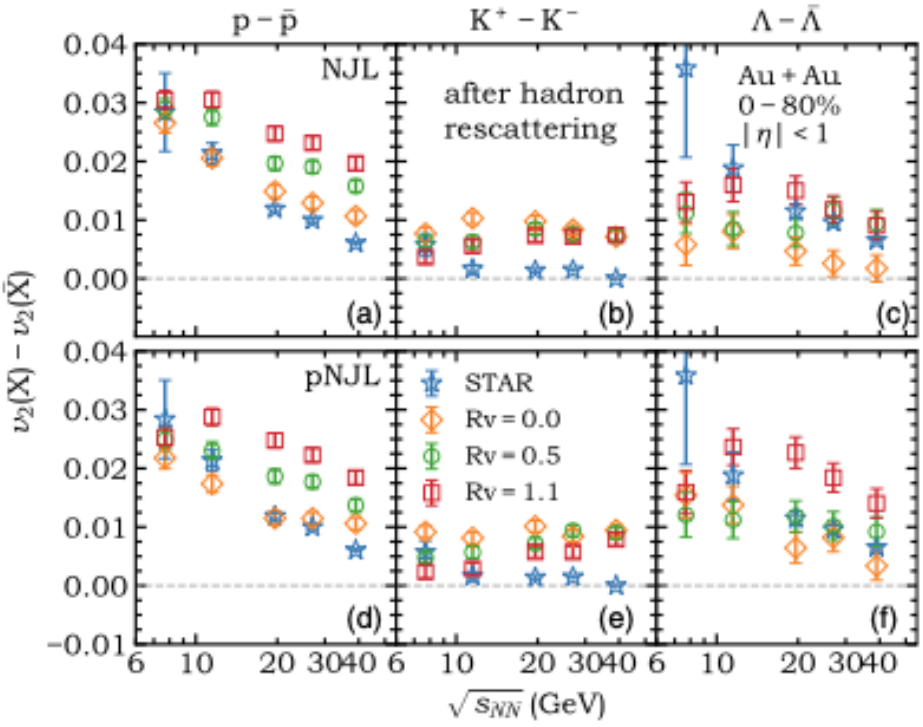

Fig. 1. Difference between the p_T -integrated elliptic flow v_2 of freeze-out nucleons and antinucleons, $\boldsymbol{K}^+$ and $\boldsymbol{K}^-$, and $\boldsymbol{\pi}^+$and $\boldsymbol{\pi}^-$at different collision energies from the extended AMPT model with the partonic phase described by the NJL (upper) or the pNJL (lower) model. Corresponding experimental data are taken from the STAR Collaboration [3].

[1] K. Fukushima, Phys. Lett. B **591**, 277 (2004).
[2] W.H. Zhou, H. Liu, F. Li, Y.F. Sun, J. Xu, and C.M. Ko, Phys. Rev. C **104**, 044901 (2021).
[3] L. Adamczyk *et al.* (STAR Collaboration), Phys. Rev. Lett. **112**, 032302 (2014).

Enhanced yield ratio of light nuclei in heavy ion collisions with a first-order chiral phase transition

Kai-Jia Sun, Che Ming Ko, Feng Li,[1] Jun Xu,[2,3] and Lie-Wen Chen[4]

[1]*School of Physical Science and Technology, Lanzhou University, Lanzhou 073000, Gansu, China*

[2]*Shanghai Advanced Research Institute, Chinese Academy of Sciences, Shanghai 201210, China*

[3]*Shanghai Institute of Applied Physics, Chinese Academy of Sciences, Shanghai 201800, China*

[4]*School of Physics and Astronomy, Shanghai Key Laboratory for Particle Physics and Cosmology, and Key Laboratory for Particle Astrophysics and Cosmology (MOE), Shanghai Jiao Tong University, Shanghai 200240, China*

Using a transport model that includes a first-order chiral phase transition between the partonic and the hadronic matter, we have studied the development of density fluctuations in the matter produced in heavy ion collisions as it undergoes the phase transition, and their time evolution in later hadronic stage of the collisions [1]. With the production of deuterons and tritons described by the coalescence model from nucleons at kinetic freeze out, we have found, as shown in Fig. 1, that the yield ratio N_tN_p/N_d^2, where N_p, N_d, and N_t are, respectively, the proton, deuteron, and triton numbers, is enhanced if the evolution trajectory of the produced matter in the QCD phase diagram passes through the spinodal region of a first-order chiral phase transition. This yield ratio in relativistic heavy ion collisions can thus be used as a signal for a first-order phase transition of produced matter as suggested in Refs. [2,3].

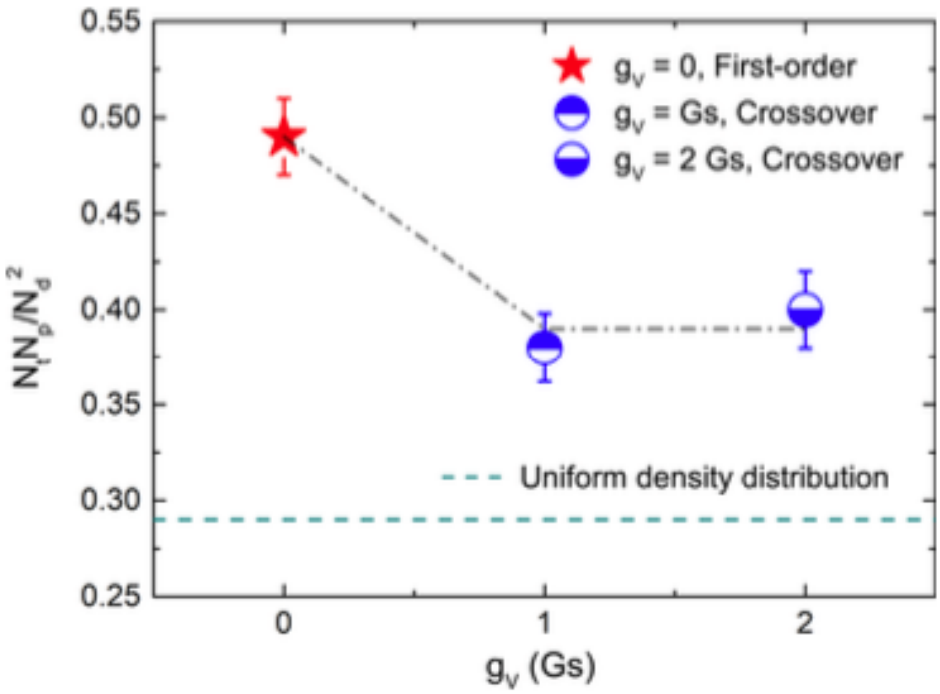

Fig. 1. Yield ratio N_tN_p/N_d^2 of proton (p), deuteron (d), and triton (t) for the case of $g_V = 0$ with a first-order phase transition (solid star) as well as for the cases of $\boldsymbol{g_V = G_S}$ and $\boldsymbol{g_V = 2G_S}$ with a smooth crossover (circles). The dashed line denotes the value of about 0.29 for this ratio when using a uniform density distribution, and the dash-dotted line is for guiding the eye.

[1] K.J. Sun, F. Li, C.M. Ko, and L.W. Chen, Eur. Phys. J. A **57**, 313 (2021).
[2] K.-J. Sun, L.-W. Chen, C.M. Ko, and Z. Xu, Phys. Lett. B **774**, 103 (2017).
[3] K.-J. Sun, L.-W. Chen, C.M. Ko, J. Pu, and Z. Xu, Phys. Lett. B **781**, 499 (2018).

Evolution of Λ polarization in the hadronic phase of heavy-ion collisions

Yifeng Sun,[1,2,3] Zhen Zhang,[4] Che Ming Ko, and Wenbin Zhao[5]

[1]*School of Physics and Astronomy, Shanghai Key Laboratory for Particle Physics and Cosmology, and Key Laboratory for Particle Astrophysics and Cosmology (MOE), Shanghai Jiao Tong University, Shanghai 200240, China*

[2]*Department of Physics and Astronomy, University of Catania, Via S. Sofia 64, 1-95125 Catania, Italy*

[3]*Laboratori Nazionali del Sud, INFN-LNS, Via S. Sofia 62, I-95123 Catania, Italy*

[4]*Sino-French Institute of Nuclear Engineering and Technology, Sun Yat-sen University, Zhuhai 519082, China*

[5]*Department of Physics and Astronomy, Wayne State University, Detroit, Michigan 48201*

Using the AMPT+MUSIC+URQMD hybrid model [1-4], we have studied the global and local spin polarizations of Λ hyperons as functions of the freeze-out temperature of the spin degree of freedom in the hadronic phase of Au+Au collisions at $\sqrt{s_{NN}}$ =19.6 GeV [5]. Including contributions from both the thermal vorticity and thermal shear of the hadronic matter, we have found that with the spin freeze-out temperature dropping from the hadronization temperature of 160 MeV to 110 MeV at the kinetic freeze-

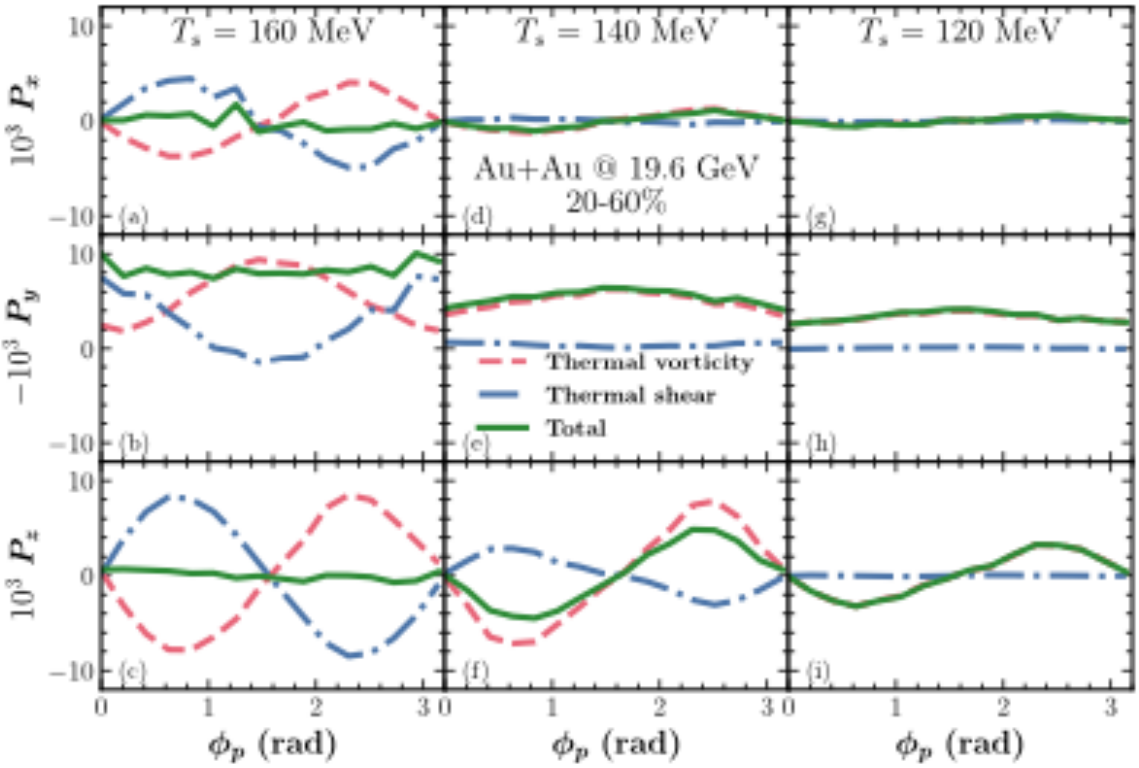

Fig. 1. The azimuthal angle dependence of the local spin polarizations $\boldsymbol{P_x}$, $-\boldsymbol{P_y}$, and $\boldsymbol{P_z}$ of **Λ** hyperons generated by thermal vorticity and thermal shear at the spin freeze-out temperatures $\boldsymbol{T_s}$ =160, 140, and 120 MeV.

out, both the global and local spin polarizations of Λ hyperons due to the thermal vorticity decrease by a factor of 2, while those due to the thermal shear decrease quickly and become negligibly small at 140 MeV, as shown in Fig.1. Our results thus suggest that it is important to consider the evolution of the spin degree of freedom in the hadronic stage of relativistic heavy-ion collisions when theoretically predicted global and local Λ spin polarizations are compared with the experimental measurements.

[1] Z.-W. Lin, C.M. Ko, B.-A. Li, B. Zhang, and S. Pal, Phys. Rev. C **72**, 064901 (2005).
[2] B. Schenke, S. Jeon, and C. Gale, Phys. Rev. Lett. **106**, 042301 (2011).
[3] S.A. Bass *et al.*, Prog. Part. Nucl. Phys. **41**, 255 (1998).
[4] M. Bleicher *et al.*, J. Phys. G: Nucl. Part. Phys. **25**, 1859 (1999).
[5] Y. Sun, Z. Zhang, C.M. Ko, and W. Zhao, Phys. Rev. C **105**, 034911 (2022)

Light nuclei production in a multiphase transport model for relativistic heavy ion collisions

Kai-Jia Sun, Che Ming Ko, and Zi-Wei Lin[1]
[1]*Department of Physics, East Carolina University, Greenville, North Carolina 27858*

Based on an improved multiphase transport (AMPT) model [1,2], which gives a good description of proton production with a smooth quark matter to hadronic matter transition in relativistic heavy ion collisions, we have studied deuteron and triton productions from the coalescence of nucleons at the kinetic freezeout of these collisions. For central Au+Au collisions at center-of-mass energies from 7.7 GeV to 200 GeV available at the Relativistic Heavy Ion Collider (RHIC), we have found that the yield ratio N_tN_p/N_d^2 of proton, deuteron, and triton is a monotonic function of collision energy, as shown in Fig. 1 [3]. Our study confirms the results from similar studies based on different dynamic model, which have

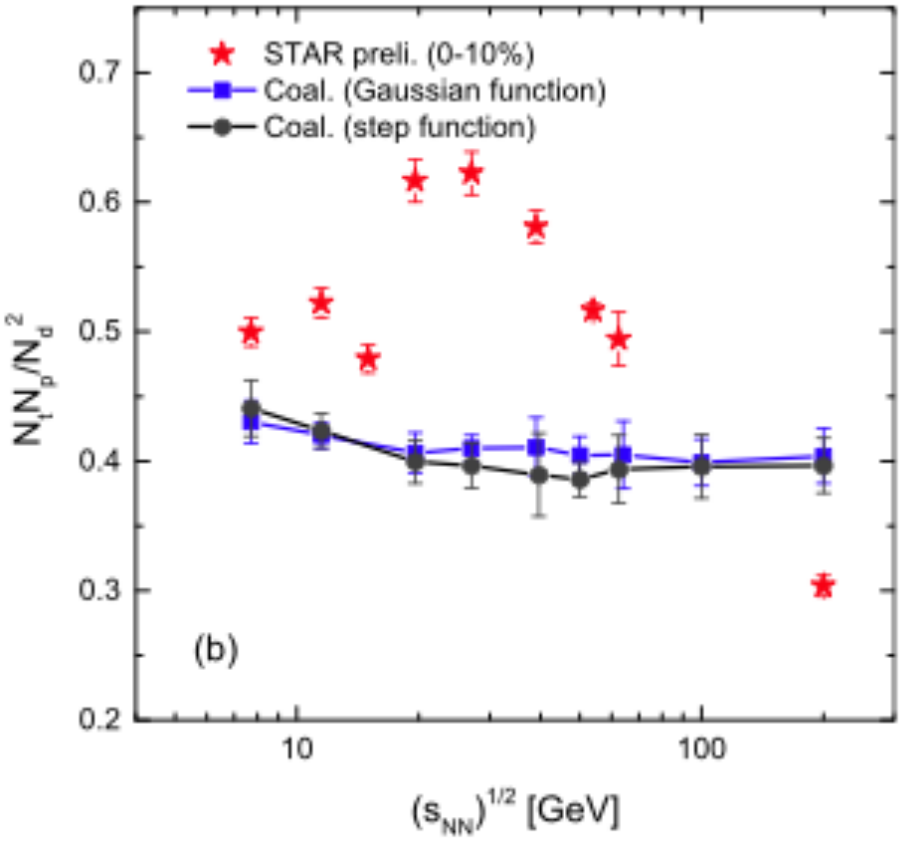

Fig. 1. . The yield ratio N_d/N_p of deuteron to proton and N_t/N_p of triton to proton (left window) as well as the yield ratio N_tN_p/N_d2(right window) as functions of the collision energy in central Au+Au collisions. Results from the AMPT model are denoted by lines with filled squares and circles obtained by using Gaussian and step functions, respectively. The experimental data taken from Refs. [4-6] are shown by solid and open stars after correcting the weak-decay contribution from hyperons to protons [7].

either no phase transition [4] or a crossover transition [5] between the quark-gluon plasma and the hadronic matter, that this yield ratio does not show any nonmonotonic behavior in its collision-energy dependence. The observed nonmonotonic structure of this ratio in the preliminary data from the STAR Collaboration [6-9], shown by stars in Fig. 1, thus indicate that the produced matter might have undergone a first-order phase transition [10,11] or evolved towards a critical point in the QCD phase diagram [12,13].

[1] Z.-W. Lin, C.M. Ko, B.-A. Li, B. Zhang, and S. Pal, Phys. Rev. C **72**, 064901 (2005).
[2] Y. He and Z.-W. Lin, Phys. Rev. C **96**, 014910 (2017).
[3] K.J. Sun, C.M. Ko, and Z.W. Lin, Phys. Rev. C **103**, 064909 (2021).
[4] H. Liu, D. Zhang, S. He, K.-j. Sun, N. Yu, and X. Luo, Phys. Lett. B **805**, 135452 (2020).
[5] W. Zhao, C. Shen, C.M. Ko, Q. Liu, and H. Song, Phys. Rev. C **102**, 044912 (2020).
[6] J. Adam *et al.* (STAR Collaboration), Phys. Rev. C **99**, 064905 (2019).
[7] D. Zhang (for STAR Collaboration), JPS Conf. Proc. **32**, 010069 (2020).
[8] D. Zhang (for STAR Collaboration), Nucl. Phys. **A1005**, 121825 (2020).
[9] L. Adamczyk *et al.* (STAR Collaboration), Phys. Rev. Lett. **121**, 032301 (2018).
[10] K.-J. Sun, L.-W. Chen, C.M. Ko, and Z. Xu, Phys. Lett. B **774**, 103 (2017).
[11] K.-J. Sun, L.-W. Chen, C.M. Ko, J. Pu, and Z. Xu, Phys. Lett. B **781**, 499 (2018).
[12] E. Shuryak and J.M. Torres-Rincon, Phys. Rev. C **100**, 024903 (2019).
[13] E. Shuryak and J.M. Torres-Rincon, Phys. Rev. C **101**, 034914 (2020).

Multiplicity scaling of light nuclei production in relativistic heavy-ion collisions

Wenbin Zhao,[1] Kai-jia Sun, Che Ming Ko, and Xiaofeng Luo[1]
[1]*Department of Physics and State Key Laboratory of Nuclear Physics and Technology, Peking University, Beijing 100871, China*

Using the nucleon coalescence model based on kinetic freeze-out nucleons from the 3D MUSIC+UrQMD [1] and the 2D VISHNU [2] hybrid model with a crossover equation of state, we have studied the multiplicity dependence of deuteron (d) and triton (t) production from central to peripheral Au+Au collisions at $\sqrt{s_{NN}}$ = 7.7, 14.5, 19.6, 27, 39, 62.4 and 200 GeV and Pb+Pb at $\sqrt{s_{NN}}$ = 2.76 TeV [3]. We have found that the ratio N_tN_p/N_d^2 of the proton yield N_p, deuteron yield N_d, and triton yield N_t exhibits a scaling behavior in its multiplicity dependence, i.e., decreasing monotonically with increasing charged-particle multiplicity, as shown in Fig. 1. A similar multiplicity scaling of this ratio is also found in the nucleon coalescence calculation based on kinetic freeze-out nucleons from a multiphase transport (AMPT) model [4]. The scaling behavior of N_tN_p/N_d^2 can be naturally explained by the interplay between

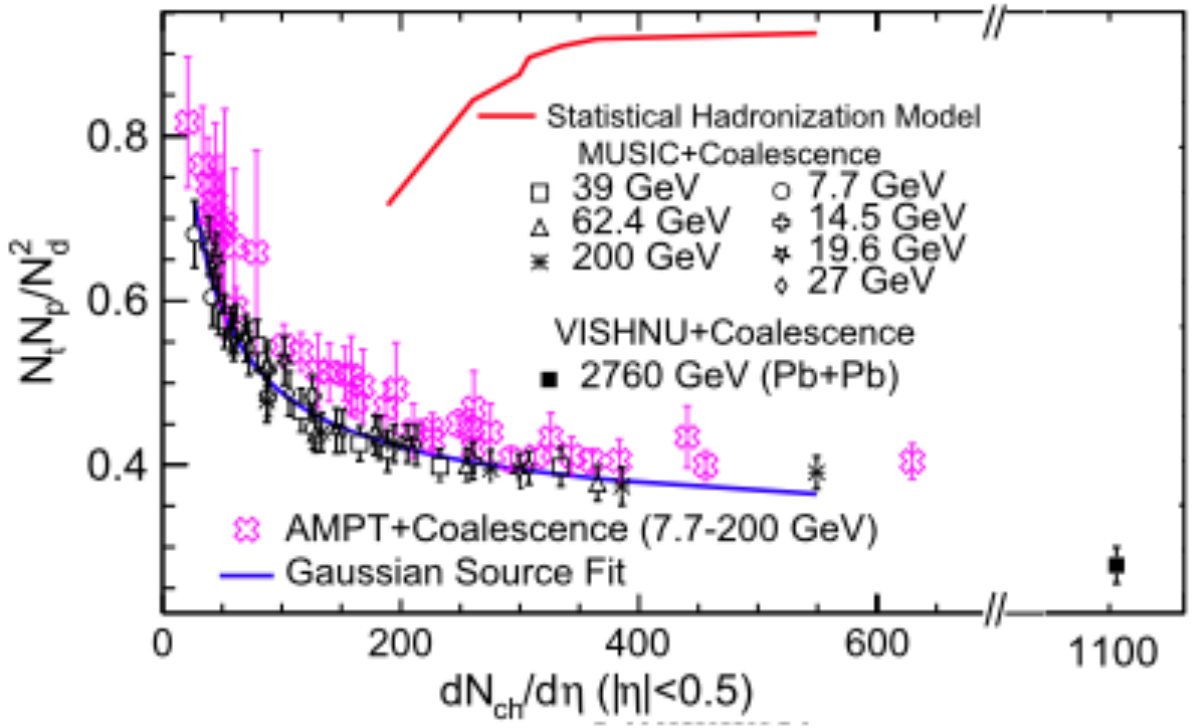

Fig. 1. Multiplicity dependence of the yield ratio N_tN_p/N_d^2 in Au+Au collisions at $\sqrt{s_{NN}}$ = 7.7 - 200 GeV and Pb+Pb collisions at $\sqrt{s_{NN}}$ = 2.76 TeV calculated from the nucleon coalescence model using kinetically freeze-out nucleons from the MUSIC+UrQMD [1], VISHNU [2] and AMPT [4] models, as well as the statistical model that includes only stable nuclei [5]. Also shown by the blue solid line is the result from fitting the results of MUSIC+UrQMD hybrid model with the mutiplication factor p_0 = 0.683 and using the relation R = $0.547(dN_{ch}/d\eta)^{0.331}$ fm between the radius R and the charged particle multiplicity $dN_{ch}/d\eta$ of the nucleon emission source.

the sizes of light nuclei and the nucleon emission source. We further argue that the multiplicity scaling of $N_t N_p / N_d^2$ can be used to validate the production mechanism of light nuclei, and the collision energy dependence of this yield ratio can serve as a baseline in the search for the QCD critical point in relativistic heavy-ion collisions.

[1] C. Shen and S. Alzhrani, Phys. Rev. C **102**, 014909 (2020).

[2] W. Zhao, H.-J. Xu, and H. Song, Eur. Phys. J. C **77,** 645 (2017).

[3] W. Zhao, K.J. Sun, C.M. Ko, and X, Luo, Phys, Lett. B **920**, 136571 (2021).

[4] Z.-W. Lin, C.M. Ko, B.-A. Li, B. Zhang, and S. Pal, Phys. Rev. C **72**, 064901 (2005).

[5] V. Vovchenko, B. Dönigus, B. Kardan, M. Lorenz, and H. Stoecker, Phys. Lett. B **809**, 135746 (2020).

Angular momentum eigenstates of the isotropic 3-D harmonic oscillator: Phase-space distributions and coalescence probabilities

R.J. Fries and C.M. Ko with Michael Kordell

We have computed the probabilities for coalescence of two distinguishable, non-relativistic particles into a bound state described by a isotropic 3-D harmonic oscillator potential [1]. The initial particles are represented by generic wave packets of given average positions and momenta. We have used a phase-space formulation, and to this end we have recalculated the Wigner distribution functions of angular momentum eigenstates for the isotropic 3-dimensional harmonic oscillator. These distribution functions have been discussed in the literature before [2], but we have utilized an alternative approach to obtain these functions. Along the way, we have derived a general formula that expands angular momentum eigenstates in terms of products of 1-dimensional harmonic oscillator eigenstates.

The expansion of quantum mechanical states in terms of angular momentum eigenstates and vice versa is often an important task. For the isotropic harmonic oscillator this expansion does not seem to be readily available in the literature. We have worked out analytic expressions for the expansion of 3-D oscillator eigenstates (k, l, m) with given radial, angular momentum, and magnetic quantum numbers, in terms of products of 1-D harmonic oscillator states given by quantum numbers (n_x, n_y, n_z). The latter are often the preferred eigenstates to deal with the 3D harmonic oscillator due to the large number of results available for the 1-D harmonic oscillator. As an example, for the case $k = 0$, we find the expansion coefficient to be

$$\langle n_x n_y n_z | 0lm \rangle = \sqrt{\frac{(l+m)!\,(l-m)!}{2^{2l} n_x!\, n_y!\, n_z!\, (2k+2l-1)!}}\, 2^{n_z} i^{n_y} \binom{n_y}{\kappa}\, {}_2F_1(-\kappa, -n_x; 1-\kappa+n_y; -1)$$

where $\kappa = (l + m - n_z)/2$, and ${}_2F_1$ is a hypergeometric function.

The Wigner distributions $W_{kl}(\boldsymbol{r}, \boldsymbol{q})$, for harmonic oscillator states (k, l) averaged over the magnetic quantum number m, are then straight forward to compute from the well-known counterparts in 1-D. Due to the symmetries of the system they only depend on the magnitudes r and q, and on the angle θ between position and momentum vectors $\boldsymbol{r}$ and $\boldsymbol{q}$. See Fig. 1 for an example.

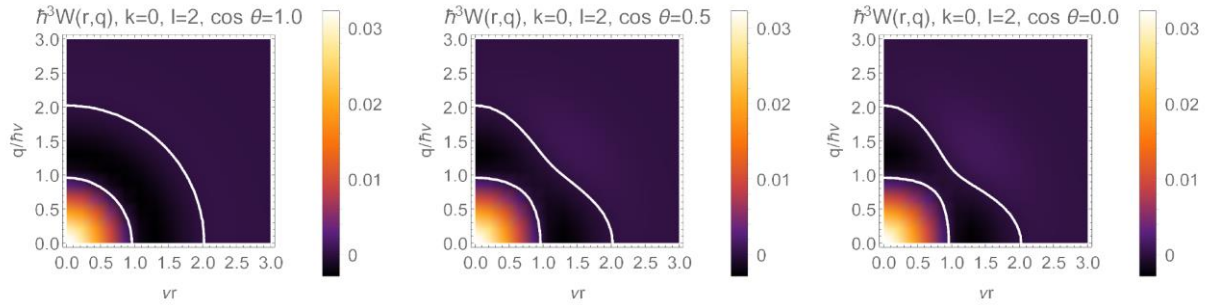

Fig. 1. Wigner distributions $\boldsymbol{W_{kl}(r, q)}$, for the harmonic oscillator state $(\boldsymbol{k = 0, l = 2})$ for three values of the angle $\boldsymbol{\theta}$, as a function of the dimensionless phase space coordinates $\boldsymbol{\nu r}$ and $\boldsymbol{q/\nu\hbar}$, where $\boldsymbol{1/\nu}$ is the typical length scale of the harmonic oscillator. White lines indicate nodal lines of vanishing $\boldsymbol{W_{02}}$.

Finally, we have computed the probabilities of two particles, described quantum mechanically by wave packets, to form a bound state through an isotropic 3-D harmonic oscillator potential between them. We make minimal assumptions about the wave packets, choosing them to be Gaussian and isotropic. The final probabilities $P_{kl}(\boldsymbol{r},\boldsymbol{p})$ for forming a bound state with quantum numbers (k,l) are expressed in terms of the relative center coordinates of the wave packets in phase space, $\boldsymbol{r}$ and $\boldsymbol{p}$. For example, in the simplest case[1]

$$P_{10} = \frac{1}{2}e^{-v}\left(\frac{1}{3}v^2 - \frac{1}{3}t\right)$$

for $k = 1,\ l = 0,$ where $v = (v^2r^2 + p^2/v^2\hbar^2)/2$ and $t = (r^2p^2 - (\boldsymbol{r}\cdot\boldsymbol{p})^2)/\hbar^2$. Since $t = L^2/\hbar^2$, where L is the classical angular momentum of the wave packet centroids, one can clearly correlate the initial angular momentum of the 2-quark system with the probabilities to form particular orbital angular momentum states l. See Fig. 2 for an example.

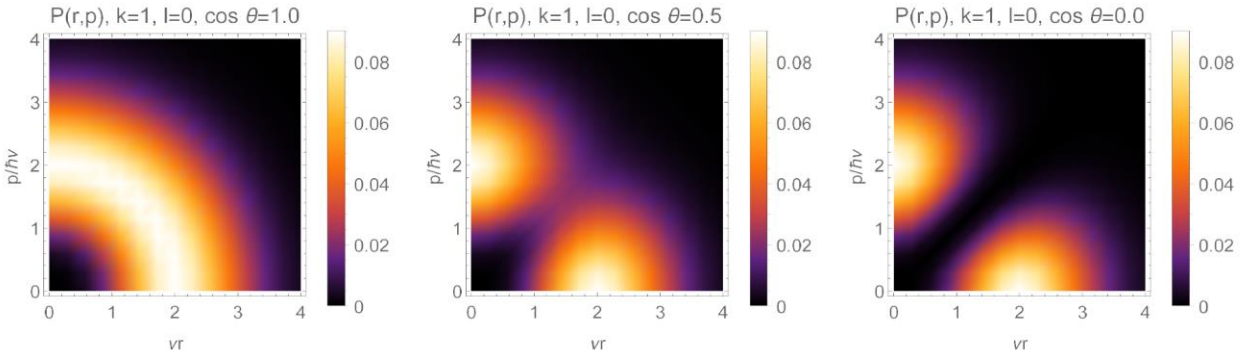

Fig. 2. Probability densities $\boldsymbol{P_{kl}(r,p)}$ to form bound states in a harmonic oscillator state $(\boldsymbol{k=1, l=0})$ for three values of the angle $\boldsymbol{\theta}$ between the relative position vector $\boldsymbol{r}$ and the relative momentum vector $\boldsymbol{p}$ of the two wave packets, as a function of the dimensionless phase space coordinates $\boldsymbol{vr}$ and $\boldsymbol{p/v\hbar}$. As a radially excited state, which is not orbital angular momentum excited, smaller values of $\boldsymbol{\theta}$ are preferred for $(\boldsymbol{k=1, l=0})$.

Work is under way to apply this formalism to the coalescence of quarks into ground state, excited, and highly excited meson states.

[1] M. Kordell II, R.J. Fries and C.M. Ko, arXiv: 2112.12269, Annals of Physics (Accepted).
[2] S. Shlomo and M. Prakash, Nucl. Phys. **A357**, 157 (1981).

[1] This refers to the fact that results are simplest if the widths of the particle wave packets and the harmonic oscillator potential are in a certain relation [1].

The JETSCAPE collaboration: X-Scape and more JETSCAPE physics

R.J. Fries, Michael Kordell, Arjun Sengupta, Cameron Parker, and JETSCAPE Collaborators

In previous versions of this report we have discussed the inception and successful launch of the JETSCAPE collaboration and their product, a flexible and modular event generator that simulates collisions of nuclei at very high energies [1]. JETSCAPE stands for *Jet Energy-loss Tomography with a Statistically and Computationally Advanced Program Envelope*. Its initial funding consisted of $3.6M from the *Software Infrastructure for Sustained Innovation* (SI2) program of the U.S. National Science Foundation. The collaboration involves theoretical and experimental physicists, computer scientists, and statisticians at various institutions around the U.S. R.J. Fries has been a PI on this project from the first minute. In 2020 the NSF has approved the *X-Scape* project as the follow-up project for the JETSCAPE collaboration with total funding of $4M. The X-Scape project will build on the existing software framework and make it more comprehensive and powerful. The new project will allow users to simulate lower energy nuclear collisions as well as proton-nucleus and electron-nucleus collisions. Thus X-Scape will offer much needed capabilities to support experiments at the Electron-Ion Collider, the next-generation nuclear physics experiment planned by D.o.E. at Brookhaven National Laboratory for 2030 and beyond. The new project has also added more institutions and PIs to the project. Fig. 1 shows a schematic flow diagram for the X-Scape framework.

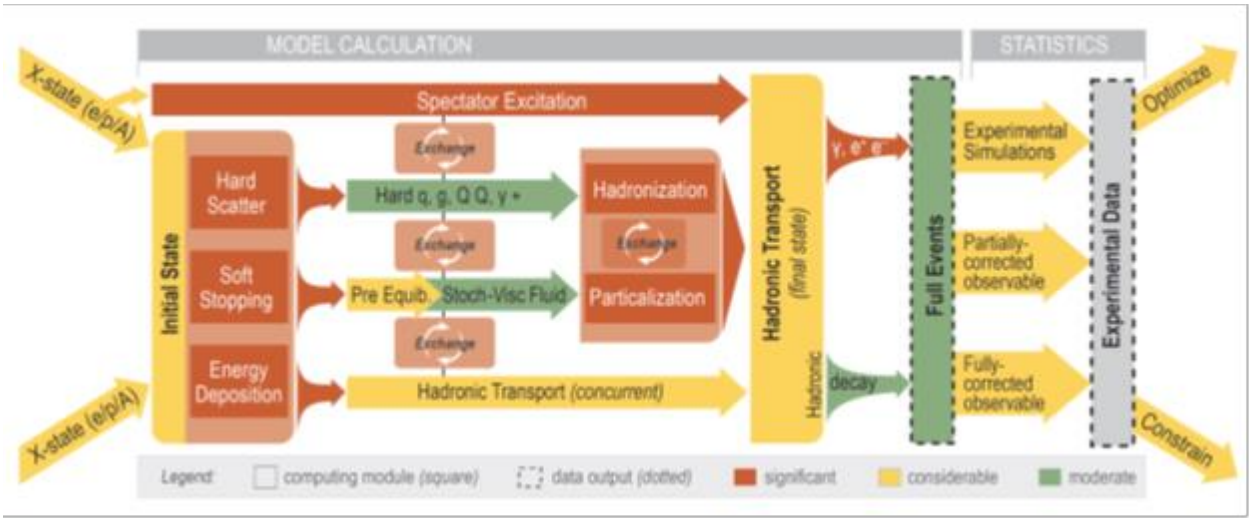

Fig. 1. Schematic Flow Diagram of the X-Scape event generator that will be able to simulate p+p, p+A, A+A, e+p and e+A collisions at high energies.

The first year of X-Scape work has seen major upgrades to the framework. A new clock was implemented that allows the framework to run backwards in time if needed, a feature that will be used to implement initial state radiation. Such an initial state radiation module, as well as a more flexible bulk dynamics manager, to allow for several different ways of computing soft background physics, have been added.

The group at Texas A&M University has continued improvements to hadronization in the JETSCAPE framework, in particular for the Hybrid Hadronization module. This includes a more robust determination of space-time information for hadrons, which is necessary to feed output from hadronization into hadronic transport models, like SMASH. The tuning of Hybrid Hadronization in vacuum was improved by including identified hadron data from both $e^+ + e^-$ and $p + p$ collisions in the pertinent determination of parameters through Bayesian inference. The effects of transverse flow on jets and their hadronization was studied and found to drag soft and intermediate momentum jet hadrons along while high momentum hadrons remain unaffected.

[1] The JETSCAPE 3.0 package, https://github.com/JETSCAPE

Collectivity of J/ψ mesons in heavy-ion collisions

M. He, B. Wu, and R. Rapp

Quarkonia - bound states of a heavy quark and antiquark - are excellent probes of the in-medium QCD force in ultrarelativistic heavy-ion collisions (URHICs). While bottomonia are increasingly suppressed when the collision energy and centrality rises, the production of J/ψ mesons is significantly enhanced in 5.02 TeV Pb-Pb at the Large Hadron Collider (LHC), relative to 0.2 TeV Au-Au collisions at the Relativistic Heavy-Ion Collider (RHIC). Since the higher energy densities reached at the LHC lead to a stronger suppression of the primordially produced J/ψ mesons relative to RHIC conditions, the enhancement is believed to be caused by a recombination of copiously produced charm and anticharm quarks in the hot QCD medium [1]. The implementation of this mechanism into kinetic transport models enables a comprehensive description of the collision energy and centrality, and momentum dependence of J/ψ observables at SPS, RHIC and the LHC [2,3], and recently also correctly predicted ψ (2S) observables at the LHC.

However, measurements of the elliptic flow (v_2) of J/ ψ mesons at the LHC are not well described by existing calculations of J/ ψ recombination for transverse momenta $p_T > 4$ GeV. Here, we revisit these calculations in two main aspects [4]. Employing the resonance recombination model (RRM) [5], we implement distribution functions of charm quarks transported through the quark-gluon plasma using state-of-the-art Langevin simulations and account for the space-momentum correlations (SMCs) of the diffusing charm and anti-charm quarks in a hydrodynamically expanding fireball [6]. This turns out extends the relevance of the recombination processes to substantially larger momenta than before. We also revisit the suppression of primordially produced J/ψ's by propagating them through the same hydrodynamic medium, leading to a marked increase of their v_2 over previous estimates. Combining these

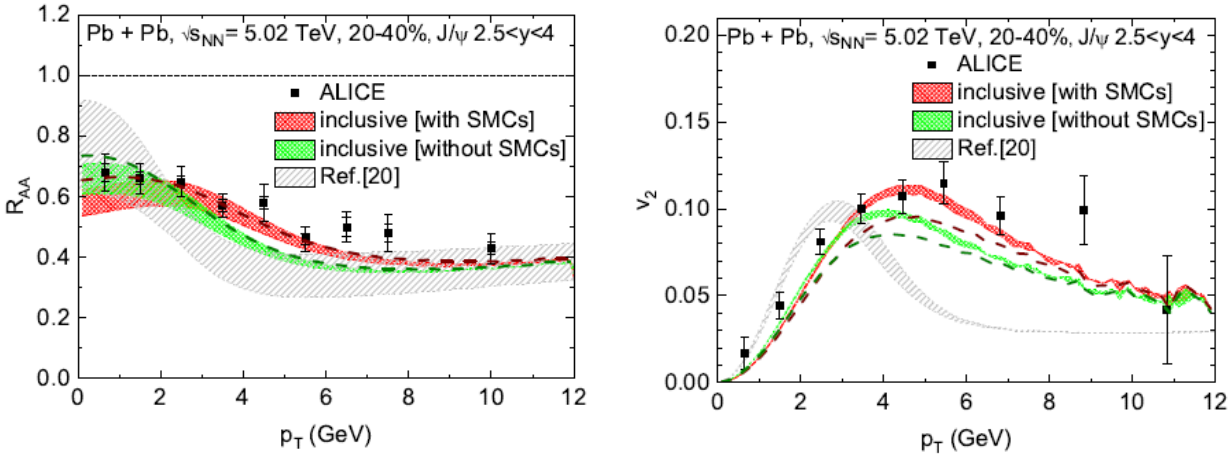

Fig. 1. Inclusive-J/ψ R_{AA} (left) and v_2 (right) in Pb-Pb collisions at the LHC, compared to ALICE data [7]. The red (green) bands employ c-quark spectra in RRM evaluated with(out) SMCs (the widths reflect a 15-25% charm and charmonium shadowing range). The dashed lines are for an earlier production time, with 15% shadowing (brown (dark-green): with(out) SMCs). Inclusive results from previous calculations [1] (grey bands) are shown for comparison.

developments into a calculation of the p_T-dependent nuclear modification factor (R_{AA}) and v_2 of inclusive J/ψ production in semi-central Pb-Pb collisions at the LHC, we find a good description of the experimental results by the ALICE collaboration [7], see Fig. 1. Our results resolve the above-mentioned v_2 puzzle and imply the relevance of recombination processes for up to $p_T \sim 8$ GeV.

[1] X. Zhao and R. Rapp, Nucl. Phys. **A859**, 114 (2011).

[2] R. Rapp and X. Du, Nucl. Phys. **A967**, 216 (2017).

[3] M. He, H. van Hees, and R. Rapp, Prog. Part. Nucl. Phys (Submitted); e-print arXiv:2204.09299.

[4] M. He, B. Wu, and R. Rapp, Phys. Rev. Lett. **128**, 162301 (2022).

[5] L. Ravagli and R. Rapp, Phys. Lett. B **655**, 126 (2007).

[6] M. He and R. Rapp, Phys. Rev. Lett. **124**, 042301 (2020).

[7] S. Acharya *et al.* (ALICE Collabration), J. High Energy Phys. **02**, 041 (2020); J. High Energy Phys. **10**, 141 (2020).

Recombination of B_c-mesons in ultra-relativistic havy-ion collisions

Biaogang Wu, Zhanduo Tang, Min He, and Ralf Rapp

The B_c meson, a bound state of *b*-quark and *c*-antiquark, has been proposed as a valuable alternative probe of the Quark Gluon Plasma (QGP) in ultra-relativistic heavy-ion collisions (URHICs) [1], relative to the more "traditional" quarkonia of charm-anticharm and bottom-antibottom quarks. The binding characteristics specific to the B_c, as well as its regeneration through the recombination of a bottom and a charm quark, offer independent tests of their melting via the screening of the heavy-quark potential in the QGP and the kinetics of regeneration processes at lower temperatures [2]. Pioneering data [3] of B_c production in URHICs indicate an enhancement relative to expectations from pp collisions.

We employ the TAMU kinetic transport model [4-6] to compute the time evolution of B_c yields in a QGP fireball in Pb-Pb collisions at the LHC, accounting for both primordial and regeneration components [7]. The in-medium binding energies are taken from in-medium T-matrix calculations of B_c spectral functions in a strongly coupled QGP [8] with a potential constrained by thermal lattice-QCD data, cf. Left panel of Fig. 1. Utilizing inelastic rates and equilibrium limits based on previously determined quasifree processes and heavy-quark fugacities, respectively, we predict the centrality and transverse-momentum (p_T) dependence of inclusive B_c production including feed-down contributions from excited states, see middle and right panels of Fig. 1.

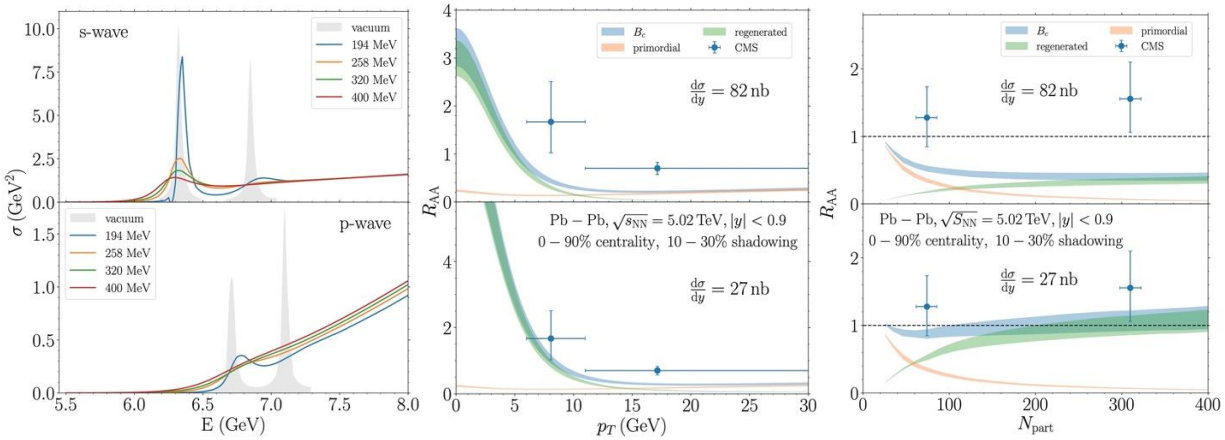

Fig. 1. Left panels: vacuum (gray band) and in-medium (solid lines) B_c spectral functions in the S- (upper panel) and P-wave (lower panel) channels (the vacuum masses are in fair agreement with experiment). Middle and right panel: p_T- and centrality-dependent nuclear modification factor, $R_{AA} = N_{Bc}^{AA} / N_{coll} N_{Bc}^{pp}$, of $\mathbf{B_c}$ production in minimum bias Pb-Pb (5 TeV) collisions, compared to CMS data (blue dots) [3]; shown are the primordial (orange lines) and regeneration (green lines) contributions, as well as their sum (blue lines; the bands represent the uncertainty in the nuclear shadowing of open-charm production); the upper (lower) panels are based on a B_c production cross section of $d\sigma^{pp}/dy = \mathbf{27}$ (82) nb figuring in the denominator of the R_{AA}. The centrality dependence in the right panels is for B_c mesons with a $p_T > 6$ GeV cut.

Our results suggest that the inclusive Bc yiled in semi-/central Pb-Pb collisions is dominated by regeneration processes, while the precise value if the RAA depends on the input cross section from pp collision figuring in the denominator, which currently has a large uncertainty. The transverse-momentum

and centrality dependence of the RAA from our calculation describe the experimental data better for smaller values of the cross section as shown in the lower middle and right panels.

[1] M. Schroedter, R.L. Thews, and J. Rafelski, Phys. Rev. C **62**, 024905 (2000).
[2] R. Rapp, D. Blaschke, and P. Crochet, Prog. Part. Nucl. Phys. **65**, 209 (2010).
[3] CMS Collaboration, Tech. Rep., CERN, Geneva (2021), https://cds. cern.ch/record/2767048.
[4] L. Grandchamp, R. Rapp, and G.E. Brown, Phys. Rev. Lett. **92**, 212301 (2004).
[5] X. Zhao and R. Rapp, Nucl. Phys. **A859**, 114 (2011).
[6] X. Du, R. Rapp, and M. He, Phys. Rev. C **96**, 054901 (2017).
[7] B. Wu, Z. Tang, M. He, and R. Rapp, in preparation (2022).
[8] S.Y.F. Liu and R. Rapp, Phys. Rev. C **97**, 034918 (2018).

Thermalization of nuclear matter in heavy-ion collisions at Fermi energies

T. Onyango, A. Bonasera, and R. Rapp

Heavy-ion collisions (HICs) are widely used to produce and analyze the properties of nuclear matter under various conditions of temperature and baryon density. The nuclear fireballs created in these reactions are governed by strong nuclear interactions and have been observed to reach local thermal equilibrium at ultra-relativistic bombarding energies [1]. Thermalization of the nuclear medium is not as clear, however, at lower energies, $E_{lab} < 1$ A•GeV [2]. In this work [3], we investigate nuclear matter as produced in HICs at low beam energies, i.e., $E_{lab} = 35$ MeV/A.

Toward this end, we employ transport simulations of central ^{40}Ca+^{40}Ca collisions using the Constrained Molecular Dynamics (CoMD) approach [4]. Specifically, we extract the isospin, position, and momentum of all nucleons during the collisions and perform a coarse-graining procedure [5,6] where the center of the collision is partitioned into eight cubic cells adjacent to the origin, each of volume 8 fm^3. In each cell the 3-momenta of the nucleons are binned to provide localized momentum distributions that we fit with a thermal ansatz, allowing, however, for off-equilibrium features. It turns out that the distributions in the transverse (x- and y-) directions are amenable to thermal fits (cf. Fig. 1 left), with Fermi distributions performing much better than Boltzmann ones, a consequence of the Pauli blocking implemented in CoMD. However, along the z-axis (beam axis) off-equilibrium features are apparent, most notably the centroid motion of the two incoming nuclei and a slight narrowing of the distributions relative to the temperatures extracted from the transverse direction, which we account for by a superposition of two momentum-shifted distributions (cf. Fig. 1 right).

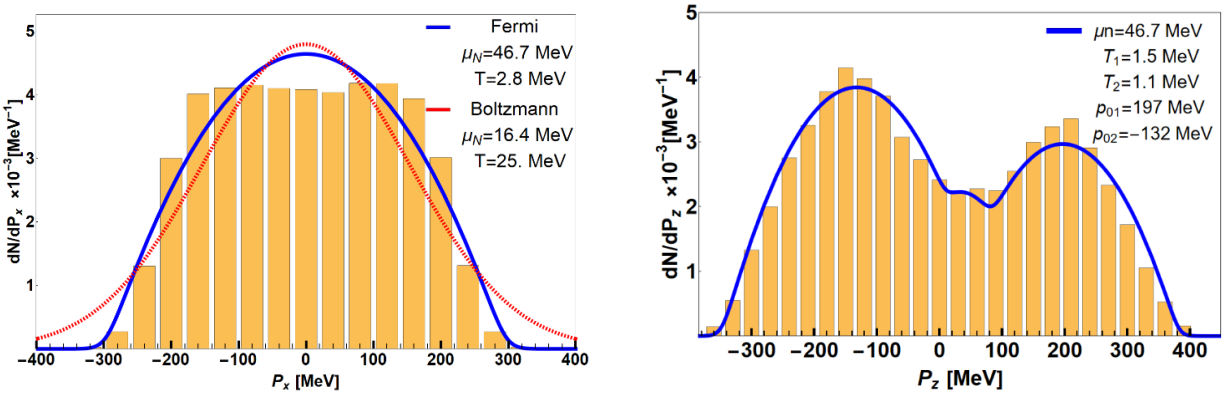

Fig. 1. Left panel: Our fits using Fermi (blue lines) or Boltzmann distributions (red dotted line) for the transverse-momentum distributions in the x-direction (left panel) compared to the CoMD transport output (orange histogram) at 65 fm/c (corresponding to maximal density). Right panel: Comparison of the Fermi fit function for the longitudinal momentum distributions (blues line) with centroid motion (characterized by parameters $p_{01,02}$) to the transport output (orange histogram) at 65 fm/c. The nuclei (when treated as classical spheres) begin to touch at t≈44 fm/c, and full overlap of the two nuclei happens at t≈77 fm/c.

From the parameterized Fermi distributions, the time evolution of the fitted parameters can be extracted, cf. Fig. 2. Initially, most of the kinetic energy of the nucleons is contained in the form of the incoming motion of the nuclei. Shortly after the initial impact, this “directed” energy starts to dissipate

Fig.

into “random” kinetic energy, and the nuclear medium starts to rapidly heat up. This process is completed at about 150 fm/c after initial impact at which point the temperature essentially plateaus. Our analysis thus gives a novel insight about the timescale of thermalization in Fermi energy nuclear collisions, made possible by the implementation of off-equilibrium effects in the longitudinal direction, as well as employing substantially smaller coarse-graining volumes than in previous extractions of thermodynamic parameters at these energies [7,8].

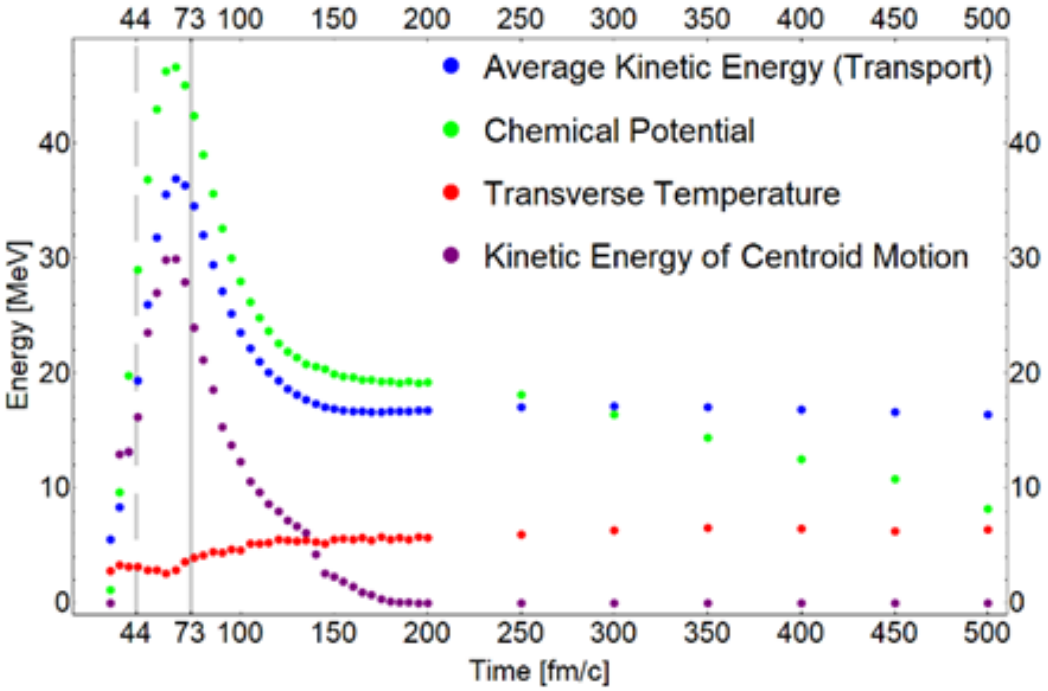

Fig. 2. Time evolution of thermodynamic properties of nuclear matter extracted from the collision center of CoMD transport simulations of 35 A·MeV ^{40}Ca +^{40}Ca collisions: average total kinetic energy (blue dots), nucleon chemical potential (green dots) and temperature (red dots) from fits of the transverse-momentum spectra, and the kinetic energy of the motion of the two centroids in the longitudinal direction (purple dots). The vertical dashed and solid lines indicate when the nuclei first touch and fully overlap, respectively.

In summary, by employing a coarse-graining procedure to CoMD transport simulations of nuclear collisions at Fermi energies, we have been able to fit thermal distribution functions to nucleon transverse-momentum spectra. Upon implementing off-equilibrium effects to account for motion of the incoming nuclear centroids, we have also achieved a fair description of the p_z dependence of the distribution functions. The time evolution of the extracted parameters for temperature, chemical potential and nuclear-centroid momenta enabled to systematically track the conversion of the incoming longitudinal energy into thermal motion. We also plan to utilize the distributions for an analysis of photon spectra using a field-theoretic calculation of local emission rates.

[1] R. Stock Editor, *Relativistic Heavy Ion Physics*, Landolt-Boernstein - Group I Elementary Particles, Nuclei and Atoms (Springer), vol. **23** (2010).

[2] M. Colonna, Prog. Part. Nucl. Phys. **113**, 103775 (2020).

[3] T. Onyango, A. Bonasera, and R. Rapp, Nucl. Phys. A. **1022**, 122426 (2022).
[4] M. Papa, G. Giuliani, and A. Bonasera, J. Comput. Phys. **208**, 403 (2005).
[5] P. Huovinen, M. Belkacem, P. Ellis, and J.I. Kapusta, Phys. Rev. C **66**, 014903 (2002).
[6] T. Galatyuk, P.M. Hohler, R. Rapp, F. Seck, and J. Stroth, Eur. Phys. J. A **52**, 131 (2016).
[7] C. Zhou, Y.G. Ma, D. Fang, and G. Zhang, Phys. Rev. C **88**, 024604 (2013).
[8] H.L. Liu, Y.G. Ma, A. Bonasera, X.G. Deng, O. Lopez, and M. Veselský, Phys. Rev. C **96**, 064604 (2017).

SECTION IV

SUPERCONDUCTING CYCLOTRON, INSTRUMENTATION AND RIB UPGRADE

K500 operations and development

D.P. May, G.J. Kim, B.T. Roeder, H.L. Clark, G. Tabacaru, and F.P. Abegglen

Introduction

During the 2021-2022 reporting period a total of 19 different beams, including 8 newly developed beams, were used for experiments, and there were a total of 22 beam tunings for these experiments. The SEE program and the radioactive-beam effort are treated separately in this progress report.

Ion Sources

Three new beams were run using sputtering. Our standard method for producing silicon beams has been to flow the highly explosive gas, silane, into the ion source. A new method, suggested by personnel of the LBL 88" cyclotron lab [1], has now been tested here. A silicon rod of 99.9% enriched ^{28}Si and separately a silicon rod of 90% enriched ^{30}Si were mounted on the rod feed for ECR4 and sputtered into the source. It was found that nitrogen was more stable than oxygen as a support gas for silicon sputtering, possibly because the silicon oxidizes easily. The sputtering voltage ranged from 1.0 to 1.5 kV. In addition a rod of natural ytterbium was used to produce beams of several of the ytterbium isotopes via sputtering into ECR4. The sputtering voltage ranged from 0.9 to 2.5 kV depending on the need for intensity of each isotope.

During this reporting period the ECR1 ion source was dismounted from its position next to ECR4 and repaired by replacing its plasma chamber. The new aluminum chamber had already been fabricated along with the chamber for ECR4 and the new NdFeB permanent magnet bars acquired. All that remained was to install the copper, water-cooling lines in the chamber and then insert the magnet bars. The source was remounted on the K500 injection line along ECR4, but it has yet to be completely reassembled with microwave and gas injection due to the x-ray danger of working close to ECR4 while it is running. However, the source could quickly be brought to operation if required.

Cyclotron Beams

New beams of ^{12}C at 35 AMeV, ^{14}N at 18.5 AMeV, ^{28}Si at 35 AMeV, ^{30}Si at 35 AMeV, ^{83}Kr at 15 AMeV, ^{170}Yb, ^{174}Yb, and ^{176}Yb all at 7 AMeV, and ^{197}Au at 8.7 AMeV were developed for experiments.

Operations

For the period April 1, 2021 through March 31, 2022, the operational time is summarized in Table I, while Table II lists how the scheduled time was divided. Unscheduled maintenance decreased back to a normal level from the last period. Scheduled time for outsider users, exclusively SEE customers increased substantially from the last reporting period.

Table I. 2021-2022 Operational Time.

Time	**Hrs**	**%Time**
Beam on Target	6246.5	71.5
Beam Development	77.5	0.9
Scheduled Maintenance	1696	19.4
Unscheduled Maintenance	716	8.2
Total	8736	100

Table II. 2020-2021 Scheduled Beam Time.

Time	**Hrs**	**%Time**
Nuclear Physics	1414.5	22.4
Nuclear Chemistry	952	15.0
Outside Collaboration	0	0
Outside Users	3880	61.4
Beam Development	77.5	1.2
Total	6324	100

[1] Janilee Benitez, private communication

K150 operations and development

G.J. Kim, B.T. Roeder, F. Abegglen, H.L. Clark, L. Gathings, D.P. May, and H. Peeler

We had a busy year operating the K150 cyclotron. For the reporting period we logged over 5600 hours of beam-on-target and 1192 hours for beam developments. Included in the beam-on-target time was 5108 hours (3608 for physics and 1500 for chemistry) for in-house science experiments, and 308 hours for the SEE tests and 184 hours for the LLNL experimentsas shown in Table I.

Table 1. 2021-2022 operational time.

Time	Hours	% Time
Beam on target	5600	64
Beam development	1192	14
Scheduled maintenance	1260	14
Unscheduled maintenance	684	8
Total	8736	100

The active users of the K150 beams were: LIG (ran 8 times and used 10 to 35 MeV proton beams), Folden group (ran six times and used mostly 6.3 AMeV $^{40}Ar^{11+}$ beam), Rogachev and Yennello groups, and the SEE testers, who used proton beams as well as heavy ion beams.

The LLNL group re-mounted their Hyperion setup to the NeutronBall Line, squeezing into the area between downstream of the neutron ball and the beam dump. The final beam focus was provided with the quad doublet 3 m upsteam of their setup, keeping the drift length from the final focal element to the target the same when the experiment was mounted on the Ion Interaction Line. The two quads were already installed previously just downsteam of the neutron ball to quiet the background events on the neutron ball by guiding the outgoing beam particles to the beam dump before hitting the long beam pipe to the beam dump. The effectiveness of the two quads in quieting the background events was not clear, however. The focusing scheme for the Hyperion experiment was to bring the beam point-to-parallel through the long neutron ball section using the two upstream quads, and then use the final two quads to focus the beam onto the Hyperion target. The focusing scheme did deliver the beam clean enough that, in the summer and fall of 2021 the LLNL and the CENTAUR groups were able to complete their experiments using 21 MeV and 27 MeV proton beams.

The usage of the deflector-extracted low-intensity proton beams increased this year. A deflector extracted 2 MeV proton beam was obtained with the main magnet at 186 A, which is the lowest magnetic field for any beam from K150. However the extraction efficiency was poor, and later a slightly higher 3.8 MeV proton beam at 256 A on the main magnet, which had a little better extraction efficiency, was used for an experiment. (Previously the lowest field beam was the 3.4 MeV proton beam produced at 252 A on the main magnet; it used an H^- beam and then strip extracted.) We also extracted 15 and 35 MeV proton beams through the deflector for SEE users, when they also wanted to test with heavy ion beams.

Regarding the heavy ion SEE beams, we wanted to add a few beams heavier than the ^{78}Kr near the 15 AMeV energy. A tiny amount of $^{90}Zr^{31+}$ beam at 15 AMeV was produced for JPL in Feb. 2022, but was deemed too weak, and instead 13 AMeV $^{90}Zr^{29+}$ was extracted and used by the SEE tester. We also worked to accelerate $^{107}Ag^{31+}$ and $^{124}Xe^{36+}$ beams at 11 AMeV, and tiny amounts were extracted and identified using a total energy detector. The search for these very heavy particles was aided by a small improvement from the ECR2 source (discussed elsewhere in this progress report), and as well as vacuum improvement on the cyclotron. With five (two 8" and three 10") cryopumps running on the cyclotron, the vacuum has improved to around 8×10^{-7} torr (without cooling the internal cryopanel). The latest modification to the source has been a 45% increase in the magnetic field with the installation of a slightly bigger and heavier, low carbon (1008) steel plug and a new 1.5" diameter and 0.39" thick bias steel disk at the front of the source. The disk was fabricated from the same low carbon steel used for the steel plug, instead of aluminum that we have used in the past.

Eight times throughout the year we provided intense 7.2 AMeV $^{4}He^{1+}$ beams for the 211 astatine production program (from 209 bismuth targets). The record for the highest beam intensity was 16 μA, and in general 8 to 12 μA was available to the astatine production program throughout the year. With intense beam currents, the frequent deflector sparking has been a problem, but it was getting better as the deflector septum and high voltage electrode positions (and consequently the deflector gap width) were adjusted to find the optimal position to run the deflector.

We wanted to investigate if we could take advantage of the low emittance output from the H^- source to inject $^{4}He^{1+}$ beam more efficiently into the cyclotron. We did verify that the H^- source could produce $^{4}He^{1+}$, and we managed to extract a small amount, less than 0.1 μA, on FC02 in May 2021. After changing the injection geometry and adjusting the permanent magnets internal to the source to convert from the H^- operation to H^+, the extracted current of 5 μA was obtained in Feb. 2022. Obviously much more work is needed to increase the beam intensity, as we can already get up to 16 μA from using the ECR2 ion source. In particular the beam injection into the cyclotron seems to need more work. However as both H^+ and He^{1+} are injected together, the true injection efficiency is unclear. Looking at injecting H^+ beam alone (it was accelerated to 20 AMeV and then extracted through the deflector), the injection was about 29% and the extraction was 42%, for the overall throughput of 12%. Compare to the H^- beams, which at various times showed much higher injection efficiency into the cyclotron, from 50 to 80%, which we assumed is due to the small emittance from the H^- source, the 29% injection efficiency for H^+ must be improved.

Texas A&M Cyclotron radiation effects facility
April 1, 2021 – March 31, 2022

H.L. Clark, G. Avila, V. Horvat, B. Hyman, M. Kennas, G.J. Kim, H. Park, C. Parker, R. Rinderknecht, B. Roeder, and G. Tabacaru

The activity of the Radiation Effects Facility (REF) increased significantly from last year and was the second highest reported year ever. In this reporting period, the facility was used for 3,852 hours, which is a 17% increase over the low reporting hours of 2020-2021 due to the ongoing travel restrictions of the COVID-19 pandemic. Users of the facility (and hours used) over the past year were: Northrop

Table I. Radiation Effects Facility usage by commercial and government customers for this and previous reporting years.

Reporting Year	Total Hours	Commercial Hours (%)	Government Hours (%)
2021-2022	3,852	3,122 (81%)	730 (19%)
2020-2021	3,300	2,435 (74%)	865 (26%)
2019-2020	3,982	2,862 (72%)	1120 (28%)
2018-2019	3,678	2,939 (80%)	739 (20%)
2017-2018	3,681	2,622 (71%)	1,059 (29%)
2016-2017	3,355	2,501 (75%)	854 (25%)
2015-2016	3,042	2,326 (76%)	716 (24%)
2014-2015	3,024	1,975 (65%)	1,049 (35%)
2013-2014	2,399	1,517 (63%)	882 (37%)
2012-2013	2,626	1,856 (71%)	770 (29%)
2011-2012	2,673	1,630 (61%)	1,043 (39%)
2010-2011	3,042	1,922 (63%)	1,121 (37%)
2009-2010	2,551	1,692 (66%)	859 (34%)
2008-2009	2,600	1,828 (70%)	772 (30%)
2007-2008	2,373	1,482 (62%)	891 (38%)
2006-2007	2,498	1,608 (64%)	890 (36%)
2005-2006	2,314	1,314 (57%)	1,000 (43%)
2004-2005	2,012	1,421 (71%)	591 (29%)
2003-2004	1,474	785 (53%)	689 (47%)
2002-2003	1,851	1,242 (67%)	609 (33%)
2001-2002	1,327	757 (57%)	570 (43%)
2000-2001	1,500	941 (63%)	559 (37%)
1999-2000	548	418 (76%)	131 (24%)
1998-1999	389	171 (44%)	218 (56%)
1997-1998	434	210 (48%)	224 (52%)
1996-1997	560	276 (49%)	284 (51%)
1995-1996	141	58 (41%)	83 (59%)

Grumman (429), Boeing Corp. (275), Texas Instruments (254), Raytheon (239), RTS (217), Infineon (181), Renesas (173), Sandia Nat Lab (168), Navy Crane (152), VPT Inc (151.5), NASA JPL (119), Honeywell (115), Air Force (106), SEAKR (104), Amazon (93), Draper (72), Blue Origin (68.5), Space X (64), Cobham (56), Vanderbilt (48), Axiom Space (48), BAE Systems (48), Millennium (48), Intel (46), Fifth Gait (40), NASA GSFC (36), BroadCom (32), L3Harris (32), Lockheed Martin (32), Microchip (32), Crane AE (31), Utah State (28), NASA JSC (24), Analog Devices (24), General Dynamics (24), Troxel Engineering (24), DRS (20), Johns Hopkins (16), SMU (16), Avalanche (16), Ball Aerospace (16), GSI Technology (16), Intuitive Machines (16), Smiths Interconnect (16), T2 Research (16), TruVentic (13), TAMU Physics (9), TAMU EE (8), Cisco (8), EPC Space LLC (8), MOOG (8), mPower Tech (8), NanoSperse (8). NanoSperse and TruVentic were the only new users.

Table I compares the facility usage by commercial and government customers. While commercial hours still dominate, the ratio from this reporting year (81% to 19%) is similar to usage from previous reporting periods (see Fig 1). Commercial usage increased by 28% and was the highest commercial usage ever. Government usage decreased by 16% and was the lowest usage since the 2004 – 2005 reporting period. This was mostly due to the ongoing travel restrictions of the COVID-19 pandemic. The 15 MeV/u ions were the most utilized and especially 15 MeV/u Au, until the K500 cyclotron RF system had failures in December. Then 24.8 MeV/u Xe was the highest ion in demand. No new beams were added to the K500 cyclotron SEELine users list. Much of the testing conducted at the facility continues to be for

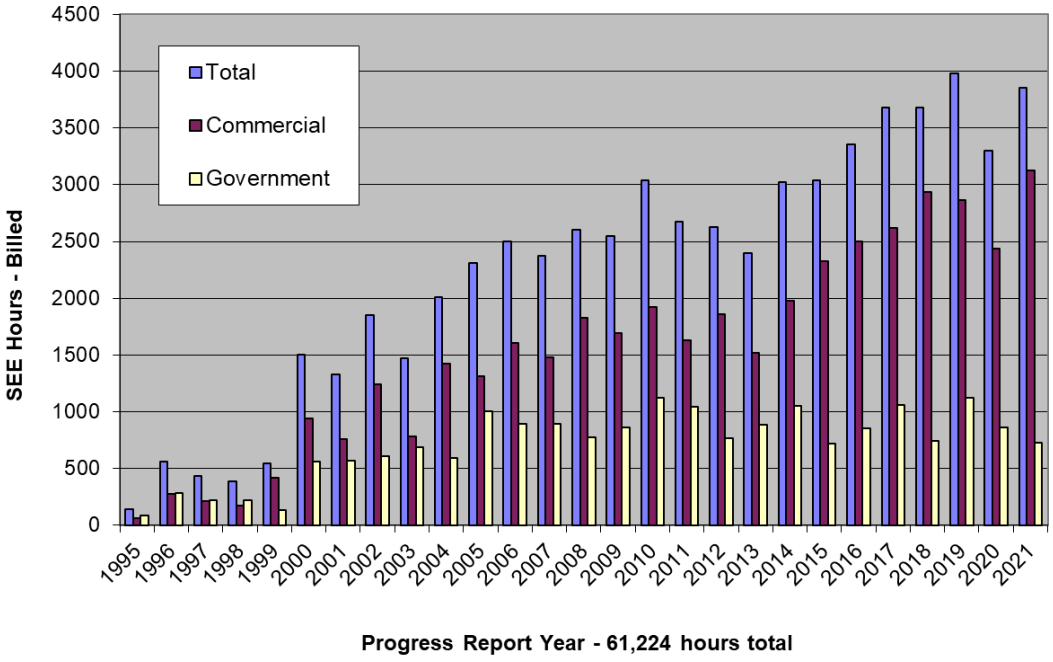

Fig. 1. Radiation Effects Facility usage by commercial and government customers for this and previous reporting years. While commercial hours still dominate, the ratio from this reporting year (81% to 19%) is similar compared to usage from prior reporting period. Usage hours increased to the second higher amount in history. 61,224 hours have been provided since the start of the project in 1995.

defense systems by both government and commercial agencies. We had no foreign users at the facility as a consequence of COVID-19 travel restrictions.

Upgrading the ECR2 magnetic field profile

D.P. May, S. Molitor, H. Peeler, F.P. Abegglen, G.J. Kim, and B.T. Roeder

In 1996 the ECR2 ion source was originally constructed with the discarded copper plasma chamber containing the original samarium-cobalt permanent-magnet hexapole from ECR1. When the ECR2 ion source was upgraded from a 6.4 GHz ECRIS used exclusively for beams of light elements such as lithium to then operate at 14.5 GHz microwave injection, the upgrade was modelled after some features of the successful AECR-U ion source at LBL but retained features of the 6.4 GHz source, e. g. much larger volume than AECR-U and the existing copper axial coils. A new aluminum plasma chamber with NdFeB permanent magnets and a steel injection plug with large slots appropriate for injection of both 14.5 GHz and 6.4 GHz microwave injection were constructed, and higher-power coil power supplies were purchased. One plan was that 6.4 GHz could be used in addition to 14.5 GHz for two-frequency operation. This idea of added 6.4 GHz injection was not successful, and ECR2 has not shown the performance of AECR-U. A study has been made of upgrade possibilities, and some of these have been implemented.

Upgrading the 14 GHz ECR2 ion source necessarily involves increasing the magnetic fields that contain the plasma. It has been shown by experiments with superconducting ECR ion sources that certain fields are optimum in obtaining plasma containment and stability along with the best performance. At the injection end of the source the magnetic field at the position of the biased plate should ideally be at least three times the resonance field, and according to some results intensities of high charge states continue to go up as this factor increases to 4.5. (For the state-of-the-art 18 GHz sources this factor is 3.9.) The pole strength of the hexapole at the radius of the plasma chamber should be approximately double that of the resonance field. The field at the plasma electrode at extraction should be slightly less than the hexapole strength, but somewhat variable depending on whether the extraction of the highest charge-states or the highest intensity of medium charge-states is desirable. The opinion on what the minimum field at the center of the plasma should be varies. BMIN equal to 75% of BECR has been quoted, but many sources function below this, and high BMIN leads to high x-ray flux. For 14.5 GHz, BECR = 0.517 T, so BINJ ≈ 2.0 T, BRAD (wall) ≈ 1.0 T and BMIN ≈ 0.39 T should lead to the best performance.

POISSON calculations showed how BINJ for ECR2 could be substantially raised with a steel injection plug with smaller slots and with a steel internal biased disk. The slots in the original ECR2 steel plug were modelled with stacking factors included along the outer radii. This may not be entirely accurate, but it does result in lowering the calculated injection field of the original plug by almost 0.2 T. Table 1 compares the fields reported for AECR-U with the calculated fields for the original plug and with the present calculated fields for ECR2. This table mainly shows that BINJ for ECR2 has been raised by about 45% into a range above that for BINJ for AECR-U.

Table I. Comparison of the axial magnetic fields of AECR-U and ECR2.

	AECR-U (1997)	ECR2 500 A (2002)	ECR2 w/steel 0.19" biased disc	ECR2 w/ Steel biased disc and new plug
B_{INJ} max (typical)	1.7 T (1.5 T)	1.28 T	1.59 T	1.85 T
B_{MIN} max	0.4 T	0.35 T	0.353 T	0.356 T
B_{EXT} max (typical)	1.0 T (0.9 T)	0.90 T	0.90 T	0.90 T

The effect of increasing BINJ has not been definitively measured due to pressure to use the source for K150 operation. However, some results have been encouraging. In cyclotron operation, the beam has seemed to be more stable, and in the observation of very low-intensity, high-charge-state ions extracted from the cyclotron, higher charge-states have been enhanced specifically for silver, xenon, and zirconium [1].

With new permanent magnets, the ECR2 hexapole can have larger magnetic fields at the position of the flutes, which lie along the poles of the hexapole, at the expense of smaller fields between the poles. Table 2 gives some fields as reported by LBNL for the 14 GHz AECR-U [2] and as calculated here for ECR2 with PANDIRA. The BRAD at the wall for ECR2 was calculated using the BR and HC measured by the vendor for the NdFeB magnets, UGIMAG. The geometry was somewhat simplified in that the grooves along the sides of the magnets were not included. A measurement of 0.757 T average at the wall was reported when the hex was first assembled here, in good agreement with the calculation when the addition of the grooves and the thickness of the Hall probe are considered.

Table II. Comparison of the hexapolar magnetic fields at the plasma-chamber wall on the poles for AECR-U and ECR2.

	AECR-U	ECR2 original
B_{RAD} (wall)	0.85 T	0.79 T

The AECR-U used 14 and 10 GHz (BECR = 0.50 and 0.36 T, respectively) when these fields were reported. The reported running fields were BINJ = 15 T and BEXT = 0.9 T.

The magnetic axes of the blocks in the ECR2 hex are oriented by an angle of 30° to the radial with each side of a bar having magnetic axis oriented 60° with respect to the axis of the other side of the bar. If the same magnetic material would be used as before with axes oriented 50° to the radial (one side 100° from the other in each bar) stronger pole fields would result but also weaker field between the poles. The inner diameter of the ECR2 plasma chamber is 5.124". These calculations use the original BR=13200 and HC= -12500 are summarized in Table III. Somewhat higher grade materials are available today.

Table III. Comparison of the ECR2 hexapolar magnetic fields with different orientations of the magnetic axis of the NdFeB.

	30°, R=2.562"	30°, R=2.50"	50°, R=2.562"	50°, R=2.50"
Pole	0.792 Tesla	0.745 T	0.954 T	0.886 T
Between Poles	0.657 T	0.654 T	0.592 T	0.60 T

The 50° case results in a 17% increase in pole strength. Fairly recently the KVI cyclotron lab increased the magnetic field pole strength for their AECR-U source from 0.72 Tesla to 0.87 Tesla by such a strategy. The angle to the radial of the magnetic axis for the new hex is 60° (Fig. 1). KVI has reported a ten-fold increase in 129Xe33+ and two more observable high-charge-states even though their 14 GHz transmitter was operating at 500 watts for the new results and 800 watts for the old [3}. Privately, KVI has reported that they had eventually doubled the production of 129Xe35+ just before the failure of their transmitter [4].

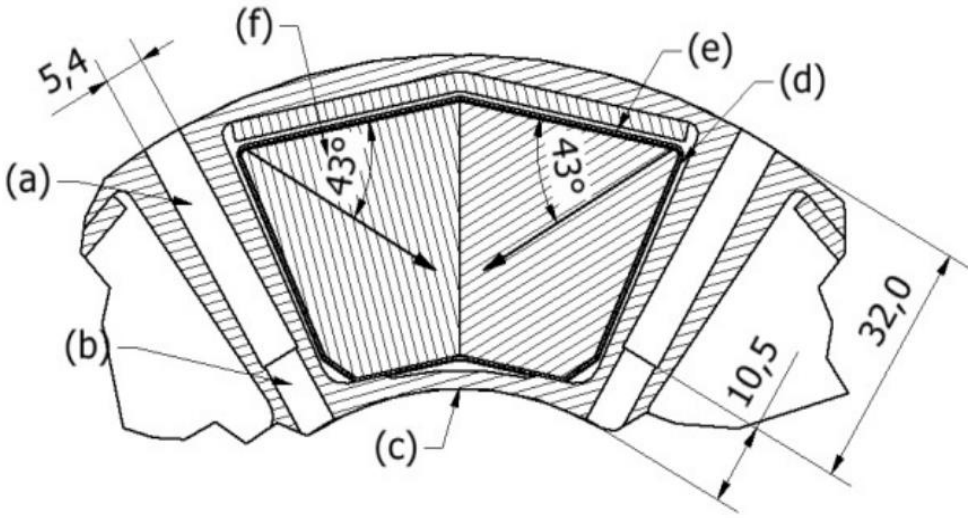

Fig. 1. The KVI permanent-magnet bars. The 43° angle of magnetization measured from the outer face translates into a 60° angle with respect to the radial direction.

The change in angle does affect the forces on the permanent-magnet bars. Using the FORCE application on the PANDIRA files gives a slightly smaller radially inward force of 2 X 21.54 lbs/in (990 lbs for a 23 in long bar) for the 50° case compared with 2 X 24.53 lbs/in (1128 lbs for a 23" bar) for the 30° case . The total radial pressure is 16.1 psi for the 50° case down from 18.3 for the 30° case. The force pushing apart the two halves of a bar, well apart from the other bars, is 56.6 lbs/in (1300 lbs for the 23" bar) for the 50° case as compared to 36.9 lbs/in (850 lbs) for the 30° case. As the six bars are inserted into their slots in the plasma chamber, the azimuthal force builds up to a maximum 141 lbs/in for 50° compared to a maximum of 134 lbs/in for 30°. In short, the radial pressure on the plasma chamber due to the bars decreases by 12% while the azimuthal force on the pinning of the bars increases by 5%. After the bars are seated this azimuthal force is shared by the structure of the plasma chamber.

At present a study is being made of the construction of a new aluminum plasma chamber although the existing plasma chamber is adequate to accommodating new NdFeB bars.

[1] B.T. Roeder *et al., Progress in Research*, Cyclotron Institute, Texas A&M University (2021-2022), p. IV-60.

[2] Z.Q. Xie and C.M. Lyneis. Proceedings of the 13th International Workshop on ECR Ion Sources, College Station, Texas, 1997, p. 16.

[3] H.R. Kremers *et al.*, Proceedings of the 23rd International Workshop on ECR Ion Sources, Catania, Italy, 2018, p. 125
[4] H.R. Kremers, private communication

Recent progress on the light ion guide project

G. Tabacaru, V. Kolhinen, J. Ärje, D.P. May, A. Saastamoinen, F.P. Abegglen, L.N. Gathings, G.J. Kim, S. Molitor, and B.T. Roeder

The Light Ion Guide Project continued to be developed at our facility. After the change of the design as described in the previous report [1], extensive off-line testing was performed using the heated alkali source with elements rubidium (Rb) and cesium (Cs). The long (approximately 2.5 m) RF-only sextupole is difficult to resonate and several resonating circuits were tweaked to get the maximum performance of the ion transport.

The next phase was to use a proton beam and test the performance of the system. Conflicting schedule and minor setbacks related with the set-up, made the advancement of the project slow. However, one major accomplishment was to re-accelerate radioactive products from a natural zirconium target produced by a proton beam, in particular ^{89}Nb. More details about this accomplishment are explained in another contribution in the current Progress Report.

The scientific interest for these relatively heavy system is low inside our community. Working towards improvement of production of radioactive products from lighter systems is needed. One particular system of interest is p+^{26}Mg to make the radioactive product ^{26}Al. The calculated cross-section is 328 mbarn at 9 MeV proton beam energy. It is well known that the charge breeding of light elements is more complicated, with low efficiency compared with the charge-breeding of heavy elements (mass 60 and higher). First we wanted to test the production and transport of ^{26}Al from the gas cell into the CB-ECRIS. A silicon detector (PIPS - Canberra) was mounted inside the plasma chamber and the radioactive products were collected on a thin aluminum foil mounted in front of the detector. The electrons coming from the decay of the metastable state ($T_{1/2}$=6.3 s) were detected and a counts vs. time graph was recorded (Fig. 1).

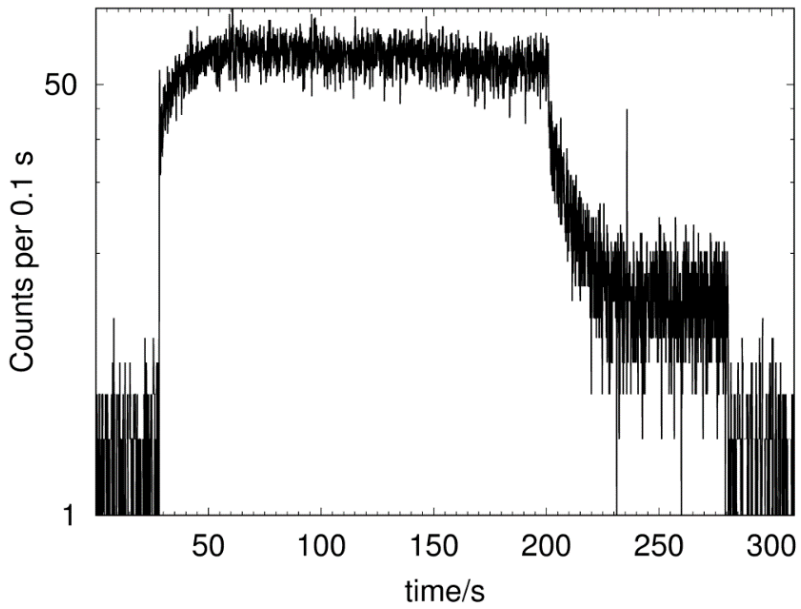

Fig. 1. Graph of counts vs. time for ^{26}Al. The flat part is the production rate and the sharp decrease corresponds to the decay of the product.

The estimated production was 600 ions/s/micro-ampere of beam current. The magnesium target used was natural, but if an enriched target would have been used, the production should increase by a factor of 10. The charge breeding of this product was not successful, triggering another set of tests to determine the problem. More work needs to be done in this direction in order to achieve the maximum charge breeding efficiency.

[1] G. Tabacaru *et al.*, *Progress in Research*, Cyclotron Institute, Texas A&M University (2020-2021), p. V-9.

Response to the proposed new requirements for radiation testing

V. Horvat

New government regulations may soon be put in place, requiring that all silicon-based devices to be used in long space-flight missions pass radiation tests at the linear energy transfer (LET) of 75 MeV·cm^2/mg, according to the recommendations from the Aerospace corporation [1]. The Cyclotron Institute's Radiation Testing Facility (also referred to as SEE-line) offers several beams that can meet this requirement. However, only a few of them can be used at normal incidence. Measurements at incidence angles θ other than zero degrees are optional for these beams, but for the other beam candidates they are necessary in order to qualify.

Since LET values change as the beam penetrates the substrate, the quantity of interest here is the depth interval Δz over which the effective LET value (L_e) is greater than or equal to 75 (in the standard units specified above). Another relevant quantity may be L_e^{max}, the maximum value of L_e reached within the depth interval Δz.

The results presented here are obtained under the assumption that the beam passes through a 1 mil thick aramica window and 3 cm of air before hitting a bare silicon substrate. If under these conditions the value of L_e at the surface of the substrate at normal incidence is less than 75, it is assumed that aluminum degraders (and/or some other layers of material) are set so that the value of L_e at the surface of the substrate is exactly 75.

For each beam and for each incidence angle the effective LET as a function of depth must be calculated in order to determine the corresponding value of Δz. Results of these calculations, obtained using our SEUSS software [2], are shown in Fig. 1 for the case of 15 MeV/u ^{165}Ho beam at normal

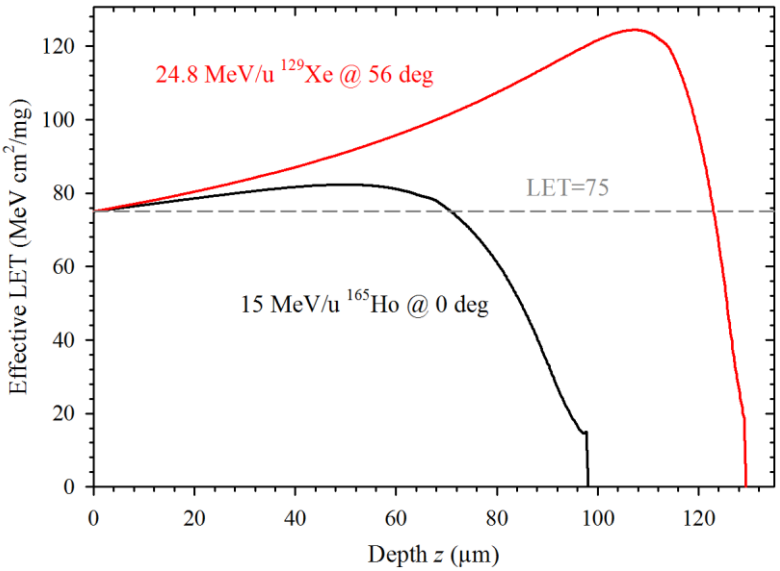

Fig. 1. Effective LET in silicon plotted against the penetration depth, for two of the standard beams used in radiation effects testing at the Cyclotron Institute. The effective LET values are expressed in the standard units of MeV·cm^2/mg. For the holmium beam it was assumed that the beam energy is slightly reduced so that the effective LET value at the surface of the substrate equals 75.

incidence and for the case of 24.8 MeV/u ^{129}Xe beam at $\theta = 56^{o}$. From these results we find that for the holmium beam $\Delta z = 71$ μm and $L_e^{max} = 82$, while for the xenon beam $\Delta z = 120$ μm and $L_e^{max} = 124$.

Table I shows the values of Δz and L_e^{max} for the standard SEE-line beams that can be used at normal incidence. Note that L_e of the gold beam at the surface of the substrate is greater than 75 and that it can be lowered only by increasing the beam energy, which is not a viable option. Therefore, any additional dead layers present above the surface of the substrate and any increased air gap would reduce the listed value of Δz.

Table I. Depth interval (Δz) in which the LET values stay at or above 75 and the maximum LET value within that interval (L_e^{max}), for the standard SEE-line beams at normal incidence. Note that for the ^{197}Au beam the LET value at the surface of the substrate is 83, exceeding the value of 75.

Beam	Δz (μm)	L_e^{max} (MeV·cm^2/mg)
15 MeV/u ^{165}Ho	71	82
15 MeV/u ^{181}Ta	94	88
15 MeV/u ^{197}Au	98	94

Table II shows the corresponding results for these and other beams used at angles θ such that the value of Δz is maximized. In the general case, provided that L_e at the surface of the substrate at normal incidence (L_o) is less than 75, $\theta = \cos^{-1}(L_o/75)$. Otherwise, the best solution corresponds to $\theta = 0$. The listed value of Δz is reduced if any additional dead layers are present above the surface of the substrate and/or the air gap is increased. Consequently, if L_B is the value of L_e at the Bragg peak, then $L_e^{max} = L_B / \cos\theta = 75\ L_B / L_o$.

Table II. Depth interval (Δz) in which the effective LET values stay at or above 75 and the maximum effective LET value within that interval (L_e^{max}), for the standard SEE-line beams at the angle of incidence θ that maximizes Δz, provided that θ does not exceed 60°.

Beam	θ (deg)	Δz (μm)	L_e^{max} (MeV·cm^2/mg)
15 MeV/u ^{109}Ag	53	56	99
15 MeV/u ^{129}Xe	41	67	93
15 MeV/u ^{141}Pr	35	70	87
15 MeV/u ^{165}Ho	15	85	85
15 MeV/u ^{181}Ta	4	95	88
15 MeV/u ^{197}Au	0	98	94
25 MeV/u ^{129}Xe	56	120	124

[1] G. Johnson-Roth, Aerospace Report No. TOR-2011(8591)-21, pp. 14; https://s3vi.ndc.nasa.gov .
[2] https://cyclotron.tamu.edu/vladimir/SeussW-Download.htm .

Status of the Radiation effects master's program: Using an SRAM based dosimeter to measure LET, fluence, and beam uniformity

R. Rinderknecht, L.E. Henderson, H.L. Clark, C.A. Gagliardi, C.E. Parker, and R. Gallegos

While the concept of using heavy ion induced single event upsets (SEU) in Static Random Access Memories (SRAM) to measure beam characteristics is nothing new, our facility has lacked such a device. Through collaboration with NASA Goddard and JPL, we have been commissioned to build such a device as a basis for a thesis in the Radiation Effects Master's Program.

This device is composed of three components: a PCB containing four delidded SRAMs, an FPGA/ SoC combo to control the SRAMs, and a computer with a simple serial terminal installed. The concept is shown in Fig. 1.

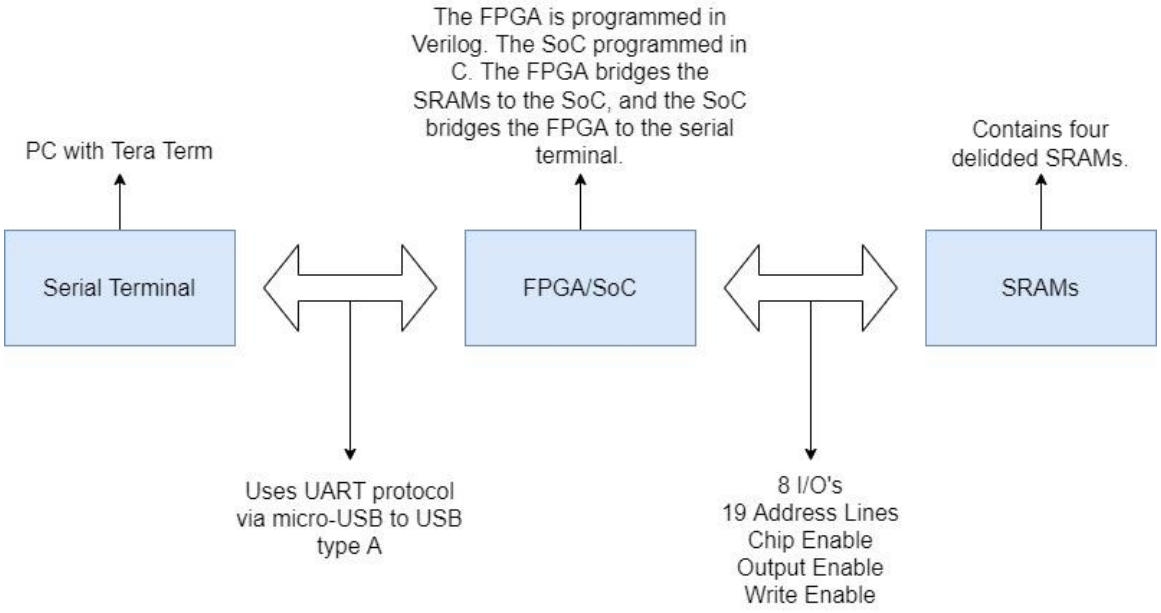

Fig. 1. Diagram detailing the dosimeter operation.

The device was tested as part of the Radiation Effects Boot camp held at the Cyclotron Institute in February 2022. 9.2 MeV/u ^{78}Kr and 13.6 MeV/u ^{14}N were delivered from the K150 cyclotron to test the cross-section[1] as a function of effective linear energy transfer (LET). Tilting the device allowed us to increase the effective LET, effectively allowing us to measure multiple LETs with the same beam. Preliminary data gathered on one of JPL's preexisting boards controlled by an FPGA/SoC programmed with our code closely matched previous results, as shown in Fig. 2.

[1] Cross-section here is defined as the number of bit errors per unit fluence.

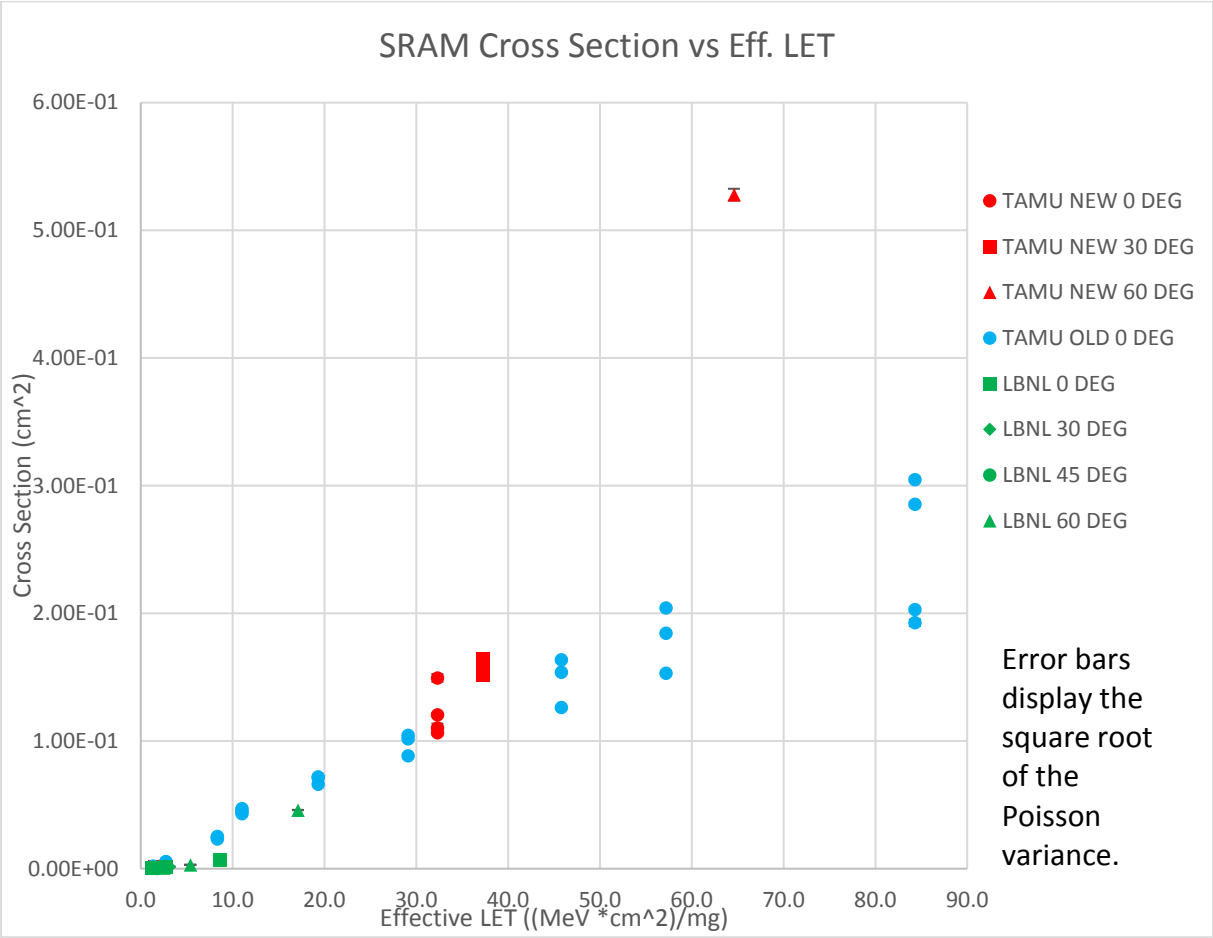

Fig. 2. Cross Section vs. LET. Data was recorded both on the K150 and at LBNL.

Our next step is to build a board in house using the cyclotron's new PCB fabrication equipment, as described in a separate paper.[2] Imaged in Fig. 3 is a rendering of the proposed design.

Once constructed, the plan is to characterize a variety of beam species, looking at variations of total bit upset and multiple bit upset (MBU) cross sections in response to differences in spatial location, effective LET, and device operational voltage. Appropriate characterization should lead to a dosimetry system that a radiation effects engineer can bring to other facilities, and confirm the beam that is reported as delivered to the device under test (DUT) is actually incident on the DUT. After characterization, and time permitting, a GUI will be created for the operation of the dosimetry system. This will either be created by R. Rinderknecht or a future Master's student.

[2] For details on the cyclotron's recently acquired PCB production capabilities, see: Printed Circuit Board Fabrication Facility: SEE Fab (L. E. Henderson *et al.*)

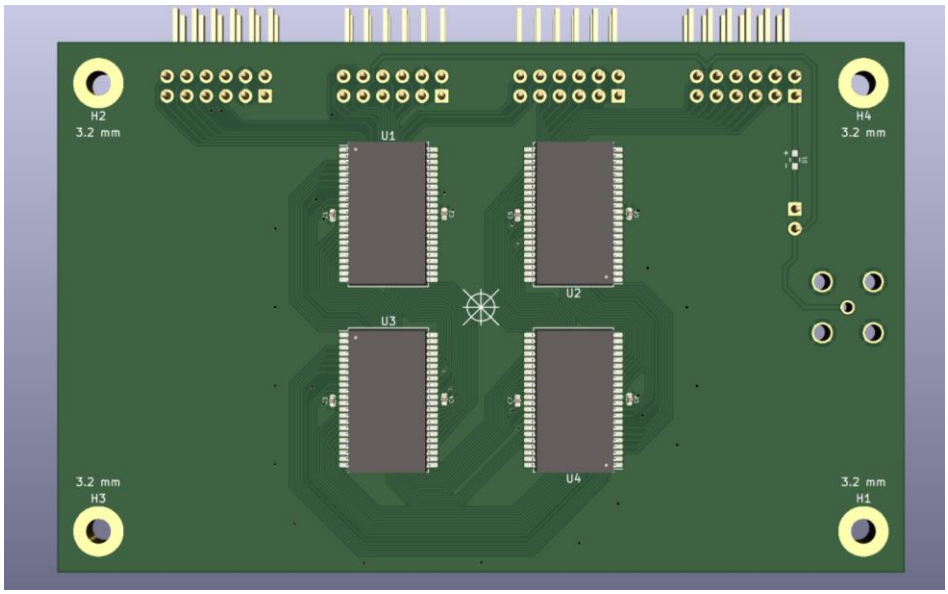

Fig. 3. The proposed 4 SRAM Dosimeter.

Once constructed, the plan is to characterize a variety of beam species, looking at variations of total bit upset and multiple bit upset (MBU) cross-sections in response to differences in spatial location, effective LET, and device operational voltage. Appropriate characterization should lead to a dosimetry system that a radiation effects engineer can bring to other facilities, and confirm the beam that is reported as delivered to the device under test (DUT) is actually incident on the DUT. After characterization, and time permitting, a GUI will be created for the operation of the dosimetry system. This will either be created by R. Rinderknecht or a future Master's student.

In addition to the dosimeter, two analog boards have been designed and built for use in future radiation effects boot camps. One board features an LM124 op-amp, and with the appropriate choice of jumpers, can be configured as either a voltage follower, a unity gain inverter, or a 10 times gain inverter. The other board is voltage comparator, outputting low if VIN < 0.5 VCC, or high if VIN > 0.5 VCC. Both boards are configured with selectable load resistors. Single event transients (SETs) can then be recorded using an oscilloscope configured by R. Gallegos.

Development of an electron cyclotron emission imaging system

L.E. Henderson, H.L. Clark, C.A. Gagliardi, and D.P. May

Prototype components for our electron cyclotron emission imaging system, such as the electronically variable reflective surfaces (EVRS) (see Fig.1), have been produced. However, the fabrication of finalized components is taking longer than anticipated in the last report, so final assembly and first light for the full imaging system is now expected later this year. This report will cover two major issues that were encountered and resolved since the last report:

1) Printed circuit board (PCB) fabrication through external manufacturers became exceedingly expensive and time-consuming, so the entire PCB fabrication process had to be brought in-house. This is described further in *"Printed Circuit Board Fabrication Facility: SEE Fab"*.
2) The reflectance spectra of the first batch of EVRS prototypes, measured in the anechoic microwave test chamber, revealed flaws in both the simulation methodology used to design EVRS and aspects of how designs are physically implemented.

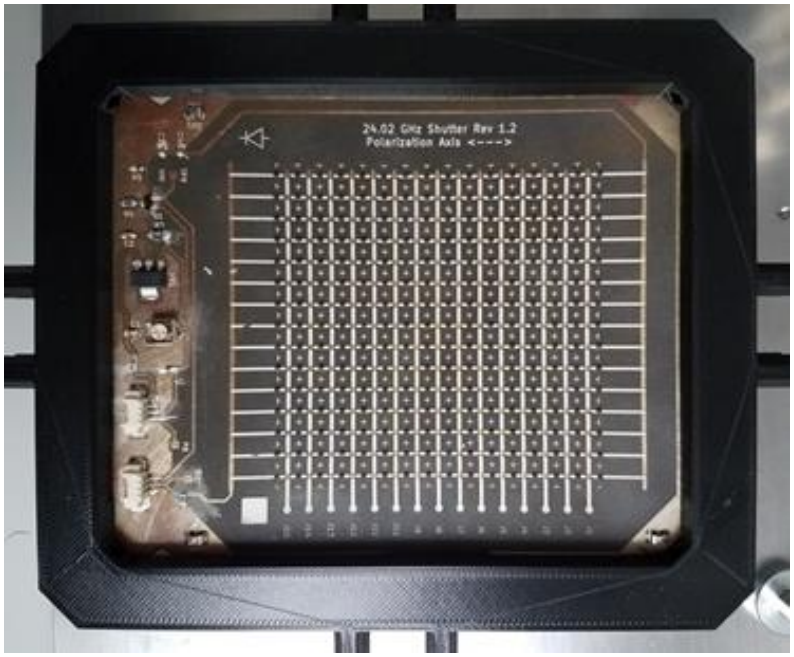

Fig. 1. The first EVRS prototype, chemically etched on RT Duroid 5880, in its mounting frame.

The physical implementation flaws had readily apparent solutions. For example, the ground plane included around the edges, meant to slightly stiffen the first prototypes, produced too much unwanted reflection and will be removed in future designs.

The simulation errors, on the other hand, were more difficult to parse. An EVRS candidate design is simulated as a unit cell with periodic boundary conditions. The simulation package, the "MIT Electromagnetic Equation Propagation" or "Meep" package, stores the simulation geometry and electromagnetic fields on a regularly spaced lattice, excites the fields with a defined current pulse, propagates the fields by timesteps, and computes integral quantities of the fields . In this case the Poynting flux is used to characterize EVRS reflectance and transmittance. It had been observed across many simulations that 10% to 40% excess electromagnetic flux exited the unit cell compared to what had entered, despite there being no gain medium in the structure. This was clearly a simulation convergence error, and some modest convergence improvements had been made prior to experimentally measuring the reflectance, but it was only after experiments were performed that the root cause of the simulation error was identified: the pillbox used to compute the electromagnetic flux entering and exiting the EVRS unit cell was too thin. Meep does not carry out any adaptive meshing, so the available memory of the computer used to run the package can easily become a limiting factor. The EVRS unit cell had therefore been made as thin as possible in the direction normal to the array, with very little simulated empty space above and below the array structure, to minimize the required memory. The flux measurement planes were spaced so closely to radiating structures that they unintentionally fell within the Fraunhofer distance at higher frequencies, which conflated near field flux with far field flux in the simulated reflectance and transmittance spectra and caused the excess

Given the periodic boundary conditions, padding the unit cell with extra empty space was the only available solution to this problem. Fortunately the simulations could be moved onto particular nodes in the Cyclotron Institute's computing cluster that allowed for the use of far more memory per simulation. Ensuring the padding distance exceeded the Fraunhofer distance across all frequencies guaranteed that only far fields contribute significantly to the final result, and along with other code revisions that help with numerical stability, the simulations now appear to be convergent with errors generally under 1%.

The new EVRS simulations have finally begun to validate intuitions about EVRS designs and inform the equivalent circuit model that will be used to describe their performance. By varying which elements of the EVRS structure are simulated and the geometric and material parameters of those elements, a correspondence between the physical EVRS parameters and the equivalent circuit elements is being built up systematically.

In the course of building this correspondence, the nature of the inductive and capactive coupling between cells will be studied (see Fig. 2). The resonance characteristics of arrays with only a few cells will be compared with the resonance characteristics of arrays of infinite size implied by single cell simulations with periodic boundary conditions. How quickly the reflectance spectra of the smaller arrays approaches that of the infinite arrays depends upon how the coupling fields fall off with distance and direction, so it should be possible to distinguish between inter-resonator coupling via surface waves and isotropic radiation. This can be studied for a variety of substrates, substrate thicknesses, and radiator shapes quite easily with the updated simulation code.

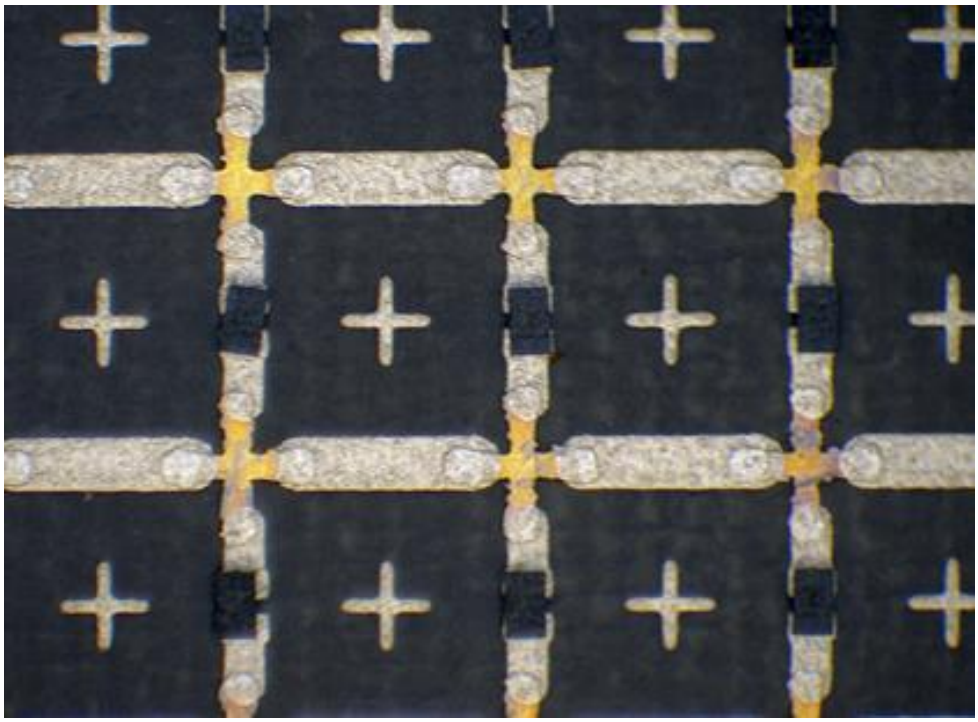

Fig. 2. Close-up of EVRS prototype, with conductive paste traces connecting resonators and PIN diodes. Resonator shape defects due to poor chemical etching are clearly visible. The alignment crosses will be omitted in future versions to further reduce unwanted reflectance.

Printed circuit board fabrication facility: SEE Fab

L.E. Henderson, H.L. Clark, C.E. Parker, R. Rinderknecht, and C.A. Gagliardi

While common research needs in physics can be met with off-the-shelf electronics in the form of computers, FPGAs, and modular crate electronics, the construction of novel detectors (and interfaces for those detectors) still frequently involves one-off or prototype printed circuit boards (PCBs). The production lines of most commercial PCB manufacturers are only suited for high-volume fabrication using fairly conventional processes. This is antithetical to the production methodology most useful to scientists and researchers: an iterative, low-volume prototyping process with the flexibility to include unconventional fabrication steps. Furthermore, the use of existing cost-effective manufacturers overseas can lead to problems including lengthy delivery delays (particularly in recent years) and export controls for material and intellectual property.

For these reasons, it was recognized that the Cyclotron Institute would greatly benefit from having an in-house PCB production capacity once again. It was also recognized that there is a significant educational opportunity present in allowing our Doctoral and Master's students to be closely involved with manufacturing process of the electronics essential to their research.

Following consultations with other laboratories and our own researchers, the primary equipment for the "SEE Fab" PCB fabrication facility was purchased from LPKF North America (see Fig. 1). This included their ProtoMat S104, a specialized CNC mill for processing copper-clad boards, their ProtoPlace E4, a surface mount device (SMD) manual placement jig, and their ProtoFlow S4, a reflow soldering oven. Other equipment purchased included an LPKF ProtoPrint S4 stencil press, LPKF's ProConduct through-hole plating kit, a lab oven for heat curing, an ultraviolet light exposure chamber, a high-resolution printer with UV-blocking ink for photomasks, a stereo microscope, and several narrow chemical immersion tanks. Together this equipment, shown in Fig. 1 enables a wide range of PCB production schemes while maintaining the option to easily acquire any additional capabilities that prove necessary.

Fig. 1. SEE Fab manufacturing facilities (left) and general workroom (right).

We anticipate that most PCBs designed for research at the Cyclotron Institute can be created by removing relatively small amounts of copper from stock copper-clad boards, which is the perfect job for a milling machine. The precision of traces and pads cut by the ProtoMat S104 rivals the stated precision of any commercial PCB manufacturer. The chemical etching system we have also implemented allows for designs that require the removal of large areas of copper, but this is expected to remain an optional pre-processing step. Chemical etching is not intended to be the primary PCB fabrication process at the Cyclotron Institute as it was many years ago.

SEE Fab is currently being optimized around a production scheme for simple but robust PCBs: two-layer boards with soldermasks, legends, plated through-holes, and a mixture of SMD and through-hole (THT) components. The ProtoMat S104 handles milling out the traces in the copper, drilling holes, routing the PCBs to their finished size, and even optionally dispensing solderpaste. Plated through-holes and conductive vias will be formed by sucking a heat-curable silver-loaded conductive paste through drilled holes to coat the interior walls of the holes. Soldermasking and legend printing will be performed using UV-curing inks. The first PCBs being manufactured under this production scheme are the SRAM-based particle beam dosimeters for Ryan Rinderknecht's Master's , shown in Fig. 2 (see *"Status of the Radiation Effects Master's Program: Using an SRAM Based Dosimeter to Measure LET, Fluence, and Beam Uniformity"*).

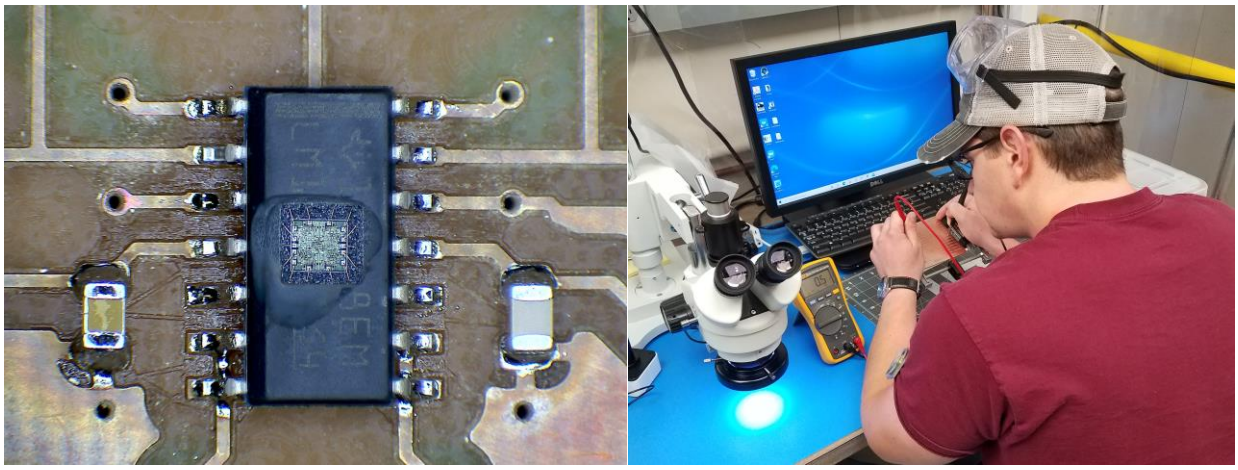

Fig. 2. PCBs produced by SEE Fab for testing purposes. To the left is a close-up of delidded LM124 on prototype interface PCB. On the right is Ryan Rinderknecht checking for electrical continuity on a row of vias to establish the reliability of the ProConduct through-hole plating process for various drilled hole sizes.

SEE Fab will also be capable of handling the more complex and precise production schemes for microwave-frequency PCBs. The first PCBs that will be produced under these schemes are PCBs needed by Lawrence Ethan Henderson's doctoral research (see "*Development of an Electron Cyclotron Emission Imaging System"*). The production of that project's microwave metamaterials involves pre-milling chemical etching, milling of tiny features on thin PTFE substrates, and precise application of blended silver/carbon heat-curable inks to form circuit elements. The microwave receiver antennas and receiver electronics for that project are slightly less complicated to manufacture, but they still require tight dimensional tolerances.

End user guidelines, general procedures, and safety protocols are currently being drafted to make SEE Fab accessible and useful to research groups at the Cyclotron Institute. Research groups will be expected to submit PCB drawings in the form of Gerber files as they would for any external manufacturer, but our in-house fabrication staff will be able to easily provide detailed feedback in-person. This means we can instruct students and staff on basic PCB design practices and avoid burdening commercial manufacturers with that particular task of education.

Computing at the cyclotron institute

R. Burch, K. Hagel, J. Gauthier, and Y.-W. Lui

Due to the premature end of life of CentOS 8 in December 2021, all the lab computational servers were migrated to Rocky Linux during fall 2021. We used Ansible to execute the migration tool provided by the Rocky Linux community on the whole cluster. All the desktop computers that were running on CentOS 8 have also been migrated to Rocky Linux. Since our web server was running on CentOS 7 and had to be replaced by summer 2024, a new Rocky Linux server has been built and configured. The new web server deployment has been performed in April 2022 as well as the old server decommissioning. Thanks to this migration, all the computers mentioned above will be compliant until 2029.

The Cyclotron WI-FI, which was already using TAMU NetID authentication but still provided by the Cyclotron Institute's own network and access points (AP) has been fully transferred to TAMU IT. The switches and APs have been replaced and the WI-FI is now outside of the Cyclotron Institute firewall and fully managed by the TAMU IT department.

The server that was hosting the cyclotron-personnel email list was no longer complying with the TAMU security requirements and we thus took the decision to decommission it. The cyclotron-personnel list has been moved to TAMU Google Groups and is managed through TAMU-Direct. The new list has been used for almost a year at the time we are writing this report and is working as expected.

Gamma-spectroscopy-based survey of the devices activated by proton beams from the K150 cyclotron

V. Horvat

Setup of the LBC-detector-based station for gamma-ray radiation survey of the RTF-customer devices exposed to cyclotron beams is now completed and the system is fully calibrated and operational. (LBC stands for lanthanum bromochloride, while RTF refers to the Cyclotron Institute's Radiation Testing Facility, also known as SEE-line [1].) Details can be found in the collection of reports from the previous reporting period [2-4]. In this reporting period the system was used several times, as described below.

Fig. 1 shows gamma-ray energy spectra (using the standard energy scale [4], corresponding to the 643.7 V detector bias) of a RTF-customer device taken immediately after the end of their K150 proton irradiation run (shown in black) and about two weeks later (shown in red). At the time the latter spectrum was taken it was already safe to ship the device back to its owner, as determined from a measurement performed using a pancake-shaped Geiger counter placed at the closest possible distance from the surface of the device. Therefore, there was no need for an elaborate analysis of these spectra.

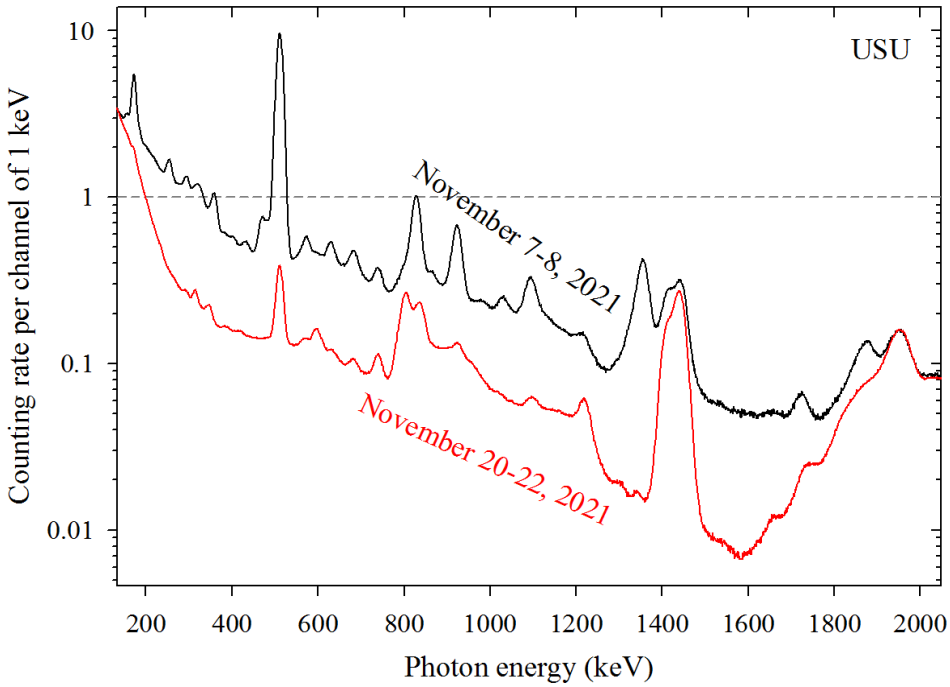

Fig. 1. Photon energy spectra of a RTF-customer device taken immediately after the end of their run (shown in black) and about two weeks later (shown in red).

Fig. 1 shows gamma-ray energy spectra (using the standard energy scale [4], corresponding to the 643.7 V detector bias) of a RTF-customer device taken immediately after the end of their K150 proton irradiation run (shown in black) and about two weeks later (shown in red). At the time the latter spectrum was taken it was already safe to ship the device back to its owner, as determined from a measurement

performed using a pancake-shaped Geiger counter placed at the closest possible distance from the surface of the device. Therefore, there was no need for an elaborate analysis of these spectra.

The spectrum shown in black was measured with the LBC detector placed about 30 cm away from the surface of the device. Such a large distance was selected in order to limit the counting rate. The spectrum shows a large number of gamma-ray peaks, but it is dominated by the 511 keV peak, which is due to positron annihilation. This was found to be typical right after irradiation by the K150 cyclotron protons. Since the Geiger counter has much higher efficiency for positrons than for gamma-rays, the 511 keV peak can be used to estimate the time it will take the overall activity to decrease to a shipping-safe level. It was found that the shipping-safe level corresponds roughly to the counting rate of 1 per second or less in the centroid-containing channel of the 511 keV peak (as indicated by the dashed line in Fig. 1), in a spectrum measured at the closest possible distance between the LBC detector and the device, provided that the 511 keV peak still dominates the gamma-ray energy spectrum. Example of such a spectrum is the one shown in red in Fig. 1.

It should be noted that the spectra shown in Fig. 1 start at about 130 keV. This is because at lower energies the spectrum was dominated by the background radiation produced by the ion sources and the cyclotrons, even though the measurement was performed within lead shielding built around the LBC detector and the device [2]. Typically, the background radiation is not steady and it is not practical to reduce it by turning off its sources. Furthermore, the peaks at 1440 keV and 1950 keV are due to radiation originating from within the LBC detector [2].

Fig. 2 shows energy spectra of the gamma rays emitted from a ZnSe window after it was irradiated by protons from the K150 cyclotron, measured two days after the irradiation (shown in black)

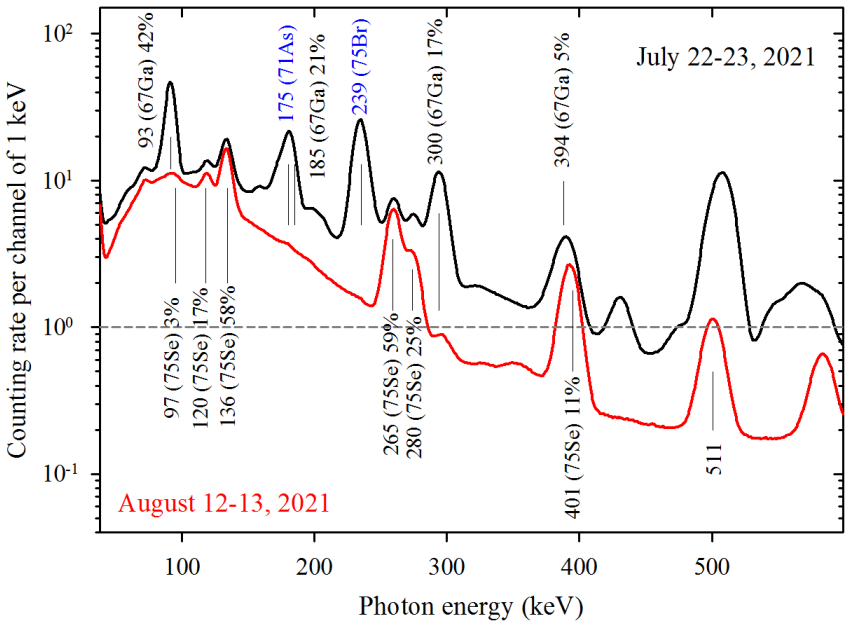

Fig. 2. Energy spectra of gamma rays emitted from a zinc selenide window after it was irradiated by protons from the K150 cyclotron, measured two days after the irradiation (shown in black) and about three weeks later (shown in red).

and about three weeks later (shown in red). This transparent, highly stable optical window was located on the cryostat that contained the target device. It was chosen for its extremely low absorption in the infrared region of the electromagnetic spectrum and high resistance to thermal shock. Its activity after proton irradiation was initially dominated by ^{71}As (65.3 h) [175@82%, 1095@4%], then by ^{67}Ga (3.26 d) [93.2@42%, 185@21%, 300@17%, 394@5%] and ^{77}Br (57h) [239@23%], and later by ^{75}Se (120 d) [97@3%, 120@17%, 136@58%, 265@59%, 280@25%, 401@11%]. It is estimated that it will be safe to ship the window back to its owner in August 2022, at which time the effect of proton irradiation on the ZnSe infrared transparency will be studied.

It should be noted that the energy spectra were recorded daily, for about 24 hours each, so that the half-lives (listed above in the parenthesis) could be verified for each isolated peak. The two numbers in the square brackets above refer to the photon energy in keV and the nominal intensity fraction. All four nuclides listed above decay by electron capture with 100% branching ratio.

In the same experiment an aluminum collimator was used to reduce diameter of the beam before it hit the ZnSe window. As a result, the collimator was activated. The main contributor to the collimator activity is 22Na (2.6 y), as illustrated in Fig. 3, where multiple spectra were shown to demonstrate that the peaks correspond to half-life much longer than 24 h. For comparison (and a more accurate energy calibration) spectra of gamma rays emitted from a 207Bi calibration source are also shown. Activity of ^{22}Na is estimated to drop below the background level in about 7.5 years.

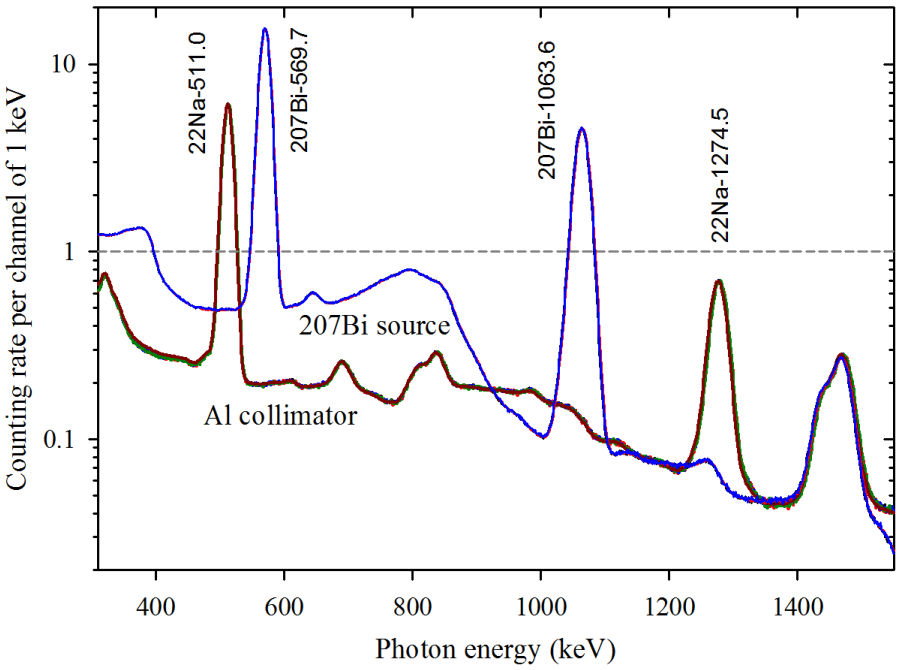

Fig. 3. Multiple energy spectra of gamma rays emitted from an aluminum collimator and from a Bi-207 calibration source.

Finally, the LBC-detector-based system was used to measure activity of a device exposed to proton beams from the K150 cyclotron and heavy-ion beams from the K500 cyclotron. Somewhat unexpectedly, the activity after irradiation was found to be dominated by ^{60}Co (1925 d) and ^{137}Cs (30.1 y),

which was verified by taking a spectrum of gamma rays from a source known to contain ^{60}Co and ^{137}Cs. A comparison of the results is shown in Fig. 4. Due to the long half-life of these nuclides and the fact that owner of the device does not have a license to possess radioactive material, the device will have to be kept at the Cyclotron Institute indefinitely.

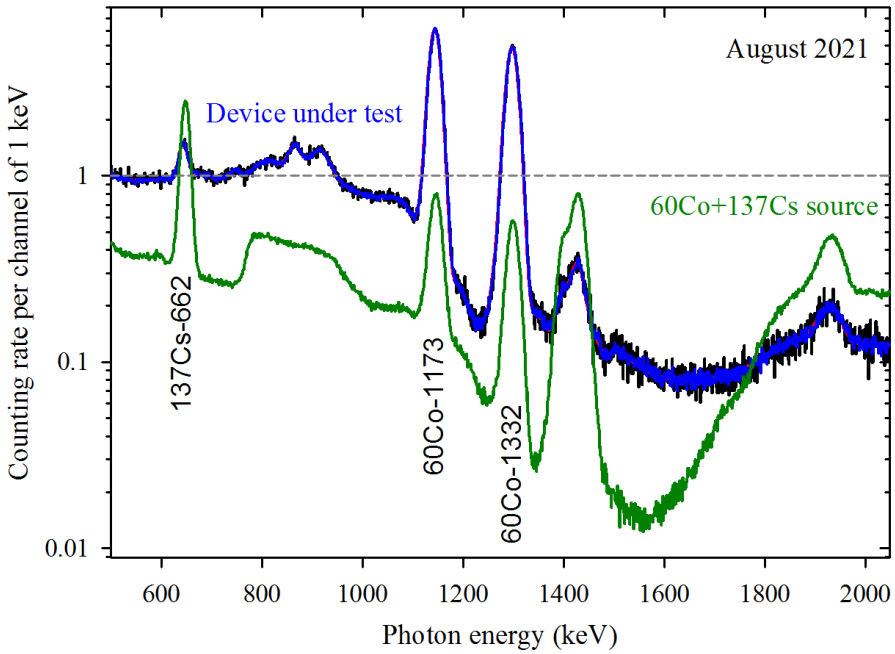

Fig. 4. Energy spectra of gamma rays emitted from a SEE-customer device and from a source containing ^{60}Co and ^{137}Cs.

[1] https://cyclotron.tamu.edu/see

[2] V. Horvat, H. L. Clark, B. Hyman, *Progress in Research*, Cyclotron Institute, Texas A&M University (2020-2021), p. V-26.

[3] V. Horvat, *Progress in Research*, Cyclotron Institute, Texas A&M University (2020-2021), p. V-29.

[4] V. Horvat, *Progress in Research*, Cyclotron Institute, Texas A&M University (2020-2021), p. V-34.

^{6}HeCRES ion trap addition

D. McClain, G. Chubarian, V. Iacob, D. Melconian, M. Nasser, and P.D. Shidling

As described last year's report [1], the ^{6}He-CRES collaboration uses the cyclotron radiation emission spectroscopy (CRES) technique developed by the Project-8 collaboration [2] to measure the β spectrum of ^{6}He, ^{14}O, and ^{19}Ne from radiation emitted due to the cyclotron radiation as a charged particle precesses in a magnetic field. The cyclotron frequency, f, of an electron is dependent on the kinetic energy $E_e$of the electron according to

$$f = \frac{1}{2\pi}\frac{eB}{m_e + E_e}$$

where e is the electron charge, B is the magnetic field, and m_e is the rest mass of the electron. The incredible sensitivity of the CRES technique gives us the ability to use the frequency measurement to deduce the energy of the electron [3]. The use of this sensitivity is to measure distortions in the beta spectrum caused by a nonzero b_{Fierz} which is an indication of physics beyond the standard model. The experiment consists of a rectangular waveguide with a U-shape turn to read frequencies from either end to negate Doppler effects. The rectangular waveguide is split on one side of the U shape to include a circular waveguide that exists as a decay volume for the isotope of interes. This decay volume also has a coil around it creating a magnetic bottle to trap βs azimuthally.

The current limitation of the experiment is caused by a lack of radial confinement of the isotope of interest. Without this radial confinement, we expect an energy dependence on countable events within a region of our decay volume. In this case, the emitted betas of the He nuclei that are near the walls are lost, and because of an increasing cyclotron radius with higher energy, higher energy betas would be more likely to hit the wall as show in Fig. 1, resulting a bias toward lower energies in our energy spectrum.

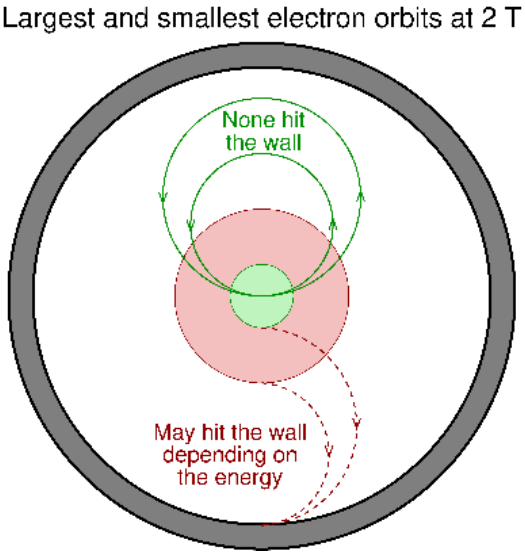

Fig. 1. The geometric effect of wall collisions in the case where there is no radial confinement of the isotopes.

With this issue it is still expected to get the uncertainty of $b_{\mathrm{Fierz}} < 10^{-3}$ [4].

In order to resolve the issues of the wall effects, two ion traps have been in development. The first, a radiofrequency quadrupole trap, will be used to cool and bunch a beam of ions before passing it to the second, a Penning trap, which will axially confine the ions while the magnetic field holds radially confines them. The Penning trap is designed with the same dimensions as the current decay volume being ~10 cm in length and 1.156 cm in diameter. This radius propagates frequencies between 18-24 GHz well. The magnetic field can be varied from 0.5-6 T to shift our 18 - 24 GHz window to different energies and scan the whole β spectrum. With radially confinement effectively eliminating wall collisions, our expected precision on $b_{Fierz} < 10^{-4}$.

In order to accomplish this, SimION was used to simulate the radiofrequency quadrupole trap (RFQ) in cooling ^{6}He ions, as described in last year's report [1]. For this experiment we have rescaled a version of the TAMUTRAP RFQ [5] from $r_0 = 6$ mm to $r_0 = 12$ mm, which allows us to operate with $V_{RF} = 200$ V, and frequencies between 0.5-1.5 MHz. These parameters in the simulation gives us a time spread of 0.84 μs and an energy spread of 2.89 eV which is used to plan the rest of the beamline after the RFQ. This timespread also defines the minimum width of our trapping region in the Penning trap. The RFQ design has been completed, though concerns of low count-rate caused by limited bunch sizes have held back development.

The Penning trap has similarly been tested with outputs from the RFQ simulation to confirm the hypothesis that we are able to radially confine ions from being within the danger zone where we see the energy dependence on our observed events. As seen in Fig. 2, the maximum radial position for ions in a bunch, we expect less than 0.24% of decays to occur within this region.

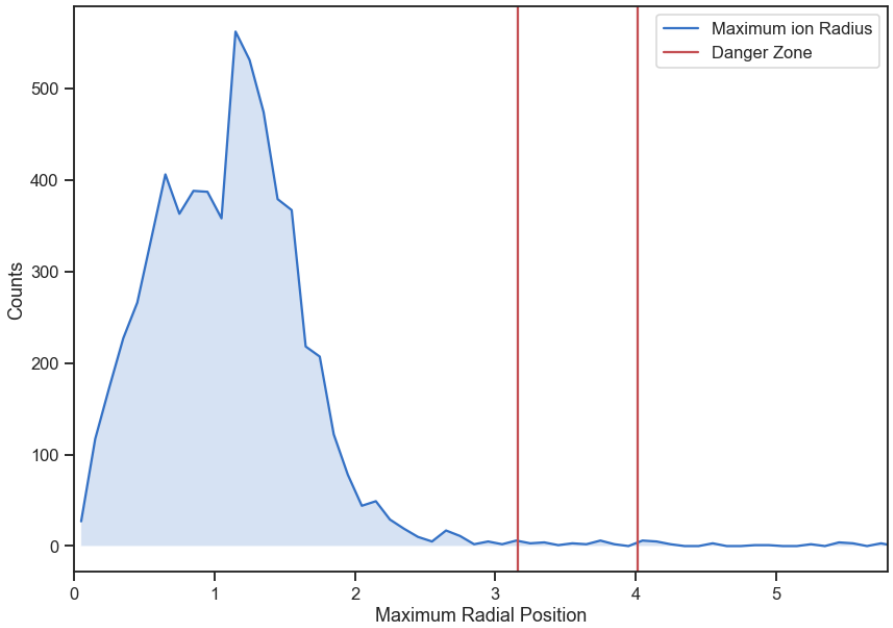

Fig. 2. A Plot of the maximum radial position in mm of every particle within a bunch during their time trapped within the Penning trap. The danger zone seen in Fig. 1 is represented as the region between the two vertical lines.

[1] D. McClain *et al*., *Progress in Research*, Cyclotron Institute, Texas A&M University (2020-2021), p V-68.
[2] D.M. Asner *et al.*, Phys. Rev. Lett. **114**, 162501 (2015).
[3] A.A. Esfahani *et al.*, J. Phys. G **44**, 054004 (2017).
[4] A. García, private communication.
[5] M.S. Mehlman, Ph.D. Thesis, Texas A & M University (2015).

GEANT4 simulations as part of an independent analysis of β-delayed-proton measurements in ^{32}Ar

M. Nasser, G. Chubarian, V.E. Iacob, V.S. Kolhinen, D. McClain, and D. Melconian

The standard model describes three of the four fundamental forces of the nature. Of these, the weak force governs beta-decay. For pure Fermi $0^+ \rightarrow 0^+$ decays, the β-ν angular correlation parameter, $\tilde{a}_{\beta\nu}$, describes the degree to which the momenta of the beta and neutrino are correlated. The standard model prediction is $\tilde{a}_{\beta\nu} = 1$, which assumes there are no scalar currents in beta decay. Current experimental measurements limit $\tilde{a}_{\beta\nu} \geq 0.9995$. Precision measurements of $\tilde{a}_{\beta\nu}$ to <0.1% with vastly different sources of systematic uncertainties are sensitive to weak scalar components to the weak interaction that are beyond the standard model.

A straightforward way to measure $a_{\beta\nu}$ would be to measure the momenta of the betas and neutrinos directly, however the near-massless and electrically neutral neutrinos are very difficult to measure directly. To circumvent this, one can focus on the momentum of the recoiling daughter isotope, however this too is difficult in practice due to the very low energies (100's of eV) of the daughter nucleus. If the daughter nucleus is itself short-lived – as in beta-delayed proton decays – the delayed proton's energy will be Doppler shifted by up to ± 15 keV depending on the relative momenta of the beta and neutrino from the beta decay. Observing the small shifts in the proton energies when in coincidence from betas can be used to measure $\tilde{a}_{\beta\nu}$.

A rough outline of the WISArD experiment was described in [1], and further detailing can be found in [2]. Continuing off [1], the simulation of protons needs to be addressed. GEANT4 [3] was used to create a simulation that can transport and measure the protons supplied from the RMat program. Unlike the PENELOPE [4] program, this needs the full geometry as the protons can approach nearly all objects in the experiment. Fig. 1 depicts the geometry as displayed in GEANT4. The measured protons are then separated into same- and opposite-hemispheres based on triggering of the scintillator via the positrons. E.g., a positron trigger in the scintillator and proton in a silicon detector opposing the scintillator would categorize under the opposite-hemisphere peak.

The experiment will produce the two peaks where the separation energy between their means will determine $a_{\beta\nu}$. To know the relation between this energy difference and the correlation parameter, simulations must be done across varies values of $a_{\beta\nu}$ to establish a calibration between the two. Fig. 2 shows this linear relationship. The program was developed in a manner such that the betas can also be fed into GEANT4 for simulation. This will serve as another comparison (the other being WISArD's) to the PENELOPE simulation.

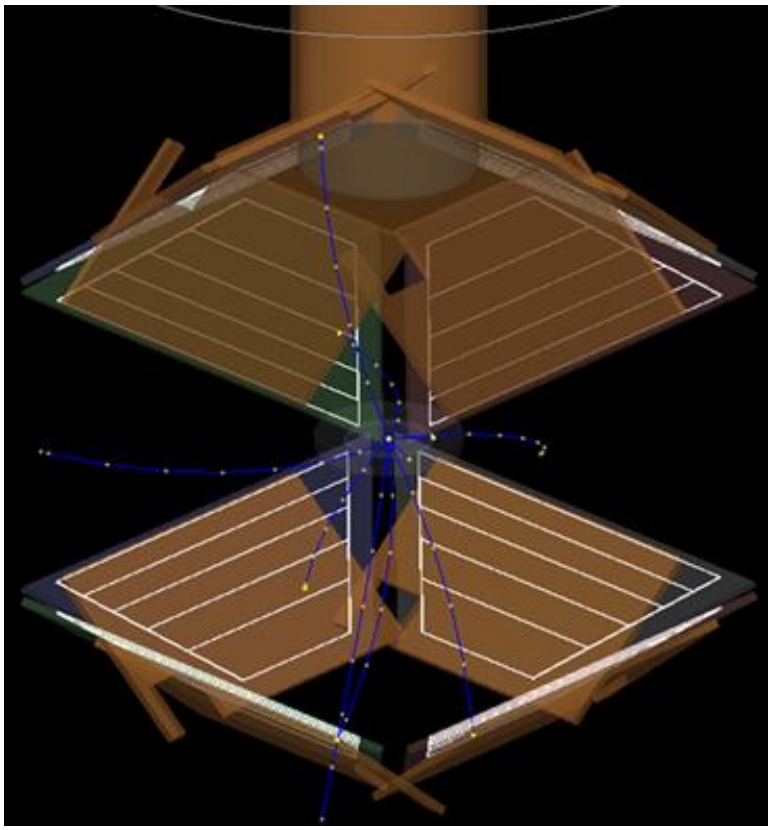

Fig. 1. Geometry of the new WISArD experiment in our GEANT4 implementation. The blue tracks are the trajectories of protons. The strips attached to the copper supports are the silicon detectors. The plastic scintillator is housed at the top, and the catcher foil in the middle.

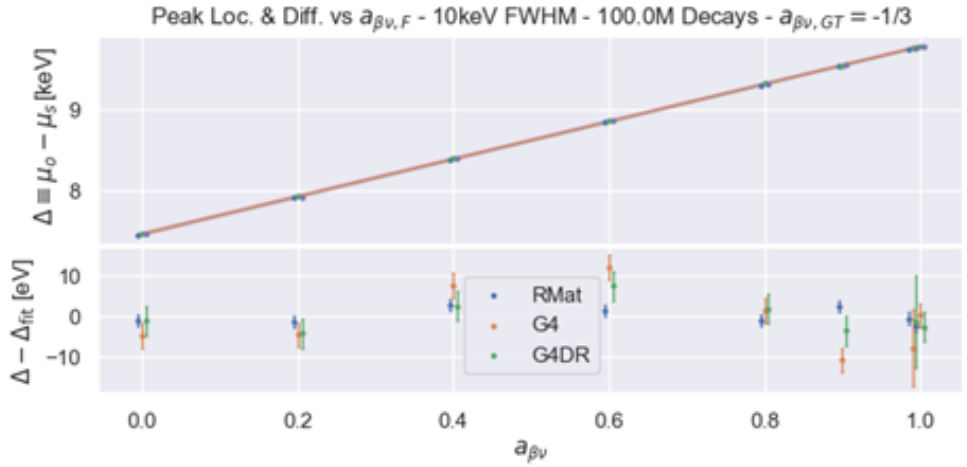

Fig. 2. Separation distance across various $a_{\beta\nu}$'s. Fluctuation in the fit are eV -scale. The fit serves as a calibration. Given another simulation's Δ (or experiment), its $a_{\beta\nu}$ can be estimated. RMat and G4 are self-explanatory. G4DR is the G4 with post-imposed 10 keV FWHM detector resolution.

Being a high-precision measurement, the quantification of uncertainties is crucial to determining $a_{\beta\nu}$. Currently systematics are being estimated through simulations varying aspects such as source distribution and material thicknesses. Figs. 3 and 4 show a few of these graphically.

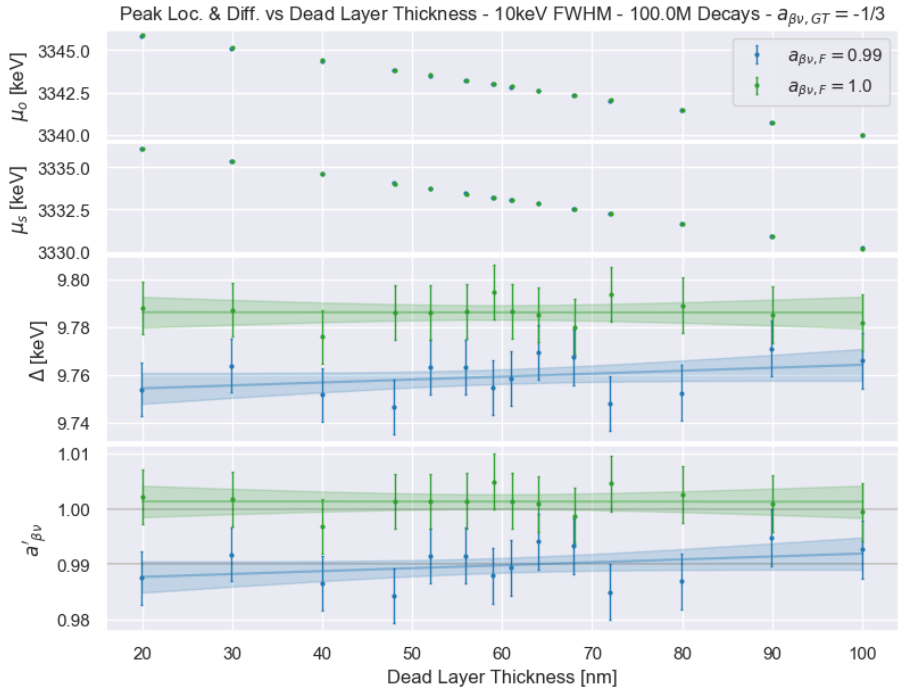

Fig. 3. Peak locations, separation distances, and estimated $\mathbf{a_{\beta\nu}}$'s at various dead layer thicknesses. Test sets of $\mathbf{a_{\beta\nu} = 0.99}$ (blue) and 1.00 (green) were used.

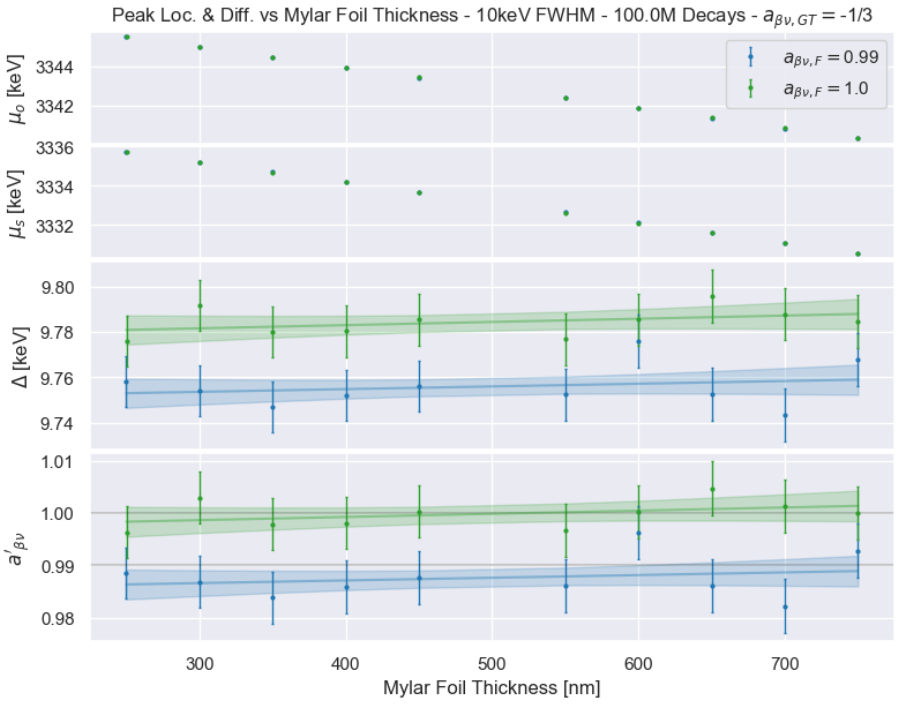

Fig. 4. Peak locations, separation distances, and estimated $\boldsymbol{a_{\beta\nu}}$'s at various mylar catcher-foil thicknesses. Test sets of $\boldsymbol{a_{\beta\nu} = 0.99}$ (blue) and 1.00 (green) were used.

The GEANT4 end of the simulation set has seen completion with regards to development. It's currently being employed to determine systematics in building an error budget table for the experiment. Future developments may potentially include use on the Cyclotron computing cluster for more statistics. The current statistics sit at 100M events per value of $a_{\beta\nu}$.

[1] M. Nasser *et al.*, *Progress in Research*, Cyclotron Institute, Texas A&M University (2021-2022) p. ?-?

[2] V. Araujo-Escalona, D. Atanasov, X. Fléchard, P. Alfaurt, P. Ascher, B. Blank*, et al.* Phys. Rev. C. **101**, 055501 (2020); DOI: 10.1103.

[3] S. Agostinelli *et al.*, GEANT4: A Simulation toolkit - GEANT4 Collaboration; Nucl. Instrum. Methods Phys. Res. **A506**, 250 (2003); SLAC-PUB-9350, FERMILAB-PUB-03-339

[4] NEA (2019), PENELOPE 2018: A code system for Monte Carlo simulation of electron and photon transport: Workshop Proceedings, Barcelona, Spain, 28 January – 1 February 2019, OECD Publishing, Paris, https://doi.org/10.1787/32da5043-en.

A novel technique for the production of robust actinide targets

S. Dede,[1,2] G. Christian,[1,3] K. Manukyan,[2] and A. Aprahamian[2]
[1]*Cyclotron Institute, Texas A&M University, College Station, TX 77843*
[2]*Department of Physics, University of Notre Dame, Notre Dame, IN 46556*
[3]*Department of Astronomy & Physics, Saint Mary's University, Halifax, NS B3H 3C3, Canada*

Accelerator experiments rely on various projectile and target combinations in order to extract key nuclear cross-section and structure information. The success of these experiments is highly influenced by the availability and the characteristics of targets with specific and well-defined properties. Especially relevant is the production of actinide targets which are typically rare in abundance and sometimes radioactive. Actinide targets are important for stockpile stewardship and nuclear science. In In this work, we have utilized solution combustion synthesis (SCS) in conjunction with electrospray deposition of chemically reactive layers that can be converted to actinide oxides by simple heat treatments, in order to produce actinide targets efficiently using the very minimum in starting materials. The produced targets are isotopically pure, cost efficient, reliable, robust, and highly uniform with controlled thicknesses and dimensions (Stewardship Science Academic Alliances Program Topic Research Area # 3: Radiochemistry). The actinides were provided by the Actinide Center of Excellence in Research in the Engineering College at the University of Notre Dame.

The initial steps consisted of the investigation of the different combinations of parameters that produced the best possible targets with respect to uniformity, thickness, and robustness. The surface treatment of both the aluminum and carbon substrates prior to spraying is where the investigation started, by determining the best treatment in order to have a thin target layer and not just droplets on the surface. Following that, the investigation turned to the parameters of the spraying itself (spraying time, uranium concentration in the solution, flow rate, heat treatment temperature) as well as the stability and robustness of the targets under irradiation with an Argon beam (from 2×10^{16} to 1.3×10^{17} ions/cm^2). Through this investigation we can draw the following conclusions:

- The surface of our targets is smooth with minimum imperfections.
- The heat treatment temperature influences the crystal structure of the deposited layer. Higher temperatures result in Mg leaking from the substrate into the UO_2 layer, thus obstructing the crystallization of our layer and forming a MgO layer inside the UO_2 layer.
- The amount of U in the target linearly depends on the duration of the spraying, which allows the control of the thickness of the target by varying the spraying duration.
- The uranium amount in the targets does not change after the irradiation but there are significant structural changes when Mg is not present in the layer.

Finally, the robustness and purity of the targets was tested under a neutron beam, utilizing the neutron beam at the Los Alamos National Lab (LANL) and the DANCE detector array [1]. The target used was deposited on pure aluminum backing and was under the neutron beam for a total of 35 hours. After the data analysis, it was concluded that the targets are fairly robust with no impurities that would interfere with our measurements (Fig. 1).

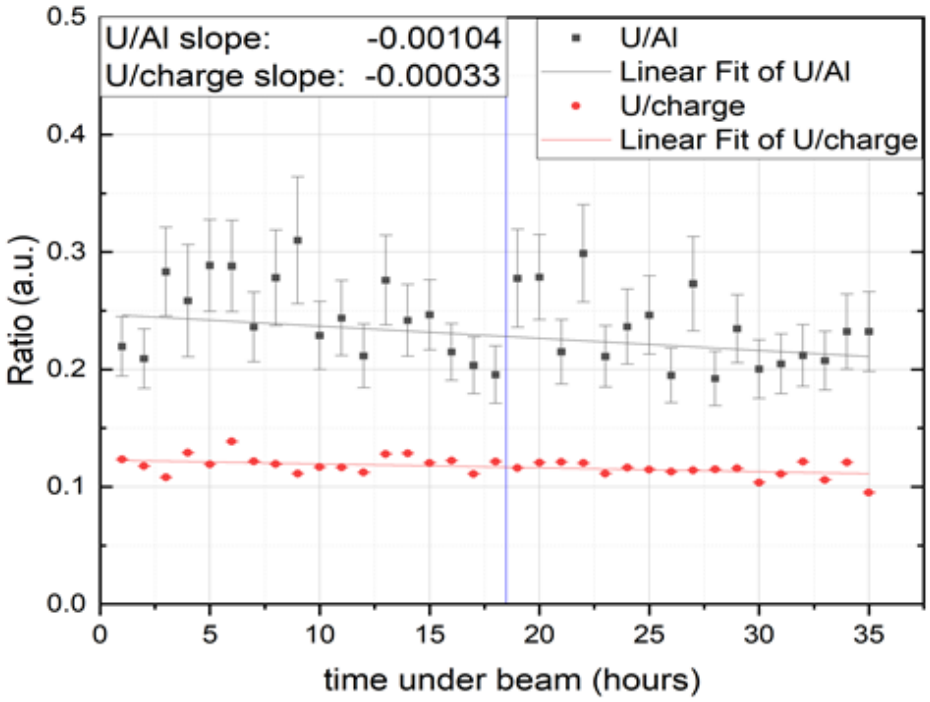

Fig. 1. The target's stability under the neutron beam.

Future work

We have started exploring the combustion properties of Eu as a surrogate for Am, which is going to be our next step in the actinide target production.

The final step would be a cross section measurement using the neutron beam at LANL as well as the neutron beam that is being developed at University of Notre Dame in the following months.

[1] J.L. Ullmann, T. Kawano, T.A. Bredeweg, A. Couture, R.C. Haight, M. Jandel, J.M. O'Donnell, R.S. Rundberg, D.J. Vieira, J.B. Wilhelmy, J.A. Becker, A. Chyzh, C.Y. Wu, B. Baramsai, G.E. Mitchell, and M. Krtička, Phys. Rev. C **89**, 034603 (2014)

[2] D.L. Duke, F. Tovesson, A.B. Laptev, S. Mosby, F.J. Hambsch, T. Brys, and M. Vidali, Phys. Rev. C **94**, 054604 (2016).

Commissioning of neutron detector array TexNeut

D.P. Scriven,[1,2] G.V. Rogachev,[1,2] J. Bishop,[1] G. Christian,[1,2,3] C.E. Parker,[1] L. Sobotka,[4] A. Alafa,[1,2] N. Dronchi,[4] A. Thomas,[4] A. Saastamoinen,[1] E. Koshchiy,[1] E. Aboud,[1,2] M. Roosa,[1,2] M. Barbui,[1] E. Harris,[1,2] D. Mulrow,[4] and C. Hunt[1,2]

[1]*Cyclotron Institute, Texas A&M University, College Station, TX 77843*

[2]*Department of Physics and Astronomy, Texas A&M University, College Station, TX 77843*

[3]*Department of Astronomy and Physics, Saint Mary's University, Halifax Nova Scotia, B3H 3C3, Canada*

[4]*Departments of Chemistry and Physics, Washington University, St. Louis, MO 63130*

The capability to detect fast neutrons has a variety of applications including basic nuclear science, astrophysics, and national security. We have constructed a neutron detector array, TexNeut, for measuring fast neutron energies which are produced in nuclear physics experiments related to these topics. In 2021 TexNeut was assembled, and a two-week commissioning run followed.

After research and development during previous years [1-3], we constructed TexNeut in 2021, as seen in Fig. 1 (left). TexNeut is an array of pseudo-bar neutron detector modules. These bars are a novel take on conventional bar-type scintillation detectors commonly used for neutron TOF spectroscopy [4]. Each bar is comprised of 6 *p*-terphenyl organic crystal scintillators of dimensions 2x2x2 cm^3 which are optically coupled to make a segmented bar. The bar is wrapped in a specular film and light collection is readout by PMTs at both ends of the bar. The construction of these bars does not noticeably suppress the PSD capabilities of *p*-terphenyl but gives rise to position sensitivity in the bar with resolution that matches the size of the crystal. This postion sensitivity can be seen in Fig. (right). A total of 48 bars were

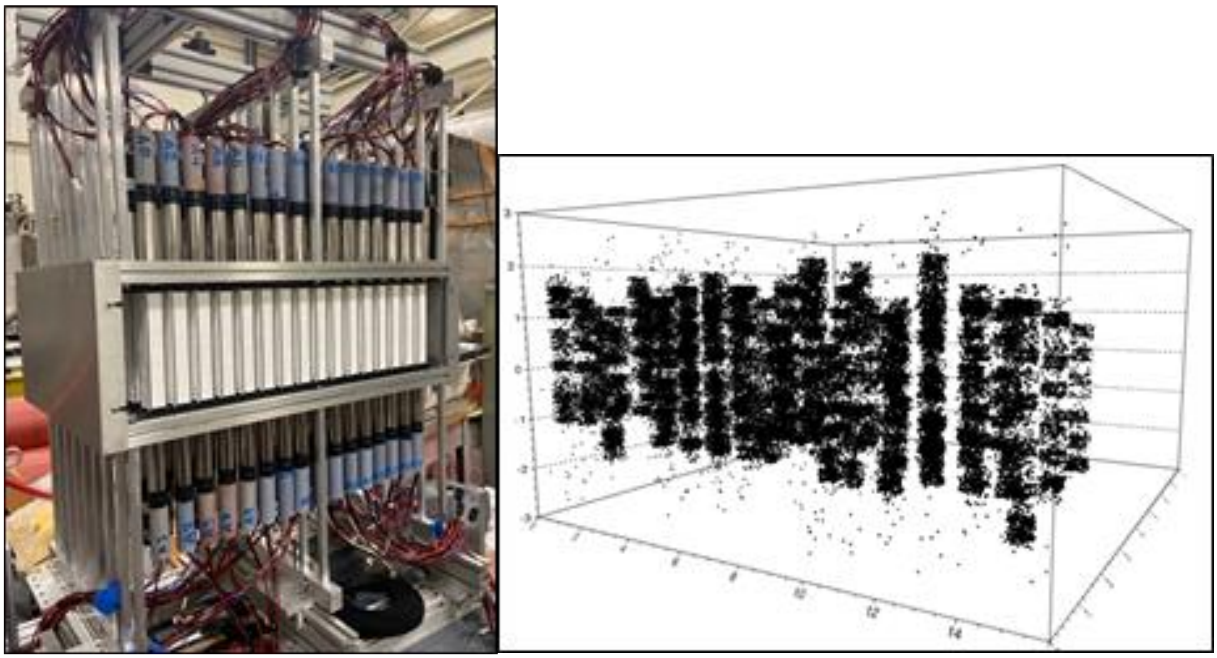

Fig. 1. (Left) A photo of the TexNeut array. (Right) A scatter plot showing the 3D hit pattern of neutrons in the array from ^{252}Cf. X- and Z- position are given in units of row number and column number. Y- is the calculated intra-bar position from pseudo-bar data. Note the discrete blobs which correspond to discernable crystals.

constructed for the commissioning run with upwards of 100 bars slated for the full assembly. Data are acquired by a Wash. U. St. Louis-developed DAQ that implements the PSD-8C ASIC chips [5].

A series of experiments were carried out during the beam time. These tests used TexAT as either a simple vacuum chamber or in its usual configuration as a gas tracking detector for thick target inverse kinematics (TTIK). First, we impinged a ^{7}Li beam on a thick tantalum foil to produce a localized γ-ray flash. A time-of-flight spectrum was generated by measuring the time between the TexNeut start trigger and the MARS scintillator, located just before the entrance to the TexAT chamber, as a stop. These γ rays were detected in TexNeut and will be used as a reference time for the event timing recorded by TDCs. We observed a γ-ray peak consistent with the TOF from the target to the detector.

After successful observation of the γ-ray peak, the tantalum foil was removed and was replaced by a solid thin polyethylene (CH_2) target with stable ^{7}Li beam. In this test, TexAT was operated as a vacuum chamber with no detectors or gas being used. We performed ^{7}Li(p,n) in this configuration and detected neutrons from the reaction and saw a peak in the timing spectrum corresponding to a ^{8}Be 3^{+} resonance that we expected to see. A preliminary spectrum for the solid target run is shown in Fig. 2 (left).

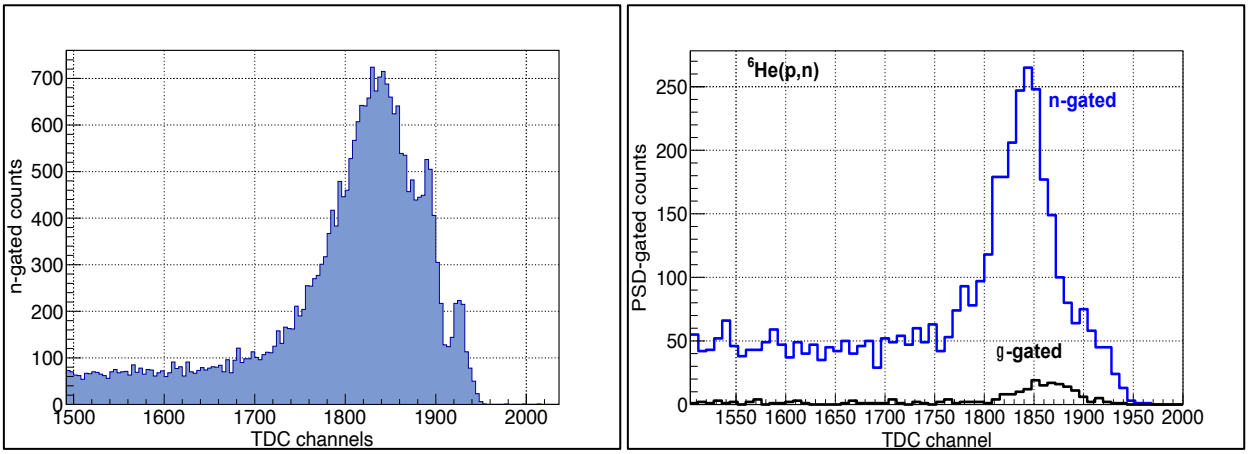

Fig. 2. (Left) Neutron TOF spectrum from ^{7}Li(p,n). Due to the nature of the triggers, low energy corresponds to the right side of the abscissa. Here, singular crystal position is not considered, causing the already broad resonance to appear slight more so. (Right) TOF spectrum for neutrons and γ-rays from the ^{6}He(p,n) reaction. Again, only the bar location is considered but not the crystal of interaction.

Following the thin target run, TexAT was filled with 200 Torr of isobutane. Using TexAT for TTIK, we performed the ^{6}He(p,n) reaction measurement. With gas in the chamber, the micromegas detectors were then employed. During online analysis, a preliminary spectrum was created which is shown in Fig. 2 (right). The spectrum seems to agree with the expected spectrum [6] which indicates the population of the T=3/2 isobaric analog state (IAS) of ^{7}He in the $J\pi$=3/2^{-} state of ^{7}Li. The last week of the run was spent with a beam of ^{9}Li from MARS to perform the ^{9}Li(p,n)^{9}Be measurement. The purpose of this reaction is to populate T=2 IAS states in ^{10}Be which are analogues to states in ^{10}Li. This will help us continue our investigation of ^{10}Li with previous reaction data of the ^{9}Li(p,p) reaction performed in late 2020 [7].

At the end of our beam time, we have begun analysis of the data. Additional data were taken from multiple γ and n/γ sources to be used for energy calibration and optimization of n/γ PSD. Background runs were also taken for later assessment. We are currently working out the energy and PSD calibrations on a crystal-by-crystal bases. Following this will be the incorporation of TDC information for kinetic energy reconstruction.

[1] D.P. Scriven *et al*., *Progress in Research*, Cyclotron Institute, Texas A&M University (2018-2019), p. IV-55.

[2] D.P. Scriven *et al*., *Progress in Research*, Cyclotron Institute, Texas A&M University (2019-2020), p. IV-112.

[3] C.E. Parker *et al*., *Progress in Research*, Cyclotron Institute, Texas A&M University (2018-2019), p. IV-52.

[4] D.P. Scriven *et al., Nucl. Instrum. Methods A* 1010, 165492 (2021)

[5] G.L. Engel *et al., Nucl. Instrum. Methods A* 612, 2009.10.058 (2009)

[6] G. V. Rogachev, *et al.,* Phys. Rev. Lett. 92, 232502 (2004).

[7] D.P. Scriven *et al*., *Progress in Research*, Cyclotron Institute, Texas A&M University (2020-2021), p. V-23.

DAPPER gamma ray response

M. Sorensen, A. Abbott, A.B McIntosh, R. Rider, K. Hagel, and S.J. Yennello

The purpose of DAPPER (Detector Array for Photons, Protons, and Exotic Resides) is to measure the photon strength function (PSF) of nuclei. The photon strength function describes the bulk quantum mechanical component of photon emission probabilities and thus it is important in describing the de-excitation process of neutron capture reactions. Of particular interest is the measurement of PSFs away from the line of stability, requiring radioactive beams. Direct neutron capture reactions on radioactive nuclei are typically not feasible due to both the beam and the target being unstable. To get around this problem, indirect (d,pγ) reactions will be used. In order to first test the methodology and setup of the proposed radioactive beam experiment, a stable ^{57}Fe(d,pγ)^{58}Fe experiment was done.

The DAPPER array is composed of 128 BaF_2 detectors and an S3 annular silicon detector. BaF_2 detectors provide high gamma ray efficiency which will be critical for future radioactive beam experiments. The proton produced in the reaction can be detected by the S3 annular silicon detector in order to measure the excitation energy of the residue. In addition, a faraday cup was installed at the end of the line to monitor the beam rate. On August 2nd 2021 the first run with DAPPER was conducted. ^{57}Fe at 7.5 MeV/u was accelerated at the end of the MARS line and impinged on a CD_2 target to produce an excited ^{58}Fe nucleus and a free proton. Carbon targets were also used in order to subtract out the gamma rays associated with reaction on carbon. A ^{13}C(d,pγ)^{14}C reaction was run in DAPPER, with a 8.0 MeV/u ^{13}C beam, in order to get high energy gamma rays for the calibration of the BaF_2 detectors.

One of the principal needs of a gamma ray detector array for radioactive beam measurements is to have high efficiency. Running a carbon subtraction on 13C (d,p) data we took allows us to test efficiency for high energy gamma rays. In Fig. 1A) the excitation energy of the ^{14}C is plotted against the

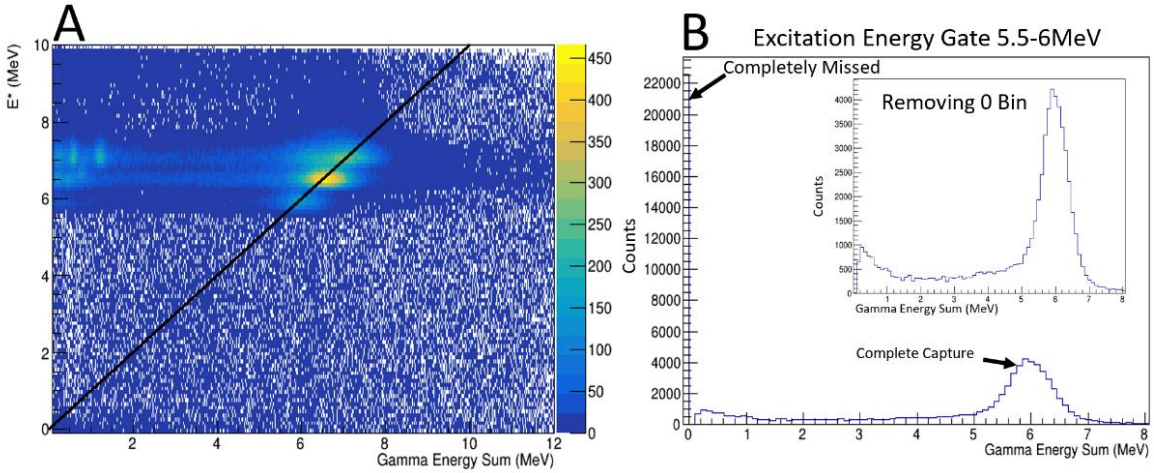

Fig. 1. A) Excitation energy of ^{14}C plotted as a function of the sum of the gamma ray energy seen in the BaF_2 detectors. The black line is the y=x line showing complete capture of the gamma rays in the array. Clear bands corresponding to the excited states of ^{14}C are seen. B) Gamma energy sum spectra, gating on excitation energies between 5.5 and 6 MeV. This gate picks up the first excited state of ^{14}C which emits a 6.0938 MeV gamma ray to the ground state. A strong complete capture peak is observed.

sum of all the energy seen in the BaF_2 detectors is shown. A strong y=x line is observed for regions of excitation corresponding to known states in ^{14}C. This indicates good collection efficiency for gamma ray collection in the DAPPER array. Gating on the first excited state of ^{14}C produces the energy sum spectrum seen in Fig. 1B). From this gate the probability we see something in the array is 73% for the 6.1 MeV gamma ray. The probability we get a sum within 300 KeV of the expected energy is 36%, if we expand the gate to be within 1 MeV this probability increases to 48%.

The energy calibration for the BaF_2 detectors has also been improved and quantified. The BaF_2 detectors were calibrated with multiple gamma ray sources placed in the target position. This allows us to both measure the efficiency of the array and get a well constrained energy calibration. In Fig. 2A) an example energy calibration is shown. Six gamma peaks are used in this energy calibration, ranging

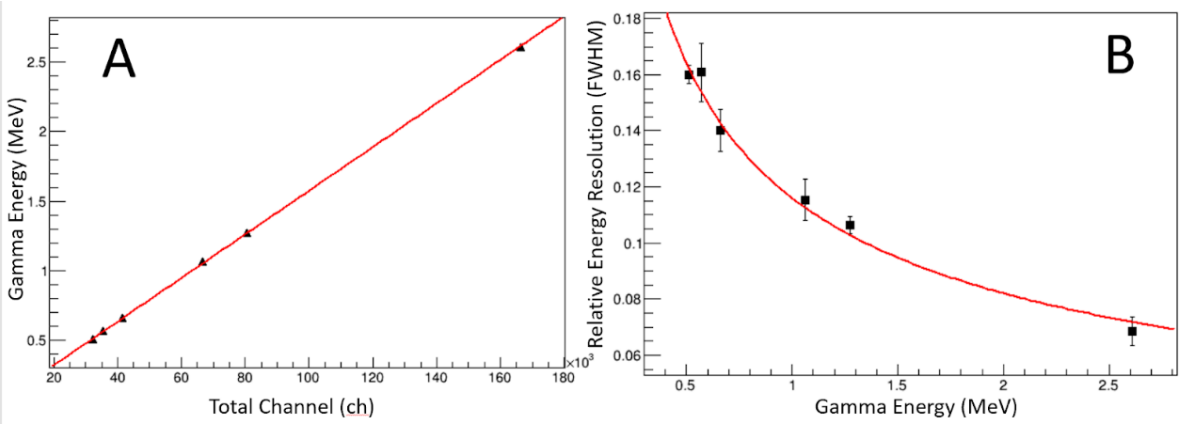

Fig. 2. A) Example energy calibration for one of the BaF_2 detectors. Red line is a linear fit through all points; error bars are smaller than marker size. The detector response looks very linear all the way up to 2.6MeV. B) Relative energy resolution as a function of gamma ray energy for the same detector. Red line is an a/√E fit to the data points, where a is a free parameter.

in energy from 0.511 MeV to 2.6 MeV. Fig. 2B) shows the energy resolution as a function of gamma ray energy; this quantity also needs to be measured in order to construct an accurate response function. A summary of all the detectors relative energy resolution at 1 MeV is shown in Fig. 3).

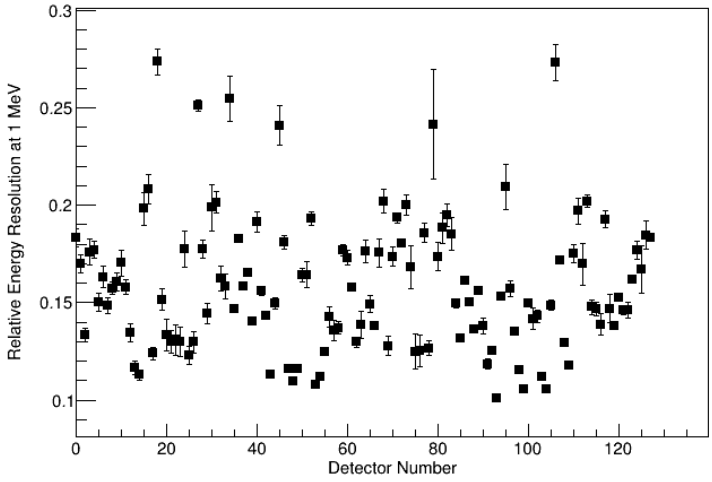

Fig. 3. Relative energy resolution at 1 MeV for each detector.

With the information from the source and $^{13}C(d,p\gamma)^{14}C$ reaction data as well as a constrained response function for the DAPPER array will soon be made. This response function will let us conduct our analysis of the ^{58}Fe PSF. In addition to being required for the current analysis, the response function will also be useful for simulating future experiments and testing their viability before they are scheduled and conducted.

DAPPER upgrade for radioactive beam contamination separation

R. Rider, A. Abbott, A.B. McIntosh, M. Sorensen, K. Hagel, and S.J. Yennello

The Detector Array for Photons, Protons, and Exotic Residues (DAPPER) has been designed to measure the photon strength function (PSF) of nuclei; specifically, to be used for radioactive beam experiments. Photon strength functions are important in the understanding of the de-excitation of neutron capture reactions. The proposed reactions that DAPPER is commissioned to complete are inverse kinematic (d,pγ) in order to get around the instability of neutron beams and radioactive targets. The first experiment in August 2021 using DAPPER was ^{57}Fe (d,pγ) ^{58}Fe to probe for the PSF of ^{58}Fe. The follow up experiment is the radioactive beam reaction ^{59}Fe (d,pγ) ^{60}Fe to probe for the PSF of ^{60}Fe.

DAPPER consists of 128 BaF_2 detectors for measuring the gamma rays and an S3 annular silicon detector which detects the protons ejected at backward angles from the projectile of interest. The ^{59}Fe beam proposed for the radioactive beam experiment has the composition given in Table 1. When the proton is measured from any (d,pγ) reaction, determining which of the incident nuclides it was, will determine if we keep the event on an event-by-event basis. As we are interested in the ^{60}Fe PSF, events where ^{59}Fe was not incident on the CD_2 targets should be thrown out. A detector capable of Co-Fe separation is necessary for the experiment, to reduce error and determine a meaningful PSF.

Table 1. ^{59}Fe Radioactive Beam Composition.

Nuclide	Percent Abundance
^{59}Fe	79%
^{59}Co	13%
^{57}Co	7%

The proposed experiment will be 7.5 MeV/u ^{59}Fe beam at $3x10^5$ pps impinged on a CD_2 target. Most detectors are unable to withstand the high rate of heavy ions without permanent damage. At Argonne National Lab and Oak Ridge National Lab, there are arrays currently using ionization chambers (IC) for (d,pγ) reactions for PSF's of interest [1]. Ionization chambers are able to handle the rate of direct beam we are interested in without permanent damage unlike a silicon. Due to the array's space constraints at the end of MARS (Momentum Achromat Recoil Separator), the preferred spot to add an ionization chamber is before the target. By placing the IC before the target, we reduce the beam velocity and increase our cross section. A reduction in beam velocity may reduce the likelihood of populating the high excitation states of ^{60}Fe. A simulation was developed using CycSrimDev to model the experimental results.

To model the experimental results, the first step was to determine how we collect charge from IC at high rate. Inside the IC there is gas (typically CF_4) at some pressure and alternating cathode and anode

foils to produce an electric field to collect the electrons from the ion-pair. Signals from all anodes can be combined and used to measure how much energy loss the particle experienced. Iron, possessing a lower Z than cobalt, results in less energy loss, a feature which can be exploited in order to separate the two nuclei. The windows will experience a bowing effect due to the pressure difference outside and inside the IC. Therefore, the area between the first foil and entrance window as well as the last foil and exit window cannot be used in data collection. Energy loss in all foils and windows themselves are accounted for in reducing beam velocity appropriately, but not used in data collection. The final summed energy loss through the areas of data collection for each nuclide are then smeared with a Gaussian of some width.

Fig. 1 shows the results from the simulation containing the following dimensions: Foils are 0.5 μm Mylar, Windows are 2 μm Mylar, CF_4 gas at 110 Torr, 9 foils in total, 5cm total gas length where the foils are equidistant across the 5cm of gas length. At 5% FWHM, the isotopic resolution can be seen, however with 10% FWHM, this isotopic resolution cannot be realized. 10% FWHM was taken from an IC similar to that in the simulation that quoted a ~10% FWHM at a rate of $3x10^5$ pps [2].

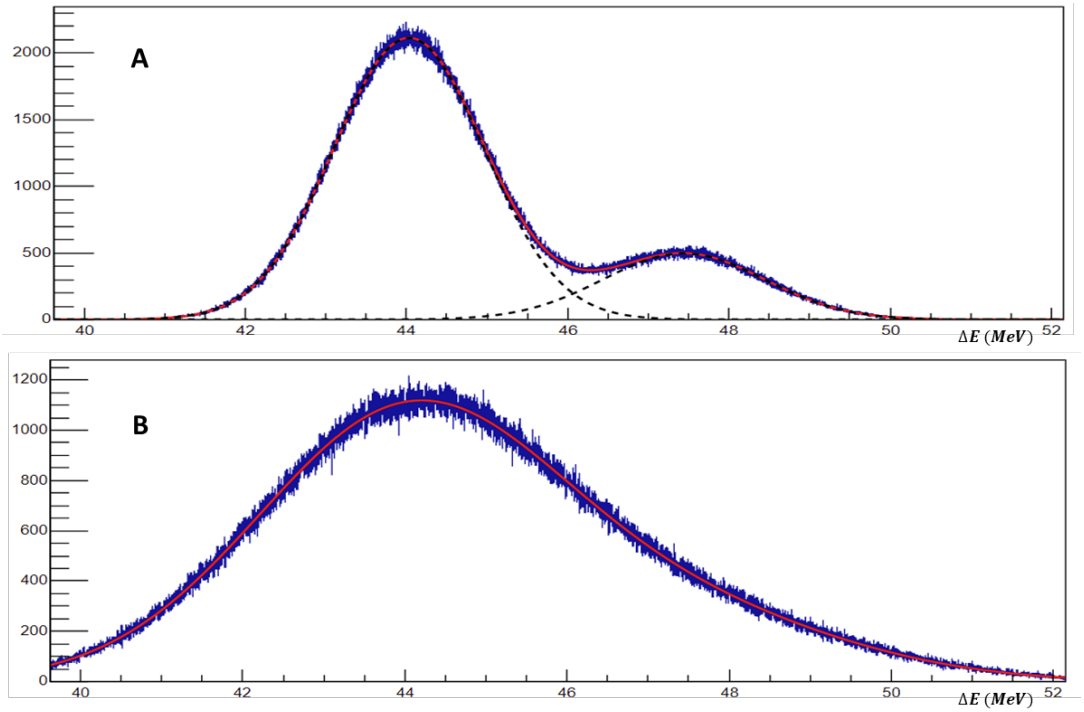

Fig. 1. Simulation results for IC that would be used for energy loss placed before the target. A is 5% FWHM. The dashed lines are fitting the two peaks respectively. Left peak represents ^{59}Fe and the right peak is both ^{59}Co and ^{57}Co. B is 10% FWHM.

At Oak Ridge and Argonne, the IC's are ΔE-E detectors at the end of the beamline. Each anode is output separately giving the experimentalist the versatility to determine which anodes in the IC are designated for the ΔE & E detector for separating contaminants optimally [1,3] . An Yttrium Aluminum Perovskite (YAP: Ce) array was constructed to be used at the end of DAPPER as a rate monitor [4]. Fig.2-A is produced by using the IC already implemented in the simulation as the ΔE detector and the YAP: Ce array for the E detector assuming 10% FWHM for both. Increasing the pressure and length of gas to 130

Torr and 15 cm respectively, we get Fig. 2-B. Fig. 2-B has some degree of separation where the densest circle represents the ^{59}Fe and the other two less dense are the cobalt isotopes. The changes to the IC for Fig. 2-B are done to model if we put the IC after the target and before the YAP: Ce array. The E detector is most useful when the particles are depositing their final energy closer to the Bragg peak as this is when the iron and cobalt nuclei have the largest difference in energy loss. If we could have a ΔE-E detector for the radioactive beam experiment, it would allow for a cut in 2-D energy space to minimize the contamination of cobalt and loss of iron events.

Currently, the specifications of the system in the simulation are being optimized to aid in the

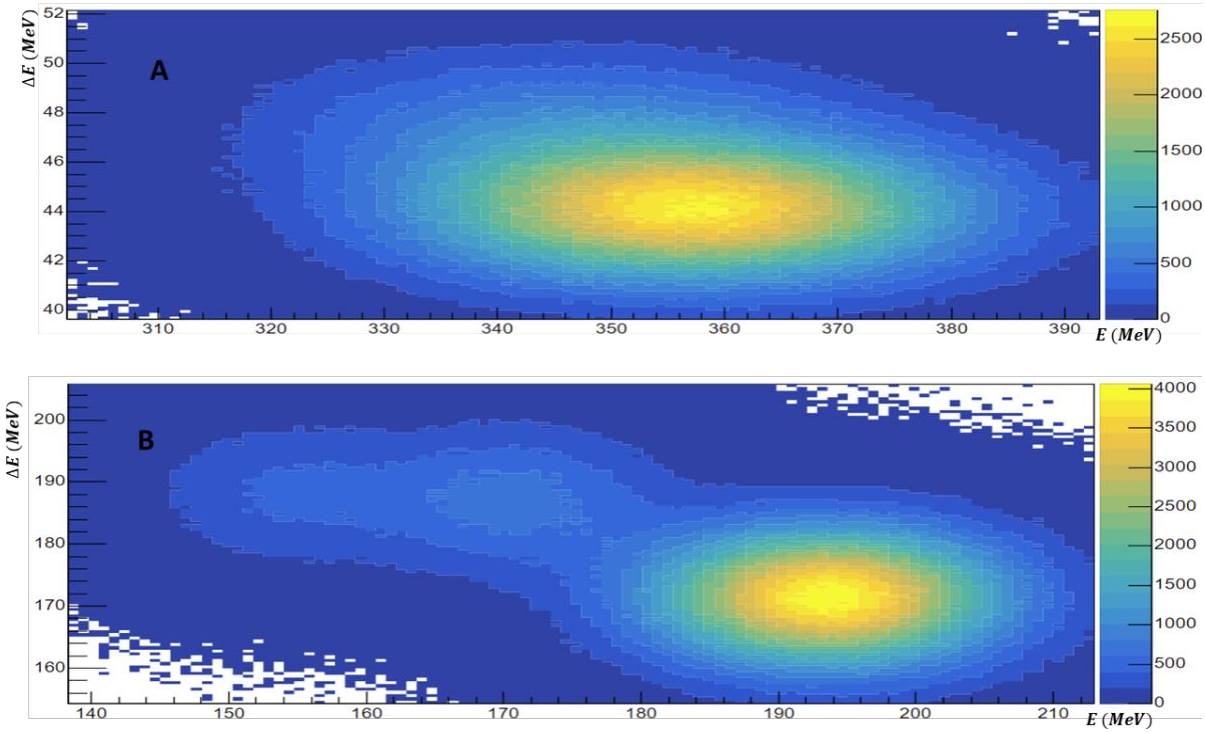

Fig. 2. Simulation results for IC as an ΔE detector and YAP:Ce array as an E detector. Both detectors have 10% FWHM. A is IC with 110 Torr and 5 cm gas length. B is C with 130 Torr and 15cm gas length.

production of a prototype of an IC for the DAPPER array's upgrade. Once the prototype is built, we will be able to with source data and/or a test run with a heavy ion "cocktail" beam be able to better understand the energy resolution of both the IC and YAP: Ce array before the proposed experiment.

[1] K.Y. Chae *et al.*, Nucl. Instrum. Methods Phys. Res. **A751**, 6 (2014).
[2] J. Vadas *et al.*, Nucl. Instrum. Methods Phys. Res. **A837**, 28 (2016).
[3] S.D. Pain *et al.*, Physics Procedia 90,455 (2017).
[4] A. Abbott *et al.*, Progress in Research, Cyclotron Institute, Texas A&M University (2020-2021), p. V-38.

Investigation of real-time and complementary particle discrimination capabilities in FAUST

T. Hankins, A. Hannaman, A.B. McIntosh, K. Hagel, B. Harvey, Z. Tobin, and S.J. Yennello

CsI(Tl) scintillating crystals as particle detectors exhibit a particle dependent light response; the optical characteristics of the light response, including absolute light output, rise time, and various decay times, provide multiple methods by which incident particles can be identified [1]. These particle identification (PID) methods have been shown to display varying degrees of success, ranging from standard *Z* discrimination [2] to stellar isotopic resolution [3]. In the case of the Forward Array Using Silicon Technology (FAUST), utilization of the zero-crossing time (ZCT) versus amplitude discrimination scheme resulted in defined isotopic resolution of hydrogen and clear discretization between ^{8}Li and α-α double hits [4].

Despite this success, problems can be encountered when employing alternate discrimination methods for data obtained from an array configuration involving secondary or tertiary detectors. In the case of FAUST, a demand for increased position sensitivity and angular resolution lead to the inclusion of a tertiary Duo-Axis Dual-Lateral (DADL) silicon detector layer. In this configuration, event triggering occurs based on signals received from the DADL and the CsI(Tl) crystal. This gives rise to a key issue: as a result of their low ionization density and stopping power, high energy protons can be improperly detected by failing to trigger the DADL but still triggering the crystal. In this instance, particle discrimination methods relying on DADL energies suffer. This problem has founded a desire for an alternate PID method that can work in tandem with a primary method (such as ZCT vs. Amplitude) and "recover" lost information. One method that does not rely on a secondary detector is pulse-shape discrimination, which instead relies directly on the characteristics of the CsI(Tl) scintillation response and therefore does not suffer as a result of missing secondary input. It is important to note that pulse-shape discrimination methods are normally not used independently or in place of other identification methods because most alternates outperform it [2], but nonetheless can provide rudimentary PID without relying on external information. As a result, the first focus of this work involves investigating the viability of pulse-shape discrimination as a supplement to particle identification methods dependent on external triggering.

Another potential issue encountered involves the event readout chain. Depending on the particle identification method, integration of either the raw or smoothed CsI(Tl) waveform is used [5]. Performing this method requires the waveform for every event be written to disk; in addition to commandeering large amounts of disk space, this approach severely inhibits the rate at which events can be read out (event rate saturation). However, the Struck Innovative Systems (SIS) 3316 VME waveform digitizer that is part of the electronics chain possesses eight integrators that perform real-time integrations of raw waveforms. Traditionally, one integrator is used to calculate the baseline of the waveform and, often, the second is used to calculate the maximum of the waveform, leaving six that can be distributed at times relative to the internal trigger. Studying the behavior of the waveforms produced by the CsI(Tl) crystal may provide insight regarding the plausibility of real-time particle discrimination using the remaining six integrators, rather than reading out entire waveforms and performing PID offline; this is the second focus of this work.

Data used in the subsequent analyses were obtained using 20 MeV/u ^{20}Ne incident on 3.1 mg/cm^2 ^{12}C; acquisition was conducted using a singular CsI(Tl) crystal optically coupled to a lucite light guide and a PIN photodiode and a DADL detector. Signals from the DADL and the CsI(Tl) crystal were read into SIS3316 digitizers programmed with a 0.75 μs pre-trigger delay.

Various PSD-related methodologies have been explored in this research. In the event that waveform characteristics were desired or waveforms had a low signal to noise ratio (SNR), information was retrieved via fit. The method used herein was of exponential functional form and minimized using the Minuit package built into the data analysis framework ROOT. The method was further improved through χ^2 and parameter variance guided trial-and-error optimization that permitted accurate fitting of waveforms independent of intrinsic SNR (Fig. 1). The most successful and therefore most explored approach was that of charge comparison, in which the waveform for each event is integrated in two separate regions, often denoted "slow" and "fast" (in reference to the nature of the decay components of CsI(Tl) scintillations), and then plotted against each other (Fig. 2). Efficiency of the method is determined based primarily on the degree of band separation, quantitated using figure-of-merit (FOM), and secondarily by the degree of spillover. Figure-of-merit is defined as the separation between the centroids of the peaks in a plot divided by the sum of the peak full widths at half maximum (FWHM) [5]; spillover is the measurement of the

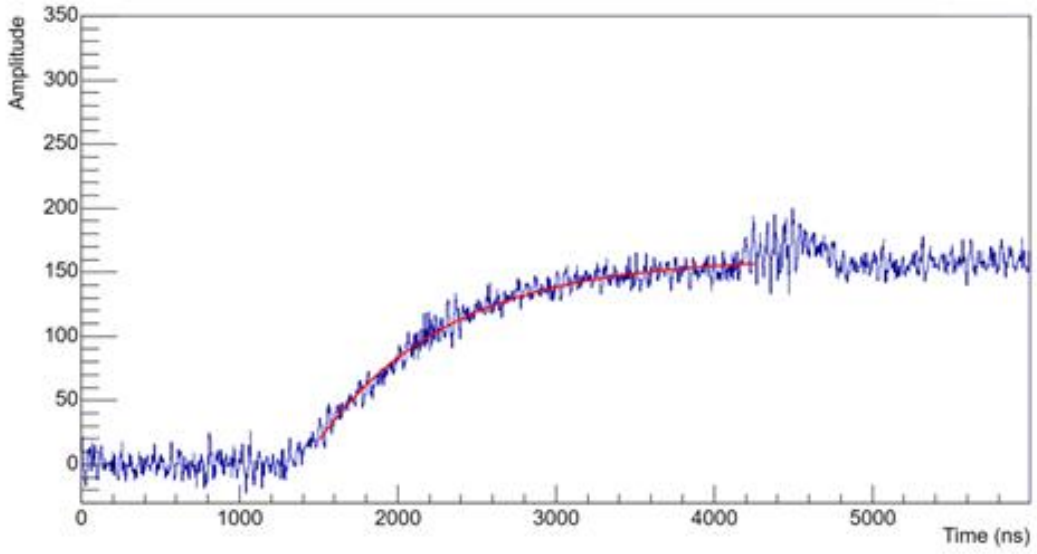

Fig. 1. Characteristic CsI(Tl) waveform (blue) superimposed with fit (red). The fit was produced using method described in the text; fit parameters have been omitted from the figure for simplicity.

percentage of events of a particular type of radiation misclassified as another type by localization in an incorrect region of interest (ROI) [2]. Spillover percentages for protons (p) and α particles are calculated

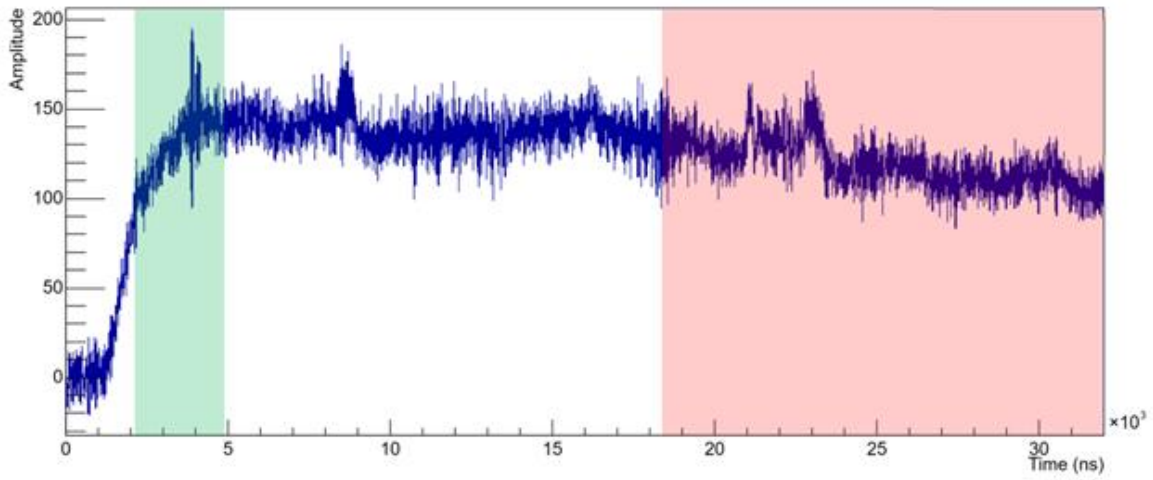

Fig. 2. Characteristic CsI(Tl) waveform (blue) superimposed with integration windows for the slow (red) and fast (green) components that yielded the greatest FOM.

by gating on localized bands in a ΔE-E plot, producing respective slow-fast plots, and determining the associated degrees of mismatch. Figures-of-merit are calculated by dividing the values in slow-fast space by either the slow or fast integration value, thus producing a resultant plot of arbitrary PID index versus the slow or fast value. This plot is then horizontally projected to produce a one-dimensional plot dependent solely on the PID index. The peaks present are fit with Gaussian functions and the associated FOM is determined from the parameters of the fits.

At the time of writing, the largest FOM achieved has been 0.981 (Fig. 2), accomplished using a slow integration across the last 13.6 μs of the total 32.0 μs waveform and a fast integration of 2.8 μs

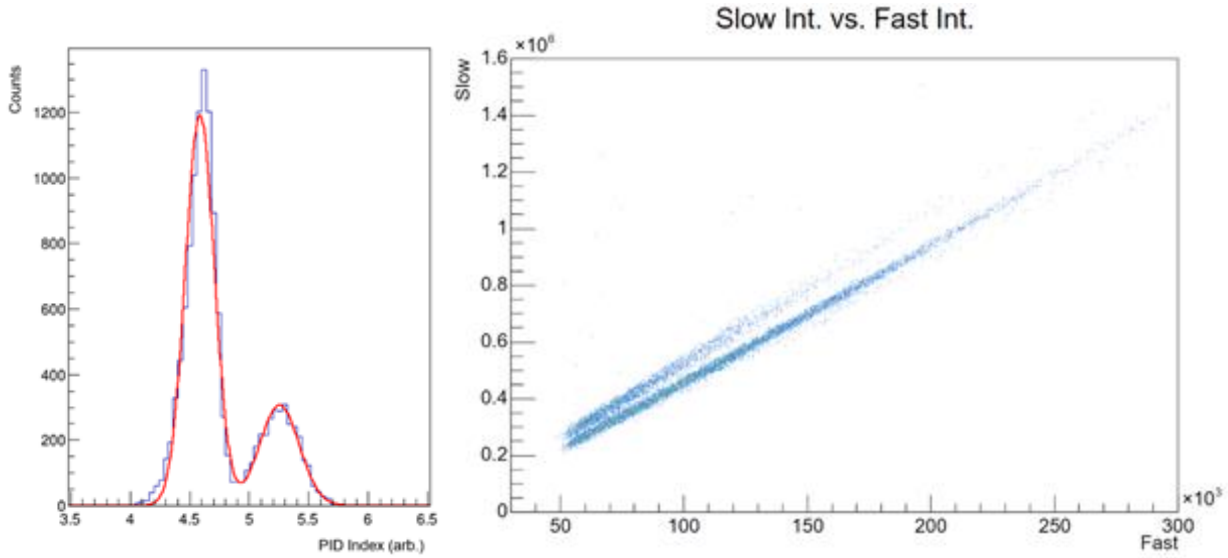

Fig. 3. Left: horizontal projection of the PID index versus number of events (counts). The FOM for this projection is 0.981; p are identified by the right peak and α by the left peak. Right: corresponding slow-fast plot of experimental data. Z-discrimination is achieved by clear band separation; isotopic resolution remains unfulfilled.

starting at an absolute time of 2.04 μs. Additionally, this configuration possessed spillover percentages of 8.94 and 1.81 for p into α and α into p, respectively. This optimization comes as a surprise; this fast configuration misses a substantial amount of the rise component of the CsI waveform (Fig. 3) which is what exhibits the greatest dependence on incident particle type [5]. Further investigation as to why this occurs is currently underway, but the Z discrimination achieved through pulse-shape integration of the waveform through predefined windows suggests that it may be possible to perform some degree of real-time particle discrimination using integrators. A FOM of 0.937 and maximum spillover of 8.94% bode well for online proton and alpha discrimination, but isotopic resolution has as of yet remained unfulfilled.

[1] R. S. Storey, W. Sack, and A. Ward, Proc. Phys. Soc. (London) **72**, 1 (1958).
[2] P. Chandrikamohan and T. DeVol, IEEE Trans. on Nucl. Sci. **54**, 2 (2007)
[3] M. Alderighi *et. al.*, Nucl. Instrum. Methods Phys. Res. **A489**, 257 (2002).
[4] R. Laforest *et al.*, Nucl. Instrum. Methods Phys. Res. **A404**, 470 (1998).
[5] W. Skulski and M. Momayezi, Nucl. Instrum. Methods Phys. Res. **A458**, 759 (2001).

Measuring charged particle reaction products from ^{28}Si + ^{12}C at 35 MeV/u using FAUST

A. Hannaman, K. Hagel, A.B. McIntosh, A. Abbott, J. Gauthier, T. Hankins, B. Harvey, Y-W. Lui, L. McCann, L.A. McIntosh, R. Rider, S. Schultz, M. Sorensen, Z. Tobin, R. Wada, and S.J. Yennello

FAUST (Forward Array Undertaking Search for Toroids) is a charged particle multi-detector array consisting of 68 Si-CsI(Tl) detector telescopes covering an angular range of 1.6° – 45°. The silicon detectors are position-sensitive (DADLs), measuring the position of incident particles through resistive charge splitting [1-4]. Due to distortions in the calculated energy and position of incident particles when using conventional electronics, detailed waveform analysis was performed, and a waveform treatment was developed to greatly minimize these distortions [5]. Additionally, multievent readout of the Struck SIS-3316 waveform digitizers used for DADL readout and the Mesytec MADC-32s used for CsI(Tl) readout was implemented to maximize the data collection rate of FAUST. With these improvements, reaction products from collisions of 35 MeV/u ^{28}Si on ^{12}C were recently measured, obtaining 150 million events containing charged particle detection. This work aims to search for further evidence of high-excitation toroidal states in the α(^{4}He)-disassembly of ^{28}Si, and to gain insight to the α-clustered structure and properties of α-conjugate nuclei [6].

Particle identification in FAUST is performed using the ΔE (DADL Si) – E (CsI(Tl)) technique that takes advantage of particle charge, mass, and energy dependence of ion energy loss through matter. The discrete bands seen in Fig. 1(a) show elemental separation, with the finer structure separating isotopes. The resolution of the DADL passage detectors and CsI(Tl) stopping detectors of FAUST allowed for isotopic resolution up through the beam species (^{28}Si). Isotopic yields for all measured particles in the present dataset are shown in Fig. 1(b). The position sensitivity of the DADL detectors afford excellent angular information for each detected particle. The angle of detected particles can be projected to give a depiction similar to viewing FAUST from the target position as shown in Fig. 1(c).

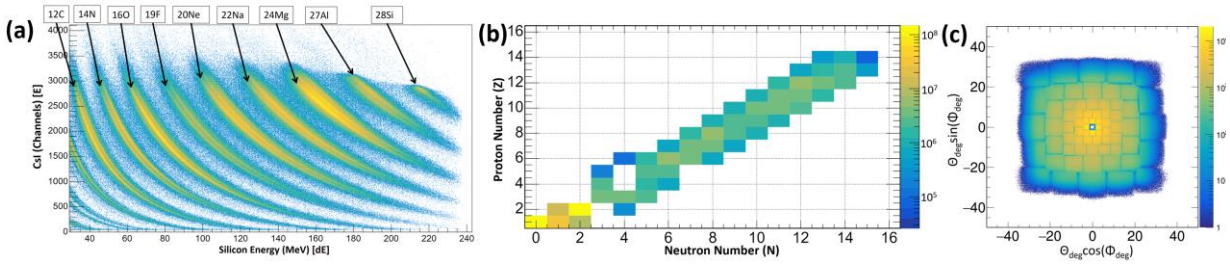

Fig. 1. (a) Representative FAUST ΔE (DADL Si) – E (CsI(Tl)) spectrum showing isotopic resolution of reaction products up through ^{28}Si. (b) Total yield as a function of isotope proton number and neutron number measured in the present dataset. (c) A projection of detection angle for all particles in FAUST.

The parallel and transverse velocities of particles with the same proton number (Z) is shown in Fig 2. The low velocity cutoff for particles up to Z = 8 is due to the threshold velocity required to punch through the DADL detector and implant in the CsI(Tl) for particle identification. For Z ≥ 9, the low velocity cutoff is due to large energy deposits in the DADL saturating the preamplifiers. The ray-like features for Z = 1 is due to the increasing difficulty of triggering on high energy light particles incident

near the edge of the DADL, as the charge splitting gives small signals on the far side of the DADL that can be below threshold.

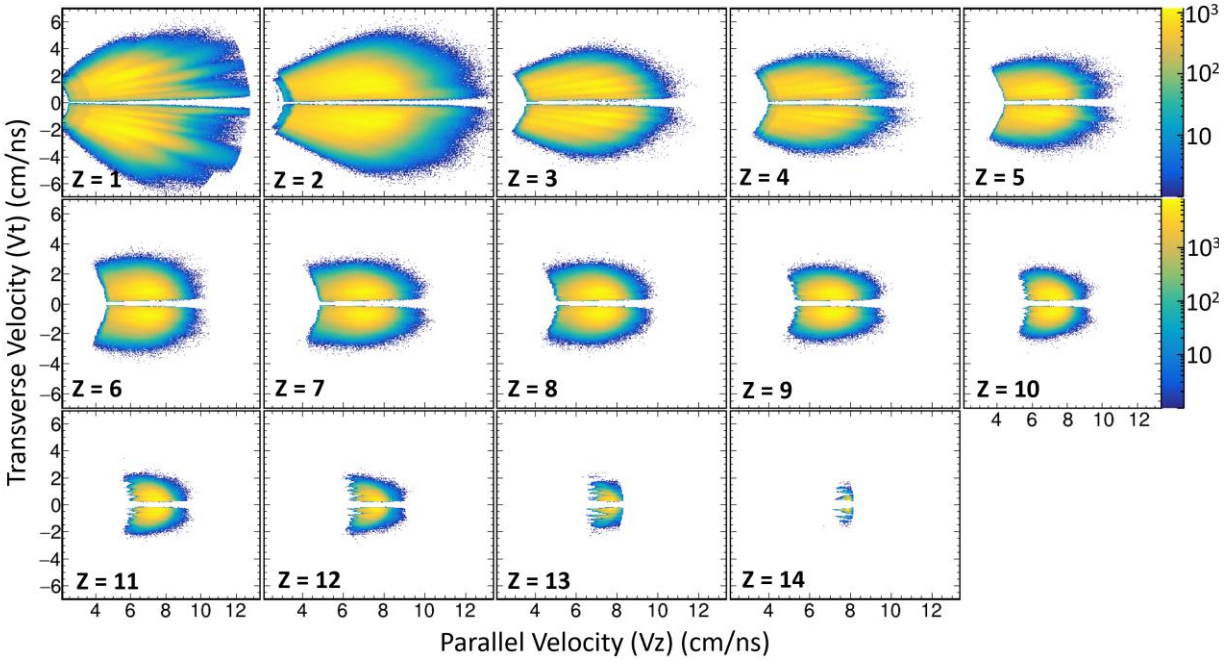

Fig. 3. Component of velocity transverse to beam axis as a function of the parallel component of velocity along beam axis in cm/ns for all particles measured in the dataset. Each panel contains particles with the same proton number.

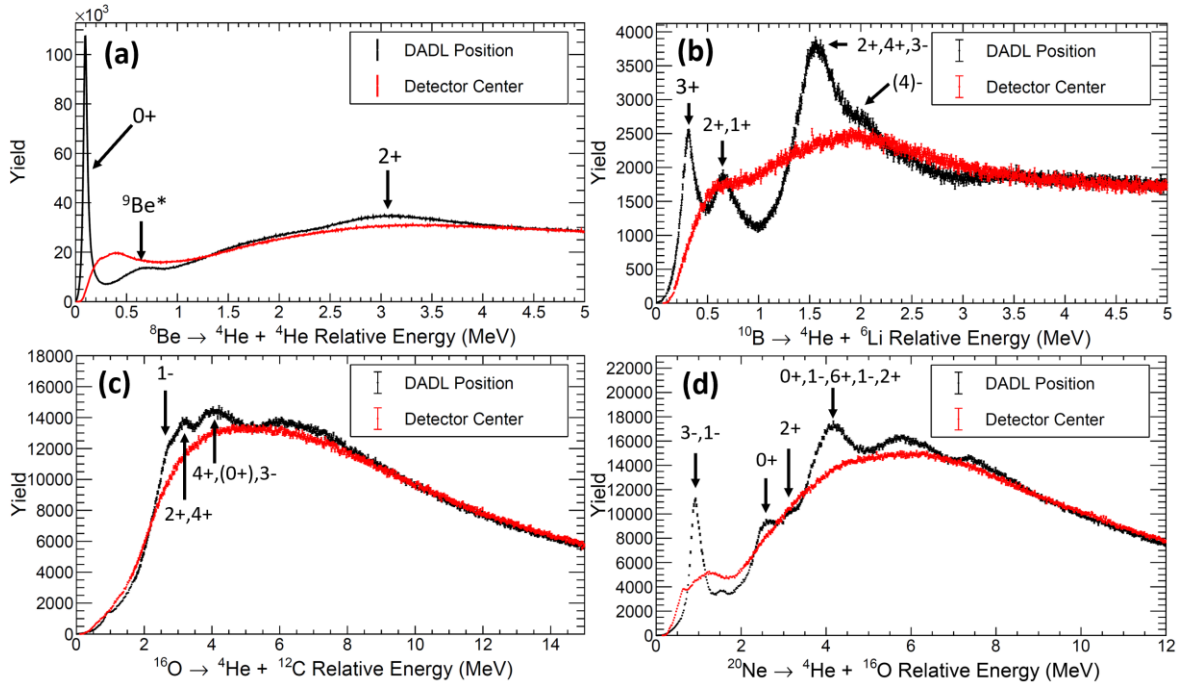

Fig. 2. Two-particle relative energy spectra for events containing at least one α-particle and a complementary particle to look for states associated with the α-emission of various N=Z nuclei. Each panel shows the distribution obtained when using the measured DADL detector position (black) and assuming the particle hit the center of the detector (red). Spin and parity of known states are assigned to some observed peaks. (a - d) α – (α, ^{6}Li, ^{12}C, ^{16}O) relative energy in MeV probing states in ^{8}Be, ^{10}B, ^{16}O, ^{20}Ne respectfully.

To resolve excited states of nuclei that undergo charged particle decay, as well as observe possible α-cluster resonances, precise angular information between measured particles is important. The position sensitivity of FAUST is crucial for this study as evidenced by Fig. 3, where multiple states are observed for these selected decay channels. Charged particles detected in arrays that use single-pad silicon detectors are typically assumed to be incident in the center of each detector, causing the angular resolution to be dictated by the angular granularity (array geometry and number of detectors). The improvement between this treatment(red) and implementing the DADL position(black) is considerable. Many states are entirely unobserved in the center-of-detector treatment due to the large systematic error in particle angle. Detailed analysis of this dataset is currently underway.

[1] L.A. Heilborn, PhD thesis, Texas A&M University, 2018; http://hdl.handle.net/1969.1/174435.
[2] L.A. McIntosh *et al.,* Nucl. Instrum. Methods Phys. Res. **A985**, 164642 (2021).
[3] S.N. Soisson *et al.,* Nucl. Instrum. Methods Phys. Res. **A613**, 240, (2010).
[4] 1 Royal Buildings, Lancing, Business Park, West Sussex, BN15 8SJ, UK. Micron Semiconductor Ltd. http://micronsemiconductor.co.uk
[5] M.W. Aslin, A. Hannaman *et. al.,* Nucl. Instrum. Methods Phys. Res. **A985**, 164674 (2021).
[6] X.G. Cao *et al.,* Phys. Rev. C **99**, 014606 (2019).

Parallel-plate avalanche counter (PPAC) detector commissioned for the MDM focal plane

E. Harris,[1,2] G.V. Rogachev,[1,2] G. Chubaryan,[1] H. Jayatissa,[1,2,3] E. Koshchiy,[1] and K. Rao[1,2,4]
[1]*Cyclotron Institute, Texas A&M University, College Station, Texas 77843*
[2]*Department of Physics & Astronomy, Texas A&M University, College Station, Texas 77843*
[3]*Argonne National Laboratory, Lemont, Illinois, 60439*
[4]*Department of Physics & Astronomy, Rice University, Houston, Texas, 77005*

PPACs have played an important role in nuclear science since the recognition of their superior performance as heavy-ion detectors [1, 2]. They exhibit many desirable characteristics such as their simple design, resistance to radiation damage, arbitrary sizing allowing for large solid angles, and straightforward particle identification from position and timing. The commissioning of such a detector for the Texas A&M Cyclotron Institute (CI) began because of the need to measure low-energy heavy ions for future experiments. The primary design criteria were that the detectors should provide a reasonable position resolution to separate ions with similar magnetic rigidities, a high time resolution, and minimal energy loss for heavy ions. A PPAC detector system has since been developed and manufactured at the CI to be used in conjunction with the Multipole-Dipole-Multipole (MDM) spectrometer [3]. TexPPAC will be utilized for experiments with low energy stable beams to constrain reaction rates and other parameters of relevant astrophysical processes. Since its installment on the MDM beamline in September 2020, it has been utilized for several experiments including the measurement of ANCs relevant to the $^{12}C(\alpha,\gamma)^{16}O$ reaction, the determination of branching ratios for the ^{12}C Hoyle state, and the study of alpha decay branches in ^{19}Ne via the $^{21}Ne(p,t)^{19}Ne$ reaction.

TexPPAC consists of two plane-parallel PPAC detectors separated by a variable distance that may be chosen to fit the needs of the experiment. Each PPAC is made of two electrodes on either side of a central biased electrode. The central cathode is made of a 220 μg/cm^2 Mylar foil with a 80 μg/cm^2 aluminum coating on both sides. The anodes consist of two PCBs with X- and Y-direction wires made of a Be-Cu alloy with a diameter of 50 μm. There is a 0.635 mm pitch between each wire which spans 40 cm x 10 cm creating the active region of the detector.

The parallel plate geometry allows for a uniform electric field between the electrodes where electron amplification occurs in the quencher gas used to fill the detector chamber. When a particle travels through the detector, it ionizes the gas between the electrodes creating electron-ion pairs. These electrons produced from the primary ions may gain sufficient kinetic energy through acceleration in the strong electric field and cause a subsequent avalanche of electrons known as a Townsend avalanche [4]. Three electrical pulses are produced from this process: two from the X-plane and Y-plane anode wires giving 2D position signals, and one from the central cathode giving the timing signal.

2D position information from the anode wires is obtained by the delay-line readout method. One side of each wire array is connected to a common ground while the other end of each wire in the array is sent to its respective delay line in the X- or Y- direction. All four delay lines were created by wrapping a coated copper wire around a PCB. The X and Y delay lines have a 287 Ω and 214 Ω impedance respectively. The position of the impinging particle is determined by the time difference between the signals that are transmitted to either end of the delay line. By utilizing the fast avalanche electron signals

from the anode wires, the detector can handle high beam rates of a few MHz (~ $5x10^6$ pps) [4]. Fig. 1 shows components of the fully assembled TexPPAC detector.

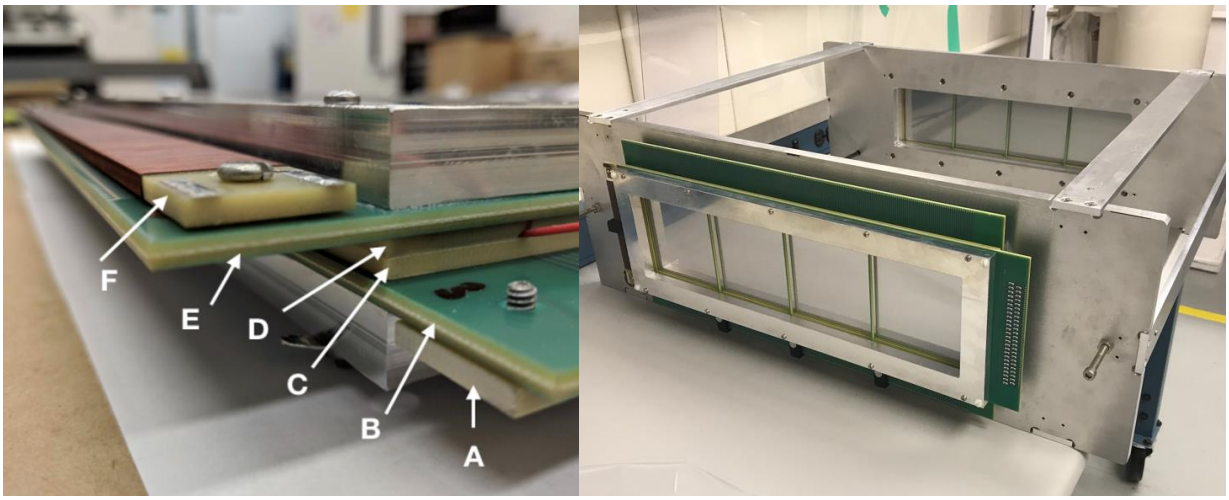

Fig. 1. (a) A picture of the order of the individual components of a PPAC detector. A) Delay line for Y-anode. B) Y-anode. C) PCB with mylar foil glued on top. D) 3mm Spacer. E) X-anode. F) Delay line for X-anode. (b) Fully assembled Tex-PPAC detector on frames.

To reduce the energy loss of the low-energy ions, the TexPPAC detectors were placed in a single gas volume with only one entrance window into the chamber. The entrance window is made of a thin Mylar film of 2 μm thickness. Very low pressures of Pentane gas between 3-8 Torr were used to further decrease interference along the ion path. The stability of the gas pressure was maintained with an inlet needle valve and an outlet scroll pump with a gas flow controller.

In order to investigate the characteristics of the TexPPAC detector, an experiment was performed using a 10 MeV/u beam of ^{20}Ne that was impinged on a ^{97}Au target of 600 μg/cm^2 thickness. With the MDM set to 15 degrees from the beam axis and the detection of scattered ^{20}Ne in TexPPAC, we were able to gather information about the detector specifications and overall performance. The position signals from each delay line and the time signals from each PPAC cathode were amplified by custom-made fast current

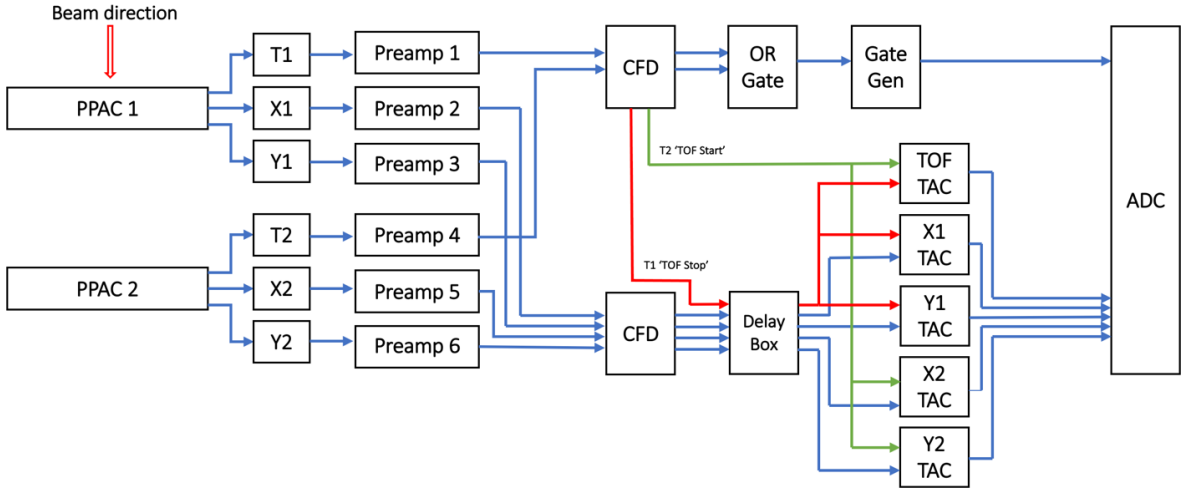

Fig. 2. Electronics and DAQ setup used for TOF, position, and efficiency measurements.

pre-amplifiers. Fig. 2 shows a schematic of the electronics used for the commissioning experiment.

The time resolution was calculated via the ion time-of-flight (TOF) between the cathodes of the two PPAC detectors. Measurements were performed with different gas pressures to find the optimal running conditions and the corresponding time resolutions. The gas pressure was increased from 2-7 Torr in steps of 1 Torr, while the bias voltage was finely tuned for each pressure setting to obtain the highest detection efficiency. Fig. 3(a) shows a typical TOF spectrum where the MDM was set to send ^{20}Ne down the center of TexPPAC, and 3(b) shows the time resolution as a function of gas pressure. It can be seen that the time resolution tends to improve as the gas pressure decreases. The ideal running condition gave a time resolution of 755.8 ps.

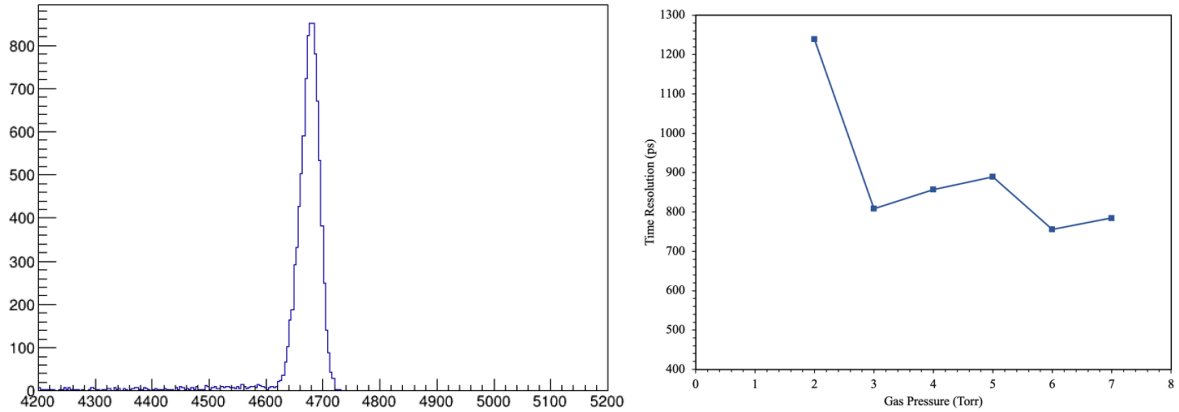

Fig. 3. (a) TOF spectrum for 6 torr of Pentane gas (Y axis in channels). (b) Plot of time resolution as a function of gas pressure.

The setup with the highest time resolution was chosen to characterize the position resolution and efficiency. The position resolution was found by setting the MDM to send scattered beam directly down the center of TexPPAC. As shown in Fig. 1(b), there is a central support column of 2 mm thickness along the active region of the detector. This column can be seen in the X-plane position spectrum of PPAC-1 in Fig. 4(a). Since it is not fully resolved, this indicates the resolution is worse than 2 mm. The '5-finger'

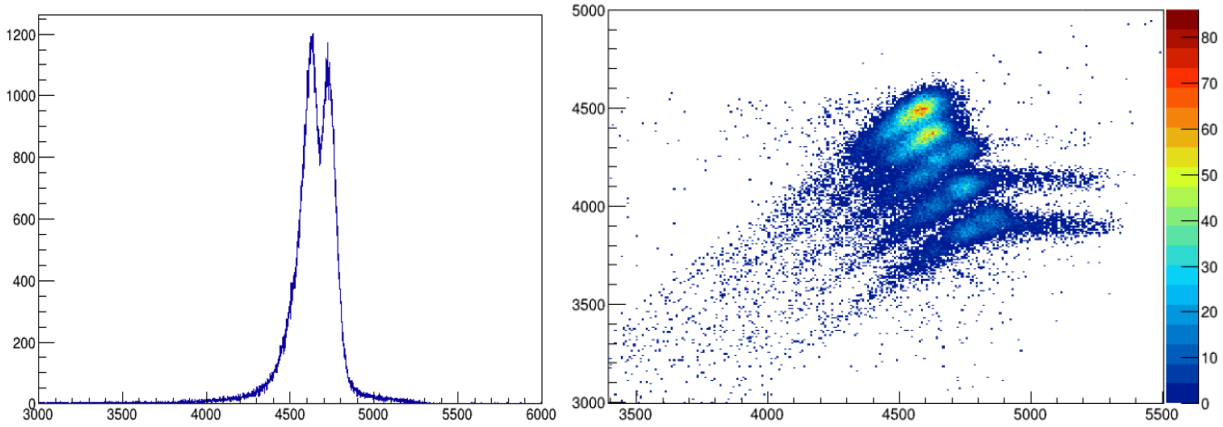

Fig. 4. (a) X position in PPAC-1 showing the effect of the 1 mm central support frame (b) Plot of X2 vs. X1 for the 5-finger mask.

mask located upstream of the MDM was also used to determine the position resolution (Fig 4(b)). The mask has five rectangular slits that are each 11.7 mm high and 1.6 mm wide. They are made of brass with a lead backing to stop particles that don't pass through the slit. A position resolution of 6.0 mm was found for the slits of 1.6 mm width.

To calculate the efficiency of both PPACs, the timing signal of either PPAC-1 or PPAC-2 was used as the trigger for the DAQ system. The detection efficiency of each setup can be calculated by:

$$\varepsilon_1 = \frac{N_1 \& N_2}{N_1} \qquad \varepsilon_2 = \frac{N_1 \& N_2}{N_2} \tag{1}$$

where N_1 and N_2 are the number of events in PPAC-1 and PPAC-2 respectively, and $N_1 \& N_2$ is the coincident number of events seen in both PPACs. High efficiencies of ε_1 = 98% and ε_2 = 99% were found.

TexPPAC has been characterized with this commissioning run and will continue to be used for experiments on the MDM beamline. The high timing resolution, reasonable position resolution, and high efficiency allows for reliable particle identification with TOF and position measurements in the MDM focal plane.

[1] J. Christiansen *et al.*, Nucl. Phys. **A239**, 253 (1975).

[2] H. Steltzer, Nucl. Instrum. Methods **133**, 409 (1976).

[3] H. Jayatissa *et al.*, *Progress in Research*, Cyclotron Institute, Texas A&M University, (2018-2019) p. IV-42.

[4] H. Kumagai *et al.*, Nucl. Instrum. Methods Phys. Res. **B317**, 717 (2013).

MARS status report for 2021-2022

B.T. Roeder and A. Saastamoinen

This year, we continued the program of providing rare isotope beams (RIBs) for the physics program at the Cyclotron Institute at Texas A&M University with the Momentum Achromat Recoil Separator (MARS) [1]. The MARS beam line was utilized in 9 separate experimental runs for various experiments involving both stable and rare isotope beams. The stable beam experiments included ^{57}Fe and ^{94}Zr beams for experiments with the DAPPER array in collaboration with Professor Yennello's group and beams of ^{170}Yb, ^{174}Yb and ^{176}Yb for experiments with the ENCORE detector in collaboration with a group from Florida State University.

Several experiments with rare isotope beams were conducted with ions that had been developed in previous years. A summary of these RIBs is given in Table I. The ^{11}Be, ^{13}O, ^{6}He, and ^{9}Li beams were produced for experiments of Professor Rogachev's group. The ^{7}Be was used in an experiment in collaboration with a group from Louisiana State University as part of the CENTAUR collaboration. The ^{29}P beam was for a precise half-life measurement for Professor Melconian's group. Finally, the search for heavy N=Z nuclei such as ^{72}Kr and ^{70}Br was part of the REU experiment for 2021.

Table I. Summary of MARS RIBs for 2021-2022.

RIB beam	Reaction	Production Rate (eV/nC)	Purity	Intensity on Target (est.)
^{11}Be	^{13}C+^{9}Be at 30 MeV/u (Fragmentation)	32 eV/nC	~90%	~10^4 p/s
^{72}Kr,^{70}Br	^{78}Kr+Ni at 35 MeV/u (Fragmentation)	Not determined	N.A.	1-2 p/hr
^{13}O	^{3}He(^{14}N,^{13}O)X	17.4 eV/μC	~80%	~10^2 p/s
^{29}P	p(^{30}Si,^{29}P)2n	855 eV/nC	~99%	~2*10^4 p/s
^{7}Be	p(^{7}Li,^{7}Be)n	3700 eV/nC	100%	1.2*10^5 p/s
^{6}He	d(^{7}Li,^{6}He)^{3}He	180 eV/nC	50%	~10^4 p/s
^{9}Li	^{18}O(^{7}Li,^{9}Li)X	8.5 eV/nC	~26%	~10^3 p/s

[1] R.E. Tribble, R.H. Burch, and C.A. Gagliardi, Nucl. Instrum. Methods Phys. Res. A**285**, 441 (1989).

SECTION V

PUBLICATIONS

PAPERS PUBLISHED
April 1, 2021– March 31, 2022

Asymptotic normalization coefficients in nuclear reactions and nuclear astrophysics, A.M. Mukhamedzhanov and L.D. Blokhintsev, Eur. Phys. J. A **58**, 29 (2022).

Controlling the worldwide chaotic spreading of COVID-19 through vaccinations, Hua Zheng and Aldo Bonasera, J. Mod. Phys. **13**, 1 (2022).

Determining impact parameters of heavy-ion collisions at low-intermediate incident energies using deep learning with convolutional neural networks, X. Zhang, X. Liu, Y. Huang, W. Lin, H. Zheng, R. Wada, A. Bonasera, Z. Chen, L. Chen, J. Han, R. Han, M. Huang, Q. Hu, Q. Leng, C.W. Ma, G. Qu, P. Ren, G. Tian, Z. Xu, Z. Yang, and L. Zhang, Phys. Rev. C **105**, 034611 (2022).

Evolution of Λ polarization in the hadronic phase of heavy-ion collisions, Yifeng Sun, Zhen Zhang, Che Ming Ko, and Wenbin Zhao, Phys. Rev. C **105**, 034911 (2022).

Elliptic flow splittings in the Polyakov–Nambu–Jona-Lasinio transport model, W.H. Zhou, H. Liu, F. Li, Y.F. Sun, J. Xu, and C.M. Ko, Phys. Rev. C **104**, 044901 (2021).

Experimental study of the ^{30}Si(^{3}He,d)^{31}P reaction and thermonuclear reaction rate of ^{30}Si(p,γ)^{31}P, D. S. Harrouz, N. de Séréville, P. Adsley, F. Hammache, R. Longland, B. Bastin, T. Faestermann, R. Hertenberger, M. La Cognata, L. Lamia, A. Meyer, S. Palmerini, R.G. Pizzone, S. Romano, A. Tumino, and H.-F. Wirth, Phys. Rev. C **105**, 015805 (2022).

Exploring the astrophysical energy range of the ^{27}Al(p,α)^{24}Mg reaction: A new recommended reaction rate, M. La Cognata, S. Palmerini, P. Adsley, F. Hammache, A. Di Pietro, P. Figuera, R. Alba, S. Cherubini, F. Dell'Agli, G.L. Guardo, M. Gulino, L. Lamia, D. Lattuada, C. Maiolino, A. Oliva, R.G. Pizzone, P.M. Prajapati, S. Romano, D. Santonocito, R. Spartá, M.L. Sergi, and A. Tumino, Phys. Lett. B **826**, 136917 (2022).

Fragment intrinsic spins and fragments' relative orbital angular momentum in nuclear fission, Aurel Bulgac, Ibrahim Abdurrahman, Kyle Godbey, and Ionel Stetcu, Phys. Rev. Lett. **128**, 022501 (2022).

Hot and dense matter equation of state probability distributions for astrophysical simulations, Xingfu Du, Andrew W. Steiner, and Jeremy W. Holt, Phys. Rev. C **105**, 035803 (2022).

Investigating the predicted breathing-mode excitation of the Hoyle state, K.C.W. Li, F.D. Smit, P. Adsley, R. Neveling, P. Papka, E. Nikolskii, J.W. Brümmer, L.M. Donaldson, M. Freer, M.N. Harakeh, F. Nemulodi, L. Pellegri, V. Pesudo, M. Wiedeking, E.Z. Buthelezi, V. Chudoba, S.V. Förtsch, P. Jones, M.

Kamil, J.P. Mira, G.G. O'Neill, E. Sideras-Haddad, B. Singh, S. Siem, G.F. Steyn, J.A. Swartz, I.T. Usman, and J.J. van Zyl, Phys. Lett. B **827**, 136928 (2022).

Isoscalar giant monopole resonance in ^{24}Mg and ^{28}Si: Effect of coupling between the isoscalar monopole and quadrupole strength, A. Bahini, V.O. Nesterenko, I.T. Usman, P. von Neumann-Cosel, R. Neveling, J. Carter, J. Kvasil, A. Repko, P. Adsley, N. Botha, J.W. Brümmer, L.M. Donaldson, S. Jongile, T.C. Khumalo, M.B. Latif, K.C.W. Li, P.Z. Mabika, P.T. Molema, C.S. Moodley, S.D. Olorunfunmi, P. Papka, L. Pellegri, B. Rebeiro, E. Sideras-Haddad, F.D. Smit, S. Triambak, and J.J. van Zyl, Phys. Rev. C **105**, 024311 (2022).

Measurement of cold nuclear matter effects for inclusive J/ψ in p+Au collisions at $\sqrt{s_{NN}}$ = 200 GeV, M.S. Abdallah, D.M. Anderson, C.A. Gagliardi, A. Hamed, T. Lin, X. Liu, Y. Liu, S. Mioduszewski, N.R. Sahoo, and R.E. Tribble, Phys. Lett. B **825**, 136865 (2022).

Measurement of inclusive electrons from open heavy-flavor hadron decays in p+p collisions at $\sqrt{s}$ = 200 GeV with the STAR detector, M.S. Abdallah, D.M. Anderson, C.A. Gagliardi, A. Hamed, T. Lin, X. Liu, Y. Liu, S. Mioduszewski, N.R. Sahoo, and R.E. Tribble, Phys. Rev. D **105**, 032007 (2022).

Modular next generation fast-neutron detector for portal monitoring, E. Aboud, S. Ahn, G.V. Rogachev, V.E. Johnson, J. Bishop, G. Christian, E. Koshchiy, C.E. Parker, and D.P. Scriven*, Nucl. Sci. Tech. **33**, 13 (2022).

Multiprobe study of excited states in ^{12}C: Disentangling the sources of monopole strength between the energy of the Hoyle state and E_x=13 MeV, K.C.W. Li, P. Adsley, R. Neveling, P. Papka, F.D. Smit, E. Nikolskii, J.W. Brümmer, L.M. Donaldson, M. Freer, M.N. Harakeh, F. Nemulodi, L. Pellegri, V. Pesudo, M. Wiedeking, E.Z. Buthelezi, V. Chudoba, S.V. Förtsch, P. Jones, M. Kamil, J.P. Mira, G.G. O'Neill, E. Sideras-Haddad, B. Singh, S. Siem, G.F. Steyn, J.A. Swartz, I.T. Usman, and J.J. van Zyl, Phys. Rev. C **105**, 024308 (2022).

Number-of-constituent-quark scaling of elliptic flow: a quantitative study, Meng Wang, Jun-Qi Tao, Hua Zheng, Wen-Chao Zhang, Li-Lin Zhu, and Aldo Bonasera, Nucl. Sci. Tech. **33**, 9 (2022).

Occupation probabilities of valence orbitals relevant to neutrinoless double β decay of ^{124}Sn, A. Shrivastava, K. Mahata, I. Stefan, M. Assié, P. Adsley, D. Beaumel, V.M. Datar, A. Georgiadou, J. Guillot, F. Hammache, N. Keeley, Y.H. Kim, A. Meyer, V. Nanal, V.V. Parkar, and N. de Séréville, Phys. Rev. C **105**, 014605 (2022).

Probing the gluonic structure of the deuteron with J/ψ photoproduction in d+Au ultraperipheral collisions, M.S. Abdallah, D.M. Anderson, C.A. Gagliardi, A. Hamed, T. Lin, X. Liu, Y. Liu, S. Mioduszewski, N.R. Sahoo, and R.E. Tribble, Phys. Rev. Lett. **128**, 122303 (2022).

Search for the chiral magnetic effect via charge-dependent azimuthal correlations relative to spectator and participant planes in Au+Au collisions at $\sqrt{s_{NN}}$ = 200 GeV, M.S. Abdallah, D.M. Anderson, C.A. Gagliardi, A. Hamed, T. Lin, X. Liu, Y. Liu, S. Mioduszewski, N.R. Sahoo, and R.E. Tribble, Phys. Rev. Lett. **128**, 092301 (2022).

Search for the chiral magnetic effect with isobar collisions at $\sqrt{s_{NN}}$ = 200 GeV by the STAR Collaboration at the BNL Relativistic Heavy Ion Collider, M.S. Abdallah, D.M. Anderson, C.A. Gagliardi, A. Hamed, T. Lin, X. Liu, Y. Liu, S. Mioduszewski, N.R. Sahoo, and R.E. Tribble, Phys. Rev. C **105**, 014901 (2022).

Separation, speciation, and mechanism of astatine and bismuth extraction from nitric acid into 1-octanol and methyl anthranilate, E.E. Tereshatov, J.D. Burns, A.L. Vonder Haar, S.J. Schultz, L.A. McIntosh, G.C. Tabacaru, L.A. McCann, G. Avila, A. Hannaman, K.N. Lofton, M.A. McCarthy, B. Zhang, M.B. Hall, and S.J. Yennello, Sep. Purif. Technol. **282**, 120088 (2022).

(^{6}Li,d) and (^{6}Li,t) reactions on ^{22}Ne and implications for s-process nucleosynthesis, S. Ota, G. Christian, W. N. Catford, G. Lotay, M. Pignatari, U. Battino, E.A. Bennett, S. Dede, D.T. Doherty, S. Hallam, F. Herwig, J. Hooker, C. Hunt, H. Jayatissa, A. Matta, M. Moukaddam, E. Rao, G.V. Rogachev, A. Saastamoinen, D. Scriven, J.A. Tostevin, S. Upadhyayula, and R. Wilkinson, Phys. Rev. C **104**, 055806 (2021).

X(3872) transport in heavy-ion collisions, Biaogang Wu, Xiaojian Du, Matthew Sibila and Ralf Rapp, Eur. Phys. J. A **57**, 122 (2021).

^{13}C(n,2nγ) γ -ray production in the 14−16 MeV incident neutron energy range, A.M. McEvoy, H.W. Herrmann, Y. Kim, T.S. Sedillo, H. Geppert-Kleinrath, C.R. Brune, T.N. Massey, A.V. Voinov, C.E. Parker, M.S. Rubery, and W. Stoeffl, Phys. Rev. C **103**, 064607 (2021).

A Constrained Molecular Dynamics (CoMD) study of nuclear near-ground-state properties, T. Depastas, G.A. Souliotis, K. Palli, A. Bonasera, and H. Zheng, HINPw6, Hellenic Institute of Nuclear Physics; 6th International Workshop; Perspectives on Nuclear Physics; From Fundamentals to Applications, EPJ web conferences **252** (Virtual), Athens, Greece (2021).

A heavy-ion production channel of ^{149}Tb via ^{63}Cu bombardment of ^{89}Y, John T. Wilkinson, Kendall E. Barrett, Samuel J. Ferran, Sean R. McGuinness, Lauren A. McIntosh, Mallory McCarthy, Sherry J. Yennello, Jonathan W. Engle, Suzanne E. Lapi, and Graham F. Peaslee, Appl. Radiat. Isot. **178**, 109935 (2021).

A novel approach to medical radioisotope production using inverse kinematics, Márcia Regina Dias Rodrigues, Victor E. Iacob, Ninel Nica, Brian Roeder, Gabriel Tabacaru, Kang Wang, Meixiang Yu, Paulo Zanotti-Fregonara, Justin Mabiala, Jedidiah Romo, Georgios A. Souliotis and Aldo Bonasera, HINPw6 –

Hellenic Institute of Nuclear Physics; 6th International Workshop; Perspectives on Nuclear Physics; From Fundamentals to Applications, EPJ Web of Conferences **252** (Virtual), Athens, Greece (2021).

A position and pulse shape discriminant p-terphenyl detector module, D.P. Scriven, G. Christian, G.V. Rogachev, C.E. Parker, L.G. Sobotka, S. Ahn, G. Chubarian, S. Ota, E. Aboud, J. Bishop, E. Koshchiy, and A.G. Thomas, Nucl. Instrum. Methods Phys. Res. **A1010**, 165492 (2021).

Abnormal flow of α particles in heavy-ion collisions at intermediate energies, G. Qu, Y. Huang, D. Peng, Z. Xu, W. Lin, H. Zheng, G. Tian, R. Han, C. Ma, M. Huang, P. Ren, J. Han, Z. Yang, X. Liu, and R. Wada, Phys. Rev. C **103**, 044607 (2021).

Advances in ^{211}At production at Texas A&M University, S.J. Yennello, L.A. McIntosh, J.D. Burns, E.E. Tereshatov, G. Tabacaru, L. McCann, S. Schultz, K. Lofton, A. Abbott, G. Avila, M. Berko, E. Engelthaler, K. Hagel, A. Hannaman, B. Harvey, A. Hood, M. McCarthy, A.B. McIntosh, M. Sorensen, Z. Tobin and A. Vonder Haar, HINPw6 -- Hellenic Institute of Nuclear Physics; 6th International Workshop; Perspectives on Nuclear Physics; From Fundamentals to Applications, EPJ Web of Conferences 252 (Virtual), Athens, Greece (2021).

Angular momentum removal by neutron and γ-ray emissions during fssion fragment decays, I. Stetcu, A.E. Lovell, P. Talou, T. Kawano, S. Marin, S.A. Pozzi, and A. Bulgac, Phys. Rev. Lett. **127**, 222502 (2021).

ARUNA: Advancing Science, Educating Scientists, Delivering for Society, Ani Aprahamian, Carl R. Brune, Michael A. Famiano, Alejandro Garcia, Calvin R. Howell, Robert V.F. Janssens, Zachary Meisel, Andrew Rogers, Ingo Wiedenhöver, Michael Wiescher, Steven W. Yates, and Sherry J. Yennello, Nucl. Phys. News **31**, 4 (2021).

Azimuthal anisotropy measurements of strange and multistrange hadrons in U+U collisions at $\sqrt{s_{NN}}$ =193 GeV at the BNL Relativistic Heavy Ion Collider, M.S. Abdallah, D.M. Anderson, C.A. Gagliardi, A. Hamed, T. Lin, X. Liu, Y. Liu, S. Mioduszewski, N.R. Sahoo, and R.E. Tribble, Phys. Rev. C **103**, 064907 (2021).

Benchmarking GEANT4 and PHITS for 14.8-MeV neutron transport in polyethylene and graphite materials, Xin Zhang, Zhi-Qiang Chen, Rui Han, Guo-Yu Tian, Bingyan Liu, Fu-Dong Shi, Hui Sun, and R. Wada, Fusion Eng. Des. **170**, 112720 (2021)

Chiral effective field theory and the high-density nuclear equation of state, C. Drischler, J.W. Holt, and C. Wellenhofer, Annu. Rev. Nucl. Part. Sci. **71**, 403 (2021).

Comparison of transverse single-spin asymmetries for forward π^0 production in polarized *pp*, *p*Al and *p*Au collisions at nucleon pair c.m. energy $\sqrt{s_{NN}}$=200 GeV, J. Adam, D.M. Anderson, C.A. Gagliardi, A.

Hamed, T. Lin, X. Liu, Y. Liu, S. Mioduszewski, N.R. Sahoo, and R.E. Tribble, Phys. Rev. D **103**, 072005 (2021).

Constraining the nonanalytic terms in the isospin-asymmetry expansion of the nuclear equation of state, Pengsheng Wen and Jeremy W. Holt, Phys. Rev. C **103**, 064002 (2021).

Coulomb field correction due to virtual e+e− production in heavy ion collisions, Thomas Settlemyre, Hua Zheng, and Aldo Bonasera, Nucl. Phys. **A1015**, 122282 (2021).

Cumulants and correlation functions of net-proton, proton, and antiproton multiplicity distributions in Au+Au collisions at energies available at the BNL Relativistic Heavy Ion Collider, M.S. Abdallah, D.M. Anderson, C.A. Gagliardi, A. Hamed, T. Lin, X. Liu, Y. Liu, S. Mioduszewski, N.R. Sahoo, and R.E. Tribble, Phys. Rev. C **104**, 024902 (2021).

Differential two-particle number and momentum correlations with the AMPT, UrQMD, and EPOS models in Pb-Pb collisions at $\sqrt{s_{NN}}$ =2.76TeV, Sumit Basu, Victor Gonzalez, Jinjin Pan, Anders Knospe, Ana Marin, Christina Markert, and Claude Pruneau, Phys. Rev. C **104**, 064902 (2021) .

Direct fusion measurement of the ^{8}B proton-halo nucleus at near-barrier energies, J.C. Zamora, V. Guimarães, G.V. Rogachev, S. Ahn, J. Lubian, E.N. Cardozo, E. Aboud, M. Assunção, M. Barbui, J. Bishop, A. Bosh, J. Hooker, C. Hunt, H. Jayatissa, E. Koshchiy, S. Lukyanov, R. O'Dwyer, Y. Penionzhkevich, B.T. Roeder, A. Saastamoinen, and S. Upadhyayula, Phys. Lett. B **816**, 136256 (2021).

Effects of QCD critical point on light nuclei production, Kai-Jia Sun, Feng Li and Che Ming Ko, Phys. Lett. B **816**, 136258 (2021).

Elastic scattering measurements for the ^{10}C+^{208}Pb system at E_{lab}= 66 MeV, R. Linares, Mandira Sinha, E.N. Cardozo, V. Guimarães, G.V. Rogachev, J. Hooker, E. Koshchiy, T. Ahn, C. Hunt, H. Jayatissa, S. Upadhyayula, B. Roeder, A. Saastamoinen, J. Lubian, M. Rodríguez-Gallardo, J. Casal, K.C.C. Pires, M. Assunção, Y. Penionzhkevich, and S. Lukyanov, Phys. Rev. C **103**, 044613 (2021).

Enhanced production of ^{99}Mo in inverse kinematics heavy ion reactions, Justin Mabiala, Marcia R.D. Rodrigues, Georgios A. Souliotis, Victor E. Iacob, Ninel Nica, Brian Roeder, Gabriel Tabacaru, Kang Wang, Jedidiah Romo, Dustin Scriven, Nolan Tenpas, and Aldo Bonasera, HINPw6 – Hellenic Institute of Nuclear Physics; 6th International Workshop; Perspectives on Nuclear Physics; From Fundamentals to Applications, EPJ Web of Conferences **252** (Virtual), Athens, Greece (2021).

Enhanced yield ratio of light nuclei in heavy ion collisions with a first-order chiral phase transition, Kai-Jia Sun, Che Ming Ko, Feng Li, Jun Xu and Lie-Wen Chen, Eur. Phys. J. A **57**, 4 (2021) .

Evidence against the Efimov effect in ^{12}C from spectroscopy and astrophysics, J. Bishop, G.V. Rogachev, S. Ahn, E. Aboud, M. Barbui, A. Bosh, J. Hooker, C. Hunt, H. Jayatissa, E. Koshchiy, R.

Malecek, S.T. Marley, M. Munch, E.C. Pollacco, C.D. Pruitt, B.T. Roeder, A. Saastamoinen, L.G. Sobotka, and S. Upadhyayula, Phys. Rev. C **103**, L051303 (2021).

Experimental investigation of abnormal transverse flow enhancement of αα particles in heavy-ion collisions, Y. Huang, W. Lin, H. Zheng, R. Wada, A. Bonasera, Z. Chen, J. Han, R. Han, M. Huang, K. Hagel, T. Keutgen, X. Liu, Y.G. Ma, C.W. Ma, Z. Majka, G. Qu, L. Qin, P. Ren, G. Tian, J. Wang, Z. Yang, and J.B. Natowitz, Phys. Rev. C **104**, 044611 (2021).

Extraction and separation of iridium(IV) and rhodium(III) from hydrochloric acid media by a quaternary ammonium-based hydrophobic eutectic solvent, Vira Zakusilova, Guillaume Zante, Evgeny E. Tereshatov, Charles M. Folden, III and Maria Boltoeva, Sep. Purif. Technol. **278**, 118814 (2021).

Extraction of the specific shear viscosity of quark-gluon plasma from two-particle transverse momentum correlations, Victor Gonzalez, Sumit Basu, Ana Marin, Jinjin Pan, Pedro Ladron de Guevara and Claude A. Pruneau, Eur. Phys. J. C **81**, 465 (2021).

Fission fragment intrinsic spins and their correlations, Aurel Bulgac, Ibrahim Abdurrahman, Shi Jin, Kyle Godbey, Nicolas Schunck, and Ionel Stetcu, Phys. Rev. Lett. **126**, 142502 (2021).

Four α correlations in nuclear fragmentation: a game of resonances, M. Huang, A. Bonasera, S. Zhang, H. Zheng, D.X. Wang, J.C. Wang, N. Song, X. Tang, L. Lu, G. Zhang, Z. Kohley, M.R.D. Rodrigues, Y.G. Ma, and S.J. Yennello, Chinese Phys. C **45**, 024003 (2021).

Global Λ-hyperon polarization in Au+Au collisions at $\sqrt{s_{NN}}$ = 3 GeV, M.S. Abdallah, D.M. Anderson, C. A. Gagliardi, A. Hamed, T. Lin, X. Liu, Y. Liu, S. Mioduszewski, N.R. Sahoo, and R.E. Tribble, Phys. Rev. C **104**, L061901 (2021)

Global microscopic description of nucleon-nucleus scattering with quantified uncertainties, T.R. Whitehead, Y. Lim and J.W. Holt, Phys. Rev. Lett. **127**, 182502 (2021).

Global polarization of Ξ and Ω Hyperons in Au+Au Collisions at $\sqrt{s_{NN}}$=200 GeV, J. Adam, D.M. Anderson, C.A. Gagliardi, A. Hamed, T. Lin, X. Liu, Y. Liu, S. Mioduszewski, N.R. Sahoo, and R.E. Tribble, Phys. Rev. Lett. **126**, 162301 (2021).

Impact of shell structure on the fusion of neutron-rich mid-mass nuclei, Varinderjit Singh, J.E. Johnstone, R. Giri, S. Hudan, J. Vadas, R.T. de Souza, D. Ackermann, A. Chbihi, Q. Hourdille, A. Abbott, C. Balhoff, A. Hannaman, A.B. McIntosh, M. Sorensen, Z. Tobin, A. Wakhle, S.J. Yennello, M.A. Famiano, K.W. Brown, C. Santamaria, J. Lubian, H.O. Sole,r and B.V. Carlson, Phys. Rev. C **104**, L041601 (2021).

Indirect determination of the astrophysical S factor for the ^{6}Li(p,γ)^{7}Be reaction using the asymptotic normalization coefficient method, G.G. Kiss, M. La Cognata, R. Yarmukhamedov, K.I. Tursunmakhatov, I. Wiedenhöver, L.T. Baby, S. Cherubini, A. Cvetinović, G. D'Agata, P. Figuera, G.L. Guardo, M. Gulino, S. Hayakawa, I. Indelicato, L. Lamia, M. Lattuada, F. Mudò, S. Palmerini, R.G. Pizzone, G.G. Rapisarda, S. Romano, M.L. Sergi, R. Spartá, C. Spitaleri, O. Trippella, A. Tumino, M. Anastasiou, S. A. Kuvin, N. Rijal, B. Schmidt, S.B. Igamov, S.B. Sakuta, Zs. Fülöp, Gy. Gyürky, T. Szücs, Z. Halász, E. Somorjai, Z. Hons, J. Mrazek, R.E. Tribble, and A.M. Mukhamedzhanov, Phys. Rev. C **104**, 015807 (2021) .

Invariant jet mass measurements in pp collisions at √s=200 GeV at RHIC, M.S. Abdallah, D.M. Anderson, C.A. Gagliardi, A. Hamed, T. Lin, X. Liu, Y. Liu, S. Mioduszewski, N.R. Sahoo, and R.E. Tribble, Phys. Rev. D **104**, 052007 (2021).

Investigation of the nuclear liquid-gas phase transition in the static AMD, W. Lin, P. Ren, X. Liu, H. Zheng, M. Huang, G. Qu and R. Wada, J. Phys. G **48**, 085103 (2021).

Isoscalar and isovector giant resonances in ^{44}Ca, ^{54}Fe, ^{64,68}Zn and ^{56,58,60,68}Ni, G. Bonasera, S. Shlomo, D.H. Youngblood, Y.-W. Lui, J. Button and X. Chen, Nucl. Phys. **A1010**, 122159 (2021).

Isospin mixing and the cubic isobaric multiplet mass equation in the lowest T=2, A=32A quintet, M. Kamil, S. Triambak, A. Magilligan, A. García, B.A. Brown, P. Adsley, V. Bildstein, C. Burbadge, A. Diaz Varela, T. Faestermann, P.E. Garrett, R. Hertenberger, N.Y. Kheswa, K.G. Leach, R. Lindsay, D.J. Marín-Lámbarri, F. Ghazi Moradi, N.J. Mukwevho, R. Neveling, J.C. Nzobadila Ondze, P. Papka, L. Pellegri, V. Pesudo, B.M. Rebeiro, M. Scheck, F.D. Smit, and H.-F. Wirth, Phys. Rev. C **104**, L061303 (2021).

Light nuclei production in a multiphase transport model for relativistic heavy ion collisions, Kai-Jia Sun, Che Ming Ko and Zi-Wei Lin, Phys. Rev. C **103**, 064909 (2021).

Longitudinal double-spin asymmetry for inclusive jet and dijet production in polarized proton collisions at √s=200 GeV, M.S. Abdallah, D.M. Anderson, C.A. Gagliardi, A. Hamed, T. Lin, X. Liu, Y. Liu, S. Mioduszewski, N.R. Sahoo, and R.E. Tribble, Phys. Rev. D **103**, L091103 (2021).

Measurement of e+e− momentum and angular distributions from linearly polarized photon collisions, J. Adam, D.M. Anderson, C.A. Gagliardi, A. Hamed, T. Lin, X. Liu, Y. Liu, S. Mioduszewski, N.R. Sahoo, and R.E. Tribble, Phys. Rev. Lett. **127**, 052302 (2021) .

Measurement of the sixth-order cumulant of net-proton multiplicity distributions in Au+Au collisions at $\sqrt{s_{NN}}$ = 27, 54.4, and 200 GeV at RHIC, M.S. Abdallah, D.M. Anderson, C.A. Gagliardi, A. Hamed, T. Lin, X. Liu, Y. Liu, S. Mioduszewski, N.R. Sahoo, and R.E. Tribble, Phys. Rev. Lett. **127**, 262301 (2021).

Measurement of transverse single-spin asymmetries of π^0 and electromagnetic jets at forward rapidity in 200 and 500 GeV transversely polarized proton-proton collisions, J. Adam, D.M. Anderson,

C.A. Gagliardi, A. Hamed, T. Lin, X. Liu, Y. Liu, S. Mioduszewski, N.R. Sahoo, and R.E. Tribble, Phys. Rev. D **103**, 092009 (2021).

Measurements of dihadron correlations relative to the event plane in Au+Au collisions at $\sqrt{s_{NN}}$ =200 GeV, H. Agakishiev, L. Chen, C.A. Gagliardi, A. Hamed, S. Mioduszewski, N.R. Sahoo, and R.E. Tribble, Chinese Phys. C **45**, 044002 (2021).

Methods for a blind analysis of isobar data collected by the STAR collaboration, J. Adam, D.M. Anderson, C.A. Gagliardi, A. Hamed, T. Lin, X. Liu, Y. Liu, S. Mioduszewski, N.R. Sahoo, and R.E. Tribble, Nucl. Sci. Tech. **32**, 48 (2021).

Multiplicity scaling of light nuclei production in relativistic heavy-ion collisions, Wenbin Zhao, Kai-Jia Sun, Che Ming Ko and Xiaofeng Luo, Phys. Lett. B **820**, 136571 (2021).

Comparison of heavy-ion transport simulations: Mean-field dynamics in a box, M. Colonna et al., Physical Review C **104**, 024603 (2021).??

Neutron occupancies and single-particle energies across the stable tin isotopes, S.V. Szwec, D.K. Sharp, B.P. Kay, S.J. Freeman, J.P. Schiffer, P. Adsley, C. Binnersley, N. de Séréville, T. Faestermann, R. F. Garcia Ruiz, F. Hammache, R. Hertenberger, A. Meyer, C. Portail, I. Stefan, A. Vernon, S. Wilkins, and H.-F. Wirth, Phys. Rev. C **104**, 054308 (2021).

New approach to precisely measure γ-ray intensities for long-lived fission products, with results for the decay of ^{95}Zr, K. Kolos, A.M. Hennessy, N.D. Scielzo, V.E. Iacob, J.C. Hardy, M.A. Stoyer, A.P. Tonchev, W.J. Ong, M.T. Burkey, B. Champine, J.A. Clark, P. Copp, A. Gallant, E.B. Norman, R. Orford, H.I. Park, J. Rohrer, D. Santiago-Gonzalez, G. Savard, A.J. Shaka, B.S. Wang, and S. Zhu, Nucl. Instrum. Methods Phys. Res. **A1000**, 165240 (2021).

New constraints on the ^{25}Al(p,γ) reaction and its influence on the flux of cosmic γ rays from classical nova explosions, L. Canete, G. Lotay, G. Christian, D.T. Doherty, W.N. Catford, S. Hallam, D. Seweryniak, H.M. Albers, S. Almaraz-Calderon, E.A. Bennett, M.P. Carpenter, C.J. Chiara, J.P. Greene, C. R. Hoffman, R.V.F. Janssens, J. José, A. Kankainen, T. Lauritsen, A. Matta, M. Moukaddam, S. Ota, A. Saastamoinen, R. Wilkinson, and S. Zhu, Phys. Rev. C **104**, L022802 (2021) .

New measurement of the $E_{c.m.}$=323keV resonance in the ^{19}F(p,γ)^{20}Ne reaction, M. Williams, P. Adsley, B. Davids, U. Greife, D. Hutcheon, J. Karpesky, A. Lennarz, M. Lovely, and C. Ruiz, Phys. Rev. C **103**, 055805 (2021).

Newtonian dynamics of imaginary time-dependent mean field theory, Aldo Bonasera, HINPw6, EPJ web conferences **252** (Virtual), Athens, Greece (2021).

Nonequilibrium information entropy approach to ternary fission of actinides, G. Röpke, J.B. Natowitz, and H. Pais, Phys. Rev. C **103**, L061601 (2021).

Normalizing flows for microscopic many-body calculations: An application to the nuclear equation of state, Jack Brady, Pengsheng Wen, and Jeremy W. Holt, Phys. Rev. Lett. **127**, 062701 (2021)

Nuclear Data Sheets for A=160, N. Nica, Nucl. Data Sheets **176**, 1 (2021).

Observation of $D^{\pm s}/D^0$ Enhancement in Au+Au Collisions at $\sqrt{s_{NN}}$ = 200 GeV, J. Adam, D.M. Anderson, C.A. Gagliardi, A. Hamed, T. Lin, X. Liu, Y. Liu, S. Mioduszewski, N.R. Sahoo, and R.E. Tribble, Phys. Rev. Lett. **127**, 092301 (2021).

Probing the symmetry energy with the spectral pion ratio, J. Estee, W.G. Lynch, C.Y. Tsang, J. Barney, G. Jhang, M.B. Tsang, R. Wang, M. Kaneko, J.W. Lee, T. Isobe, M. Kurata-Nishimura, T. Murakami, D.S. Ahn, L. Atar, T. Aumann, H. Baba, K. Boretzky, J. Brzychczyk, G. Cerizza, N. Chiga, N. Fukuda, I. Gašparić, B. Hong, A. Horvat, K. Ieki, N. Inabe, Y.J. Kim, T. Kobayashi, Y. Kondo, P. Lasko, H.S. Lee, Y. Leifels, J. Łukasik, J. Manfredi, A.B. McIntosh, P. Morfouace, T. Nakamura, N. Nakatsuka, S. Nishimura, H. Otsu, P. Pawłowski, K. Pelczar, D. Rossi, H. Sakurai, C. Santamaria, H. Sato, H. Scheit, R. Shane, Y. Shimizu, H. Simon, A. Snoch, A. Sochocka, T. Sumikama, H. Suzuki, D. Suzuki, H. Takeda, S. Tangwancharoen, H. Toernqvist, Y. Togano, Z.G. Xiao, S.J. Yennello, Y. Zhang, and M.D. Cozma, Phys. Rev. Lett. **126**, 162701 (2021).

Pseudorapidity distributions of charged particles in pp($\overline{p}$), p(d)A and AA collisions using Tsallis thermodynamics, J.Q. Tao, M. Wang, H. Zheng, W.C. Zhang, L. L. Zhu, and A. Bonasera, J. Phys. G **48**, 105102 (2021).

Radius and equation of state constraints from massive neutron stars and GW190814, Yeunhwan Lim, Anirban Bhattacharya, Jeremy W. Holt, and Debdeep Pati, Phys. Rev. C **104**, L032802 (2021).

Rapid extraction of short-lived isotopes from a buffer gas cell for use in gas-phase chemistry experiments, Part II: On-line studies with short-lived accelerator-produced radionuclides, S. Götz, S. Raeder, M. Block, Ch. E. Düllmann, C.M. Folden, III, K.J. Glennon, M. Götz, A. Hübner, E. Jäger, O. Kaleja, J. Khuyagbaatar, B. Kindler, J. Krier, L. Lens, B. Lommel, A.K. Mistry, Ch. Mokry, J. Runke, A. Såmark-Roth, E.E. Tereshatov, P. Thörle-Pospiech, M.F. Volia, A. Yakushev, and V. Yakusheva, Nucl. Instrum. Methods Phys. Res. **B507**, 27 (2021).

Rapidity distributions of Z=1 isotopes and the nuclear symmetry energy from Sn+Sn collisions with radioactive beams at 270 MeV/nucleon, M. Kaneko, T. Murakami, T. Isobe, M. Kurata-Nishimura, A. Ono, N. Ikeno, J. Barney, G. Cerizza, J. Estee, G. Jhang, J.W. Lee, W.G. Lynch, C. Santamaria, C.Y. Tsang, M.B. Tsang, R. Wang, D.S. Ahn, L. Atar, T. Aumann, H. Baba, K. Boretzky, J. Brzychczyk, N. Chiga, N. Fukuda, I. Gašparić, B. Hong, A. Horvat, T. Ichihara, K. Ieki, N. Inabe, Y.J. Kim, T. Kobayashi, Y. Kondo,

P. Lasko, H.S. Lee, Y. Leifels, J. Łukasik, J. Manfredi, A.B. McIntosh, P. Morfouace, T. Nakamura, N. Nakatsuka, S. Nishimura, R. Olsen, H. Otsu, P. Pawłowski, K. Pelczar, D. Rossi, H. Sakurai, H. Sato, H. Scheit, R. Shane, Y. Shimizu, H. Simon, T. Sumikama, D. Suzuki, H. Suzuki, H. Takeda, S. Tangwancharoen, Y. Togano, H. Törnqvist, Z. Xiao, S.J. Yennello, J. Yurkon, and Y. Zhang, Phys Lett B **822**, 136681 (2021).

Restoring broken symmetries for nuclei and reaction fragments, Aurel Bulgac, Phys. Rev. C **104**, 054601 (2021).

Search for in-band transitions in the candidate superdeformed band in ^{28}Si, L. Morris, D G. Jenkins, M.N. Harakeh, J. Isaak, N. Kobayashi, A. Tamii, S. Adachi, P. Adsley, N. Aoi, A. Bracco, A. Brown, M.P. Carpenter, J.J. Carroll, S. Courtin, F.C.L. Crespi, P.J. Davies, G. Fruet, Y.D. Fang, H. Fujita, G. Gey, T.H. Hoang, N. Ichige, E. Ideguchi, A. Inoue, C. Iwamoto, T. Koike, M. Kumar Raju, M.L. Liu, D. Montanari, P. von Neumann-Cosel, S. Noji, H.J. Ong, D. Savran, J.M. Schmitt, C. Sullivan, B. Wasilewska, M. Weinert, V. Werner, Y. Yamamoto, R.G.T. Zegers, X.H. Zhou, and S. Zhu, Phys. Rev. C **104**, 054323 (2021).

Semiclassical shell-structure micro-macroscopic approach for level density, A.G. Magner, A.I. Sanzhur, S.N. Fedotkin, A.I. Levon, and S. Shlomo, Phys. Rev. C **104**, 044319 (2021)

Shell-structure and asymmetry effects in level densities, A.G. Magner, A.I. Sanzhur, S.N. Fedotkin, A.I. Levon, and S. Shlomo, Int. J. Mod. Phys. E **30**, S0218301321500920 (2021) .

Semi-classical approximation description of static properties of nuclei, S. Shlomo and A.I. Sanzhur, Mod. Phys. Lett. A **36**, 213008 (2021).

Spin quantization in heavy ion collision, Hua Zheng and Aldo Bonasera, Symmetry **13**, 1777 (2021).

Texas A&M US Nuclear data program, Ninel Nica, HINPw6 – Hellenic Institute of Nuclear Physics; 6th International Workshop; Perspectives on Nuclear Physics; From Fundamentals to Applications, {EPJ} Web of Conferences **252** (Virtual), Athens, Greece (2021).

The TAMUTRAP facility: A Penning trap facility at Texas A\&M University for weak interaction studies, P.D. Shidling, M. Mehlman, V.S. Kolhinen, G. Chubarian, L. Cooper, G. Duran, E. Gilg, V.E. Iacob, K.S. Marble, R. McAfee, D. McClain, M. McDonough, M. Nasser, C. Gonzalez-Ortiz, A. Ozmetin, B. Schroeder, M. Soulard, G. Tabacaru, and D. Melconian, Int. J. Mass Spectrom. **468**, 116636 (2021).

SECTION VI

APPENDIX

TALKS PRESENTED
April 1, 2021 – March 31, 2022

Status of $^{12}C+^{12}C$ fusion and Trojan horse as invaluable tool to advance it, **A. Zhanov**, **Invited talk**, IReNA/ChETEC meeting on nuclear reaction measurements underground, Rome Global Gateway, Roma Italia (April 2021).

Probing the nuclear symmetry energy with rare isotope beams, **C.M. Ko**, **Invited talk**,Fudan University, Shanghai, China (September 2021).

Coalescence production of light nuclei in HIC, **C.M. Ko**, **Invited talk**, Fudan University, Fudan University, Shanghai, China (December 2021).

Chiral kinetic model study of chiral magnetic and vortical effects, **C.M. Ko**, **Invited talk**, Fudan University, Shanghai, China (February 2022).

Development of a methodology for the radiochronometric analysis of ^{226}Ra-containing radiological samples for nuclear forensics, **J. Garcia**, **Talk**, ACS Spring 2022 National Meeting & Exposition, San Diego, California (March 2022).

Automation of astatine recovery from nitric acid media, **E. Tereshatov**, **Talk**, ACS Spring 2022 National Meeting & Exposition, San Diego, California (March 2022).

Metal adsorption on functionalized silicon detectors for the future study of meitnerium chemistry, **V. Zakusilova**, **Talk**, American Chemical Society Spring 2022, Bonding Through Chemistry, San Diego, California (March 2022).

Inclusive excellence: You can make a difference, **S.J. Yennello**, **Invited talk**, Argonne National Laboratory, Argonne, Illinois (March 2022).

Probing the equation-of-state with heavy ion collisions, **S.J. Yennello**, **Invited talk**, TRIUMF, Vancouver, Canada (March 2022).

Diving deep on the periodic table to find a treatment for cancer, **S.J. Yennello**, **Invited talk**, Simon Frasier University, Burnaby, Canada (March 2022).

Diving deep on the periodic table to find a treatment for cancer, **S.J. Yennello**, **Invited talk**, University of British Columbia, Vancouver, Canada (March 2022).

Diving deep on the periodic table to find a treatment for cancer, **S.J. Yennello**, **Invited talk**, University of Victoria, Victoria, Canada (February 2022).

Characterizing and correcting effects on measured excitation energies in DAPPER, **A. Abbott**, **Virtual Talk**, 2022 SSAP Symposium, College Station, Texas (February 2022).

Novel experiments with a TPC: beta-delayed charged-particle spectroscopy and neutron-induced reactions, **J. Bishop**, **Invited Talk**, IOP Nuclear Physics Group Colloquium, University of Birmingham (Remote), Birmingham, United Kingdom (February 2022).

Nuclear chemistry: Fundamental science serving society, **S.J. Yennello**, **Invited Talk**, International Atomic Energy Agency CUWiP, virtual (January 2022).

Neutron-upscattering enhancement of the triple-alpha process, **J. Bishop**, **Invited Talk**, Saint Mary's University (Remote), Halifax, Canada (January 2022) .

Status of $^{12}C+^{12}C$ fusion and Trojan horse as Invaluable tool to advance it, **A. Zhanov**, **Invited talk**, IReNA/ChETEC meeting on nuclear reaction measurements underground, Rome Global Gateway, Roma Italia (April 2021).

Probing the nuclear symmetry energy with rare isotope beams, **C.M. Ko**, **Invited talk**,Fudan University, Shanghai, China (September 2021).

Coalescence production of light nuclei in HIC, **C.M. Ko**, **Invited talk**, Fudan University, Fudan University, Shanghai, China (December 2021).

Developing isotope production capabilities with heavy-ion beams at Texas A&M University, **L. McIntosh**, **Talk**, The International Chemical Congress of Pacific Basin Societies 2021, Honolulu, Hawaii (December 2021).

Fast and efficient recovery of ^{211}At at Texas A&M University: Gaining insight of at chemistry in the liquid phase, **E. Tereshatov**, **Talk**, Pacifichem 2021, College Station, Texas (December 2021).

Time-resolved equilibration: How to measure the motion of protons and neutrons on a subzeptosecond timeframe time-resolved equilibration: How to measure the motion of protons and neutrons on a subzeptosecond timeframe, **A. McIntosh**, **Invited Talk**, 21st Zimanyi School Winter Workshop on Heavy Ion Physics, Wigner Research Center for Physics (Zoom), Budapest, Hungary (December 2021).

The asymmetry dependence of temperatures measured in fusion-evaporation reactions and in multi-fragmentation reactions The asymmetry dependence of temperatures measured in fusion-evaporation reactions and in multi-fragmentation reactions, **A. McIntosh**, **Invited Talk**, 2021 International Workshop on the Multi-facets of EOS and Clustering (IWM-EC 2021), GANIL, Caen, France (November 2021).

High and low energy nucleon productions in intermediate heavy ion collisions, using AMD with Fermi boost and 3Body collision terms, **R. Wada**, **Invited Talk**, IWM-EC 2021: International workshop on Multi-facets of EOS and Clustering, GANIL, CAEN, France (November 2021).

V_{ud} from superallowed nuclear β+ decays: new high-precision experimental results, **V. Iacob**, **Talk**, 11th International Workshop on the CKM Unitarity Triangle (CKM 2021), (Virtual), Melbourne, Australia (November 2021).

TAMU NSDD CENTER report 2021, **N. Nica**, **Talk**, Nuclear Data Week(s) 2021 (CSEWG-USNDP-NDAG), Brookhaven National Laboratory, National Nuclear Data Center (NNDC) (Virtual), Upton, New York (November 2021).

Medical radioisotopes production studies: ^{67}Cu case, **N. Nica**, **Talk**, Nuclear Data Week(s) 2021 (CSEWG-USNDP-NDAG), Brookhaven National Institute, National Nuclear Data Center (NNDC) (Virtual), Upton, New York (November 2021).

Nuclear science serving society: Advances in ^{211}At production at Texas A&M University, **S.J. Yennello**, **Invited Talk**, Massachusetts Institute of technology, Cambridge, Massachusetts (October 2021).

Evidence against the Efimov effect in ^{12}C from spectroscopy and astrophysics, **J. Bishop**, **Talk**, 2021 Fall Meeting of the APS Division of Nuclear Physics, Virtual (October 2021).

Current capabilities in astatine-211 production at Texas A&M University, **L. McIntosh**, **Talk**, Division of Nuclear Physics, American Physical Society, Boston, Massachusetts (October 2021).

Probing the asymmetry dependence of the nuclear caloric curve in fusion-evaporation reactions, **A. McIntosh**, **Talk**, 2021 International Symposium on the Nuclear Symmetry Energy (NuSym21), Virtual (October 2021).

Evidence for the asymmetry dependence of the nuclear caloric curve in fusion reactions, **A. McIntosh**, **Talk**, Meeting of the Division of Nuclear Physics of the American Physical Society, Virtual (October 2021).

Probing a possible excited-state of tritium via the ^{6}He(p,t) reaction with TexAT, **C. Parker**, **Talk**, 2021 Fall Meeting of the APS Division of Nuclear Physics, Virtual (October 2021).

Using DAPPER to measure ^{58}Fe Photon Strength Function via the Oslo method, **A. Abbott**, **Talk**, CENAUR LANL Visit, Los Alamos National Lab, Los Alamos, New Mexico (October 2021).

Development of the TexNeut array for basic science, **C. Parker**, **Talk**, CENTAUR-JINPA Neutron Detector Workshop, Virtual, College Station, Texas (September 2021).

From there and back again: perspectives of an Ohio graduate student and visitor, **C. Parker**, **Talk**, 50 Years of Discovery at the Edwards Accelerator Laboratory, Ohio University, Athens, Ohio (September 2021).

Impacts of neutron excess on equilibrating and equilibrated nuclear systems, **A. McIntosh**, **Talk**, Texas A&M University Cyclotron Institute, College Station, Texas (September 2021).

Characterization of thiolate self-assembled monolayers on gold-coated silicon chips for future detection of radioactive isotopes, **V. Zakusilova**, **Talk**, American Chemical Society Fall 2021, Resilience of Chemistry, Virtual, Atlanta, Georgia (August 2021).

Investigation of signatures of short-range correlations in intermediate energy heavy ion collisions, **K. Hagel**, **Talk**, Sherry Yennello Glenn Seaborg Award Symposium, Atlanta, Georgia (August 2021).

Thermodynamics, dynamics and equilibration, **A. McIntosh**, **Talk**, Glenn Seaborg award symposium in honor of Sherry Yennello, ACS Fall Meeting, Atlanta, Georgia (August 2021).

Fundamental science impacting society, **S.J. Yennello**, **Invited talk**, ACS meeting, Atlanta, Georgia (August 2021).

Using DAPPER to measure Photon Strength Functions via the Oslo Method, **A. Abbott**, **Talk**, ACS Seaborg Symposium , Georgia World Congress Center, Atlanta, Georgia (August 2021).

Non-conventional solvents for astatine and bismuth separation, **E. Tereshatov**, **Talk**, ACS Fall 2021, Atlanta, Georgia (August 2021).

Advancing research in Texas through experiments in medical isotope science, **L. McIntosh**, **Talk**, ACS Fall Meeting, Atlanta, Georgia (August 2021).

Advances in nuclear spectroscopy with TPCs, **J. Bishop**, **Talk**, Low-Energy Community Meeting, Virtual (August 2021).

Steps forward in astatine-211 production and chemistry at Texas A&M University, **L. McIntosh**, **Talk**, DOE Isotope Program Astatine-211 User Meeting, Knoxville, Tennessee (August 2021).
Search for Bose condensation in nuclei, **G. Rogachev**, **Invited talk**, From quasi-classics to Bose condensation and everything in between, College Station (Virtual) (August 2021).

Ongoing experiments with TexAT: Neutron-induced, transfer, and elastic scattering reactions, **J. Bishop**, **Talk**, Low-Energy Community Meeting, Virtual (August 2021).

Recent experimental progresses in balance function measurements from ALICE and STAR experiments, **J. Pan**, **Talk**, Balance Function Workshop, Michigan State University, East Lansing, Michigan (August 2021).

New class of chemical compounds for studying medical radioisotopes and superheavy elements, **E. Tereshatov**, **Talk**, Promotion Seminar, Texas A&M University, College Station, Texas (August 2021).

Astatine production toward targeted alpha therapy, **S.J. Yennello**, **Invited Talk**, NSCL - MSU, East Lansing, Michigan (July 2021).

Diversifying physics via a nuclear science summer camp, **L. McIntosh**, **Talk**, 7th IUPAP International Conference on Women in Physics, Virtual (July 2021).

Geant4 Masterclass: simulation of TPCs, **J. Bishop**, **Invited talk**, University of Connecticut, LNS Avery Point, Groton, Connecticut (July 2021).

Clustering in light nuclei, Hoyle state and Efimov effect, **G. Rogachev**, **Invited talk**, Nuclear Physics at the Edge of stability, Virtual, Trento, Italy (June 2021).

Using trapped atoms and ions for fundamentally cool physics, **D. Melconian**, **Invited Talk**, REU seminars at the CI, Cyclotron Institute, Texas A&M University, College Station, Texas (june 2021).

Functionalized surfaces and oxidation states of on-line produced thallium, **E. Tereshatov**, **Talk**, TASCA 21, Darmstadt, Germany (June 2021).

Development of a neutron detector array for basic science: TexNeut, **C. Parker**, **Invited Talk**, ISR-1 Seminar, LANL, virtual (June 2021).

Towards measuring the Fierz interference parameter in ^{6}He β decay from a Penning trap using the CRES technique, **D. Melconian**, **Invited talk**, 2021 CAP Congress, Virtual, Canada (June 2021).

Direct and indirect measurements of charged-particle capture reactions, **G. Christian**, **Invited talk**, Canadian Association of Physicists Annual Congress, Virtual, Canada (June 2021).

TAMU NSDD evaluation center report 2021, **N. Nica**, **Talk**, Technical Meeting of the NSDD network (Virtual), Nuclear Data Services, IAEA Vienna , Vienna, Austria (May 2021).

Texas A&M US Nuclear DATA Program, **N. Nica**, **Talk**, HINPw6 – Hellenic Institute of Nuclear Physics; 6th International Workshop; Perspectives on Nuclear Physics; From Fundamentals to Applications, Hellenic Institute of Nuclear Physics, Athens, Greece (May 2021)

Precise branching ratio measurement for the superallowed β+ decay of ^{34}Ar, **V. Iacob**, **Talk**, 6th Workshop of The Hellenic Institute of Nuclear Physics (HINPw6), (Virtual), Athens, Greece (May 2021).

Calculation of the $^{12}C+^{12}C$ sub-barrier fusion cross section in an imaginary time-dependent mean field theory, **A. Bonasera**, **Invited talk**, HINPw6 workshop, Athens, Greece (May 2021).

CENTAUR and LANSCE synergistic science, **S.J. Yennello**, **Invited talk**, LANSCE Futures Spring Workshop 2021: Nuclear Science, LANL, Virtual, Texas (May 2021).

Preparing DAPPER to measure Photon Strength Functions, **A. Abbott**, **Talk**, 2021 CENTAUR Review, Virtual, College Station, Texas (April 2021).

About difficult evaluation decisions: a case study, **N. Nica**, **Talk**, ENSDF 2021, National Nuclear Data Center, Brookhaven National Laboratory , Upton, New York (April 2021).

Normalizing flows for microscopic calculations of the equation of state, **J. Holt**, **Invited talk**, Nuclear forces for precision nuclear physics, Institute for Nuclear Theory, Seattle, Washington (April 2021).

Identification of multinucleon transfer products with short-lived daughter nuclei, **A. Hood**, **Talk**, American Physical Society, Online, Virtual (April 2021).

Constraining the nonanalytic terms in the isospin-asymmetry expansion of nuclear equation of state, **P. Wen**, **Talk**, APS April Meeting 2021, College Station, Texas (April 2021).

Influence of Z and N on fusion-evaporation cross sections for heavy element synthesis, **C. Folden III**, **Invited talk**, APS Virtual April Meeting, College Park, Maryland (April 2021).

Experimental tests of isospin symmetry breaking in superallowed beta decay, **V. Iacob**, **Talk**, APS Virtual April Meeting, College Park, Maryland (April 2021).

Isotope production capabilities at Texas A&M University, **L. McIntosh**, **Talk**, APS Virtual April Meeting, College Park, Maryland (April 2021).

Response functions for hot and dense nuclear nuclear matter from chiral nuclear forces, **E. Shin**, **Talk**, APS Virtual April Meeting, College Park, Maryland (April 2021).

Progress in the development and characterization of position- and n/γ-discriminating neutron detector modules, **C. Parker**, **Talk**, APS Virtual April Meeting, College Park, Maryland (April 2021).

Characterization of 1-(11-mercaptoundecyl)imidazole self-assembled monolayers on gold-coated silicon chips, **V. Zakusilova**, **Talk**, American Chemical Society Spring 2021, Macromolecular Chemistry: The Second Century, Virtual , San Antonio, Texas (April 2021).

Smashing gold on gold: producing and identifying trans-target multinucleon transfer products, **A. Hood**, **Talk**, Texas Section of the APS, Texas A&M University at Corpus Cristi, Virtual, Texas (April 2021).

Influence of Z and N on the synthesis of heavy elements in fusion-evaporation reactions, **C. Folden III**, **Invited talk**, ACS Spring 2021 Virtual Meeting & Expo, Washington, DC (April 2021).

Conventional solvents for astatine and bismuth separation, **E. Tereshatov**, **Talk**, ACS Spring 2021, Virtual, College Station (April 2021).

Normalizing flows for microscopic calculations of the equation of state, **J. Holt**, **Invited talk**, Nuclear Physics Journal Club, University of Illinois Urbana Champaign, Urbana, Illinois (April 2021).

RESEARCH PERSONNEL AND ENGINEERING STAFF

April 1, 2021 - March 31, 2022

Faculty and Research Group Leaders

Adsley, Philip – Assist. Prof. of Physics – From 8/1/2021
Bonasera, Aldo - Senior Scientist
Christian, Gregory – Adjunct Professor
Fries, Rainer - Professor of Physics
Folden, III, Charles M. - Assoc.. Prof. of Nuclear Chemistry
Gagliardi, Carl A. - Professor of Physics
Hardy, John C. - Professor Emeritus
Holt, Jeremy - Assist. Professor of Physics
Ko, Che Ming – Professor of Physics
Melconian, Dan - Professor of Physics
Mioduszewski, Saskia - Professor of Physics
Natowitz, J. B. - Professor Emeritus
Rapp, Ralf - Professor of Physics
Rogachev, Grigory - Professor of Physics and Department Head of Physics and Astronomy
Shlomo, Shalom - Senior Scientist
Tribble, Robert E. – Professor of Physics (20%)
Yennello, Sherry J. - Professor of Chemistry, Bright Chair, Director
Youngblood, Dave H. - Professor Emeritus
Zhanov, Akram M. - Senior Scientist

Research Staff

Ärje, Juha – Research Scientist
Barbui, Marina - Assist. Research Scientist
Bishop, Jack – Assist. Research Scientist – From 11/1/2021
Chubaryan, Grigor - Research Scientist
Clark, Henry - Accelerator Physicist (50%)
Gauthier, Jerome - Assist. Research Scientist
Goldberg, Vladilen - Research Scientist, Retired
Hagel, John C. - Research Scientist (50%)
Horvat, Vladimir - Research Scientist (50%)
Iacob, Victor - Research Scientist
Koshchiy, Yevgen - Assoc. Research Scientist
Lui, Yiu-Wing - Research Scientist
McIntosh, Alan - Assoc. Res. Scientist – From 10/1/2021
McIntosh, Lauren –Assist. Research Scientist
Nica, Ninel - Associate Research Scientist
Rodrigues, Marcia Dias - Assist. Res. Scientist
Saastamoinen, Antti (50%)
Shidling, Praveen - Assist. Research Scientist – To 12/16/2021
Tereshatov, Evgeny - Assoc. Research Scientist – From 11/1/2021
Wada, Roichi (40%)

Accelerator Physics and Radiation Line Staff

Avila, Geoffrey – Research Assistant
Clark, Henry - Accelerator Physicist (50%)
Horvat, Vladimir - Research Scientist (50%)
Hyman, Bruce - Research Associate
Kim, George - Accelerator Physicist
May, Don – Senior Accelerator Physicist
Roeder, Brian - Accelerator Physicist
Park, Hyo-In - Accelerator
Saastamoinen, Antti (50%)
Tabacaru, Gabriel - Accelerator Physicist

Computer Systems Staff

Burch, Jr. Robert Lead Microcomputer/LAN Administrator
Hagel, John C. Research Scientist (50%)

Engineering Staff

Molitor, Stephen - Senior Mechanical Engineer
Olsen, Robert - Senior Mechanical Engineer

Postdoctoral Research Associates

Bishop, Jack – To 10/31/2021
Childers, Katherine – To 11/12/2021
Hood, Ashley - To 9/30/2021
Kolhinen, Veli Sakari
Kordell, Michael
Pan, Jinjin
Parker, Cody
Picayo, Gabriela – From 11/15/2021
Sun KaiJia

STUDENTS

April 1, 2021 - March 31, 2022

Graduate Students and Research Assistants

Abbott, Austin
Aboona, Bassam
Aboud, Eric
Anderson, Derek
Atchison, Joseph - To 5/31/2021
Dede, Stefania
Glennon, Kevin
Hankins, Travis – From 9/1/2021
Hannaman, Andy
Harris, Emily
Haynes, Isaac – From 9/1/2021
Henderson, Lawrence
Hunt, Curtis – To 1/15/2022
Kim, Byunggyu
Kirkland, Amelia – From 9/1/2021
Liu, Yanfang
Loftin, Sarah – From 9/1/2021 (on leave)
Ma, Tianyang – From 2/1/2022
McCain, David
Mildon, Jordan – From 9/1/2021
Nasser, Morgan
Onyango, Thomas
Ozmetin, Asim
Rider, Robert – From 9/1/2021
Robicheaux, Stephen
Roosa, Michael
Sarver, Issac
Schultz, Steven
Scriven, Dustin
Sengupta, Arjun
Settlemyre, Thomas
Shin, Eunkyoung
Sorensen, Maxwell
Tang, Zhanduo
Tobin, Zachary
Tyler, Jace – From 9/10/2021
Wen, Pengshen
Whitehead, Taylor – To 5/31/2021
Zakusilova, Vera
Zamora, Cirilo – To 6/12/2021

Undergraduates and Student Technicians

Alafa, Alex – From 6/1/2021
Ascione, Alexander
Daye, Niya – From 3/24/2022
Drgac, Delayni – From 7/5/2021 to 10/1/2021
Gallegos, Rachel – From 9/13/2021
Godoy, Nicolas – From 11/1/2021 To 3/20/2022
Griffin, Morgan – To 5/31/2021
Jeffery, Logan
Jeske, Colby
Kovacs, Isabel – From 2/4/2022
Lofton, Kylie
Reuter, Madison – From 11/17/2021
Reyes, Aaron – To 12/1/2021
Roa, Karthik – To 9/6/2021
Romo, Jedidiah – To 1/14/2022
Stewart, Laynie – From 11/16/2021
Tagoe, Eric – From 3/22/2022

ORGANIZATIONAL CHART - CYCLOTRON INSTITUTE

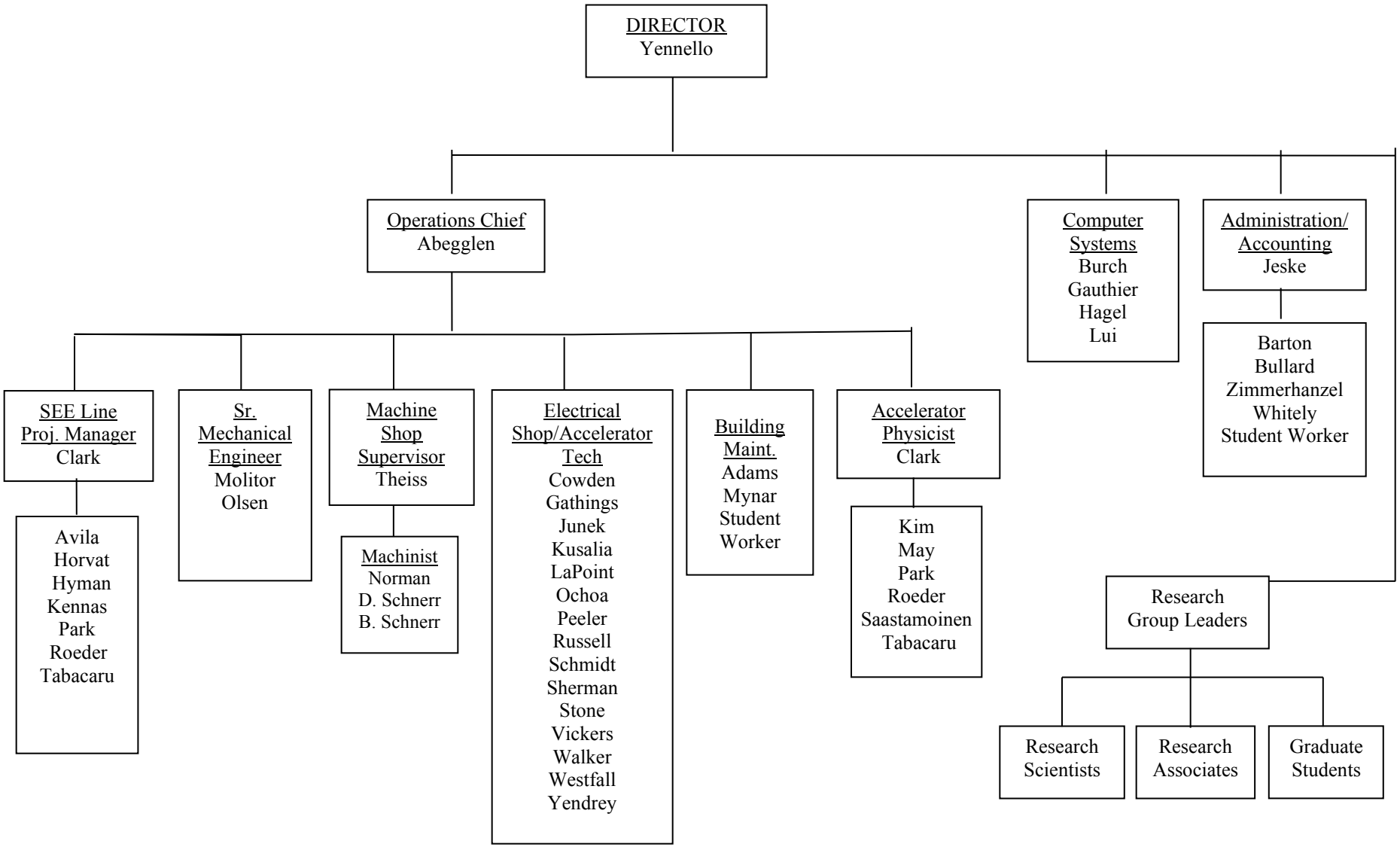

STUDENTS WHO RECEIVED GRADUATE DEGREES
FROM THESIS WORK CONDUCTED
AT
THE CYCLOTRON INSTITUTE

April 1, 2021 – March 31, 2022

Name	Year	Thesis Title	Advisor	Present Position
Joseph Atchison	2021	*The electric conducitivity of hot pion matter*	R. Rapp	Postdoctoral research associate at Abilene Christian University (ACU)
Taylor Whitehead	2021	*Microscopic Nucleon-Nucleus Optical Potentials from Chiral Effective Field Theory*	J.W. Jeremy	postdoc at Michigan State University
Curtis Hunt	2022	*The study of neutron-rich nuclei, ^{9}Li and ^{13}Be, through isobaric analogue states using resonant scattering*	G. Rogachev	Postdoc. At Facility for Rare Isotope Beams at Michigan State University

INSTITUTE COLLOQUIA AND SEMINARS

April 1, 2021 - March 31, 2022

2021

April 6	Dr. Christian Drischler, FRIB Theory Fellow, Michigan State University, East Lansing, Michigan	*From chiral interactions to neutron stars and why EFT truncation error matter*
April 13	Dr. Michael Wiescher, Freimann Professor of Physics, University of Notre Dame, South Bend, Indiana	*Carbon fusion in late stellar evolution*
April 20	Dr. Joaquin Drut, Associate Professor, University of North Carolina at Chapel Hill, North Carolina	*From dilute to dense, one particle at a time: calculating and resuming the viral expansion of quantum hases*
April 27	Dr. Paul Schaffer, Ph. D. Associate Laboratory Director, Life sciences, TRIUMF, Associate Professor, Radiology, University of British Columbia, and Adjunct Professor, Chemistry, Simon Fraser University, British Columbia, Canada	*Accelerator-based radionuclide and radiopharmaceutical research at TRIUMF*
July 22	Dr. Jack Bishop, Postdoctoral Research Associate, Cyclotron Institute, Texas A&M University, College Station, Texas	*Experimental studies of ^{12}C with the TexAT TPC*
September 15	Dr. Alan Mcintosh, Assistant Research Scientist, Cyclotron Institute, Texas A&M University, College Station, Texas	*Impacts of neutron excess on equilibrating and equilibrated nuclear systems*
October 5	Professor Ariel Zhitnitsky, Department of Physics and Astronomy, university of British Coulumbia, British Columbia, Canada	*Axion quark nuggets and matter-antimatter asymmetry as two sides of the samecoin: theory, observations and future searches*
November 9	Dr. Giuseppe Cardella, Research Director, INFN Catania, Catania, Italy	*On the gamma and particle decay of excited levels of ^{12}C: the case of the Hoyle and 9.64 MeV levels*
November 16	Professor Dellon Doru, Senior Research, Horia Hulubel National Institute of Physics and Nuclear Engineering	*Alpha-decay versus alpha-clustering*

November 23	Dr. Abdou Chbihi, CNRS Research Director, Grand Accélérateur National d'Ions Lourds (GANIL), Caen, France	*Exploring the EOS at low densities*
November 30	Dr. Taka Kajino, Beihang University, Beijing, China	*Origin of heavy nuclei and the roles of fission and RNB physics*
December 6	Dr. Ian Thompson, Staff Scientist, Lawrence Livermore national Laboratory, Livermore, California	*Using experiments and theories for nuclear data evaluations*

2022

February 22	Dr. Remco Zegers, NSCL Associate Director for Experimental Nuclear Science and Professor at Michigan State University, East Lansing, Michigan	*Electron captures in supernovae*
March 1	Dr. Phiala Shanahan, Assistant Professor, Massachusetts Institute of Technology, Cambridge, Massachusetts	*From quarks to nuclei: A computational revolution*